ISRES Publishing

The Eurasia Proceedings of Science, Technology, Engineering & Mathematics

EPSTEM

ISSN: 2602-3199

IConTES 2020: International Conference on Technology, Engineering and Science

October 29- November 1, 2020

Antalya, Turkey

Edited by: Mehmet Ozaslan (Chair), Gaziantep University, Turkey

The Eurasia Proceedings of
Science, Technology, Engineering & Mathematics (EPSTEM)
ISSN: 2602-3199

IConTES 2020 DECEMBER

Volume 11, Pages 1-179 (December 2020)
The Eurasia Proceedings of Science, Technology, Engineering & Mathematics
EPSTEM
e-ISSN: 2602-3199

Address: Istanbul C. Cengaver S. No 2 Karatay/Konya/TURKEY
Website: www.isres.org
Contact: isresoffice@gmail.com

Edited by: Mehmet Ozaslan
Articles: 1-29
Conference: IConTES 2020: International Conference on Technology, Engineering and Science
Dates: October 29 – November 1, 2020
Location: Antalya, Turkey
Conference Chair(s): Prof. Dr. Mehmet Ozaslan, Gaziantep University, Turkey

CONTENTS

The Eurasia Proceedings of
Science, Technology, Engineering & Mathematics (EPSTEM)
ISSN: 2602-3199

The Eurasia Proceedings of
Science, Technology, Engineering & Mathematics (EPSTEM)
ISSN: 2602-3199

The Eurasia Proceedings of Science, Technology, Engineering & Mathematics (EPSTEM)
ISSN: 2602-3199

The Eurasia Proceedings of Science, Technology, Engineering & Mathematics (EPSTEM), 2020

Volume 11, Pages 1-4

IConTES 2020: International Conference on Technology, Engineering and Science

Screening Design of Experiment Applied to Dispersive Liquid-Liquid Microextraction of UV Filters from Water

Jelena LUKIĆ
Innovation Center of the Faculty of Technology and Metallurgy

Tatjana ĐURKIĆ
Belgrade University

Jelena RADULOVIĆ
Anahem Laboratory

Tamara BAKIĆ
Innovation Center of the Faculty of Technology and Metallurgy

Antonije ONJIA
Belgrade University

Abstract: A Plackett-Burman factorial design (PBD) has been used for the optimization of dispersive liquid-liquid microextraction (DLLME) of UV filters from water. The experimental procedure included a DLLME sample preparation prior to high-performance liquid chromatography triple quadrupole mass spectrometry (HPLC-MS/MS) measurements. The variables of the DLLME process for simultaneous preconcentration of UV filters (avobenzone and octocrylene) have been studied using PBD with twelve experimental runs. Several experimental variables including the extractant type, pH value, the disperser type, extractant volume, disperser volume, vortexing/sonication, centrifugation speed, reconstitution solvent, salt content, temperature, and centrifugation time were considered in the optimization process. PBD results revealed the most important variables that affected the extraction efficiency (EF). The first three most influential variables, as showed using a Pareto graph, were in the following order: the extractant volume > the disperser type > the extraction temperature. Based on the main effects plot, it was revealed that some variables (pH value, the disperser type, extractant volume, temperature, centrifugation speed, salt content) increased over the experimental domain, while the others (the extractant type, disperser volume, vortexing/sonication, centrifugation time, reconstitution solvent) decreased.

Keywords: UV filters, Plackett- Burman, DLLME, HPLC-MS/MS

Introduction

Organic UV filters are the main ingredients in many personal care products intended to protect users from UV solar radiation (Chisvert & Salvador, 2018). The daily use of these products has led to the increased detection of UV filters in water samples. The wide range of UV filters discovered in water samples around the World has caused concern due to the persistence of these compounds, as well as the harmful biological effects on aquatic organisms (Brausch & Rand, 2011). Since the complexity of the matrix and low concentrations of UV filters in the environmental water samples, a pre-treatment step for sample enrichment and clean-up is necessary.

Recently, in addition to traditional techniques, alternative ones such as dispersive liquid-liquid microextraction (DLLME) have been used for this purpose (Ramos et al., 2019). This technique is based on a ternary solvent system comprising an aqueous donor sample, an organic extraction solvent (non-miscible in water), and a disperser solvent (miscible in both extraction and donor phases) (Chisvert, Benedé, & Salvador, 2018).

- Selection and peer-review under responsibility of the Organizing Committee of the Conference

A large number of the DLLME experimental variables should be studied in order to optimize the analytical recovery. Traditional the one-variable-at-a-time (OVAT) optimization approach, in which one variable is changed while keeping all others constant, is time-consuming and inefficient to study the interactions among the variables. The modern approach to the optimization uses the design of experiment (DOE) methodology that enables all variables to be changed at the same time (Onjia, 2016). Plackett-Burman DOE (PBD), as one of the most frequently used variables screening tool, is applied in this work to optimize DLLME of octocrylene and avobenzone from water.

Method

The variables of the DLLME process for simultaneous preconcentration of octocrylene and avobenzone have been studied using PBD with twelve experimental runs. Several experimental variables including volume (V_{ex}, V_{disp}) and type (Ex, Disp) of both dispersive and extraction solvents, pH value, vortexing/sonication (Vor/US), temperature (T_{ex}), centrifugation speed (r_{centr}), reconstitution solvent (R_{st}), the salt content (NaCl) and centrifugation time (t_{centr}) were considered in the optimization process.

Table 1. The variables included in the PBD and their values

Run	pH	Ex	Disp	V_{ex}	V_{disp}	Stir	T_{ex}	t_{centr}	r_{centr}	R_{st}	NaCl
1	8	$CHCl_3$	MeOH	400	600	Vor	25	2	2000	MeOH	10
2	2	C_2Cl_4	MeOH	200	1000	Vor	5	2	2000	MeOH	0
3	2	$CHCl_3$	MeOH	200	1000	US	25	7	2000	ACN	10
4	8	C_2Cl_4	ACN	200	1000	Vor	25	7	4000	MeOH	10
5	2	C_2Cl_4	ACN	400	1000	Vor	25	7	2000	ACN	0
6	8	$CHCl_3$	MeOH	400	600	Vor	5	7	4000	ACN	0
7	8	C_2Cl_4	MeOH	200	1000	US	25	2	4000	ACN	0
8	8	C_2Cl_4	ACN	400	600	US	5	2	2000	ACN	10
9	2	C_2Cl_4	MeOH	400	1000	US	5	7	4000	MeOH	10
10	2	$CHCl_3$	ACN	200	600	Vor	5	2	4000	ACN	10
11	8	$CHCl_3$	ACN	200	600	US	5	7	2000	MeOH	0
12	2	$CHCl_3$	ACN	400	600	US	25	2	4000	MeOH	0

Ten milliliters of water containing target analytes were pipetted into a 15 mL centrifuge tube. Next, different amounts of NaCl (0-10 %) were added. The pH effect on the OC and AVO extraction from the sample solution was studied within the range of 2-8 using HCl and NaOH. When the required sample temperature was reached, a mixture of extraction and disperser solvents was added. The sample solutions were shaken for 1 min using US irradiation or vortex agitator. After centrifugation, the organic phase was withdrawn through a syringe and evaporated under nitrogen steam. The residue was dissolved with 200 µL of reconstitution solvent. Finally, 10 µL of the solution was injected into the HPLC-MS/MS system for analysis.

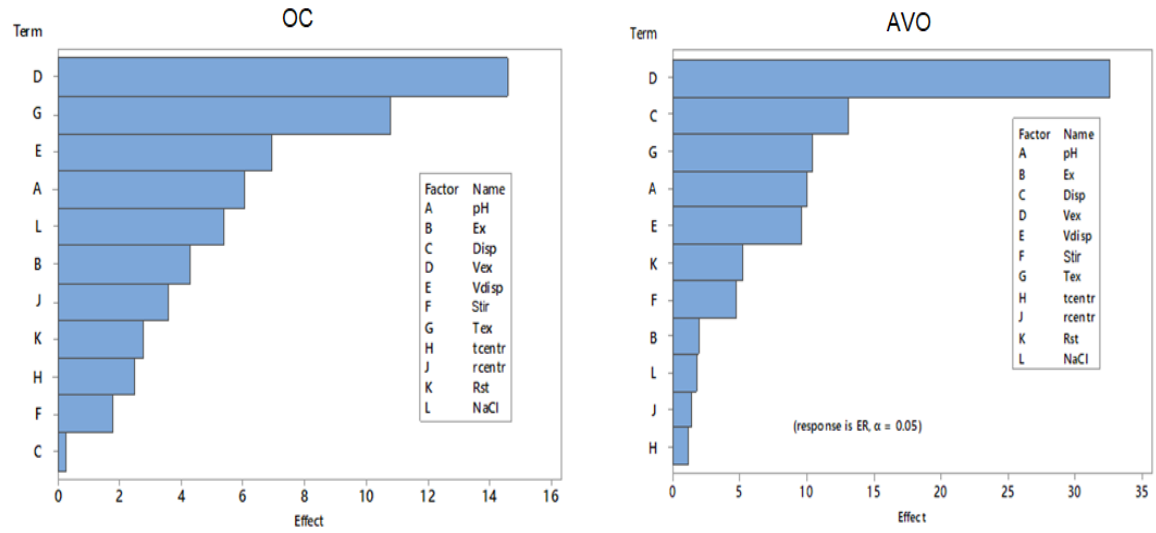

Figure 1. Pareto chart of investigated effects in the screening PBD.

Results and Discussion

Graphical data representations, Pareto chart (Fig. 1), and main effect graphs (Fig. 2) can be used to find the relationship between input variables and system responses. The effect of a variable is the change in response that is caused by a change in the level of the variable. The Pareto chart represents the ANOVA effect estimates that are sorted from the largest absolute value to the smallest one.

Results indicate that the volume of extraction solvent, temperature, the volume of disperser solvent, and pH of aqueous solution were the most significant variables and were estimated for further assessment in DLLME of avobenzone. C_2Cl_4, MeOH and ACN, are selected as the extraction, disperser, and reconstitution solvent, respectively. This selection significantly improved DLLME performances for both analytes.

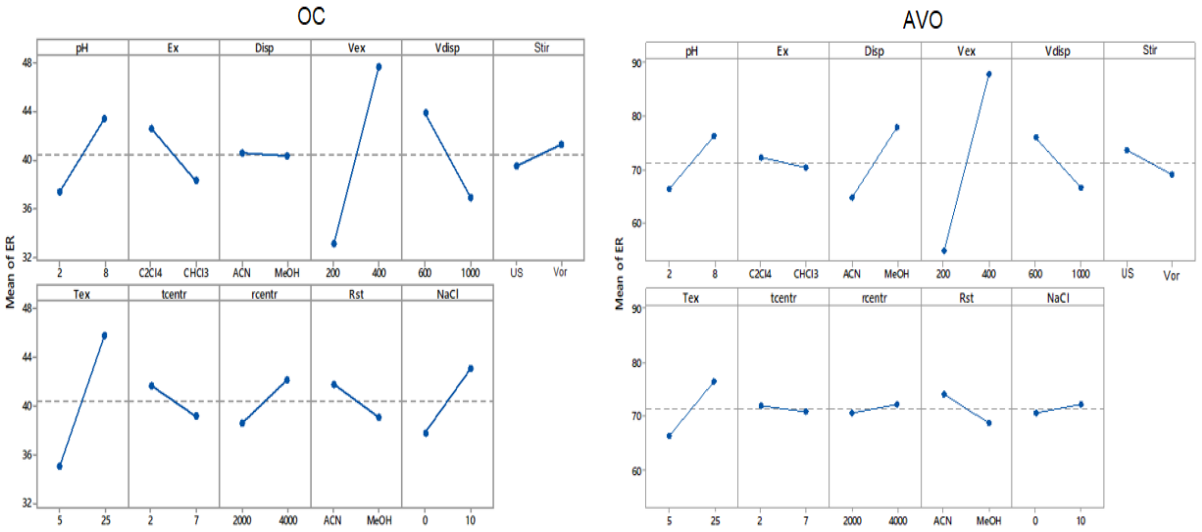

Figure 2. Main effects graph of variables in the screening PBD.

Fig. 2. shows the main effects graph of variables in the screening PBD. These results are used to analyze differences among level for variables. The response for each variable level connected by a line is plotted. The main effect plots reveal whether the responses differ at different levels. The slopes on two-level plots shown in Fig. 2 are the main effects. In the case of avobenzone, the least important variable is the type of dispersant. For DLLME of octocrylene, four variables: the type of extraction solvent, the salt content, centrifugation speed, and centrifugation time have the lines connecting the responses at both levels parallel to the x-axis with the slopes close to zero. It means that their influences on DLLME performances could be neglected.

Both the avobenzone and octocrylene extraction efficiencies are most dependents on the extractant solvent volume. Based on the liquid-liquid extraction theory, the analyte migration rate from aqueous into the organic phase is proportional to the organic-phase volume since the interfacial area between the two liquid phases is directly related to this volume. However, it should bear in mind that when the extractant solvent volume increases, i.e., the extractant/sample volume ratio increases, the enrichment factor decreases.

In this study, this volume was studied in the range of 200 - 400 µL. It was observed that at 400 µL, the extraction efficiencies for both analytes are at their maximum. Hence, 400 µL of C_2Cl_4 was chosen as the optimum extractant solvent volume. The enrichment factors of avobenzone and octocrylene were in the range of 40 - 50, and the sample preparation is very time-saving. These results indicated the successful application of the DLLME technique in the preconcentration of low concentration UV filters, such as avobenzone and octocrylene, in water samples.

Conclusion

DLLME technique represents an improvement in the sample preparation, which especially addresses the issues of miniaturization and time efficiency. PBD has generated the most information about the DLLME process for the fewest optimization runs. It identified the most influencing DLLME variables. Also, the main effects in the

system have been estimated. A large number of variables analyzed simultaneously are reduced to a few to be examined more closely. The most critical variable in this work is the extractant volume, both for avobenzone and octocrylene DLLME.

Acknowledgments

This work was supported by the Ministry of Education, Science and Technological Development of the Republic of Serbia (Contract No. 451-03-68/2020-14/200135).

References

Chisvert, A., Benedé, J. L., & Salvador, A. (2018). Current trends on the determination of organic UV filters in environmental water samples based on microextraction techniques – A review. *Analytica Chimica Acta*, *1034*, 22–38.

Onjia, A. (2016). *Chemometric approach to the experiment optimization and data evaluation in analytical chemistry.* Faculty of Technology and Metallurgy, University of Belgrade Publication, Serbia, p. 143.

Brausch, J. M., & Rand, G. M. (2011). A review of personal care products in the aquatic environment: Environmental concentrations and toxicity. *Chemosphere*, *82*(11), 1518–1532.

Chisvert, A., & Salvador, A. (2018). *Ultraviolet Filters in Cosmetics : Regulatory Aspects and Analytical Methods.* In Analysis of Cosmetic Products (Second Edi). Elsevier B.V.

Ramos, S., Homem, V., & Santos, L. (2019*).* Simultaneous determination of synthetic musks and UV-filters in water matrices by dispersive liquid-liquid microextraction followed by gas chromatography tandem mass-spectrometry. *Journal of Chromatography A*, *1590*(2018), 47–57.

Author Information

Jelena Lukić
Innovation Center of the Faculty of Technology and Metallurgy,
Karnegijeva 4, 11000 Belgrade, Serbia
jlukic@tmf.bg.ac.rs

Tatjana Đurkić
Belgrade University
Faculty of Technology and Metallurgy, University of Belgrade
Karnegijeva 4, 11000 Belgrade, Serbia

Jelena Radulović
Anahem Laboratory,
Mocartova 10, 11160 Belgrade, Serbia

Tamara Bakić
Innovation Center of the Faculty of Technology and Metallurgy,
Karnegijeva 4, 11000 Belgrade, Serbia

Antonije Onjia
Belgrade University
Faculty of Technology and Metallurgy, University of Belgrade
Karnegijeva 4, 11000 Belgrade, Serbia

The Eurasia Proceedings of Science, Technology, Engineering & Mathematics (EPSTEM)
ISSN: 2602-3199

The Eurasia Proceedings of Science, Technology, Engineering & Mathematics (EPSTEM), 2020

Volume 11, Pages 5-8

IConTES 2020: International Conference on Technology, Engineering and Science

Effects of Deep Cryogenic Treatment on the Microstructural Properties of Medium Carbon Spring Steels

Reşat Can OZDEN
Eskişehir Osmangazi University

Ersu LOKCU
Eskişehir Osmangazi University

Mustafa ANIK
Eskişehir Osmangazi University

Abstract: The cryogenic treatment is a complementary procedure that has been applied to a variety of materials to improve their mechanical and physical properties. It was first commercially recognized as an effective method in achieving complete martensitic transformation in the alloyed steels. In this study, microstructural investigations were carried out in order to relate the microstructural properties to the mechanical properties following the cryogenic treatment. For this purpose, the conventional heat treatment (CHT) and the deep cryogenic treatment (DCT: -196°C) procedures were applied to various medium carbon spring steels. Microstructural examinations were carried out by using scanning electron microscopy. The martensite lattice parameters and the amount of retained austenite were measured by using a high-resolution X-ray diffractometer. Rietveld analysis was used to deconvolute the overlapping peaks of martensites.

Keywords: Steels, Cryogenic Treatment, Microstructure, Alloying

Introduction

Martensite is a microstructure that increases the strength and wear resistance of steels. It is generally accepted that martensite has a body-centered tetragonal (bct) structure. The linear relationship between tetragonal martensite and the carbon content is traditionally expressed as in Eq. (1) (Lu, Yu, & Sisson, 2017).

$$c/a = 1 + 0{,}045 \text{ wt. \%C} \quad (1)$$

However, Nishiyama et al. used steels with a carbon ratio of more than 0.6% by weight while demonstrating this equation. Since the c / a ratio could not be determined correctly in steels whose carbon ratio was lower than 0.6% at that time, they assumed that steels containing lower carbon content would also tend to have the same trend.

In the study conducted by Lu et al., the c/a ratios of martensite in the structure were calculated after normalization, austenitization and quenching processes using low carbon AISI 9310, medium carbon AISI 4140, AISI 4150 and AISI 4161, high carbon AISI 1080, AISI 52100 steels. Accordingly, it was determined that as the carbon ratio in steel increases, the angles and the intensity of both (200) and (002) martensite peaks decrease. It was observed that the peaks began to overlap with the decrease of d distance between (200) and (002) peaks in AISI 9310, AISI 4140, AISI 4150 and AISI4161 steels which carbon ratio is below 0.6%. This situation created difficulties in calculating the c/a ratio. It has been determined by SEM examinations that the microstructure is generally lath martensite in AISI 9310 and AISI 4140 steels, plate martensite in AISI 52100 steel and both martensite types in AISI 4161 and AISI 1080 steels. Using the Rietveld analysis, the researchers stated that the traditional c / a calculation model (above equation) can be used in steels containing more than

- Selection and peer-review under responsibility of the Organizing Committee of the Conference

0.6% carbon. By deconvoluting the peaks of (002) and (200), it is stated that martensite has bct structure and the c/a ratio is as follows in Eq (2).

$$c/a = 1 + 0{,}031\ \%C \qquad (2)$$

Although it is generally accepted that martensite lattice structure in carbon steels is bct, it has been reported in the study conducted by Lobodyuk et al. that martensite cage cannot form a smooth bct structure in steels with a carbon ratio of 0.2 to 1.5%. Besides, the mechanism of local distortions in the crystalline structure to change the c lattice parameter is explained using a tetragonal-ish (pseudo-tetragonality) structure. The researchers reported that the crystalline structure of the martensite lattice should be named pseudo-tetragonal because it contains interstitial C atoms.

In the research conducted by (Maruyama, Tabata, & Kawata, 2020), the crystal structure and carbon dispersion behavior of quenched steel with 10 different carbon compositions with carbon ratios between 0.07 and 0.8 were investigated using Rietveld analysis and atom probe tomography (APT). A tetragonal structure has been observed in steels with a carbon composition of 0.1 to 0.7% by weight. It has also been found that during cooling, the carbon atoms tend to remain in the lath martensite regions with dense dislocation. When all steels were examined, it was found that the amount of carbon in solid solution of martensite steels was much more than it could be dissolved in the bcc-Fe structure. It has been stated that since carbon atoms precipitate inhomogeneously by forming carbide or cluster in dislocations due to auto-tempering. The martensite structure provides excess solid solubility in auto-tempered low and medium carbon steels due to tetragonal distortions caused by the slow kinetics of tetragonality decreasing during cooling. Therefore, they stated that it is possible to control tetragonality by changing the cooling rate.

In this study, cryogenic process was applied to three medium carbon spring steels containing different alloying elements and the effect of cryogenic process was investigated microstructurally using SEM. Rietveld analysis was applied to the samples to quantitatively determine the tetragonality of martensite.

Method

Three spring steels with different alloys were selected in the study. The average chemical compositions of spring steels are given in Table 1. Conventional heat treatment (CHT) and deep cryogenic process (DCT) at -196°C were applied to steels and the effect of the cryogenic process on microstructural properties was investigated. The flow chart of the experiment is given in Figure 1.

Table 1. Average Chemical Compositions of Spring Steels

Material	%C	%Si	%Mn	%Cr	%V	%Mo
55Cr3	0,57	0,30	0,85	0,80	-	-
51CrV4	0,50	0,25	0,90	1,10	0,12	-
52CrMoV4	0,50	0,25	0,90	1,10	0,10	0,25

For XRD (Rietveld) analysis, the samples were electrolytically polished in accordance with ASTM E1558 - 99 standard. Experiments were carried out with Panalytical EMPYREAN brand XRD device. Rietveld analyzes were carried out with Maud 2.92v analysis program. The PDF 4+ program containing the ICDD database was used for the "cif" (crystallographic information file) files required for Rietveld analysis.

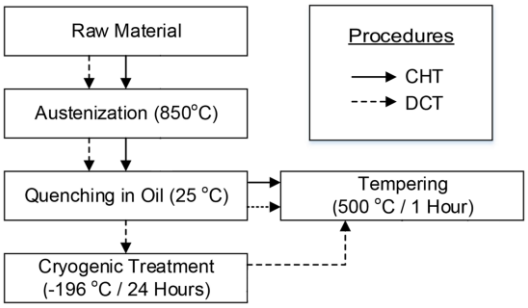

Figure 1. Flow chart of heat treatment procedures

Results and Discussion

In order to examine the formal effect of the cryogenic process on the microstructure, the samples were examined using a scanning electron microscope. SEM microstructures of CHT and DCT samples of 55Cr3 are presented in Fig. 2a and Fig 2b, respectively. It is seen that the DCT sample has a significant increase in the density of carbides as compared to the CHT sample. Besides, a coarsening was observed in the carbide structures. The carbide structure becomes more rounded and is more homogeneously distributed in the matrix.

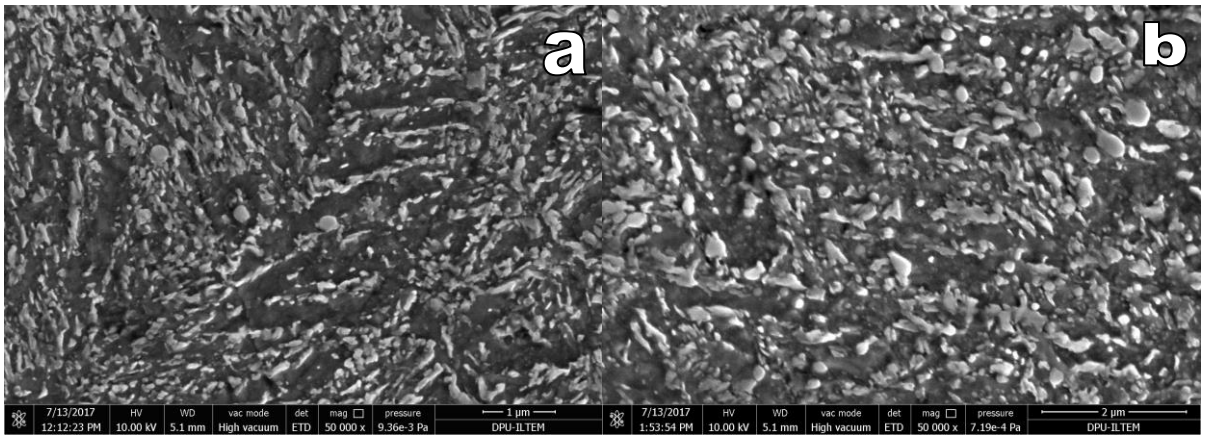

Figure 2. SEM pictures of the samples (a) 55Cr3 – CHT (b) 55Cr3 – DCT

In Figure 2a, XRD patterns of the samples are presented. As expected, the amount of retained austenite in the samples is minimal and the carbide peaks are not evident. The results from the Rietveld analysis performed as seen in Figure 2b are presented in Figure 3.

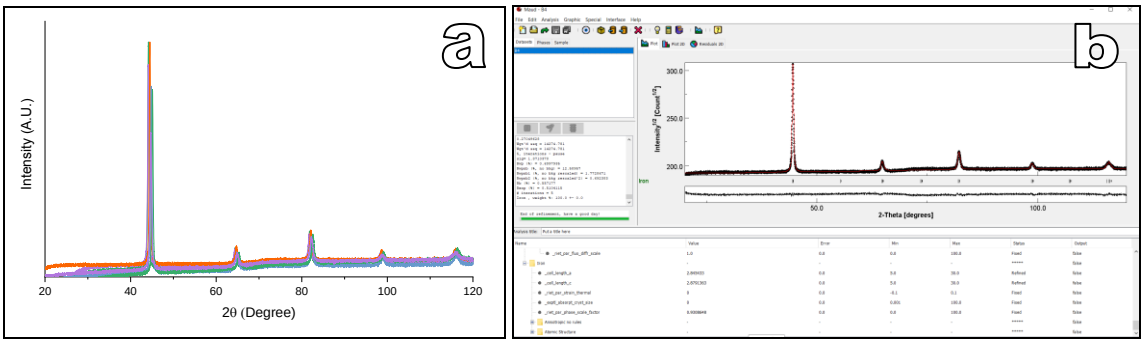

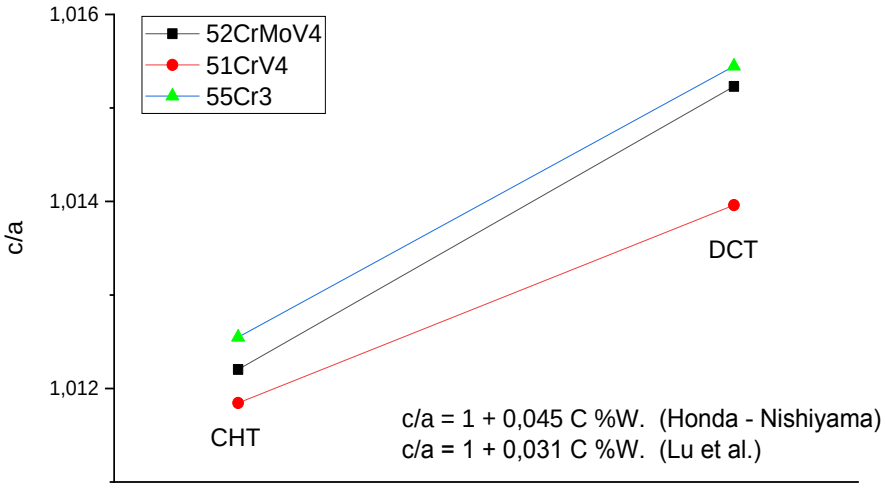

Figure 3. Results of Rietveld analysis performed as seen in Figure 2b

According to the results of Rietveld analysis, an increase in the tetragonality of martensite was observed in all samples after cryogenic treatment. In the case of cryogenic effect, basic parameters that define the change of tetragonality of martensite are mentioned. These are the austenite - martensite transformation that occurs depending on the cryogenic temperature and time (Villa, Hansen, & Somers, 2017), the blurring of the grain boundaries of martensite that changes depending on the tempering temperature and the carbide formation (Su, Chiu, Chen, Lin, & Pan, 2014). It has been reported in our previous studies that these microstructural changes add toughness to the steel material without losing its strength (Özden & Anik, 2020). The results obtained confirm the work of Lu et al. for medium carbon spring steels

Conclusion

Homogenization and increased carbide precipitation were observed in the SEM examination performed as a result of the cryogenic process applied to medium carbon spring steels. It has been observed that this effect increases as the alloying increases. After the Rietveld analysis performed after XRD analysis, it was reported that the c / a ratio in the martensite structure, ie tetragonality, increased.

Acknowledgment

Financial assistance from Eskisehir Osmangazi University Research Fund is gratefully acknowledged (Project No: 201615A230). The authors wish to thank MMD Mechanical and Materials Technologies R&D Consulting Engineering Services Industry and Trade Limited Company for the deep cryogenic treatments.

References

Lobodyuk, V. A., Meshkov, Y. Y., & Pereloma, E. V. (2019). On Tetragonality of the Martensite Crystal Lattice in Steels. *Metallurgical and Materials Transactions A: Physical Metallurgy and Materials Science*, *50*(1), 97–103. https://doi.org/10.1007/s11661-018-4999-z

Lu, Y., Yu, H., & Sisson, R. D. (2017). The effect of carbon content on the c/a ratio of as-quenched martensite in Fe-C alloys. *Materials Science and Engineering A*, *700*(April), 592–597. https://doi.org/10.1016/j.msea.2017.05.094

Maruyama, N., Tabata, S., & Kawata, H. (2020). Excess Solute Carbon and Tetragonality in As-Quenched Fe-1Mn-C (C:0.07 to 0.8 Mass Pct) Martensite. *Metallurgical and Materials Transactions A: Physical Metallurgy and Materials Science*, *51*(3), 1085–1097. https://doi.org/10.1007/s11661-019-05617-y

Nishiyama, Z. (1978). *Martensitic Transformation*. (M. E. Fine, M. Meshii, & C. M. Wayman, Eds.). Kawasaki: Academic Press Inc.

Özden, R., & Anik, M. (2020). Enhancement of the mechanical properties of EN52CrMoV4 spring steel by deep cryogenic treatment Verbesserung der mechanischen Eigenschaften von EN52CrMoV4 Federstahl durch Tieftemperaturbehandlung. *Materialwissenschaft Und Werkstofftechnik*, *51*, 422–431. https://doi.org/10.1002/mawe.201900122

Su, Y. Y., Chiu, L. H., Chen, F. S., Lin, S. C., & Pan, Y. T. (2014). Residual stresses and dimensional changes related to the lattice parameter changes of heat-treated JIS SKD 11 tool steels. *Materials Transactions*, *55*(5), 831–837. https://doi.org/10.2320/matertrans.M2014031

Villa, M., Hansen, M. F., & Somers, M. A. J. (2017). Martensite formation in Fe-C alloys at cryogenic temperatures. *Scripta Materialia*, *141*, 129–132. https://doi.org/10.1016/j.scriptamat.2017.08.005

Author Information

Reşat Can Özden
Eskisehir Osmangazi University
Department of Metallurgical and Materials Engineering,
Eskisehir Osmangazi University, 26040, Eskisehir, Turkey
Contact e-mail: *rcanozden@ogu.edu.tr*

Ersu Lökçü
Eskisehir Osmangazi University
Department of Metallurgical and Materials Engineering,
Eskisehir Osmangazi University, 26040, Eskisehir, Turkey

Mustafa Anik
Eskisehir Osmangazi University
Department of Metallurgical and Materials Engineering,
Eskisehir Osmangazi University, 26040, Eskisehir, Turkey

The Eurasia Proceedings of Science, Technology, Engineering & Mathematics (EPSTEM)
ISSN: 2602-3199

The Eurasia Proceedings of Science, Technology, Engineering & Mathematics (EPSTEM), 2020

Volume 11, Pages 9-13

IConTES 2020: International Conference on Technology, Engineering, and Science

Resistance Spot Welding of ZAMAK 12

Osman TORUN
Afyon Kocatepe University

Bedri BAKSAN
Eskişehir Osmangazi University

Ibrahim CELIKYUREK
Eskişehir Osmangazi University

Abstract: Zamak 12 offers high hardness and high tensile strength. This is the preferred alloy for permanent mold applications although it can also be cold-chamber die-cast with excellent results. It combines low temperature melting efficiency and thin wall capabilities with premium mechanical properties. ZA-12 can usually be poured directly into molds designed for aluminum and brass. In this work, the weldability of the ZA-12 alloy using the resistance spot welding technique was investigated. The alloy was melted in a melting furnace and casted in a sand mold. The resistance spot welding processes were carried out using the welding current of 3 kA and the welding times of 30, 40, 50 cycles under the electrode loads of 500 N. The microstructures of the interfaces of welded samples were examined with light optical microscopy (LOM). The tensile-shear tests were carried out at room temperature to determine weld strength. The welding time affected slightly the welding strength. The hardness of the welding zone and matrix was measured. The hardness of the weld interface and base material was similar for all welding conditions.

Keywords: Zamak 12, Hardness, Welding

Introduction

Various welding methods are used in manufacturing industries such as gas tungsten arc welding, submerged arc welding, shielded metal arc welding, flux core arc welding, and resistance spot welding. Among them, resistance spot welding is widely used in manufacturing processes due to its easy applicability and low equipment cost (Vural and Akkus, 2004). In the RSW method, overlapping plates are placed between two electrodes, and heat is obtained by passing a large electric current for a short time (Pouranvari and Marashi, 2011). Then, the electrical resistance at the metal interface causes local heating for the joint and finally melting. In the literature, there is a lot of study on resistance spot welding such as steel (Shirmohammadi et al., 2017), aluminum alloys (Florea et al., 2012), magnesium alloys (Niknejad et al., 2014), titanium alloys (Kahraman, 2007), iron/aluminum (Qiu et al., 2009) and (Bemani and Pouranvari, 2020). Zinc-Aluminum based alloys (ZAMAK) have become interesting in many industrial applications in recent years due to their advantages such as high wear resistance, high specific strength, easy and economical production (Fatile et al., 2017; Şevik, 2014; Shivakumar et al., 2017).

Zamak alloys, which have a high usage area in the building used widely in automotive sectors, in electronic devices. It is frequently preferred in household goods, ready-to-wear, toys, sports, business machines, hardware, agriculture, and mining (Polat 2009). The most common zinc-aluminum alloy (ZAMAK, ZA, ALZEN) are ZA-8, ZA-12, and ZA-27 alloys. These alloys contain higher amounts of aluminum than other ZAMAK alloys. Since the casting quality will increase with increasing Al concentration, better engineering properties can be obtained. A small amount of some alloying elements (Cu, Mg, Si, Ni) improve the mechanical and tribological properties of the cast ZA alloys (Ayday,2018).

A high-quality joint of zinc-based die-cast alloys can be hardly achieved by conventional fusion welding. In this study, Zamak 12 alloy was welded using the resistance spot welding and examined microstructure and determined mechanical properties.

Method

Zinc alloy ZAMAK-12 was produced by an induction melting furnace at the nominal composition of 88%Zn, 11.0%Al, and 1.0%Cu (wt%). Firstly, Zn was melted, then Al was added, finally, Cu was dissolved in the melt. The melted liquid was stirred slowly using a steel rod. After obtaining a homogenous mixture the alloy was gravity casted into a graphite mold. Then, obtained rectangular form samples were hot-rolled until the thickness of samples has 1 mm. The dimensions of the samples for the resistance spot welding processes were prepared to be 40x10x1 mm3. The welding processes were performed for 30, 40, and 50 cycles under the compression time of 40 cycles, the welding current of 3 kA, and the electrode load of 500 N. A fixture was prepared to prevent the overlapping plates from slipping from the axis during the welding process (Figure 1).

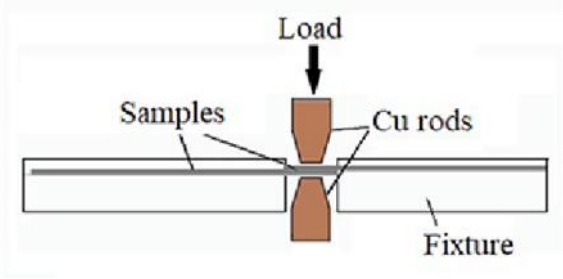

Figure 1. Resistance spot welding geometry.

The welding processes were carried out in a water-cooled and pneumatically controlled spot resistance welding machine. A schematic illustration of the resistance spot welding process was given in Fig 1. The microstructural and mechanical properties of the welded samples were investigated under experimental conditions. For this purpose, four samples were prepared for each test parameter. One of them was cut from the center of the melting zone (nugget) and molded for metallographic examinations, the others were used for mechanical characterization. The molded sample was grounded and polished with 1 µm diamond paste, then the samples were etched with nital %3. The welding interface of the samples was examined using light optical microscopy. The hardness measurements were carried out by applying a load of 300 gr. with Shimadzu HMV type device.
Three welded samples were subjected to a tensile test in a Shimadzu AGIS tensile-compression testing device for each welding parameter. The tests were carried out at room temperature with a loading speed of 5 mm/min. The schematic illustration of the test geometry was given in Fig. 2. The welding interface strength was determined by taking the average of three samples.

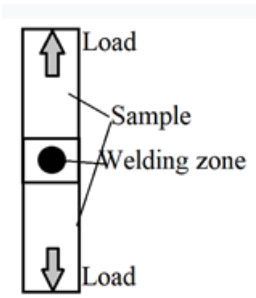

Figure 2. The tensile test geometry of the welding zone.

Results and Discussion

Optical microscope photos of the welded samples for 30, 40, and 50 cycles at a welding current of 3kA under electrode force of 500 N are given in Fig.3. It is clearly seen that a nugget region is formed at the interface of the welded samples for all welding times from photographs. New grains have formed in the nugget zone occurred

at the interface of welded samples. The grain shape in the nugget zone is equ-axial. Normally, while the matrix material has axially elongated grains, after welding, equ-axial grains were formed at the welding interface. The nugget zone was expanded with an increase in welding time. The increase in welding time caused an increase in the heat input in the interface of welded samples. More melting occurred at the interface of the welded samples. As a result of this situation the nugget zone expanded.

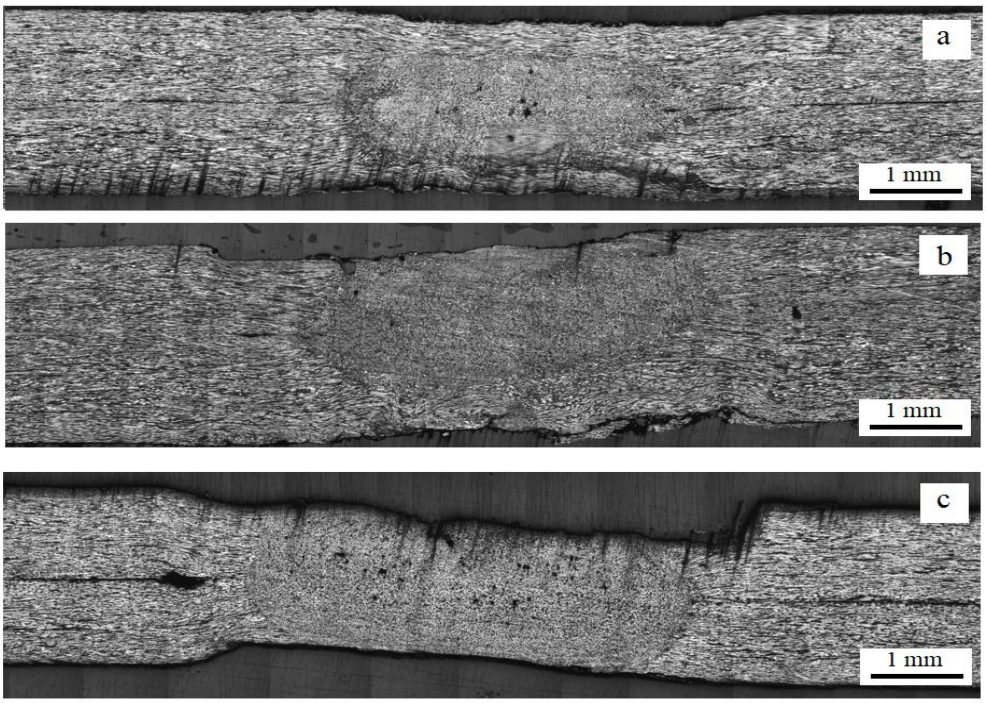

Figure 3. Optical micrographs of welded samples. a) 30 cycle b) 40 cycle c) 50 cycle

As shown schematically in Fig. 4 the microhardness values of the samples were measured from the center of the nugget zone to both sides of the matrix. The hardness values are given in Figure 5. As can be seen from the figure, in the hardness values of the nugget and the heat-affected zone no significant change was observed.

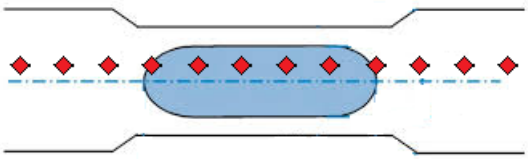

Figure 4. Schematic illustration of hardness measurement

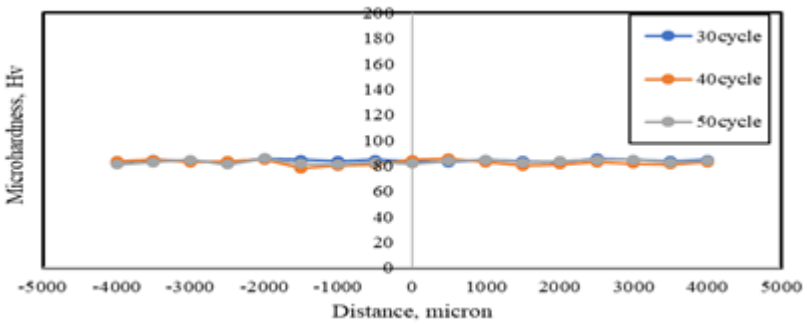

Figure 5. The hardness variation of the welding zone and matrix.

Tensile-shear tests were performed out an electromechanical universal testing machine with a speed of 5 mm/min at room temperature. The strength values obtained in the tests were given in Figure 6. The test results show that shear force values increase with increases in the welding time in the welded samples. The heat input

increased with the increase in welding time and the nugget zone expanded. Thus, more melting occurred on the surfaces contacting the interface of the welded samples. As a result, the sheer force slightly increased with increasing the welding time.

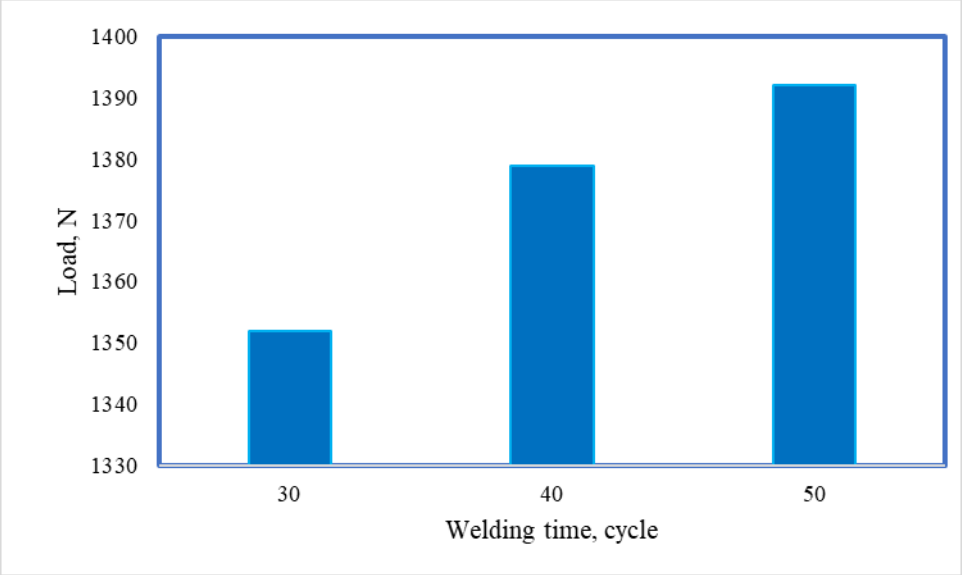

Figure 6. The strength values of the welded samples

Conclusion

In this study, the resistance spot welding of ZAMAK 12 was carried out using the welding current of 3 kA and the welding times of 30, 40, 50 cycles under the electrode loads of 500 N. A crack-free and oxide-free weld interface in microstructural studies observed. With the increase in welding time, the heat input increased and as a result of this situation, the nugget zone expanded. The microhardness values of the weld zone and the matrix structure were measured close to each other and there was no significant change in the hardness values. The shear forces of the welded specimens increased depending on the welding time and the highest shear force was found as 1392 N for 30 cycles.

References

Ayday A., (2018). Çinko-Alüminyum esaslı ZA-12 alaşımının mikroyapı ve darbe dayanımına bor elementinin etkisi, *BAUN Fen Bil. Enst. Dergisi*, *20*(1), 243-249.

Bemani M., Pouranvari M. (2020) Microstructure and mechanical properties of dissimilar nickel-based superalloys resistance spot welds, *Mater. Sci. Eng. A. 773*, 138825.

Fatile B.O., Adewuyi B.O., and Owoyemi H.T.(2017). Synthesis and characterization of ZA-27 alloy matrix composites reinforced with zinc oxide nanoparticles, *Engineering Science and Technology. 11*, 47–1154.

Florea R.S., Solanki K.N., Bammann D.J., Baird J.C., Jordon J.B., Castanier M.P. (2012). Resistance spot welding of 6061-T6 aluminum: Failure loads and deformation. *Materials and Design 34*, 624–630.

Kahraman N. (2007). The influence of welding parameters on the joint strength of resistance spot-welded titanium sheets. *Mater Des*, *28*:420–7.

Niknejad S., Liu L., Lee M., Esmaeili S., Zhou N. Y. (2014). Resistance spot welding of AZ series magnesium alloys: Effects of aluminum content on microstructure and mechanical properties *Mater. Sci. Eng. A 618*, 323–334.

Polat B.D.(2009). Zamak alaşımı nedir? Zamaktan nasıl para kazanılır? *Metalürji Dergisi*, sayı 159.

Pouranvari M, Marashi SPH (2011). Failure mode transition in AHSS resistance spot welds. Part I. Controlling factors. *Mater Sci Eng A; 528*:8337–43.

Qiu R, Iwamoto C, Satonaka S. (2009). Interfacial microstructure and strength of steel/aluminum alloy joints welded by resistance spot welding with cover plate. *J Mater Process Technol. 209*:4186–93.

Shirmohammadi D., Movahedi M., Majid P. (2017). Resistance spot welding of martensitic stainless steel: Effect of initial base metal microstructure on weld microstructure and mechanical performance, *Mater. Sci. Eng. A 703*,154–161.

Shivakumar, N., Vasu, V., and Narasaiah N. (2017). Processing and dry sliding wear behavior of Al2O3 nanoparticles reinforced ZA-27 composites, *Materials Today*: Proceedings, 4, 4006–4012.

Şevik H. (2014). The effect of silver on wear behavior of zinc–aluminum-based ZA-12 alloy produced by gravity casting, *Materials Characterization, 89*, 81–87.

Vural M, Akkus A. (2004). On the resistance spot weldability of galvanized interstitial free steel sheets with austenitic stainless steel sheets. *J Mater Process Technol, 153*–154:1–6.

Author Information

Osman TORUN
Afyon Kocatepe University
Afyon Kocatepe University, Technology Faculty, Department of Mechatronic Engineering
otorun@aku.edu.tr

Bedri BAKSAN
Eskişehir Osmangazi University
Eskişehir Osmangazi University, Department of Metallurgy and Materials Engineering

İbrahim ÇELİKYÜREK
Eskişehir Osmangazi University
Eskişehir Osmangazi University, Department of Metallurgy and Materials Engineering

The Eurasia Proceedings of Science, Technology, Engineering & Mathematics (EPSTEM)
ISSN: 2602-3199

The Eurasia Proceedings of Science, Technology, Engineering & Mathematics (EPSTEM), 2020

Volume 11, Pages 14-19

IConTES 2020: International Conference on Technology, Engineering and Science

Multivariate Short-term Load Forecasting Using Deep Learning Algorithms

Duygu ALTUNKAYA
Konya Food and Agriculture University

Burak YILMAZ
Konya Food and Agriculture University

Abstract: Load forecasting is important in energy market. In fact electricity is a type of energy that cannot be stored, thus it is more important in electrical energy. The facilities need to balance between electricity generation and consumption by making plans. Computer-aided forecasting models are developed to reduce the effects of factors that disrupt this supply-demand balance. Generally, daily, weekly and monthly forecasts are made in demand forecast. In this study, hourly demand estimation is made. By using the past 24-hour consumption data and weather data such as temperature, humidity, wind speed and radiation in Konya, the next hour's consumption value was tried to forecast. Forecasting models were created using deep learning algorithms such as RNN, LSTM and GRU and the most successful model was determined by comparing the models.

Keywords: Load forecasting, Deep learning, Time series, Consumption of electricity, Short-term

Introduction

The need for electrical energy is increasing day by day due to reasons such as the development of industry and technology, the increase in population, factories and mechanization. It is necessary to make a planning that will ensure the supply-demand balance for increasing energy need. This plan is very important in order to prevent energy losses due to overestimation, to eliminate negative effects on costs and to prevent problems such as power cut that may occur due to underestimation. Therefore, load forecasting should be close to the actual value. It is possible to categorize the load forecast as short, medium and long term. Short-term load forecasting is in a period of a few minutes of a day. The medium-term load forecasting is in the time range of one day to one year, while the long-term load forecasting includes estimates that last more than one year (Nalbant et al., 2005).

There are different studies for short, medium- and long-term forecasting. Mori and Ogasawara (1993) developed recurrent neural network for short-term load forecasting using methods of time series and diffusion learning methods. In another study, attributes such as hours, days of week, holidays, past twenty-four hour of consumption and average consumption were used and RNN,LSTM and GRU methods were more successful than ARIMA and YSA methods (Tokgoz & Unal, 2018). Choi, Ryu and Kim (2018) presented a new model by combining ResNET and LSTM to perform one day ahead 15-minutes interval load forecasting. In this study, ResNET improved the model by providing that the neural network extracts the latent features of input historical load data. A new neural network model that integrates the hidden feature of CNN and LSTM is proposed to improve the forecasting accuracy (Tian et al., 2018) . Siddarameshwara et al. (2010) used Elman recurrent network with weather data such as average wind speed, speed, humidity, minimum and maximum temperature for short-term forecasting. There are many studies that used LSTM model for load forecasting (Jiang et al., 2018; Kong et al., 2019; Zheng et al., 2017).

In this study, three different forecasting models was created by using deep learning methods for short-term load forecasting and they were compared. Electricity consumption and weather data between 2016-2020 were used. In addition, this study is different from others in terms of regional and hourly. A multivariate model was created by using weather data such as temperature, wind speed and radiation in addition to past twenty-four hour of

- Selection and peer-review under responsibility of the Organizing Committee of the Conference

consumption and the next hour's consumption was tried to be forecasted. When the results were compared, it was seen that the forecasting value is close to the actual value.

Method

Data Preparation

In this study, 30758 hourly data of Konya province between 2016 and 2020 is used. In addition, eight features is used namely temperature, relative humidity, wind speed, wind direction, cloud cover, radiation, precipitation and consumption. 70% of data for training, 15% for validation and 15% for test is divided. Some preprocessing was implemented to data before the training of the models. Also, standardization was implemented input and output of the models using formula given in Equation-1 to give for the model to give more accurate results.

$$z = \frac{x_i - \mu}{\sigma} \qquad (1)$$

The hourly change of consumption data of Konya province between 2016-2020 is shown in Figure-1.

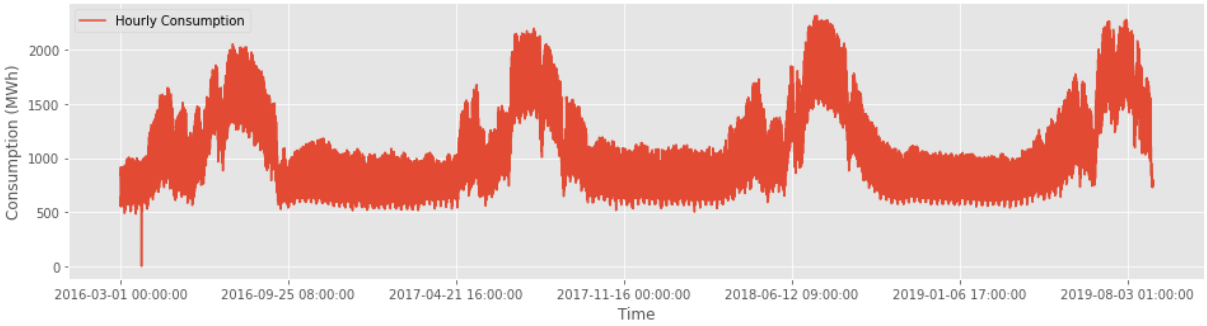

Figure 1. Electricity consumption data graph

Recurrent Neural Network (RNN)

Recurrent neural network is a neural network which allows hidden states to use previous outputs. Inputs are independents from each other in standard neural network. In other words, previous data is not important for next data. But previous data is needed for problems such as time series that contains sequence pattern. In this case, RNN which keep in memory to information from previous data was discovered.

Figure-1 shows the architecture of Jordan and Elman networks, which are among first recurrent network. Jordan networks are similar to MPL with input, output and hidden layers (Figure 2a). It has state units in addition to MLPs. This state units transport the data from output layer to hidden layer in the next iteration. Also, these units have a connection to themselves. on the other hand, Elman networks have a context layer. While input of this context layer derived from outputs of hidden layers, its output sent back to input of hidden layers (Figure 2b).

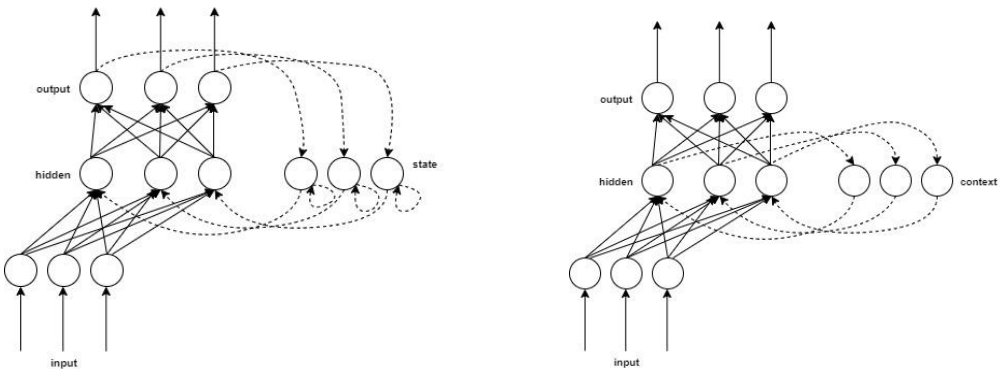

(a) (b)

Figure 2. (a) Architecture of Jordan recurrent network (b) Architecture of Elman recurrent network

The memory structure of the RNN can be understood by looking at the opened version of the RNN in Figure-3. When each new input comes, hidden layer information of the previous input in addition to this new input is also given to the model. Thus, previous input is kept in memory.

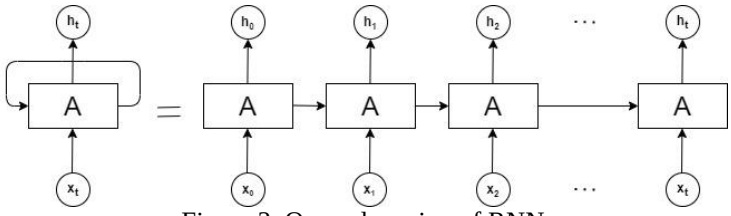

Figure 3. Opened version of RNN

Long Short-Term Memory (LSTM)

Past data is used while training the model in the RNN. However, as the time interval increases, it becomes difficult for RNN to use historical data and effects of the input on the output is decreases due to gradient vanishing problem. To solve this problem, LSTM which is special type of RNN and can learn long-term dependencies has developed. LSTMs is similar to the architecture of RNN in the Figure-3. However, while recurrent module in RNNs contains single layer as shown Figure 4a, the structure of this module in LSTMs is different and includes four layers (Figure 4b).

LSTMs consist of three gates as input, output and forget gate.

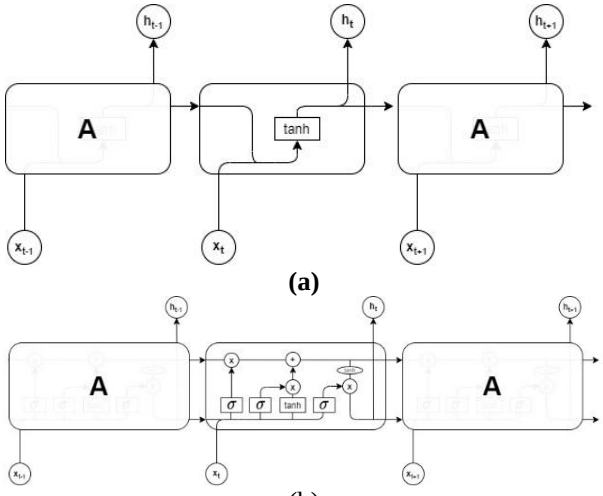

(a)

(b)

Figure 4. (a) Internal structure of RNN (b) Internal structure of LSTM

Gated Recurrent Units (GRU)

The Gated Recurrent Unit can be viewed as simplification of the LSTM, which does not use explicit cell states. There are some differences between the two models. The LSTM directly controls the amount of information changed in the hidden state using separate forget and output gates. On the other hand, a GRU uses a single reset gate to achieve the same goal. Just as the LSTM uses input, output, and forget gates to decide how much of the information from the previous time-stamp to carry over to the next step, the GRU uses the update and the reset gates (Aggarwal, 2018). The update gate preserves the previous data for current state. However, reset gate is the gate that define whether combined to data in current and previous state.

Results and Discussion

The result of the three model is applied were evaluated with performance metrics such as MSE, RMSE, MAE and R square. While high R square value indicates that relationship of forecasting is good, low values of other metrics indicate that the performance of the model is high.

In this study, consumption of the next hour is tried to be forecasted by the 24-hour historical data of the province of Konya for 2016-2020. Timesteps value is selected as 24 to give for input 24-hour historical data. Two hidden layer that has 50 and 45 neurons respectively is used. It was seen that the increase in the number of layers and neurons negatively affected the results, so these values were kept to a minimum. In addition, the Grid Search algorithm is used for learning rate selection and the best value is $1e^{-3}$. As a result, models were created with 8 inputs and 1 output parameters. Deep learning algorithms is stochastic. In other words, these models have randomness such as initializing to random weights and model can produce different results. For this reason, training of models repeats many times for robust results and is used summary statistics of results to compare models. The results of each iteration are shown in Table-1. Then, the average error values of these experiments are calculated, and the best performing algorithm is determined. The values in Table-2 show that the best performing algorithm is RNN.

Table 1. 10 iteration results of models

	MSE			RMSE			MAE			R^2		
	RNN	LSTM	GRU	RNN	LSTM	GRU	RNN	LSTM	GRU	RNN	LSTM	GRU
1	0,0472	0.0749	0,0512	0,2173	0.2737	0,2264	0,1637	0,1906	0,1645	0,9598	0,9363	0,9564
2	0,0492	0.0538	0,0968	0,2218	0.2319	0,3112	0,1650	0,1766	0,2346	0,9582	0,9542	0,9176
3	0,0419	0.0897	0,0502	0,2047	0.2995	0,2240	0,1583	0,2220	0,1697	0,9644	0,9237	0,9573
4	0,0570	0.1132	0,0843	0,2388	0.3365	0,2904	0,1791	0,2554	0,2092	0,9515	0,9037	0,9283
5	0,0569	0.0562	0,0625	0,2385	0.2371	0,2499	0,1827	0,1811	0,1871	0,9516	0,9522	0,9469
6	0,0406	0.0573	0,0595	0,2015	0.2393	0,2439	0,1493	0,1812	0,1861	0,9655	0,9513	0,9494
7	0,0510	0.0455	0,0618	0,2259	0.2135	0,2486	0,1691	0,1535	0,1835	0,9566	0,9612	0,9474
8	0,0537	0.1129	0,0535	0,2318	0.3360	0,2312	0,1729	0,2505	0,1666	0,9543	0,9040	0,9545
9	0,0541	0.0841	0,0699	0,2325	0.2900	0,2643	0,1790	0,2189	0,1994	0,9540	0,9285	0,9406
10	0,0599	0.0405	0,0657	0,2447	0.2014	0,2564	0,1847	0,1510	0,1884	0,9491	0,9655	0,9441

Table 2. Average performance of multivariate models

Model	MSE	RMSE	MAE	R^2
RNN	0.0512	0.2258	0.1704	0.9565
LSTM	0.0729	0.2659	0.1981	0.9380
GRU	0.0655	0.2546	0.1889	0.9443

Actual and predicted values of test data are shown in Figure-5. When these graphs are examined, it is seen that the trend of all three models approaches the actual values.

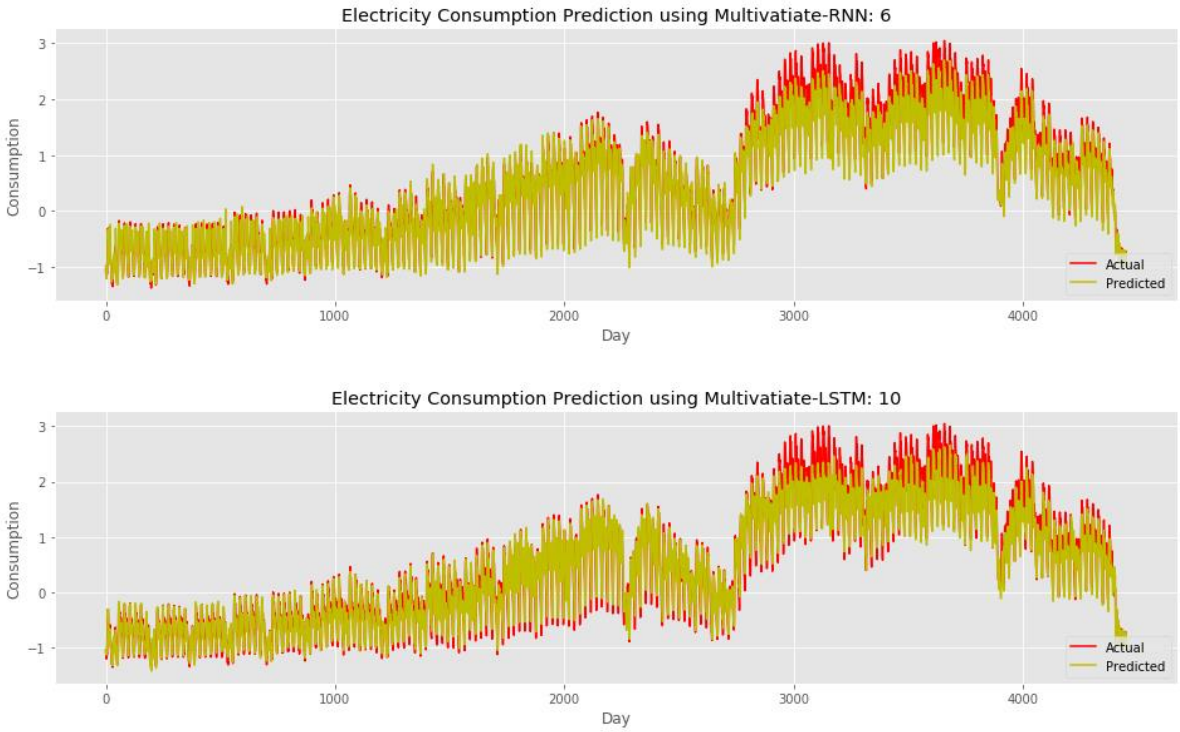

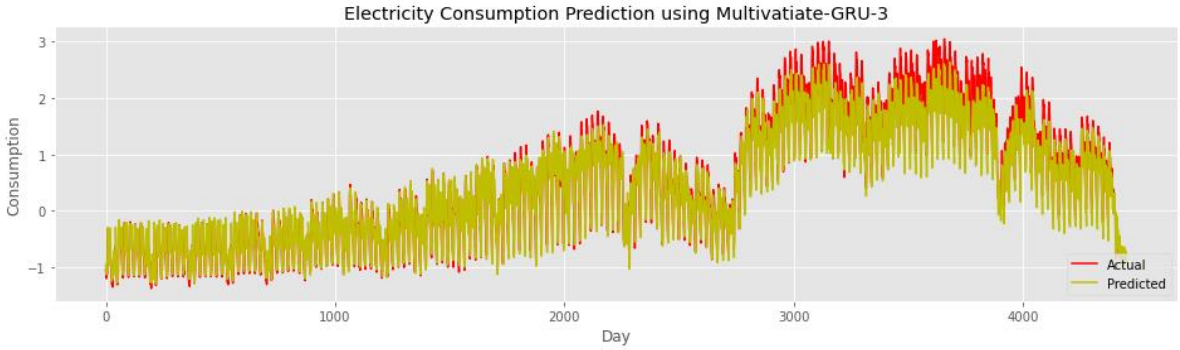

Figure 5. Actual and predicted values of model results

In order to analyze the estimation results in more detail, a certain section is taken from the model results and shown in Figure-6. In some parts, the GRU algorithm overestimates the true value, while LSTM algorithm underestimates it slightly. Despite these, it was seen that the closest estimate to the actual values was made in RNN model.

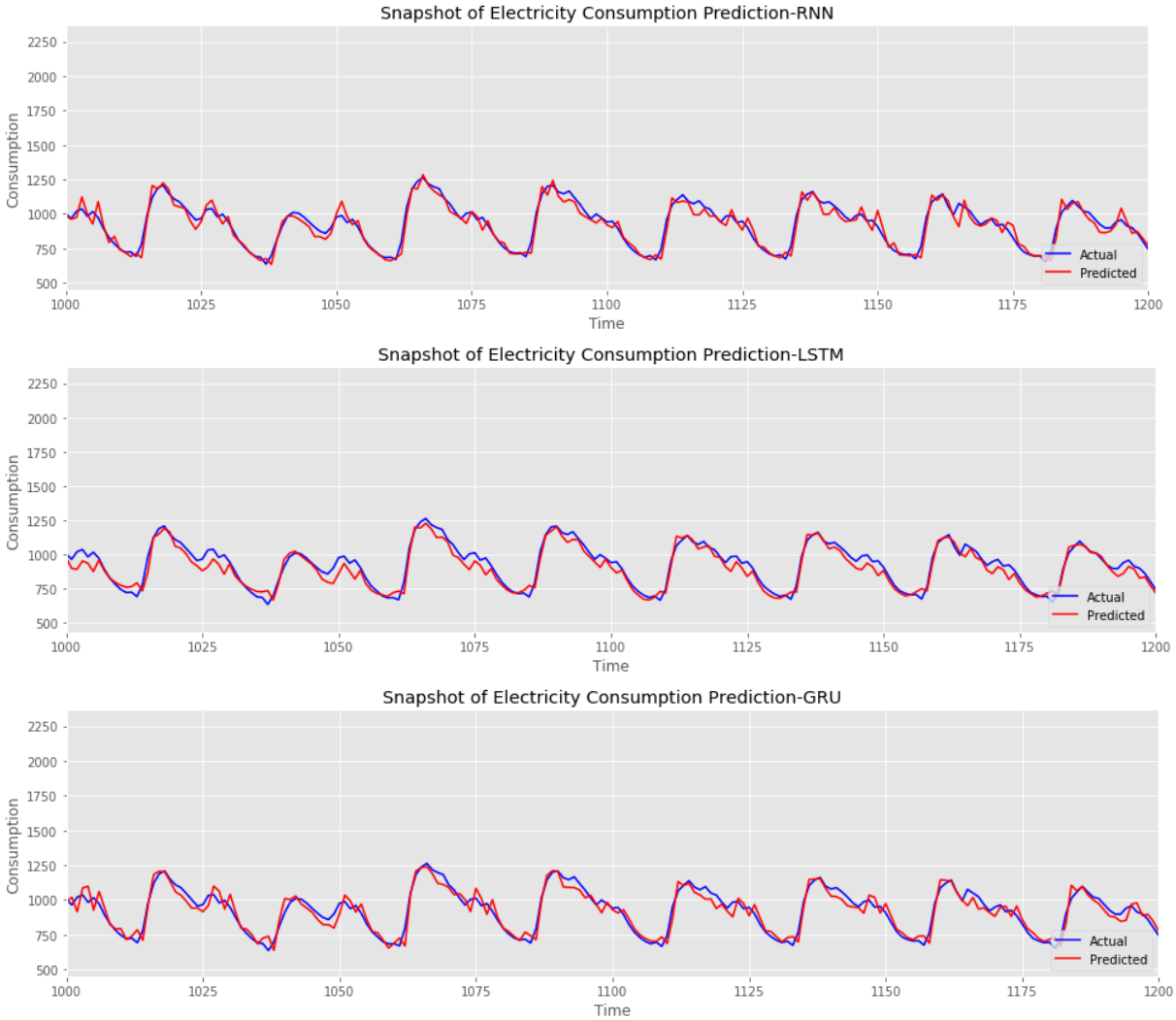

Figure 6. Snapshot of actual and predicted values of model results

Conclusion

The planning of consumption forecast is importance in energy sector. For this reason, the estimation should be as close to the truth. Negative effects that occur due to overestimation and underestimation should be prevented

by maintaining the balance supply and demand. Computer aided applications have been developed in order to minimize the errors originated from human and sensor data in the estimation data. The aim of this study is to estimate hourly consumption by using three different deep learning models.

In general, estimation models have been developed with time series methods using only consumption data. However, other factors affecting consumption are ignored. In this study, weather data were used in addition to consumption data for the training of the network and multivariate prediction models were created. Also, the addition of historical data has increased the accuracy rates by directly affecting the learning process of the models. In order to reduce the stochasticity of deep learning models and to reach more precise results, the models were run multiple times and their statistical averages. According to these results, the most successful algorithms are listed as RNN, GRU and LSTM.

Acknowledgements

We would like to thank Meram Elektrik Perakende Satış A.Ş (MEPAŞ) for providing consumption and weather data used in models designed in this study.

References

Aggarwal, C. C. (2018). Neural Networks and Deep Learning: A Textbook. In *Artificial Intelligence*, Springer Publishing. https://doi.org/10.1007/978-3-319-94463-0

Choi, H., Ryu, S., & Kim, H. (2018, December 24). Short-Term Load Forecasting based on ResNet and LSTM. *2018 IEEE International Conference on Communications, Control, and Computing Technologies for Smart Grids, SmartGridComm 2018*. https://doi.org/10.1109/SmartGridComm.2018.8587554

Jiang, Q., Zhu, J. X., Li, M., & Qing, H. Y. (2018). Electricity Power Load Forecast via Long Short-Term Memory Recurrent Neural Networks. *Proceedings - 2018 4th Annual International Conference on Network and Information Systems for Computers, ICNISC 2018*, 265–268. https://doi.org/10.1109/ICNISC.2018.00060

Kong, W., Dong, Z. Y., Jia, Y., Hill, D. J., Xu, Y., & Zhang, Y. (2019). Short-Term Residential Load Forecasting Based on LSTM Recurrent Neural Network. *IEEE Transactions on Smart Grid*, *10*(1), 841–851. https://doi.org/10.1109/TSG.2017.2753802

Mori, H., & Ogasawara, T. (1993). A recurrent neural network for short-term load forecasting. *Proceedings of the 2nd International Forum on Applications of Neural Networks to Power Systems, ANNPS 1993*, 395–400. https://doi.org/10.1109/ANN.1993.264315

Nalbant, A., Aslan, Y., & Yaşar, C. (2005). Kütahya İli Elektrik Puant Yük Tahmini. *Elektrik Elektronik Bilgisayar Mühendisliği, 11. Ulusal Kongresi, Bildiri Kitapçığı I, Sayfa:211-214 , İstanbul,*

Siddarameshwara, N., Yelamali, A., & Byahatti, K. (2010). Electricity short term load forecasting using Elman recurrent neural network. *Proceedings - 2nd International Conference on Advances in Recent Technologies in Communication and Computing, ARTCom 2010*, 351–354. https://doi.org/10.1109/ARTCom.2010.44

Tian, C., Ma, J., Zhang, C., & Zhan, P. (2018). A deep neural network model for short-term load forecast based on long short-term memory network and convolutional neural network. *Energies*, *11*(12). https://doi.org/10.3390/en11123493

Tokgoz, A., & Unal, G. (2018). A RNN based time series approach for forecasting turkish electricity load. *26th IEEE Signal Processing and Communications Applications Conference, SIU 2018*, 1–4. https://doi.org/10.1109/SIU.2018.8404313

Zheng, J., Xu, C., Zhang, Z., & Li, X. (2017, May 10). Electric load forecasting in smart grids using Long-Short-Term-Memory based Recurrent Neural Network. *2017 51st Annual Conference on Information Sciences and Systems, CISS 2017*. https://doi.org/10.1109/CISS.2017.7926112

Author Information

Duygu Altunkaya
Konya Food and Agriculture University
Melikşah Mah. Beyşehir Cad. No:9, 42080 Meram/Konya, Turkey
Contact e-mail: d*uygu.altunkaya@gidatarim.edu.tr*

Burak Yılmaz
Konya Food and Agriculture University
Melikşah Mah. Beyşehir Cad. No:9, 42080 Meram/Konya, Turkey

The Eurasia Proceedings of Science, Technology, Engineering & Mathematics (EPSTEM)
ISSN: 2602-3199

The Eurasia Proceedings of Science, Technology, Engineering & Mathematics (EPSTEM), 2020

Volume 11, Pages 20-28

IConTES 2020: International Conference on Technology, Engineering and Science

Electrical Conductance Study of Glutamic Acid Complex with [Mn(II)] in Different Solvents and Temperatures

Fanar M. AL-HEALY
Mosul University

Abstract: The electrical conductivities of glutamic acid complex with [Mn(II)] was study in different solvents (water, methanol, ethanol) in the beginning Kohlrausch equations was used to discover types of electrolyte through plot the relation between equivalent conductivity against the square root of molar concentration at different temperature from (288.16 -313.16) kilven. The plot indicate that complex of amino acid was weakly associated in different solvents and temperatures. The molar conductivity of glutamic acid complex measured by processing the obtained data using the conductivity equation of Lee-Wheaton equation to calculation the Equivalent conductance at infinite dilution (Λo) ,The association constant (KA), distance parameter (R), and standard deviation (σΛ).Thermodynamic information from association and examining the nature of the interaction was obtained and calculation of the standard thermodynamic quantities have be measure.A multi parameter curve fitting procedure is used to give the lowest value of curve fitting parameter (σ Λ) between the experimental and calculated values. An iterative numerical method which was found to be very successful has been used to find the minimum(σΛ), show the results of analysis that complex ions were separated by solvent molecules (SSIP).The values of (KA) , (Λo) and (R) differ from solvent to another depending on the interactions in solution.The walden product(Λη) for this complexe have been studied in water, methanol and ethanol.

Keywords: Glutamic acid, Glutamic acid complexe with [Mn(II)], Electrical conductivities, Lee-Wheaton equation, Thermodynamic parameter

Introduction

Thermodynamic properties are very useful study of the intermolecular interactions and geometrical effects in the systems and thermo-physical and bulk properties of solutions, Studying the information of the transport properties (conductance, viscosity, ionic mobility) of electrolytes in aqueous and partially aqueous media tell us all about ion-ion and ion-solvent interactions in these solutions(Wagner, 2012). The Lee-Wheaton equation which is one of the mathematic equations of conductivity theories has been successfully used to investigate many electrolytes in solutions (Lee & Wheaton, 1978). The physical properties of the binary mixed solvents like the viscosity and the relative permittivity can be varied making them more favor to solvent system for the study of ion association and ion mobility (Al-Healy, 2020). Many amino acids and their derived complexes were prepared and identified by using different methods since amino acids as ligands contain two donor atoms (N and O) (William, 2012), therefore the complexes of amino acids with metals are interesting to study.The conductivity of Tyrosine has been studied in aqueous solutions at 310.16K,The prepared complexes of tyrosine with Co(II) , Mn(II) , Ni(II) , Fe(II) , to form [Ni(tyr)3]Cl2, [Co(tyr)3]Cl2, [Fe(tyr)3]Cl2, [Mn(tyr)3]Cl2 complexes are measured using in the temperature range from (288.16–313.16K) in steps of 5 K. To give information about ionic molar conductivity(Λ), the association constant (KA), distance parameter (R), and standard deviation (σΛ) and the thermodynamic quantities (ΔH°, ΔG°, ΔS°) have been calculation (Al-Healy &Hamed, 2019). The complexes of Ca(II),Ni(II) ,Fe(II)with mixed ligands of amino acids (Glycine, Histidine, Cysteine and Arginine) were prepared and identified by elemental analysis, electrochemical conductivity measurements at different temperatures at PH=7,the thermodynamic data were calculated then the conductivity data were compared with other electrical method(Abdel –Rahman, 2007).The complexes of Co(II),Zn(II) with mixed ligands of amino acids (systine, histidine, systine methyl ester and histidine methyl ester) were prepared

and identified by elemental analysis, electrochemical conductivity, magnetic measurements and IR spectra (Rabindra, et al., 2005). Molar conductivities of dilute solutions for the complexes: Co(II)(alanine + valine),Ni(II)(valine + serine), Ca(II)(alanine + serine), Mg(II)(valine + serine) in water were measured in the temperature range from (293.16–313.16K). The ionic molar conductivity (Λ), the association constant (KA), distance parameter (R), and (σΛ) at best fit values were determined by treating experimental data with Lee-Wheaton conductivity equation. Thermodynamic quantities for the ion association reaction were derived from the temperature dependence of KA. The obtained results provide information on ion – ion and ion-solvent interactions (Al-Allaf, et al., 2013). Using the expanded Lee-Wheaton equation of electric conductivity, constants of ionic association are defined. It is determined that LiClO4 in propylene carbonate is a non-associated electrolyte. In order to account on the dynamics of ionic solvation, separation into ionic components is made, Results of conductometric investigations of solutions of several 1-1 electrolytes in propylene carbonate in the range of temperatures from 298 to 398 K are presented (Chernozhuk & Kalugin, 2016). *Glutamic acid* is an amino acid occurring in substantial amounts as a product of the hydrolysis of proteins. Certain plant proteins (e.g., gliadin) yield as much as 45 percent of their weight as glutamic acid; other proteins yield 10 to 20 percent. Much of this content may result from the presence of a related substance,glutamine, in proteins; glutamine is converted to glutamic acid when a protein is hydrolyzed. First isolated in 1865 (Okubo,*.et al*.,2010), glutamic acid is an important metabolic intermediate. It is one of several so-called nonessential amino acids; i.e., animals can synthesize it from oxoglutaric acid (formed in the metabolismof carbohydrates) and do not require dietary sources. Monosodium glutamate (MSG), a salt of glutamic acid, is sometimes used as a condiment for flavouring foods (Flickinger, 2010).

Experimental

Conductivity water was prepared by redistilling water three times with the addition of little amount of potassium permanganate and a small pellets of (KOH) (Palmer, 1954). The complexe of Mn(II) with glutamic acid was prepared by mixing (0.001mole,0.125g) from ($MnCl_2.4H_2O$) in 25 ml of conductivity water with (0.003 mole ,0.4414g) of glutamic acid in 25 ml of conductivity water and refluxed for about two hours On cooling, each complex was precipitated(Hummodat & Mustafa, 2013). Magnetic electronic spectra, IR measurement was used to make sure of the resulting complexes. A general method has been used for measuring the conductance of the electrolytes, the conductivity cell was washed , dried and then weighed empty and kept at a constant temperature (± 0.1ºC) using a water circulating ultra thermostat. A certain amount of solution was injected into the conductivity cell and the conductivity of solution was measured by WTW Inolab 740 computerized conductivity meter. Another known amount of solution was injected by a syringe of 1ml and the measurement was repeated. Generally about (14) addition have been made by weighing the amount for each one.

Results and Discussion

Conductometric data were treated using Lee-Wheaton equation in which a wide dielectric range for electrolytes solution can give detailed information concerning ion-ion and ion-solvent interaction.

$$M^{2+} + X^- \xleftrightarrow{KA1} MX^+$$

$$MX^+ + X^- \xleftrightarrow{KA2} MX_2$$

Ka: association constant

For unsymmetrical electrolyte 2:1 a program (RM1) is used to analyze the concentration- conductivity measurements in which the input data are (T, D, η) where T is temperature in Kelvin, D and η are the dielectric constant and viscosity (poise) of the solvent at (37oC). Lee and Wheaton obtained an equation of unsymmetrical electrolytes of the form (Lee & Wheaton, 1979).

$$\Lambda = \Lambda_o[1 + C_1(KR)(\varepsilon K) + C_2(KR)(\varepsilon K)^2 + C_3(KR)(\varepsilon K)^3 - (PK/(1+KR))\{1 + C_4(KR)(\varepsilon K) + C_5(KR)(\varepsilon K)^2 + KR/12\}$$

All the terms are defined in the original paper (Lee & Wheaton, 1978). The program (RM1) is used to determine values of KA , Λº and R where KA is the association constant; R is the average center to center distance for the

ion pairs; Λ^o, is the equivalent conductance of each ion in solution. A multi parameter "Least square" curve fitting procedure is used to give the lowest value of curve fitting parameter, ($\sigma\Lambda$), between the experimental and calculated values. An iterative numerical method which was found to be very successful has been used to find the minimum ($\sigma\Lambda$).

Therefor the Tables (1) (a-c) and figures (A)(1-3) show the relations between (Λ) and concentration ($\sqrt{c}$) for the studied complexes at different temperatures. A general look at the tables of the solution complexes of amino acids with Mn(II) at different temperatures and at different solvent shows that the equivalent conductance(Λ) increases with increasing temperatures, Probably because of the effect of the temperature on the properties of solution and with increase the degree of temperature decrease the density and the viscosity and may be increase association (Dabbagh & Akrawi,1992).

Table 1a. Molar concentration (M) and equivalent conductance of $[Mn(C_5H_7NO_4)_3]Cl_2$ in water at different temperatures

Conc. Mole/L*10^{-7}	Λ (Ohm- 1 . equive-1.cm2) 288.16 °K	Λ (Ohm- 1 . equive-1.cm2) 293.16 °K	Λ (Ohm- 1 . equive-1.cm2) 298.16 °K	Λ (Ohm- 1 . equive-1.cm2) 303.16 °K	Λ (Ohm- 1 . equive-1.cm2) 308.16 °K	Λ (Ohm- 1 . equive-1.cm2) 313.16 °K
3.0419	190.8092	186.5064	187.2148	190.5933	192.4664	190.2133
5.5837	162.4498	158.8135	127.5207	162.2564	131.0804	129.553
8.2203	151.2950	147.9345	106.0480	151.1059	108.9931	107.7291
10.4578	149.3133	146.0206	97.6883	149.1180	100.3888	99.22949
12.8893	146.0287	142.8327	91.2036	145.8294	93.7122	92.63486
15.4092	144.5078	141.3914	86.9463	144.2940	89.3260	88.3037
17.8822	143.9474	141.0144	85.1083	143.7427	87.4271	86.43068
20.1587	137.2175	141.0390	83.2094	143.8778	85.4656	84.49575
22.2411	136.2117	140.8209	81.7194	143.8409	83.9246	82.97646
24.6559	136.9926	140.7240	80.8314	143.5502	83.0026	82.06878
27.3819	135.6228	140.2216	80.4530	142.9758	81.6064	80.69244
29.8709	134.7634	140.5403	79.4821	138.5195	81.5974	80.68699
32.3825	134.4476	140.2063	79.2155	134.2039	81.3141	80.41058
34.2517	130.1749	140.2204	78.6700	129.9319	80.7443	79.85097

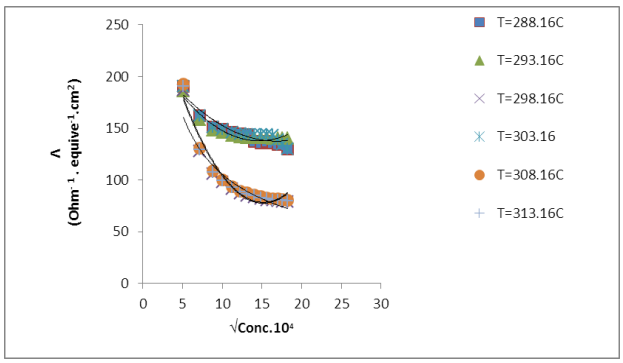

Figure 1a. Equivalent conductance of $[[Mn(C_5H_7NO_4)_3]Cl_2$ in water at different temperatures

Table 1b. Molar concentration (M) and Equivalent conductance of $[Mn(C_5H_7NO_4)_3]Cl_2$ in methanol at different temperatures

Conc. Mole/L*10^{-7}	Λ (Ohm- 1 . equive-1.cm2) 288.16 °K	Λ (Ohm- 1 . equive-1.cm2) 293.16 °K	Λ (Ohm- 1 . equive-1.cm2) 298.16 °K	Λ (Ohm- 1 . equive-1.cm2) 303.16 °K	Λ (Ohm- 1 . equive-1.cm2) 308.16 °K	Λ (Ohm- 1 . equive-1.cm2) 313.16 °K
2.6837	124.2027	126.5987	128.4337	126.0031	127.5169	123.8668
5.2189	95.8047	97.5994	99.0139	97.1759	98.3379	95.5342
7.71234	64.8308	50.2506	66.9655	65.7465	66.5290	64.6396
10.0287	49.8562	39.3153	51.4703	50.5513	51.1503	49.7030
12.6141	43.8527	34.0451	40.8987	44.4473	40.6569	39.5113
15.2023	41.8051	31.2963	38.8931	40.1831	33.7268	32.7804
17.6669	39.6379	26.0004	34.6279	38.2398	29.0149	28.2040
19.9337	37.7351	22.3996	34.4525	34.0819	25.7097	24.9937
22.4324	37.1486	21.3782	33.9170	30.9444	22.8406	22.2071
24.7648	36.6691	19.8737	32.1771	33.8855	20.6847	20.1132
27.2709	33.8573	19.4369	31.4292	30.1057	18.7795	18.2628
29.5357	33.6498	17.9657	30.5986	28.5667	17.3357	16.8604
31.9319	31.3166	17.6812	30.0905	26.4185	16.0312	15.5935
34.1291	29.3004	16.6366	29.0045	24.7136	14.9958	14.5879

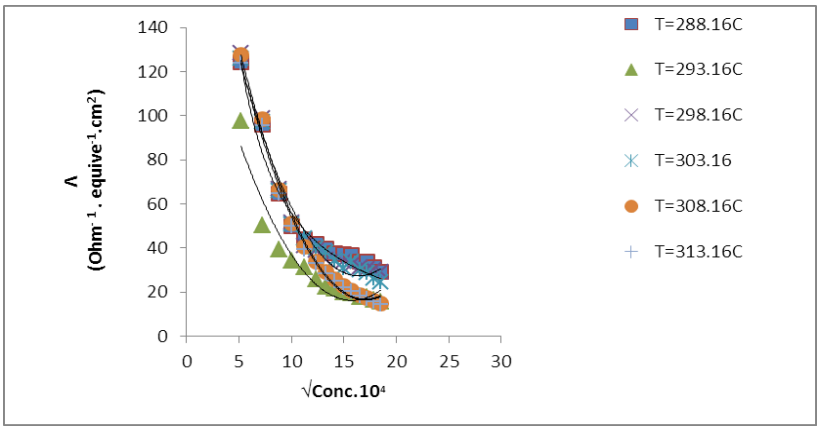

Figure 1b. Equivalent conductance of $[Mn(C_5H_7NO_4)_3]Cl_2$ in methanol at different temperatures

Table 1c. Molar concentration (M) and Equivalent conductance of $[Mn(C_5H_7NO_4)_3]Cl_2$ in ethanol at different temperatures

Conc. Mole/L*10^{-7}	Λ (Ohm- 1 . equive- 1.cm2) 288.16 °K	Λ (Ohm- 1 . equive- 1.cm2) 293.16 °K	Λ (Ohm- 1 . equive- 1.cm2) 298.16 °K	Λ (Ohm- 1 . equive- 1.cm2) 303.16 °K	Λ (Ohm- 1 . equive- 1.cm2) 308.16 °K	Λ (Ohm- 1 . equive- 1.cm2) 313.16 °K
4.9886	65.8186	66.1697	59.3676	67.0649	67.3797	67.5368
10.4565	30.8780	31.6332	29.7871	33.1230	33.2812	32.2180
15.1464	22.0073	21.8826	28.5462	31.9908	32.1422	32.1422
20.0693	16.6090	16.5479	22.6503	24.9944	25.1148	25.1755
24.9671	13.3508	19.9922	18.3425	20.0884	20.1860	20.2353
30.0471	12.6012	16.6447	15.3532	16.6898	16.7715	16.8129
34.9044	11.2307	14.3562	13.3119	14.3652	14.4361	14.4722
39.6784	11.0936	12.6532	11.7932	13.5278	13.5961	12.7300
44.5205	10.1215	11.2984	10.5840	12.6350	12.6350	11.3446
49.3997	9.5498	10.2016	9.6042	12.2880	12.2880	10.2234
54.3762	9.1951	9.2851	8.7844	11.2593	12.3506	9.2870
59.1615	8.4514	8.5498	8.1276	11.2926	11.3158	8.5352
63.6382	7.8569	7.9628	7.6054	10.4968	10.5510	7.9348
68.2427	7.3267	7.4389	7.1380	9.78730	9.78730	7.398449

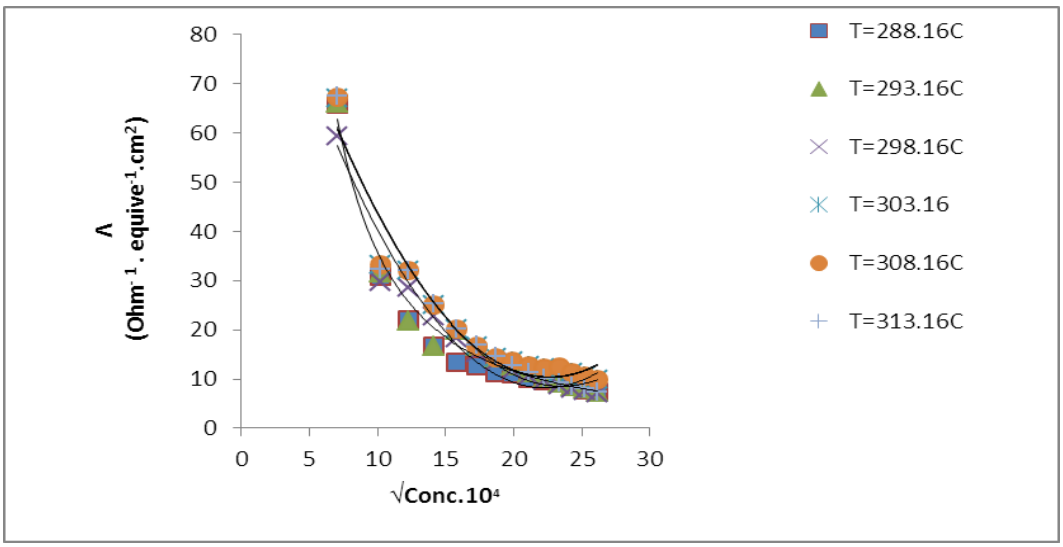

Figure 1c. Equivalent conductance of $[Mn(C_5H_7NO_4)_3]Cl_2$ in ethanol at different temperatures

It was found that equivalent conductivity at different temperatures decrease with in crease concentration. This may be understand as discussed by (Lee & Wheaton, 1978). That in water (D~79) and in presence of hydrogen

bonding and we show the equivalent conductivity of water > methanol > ethamo, the solvation will be higherin water more than methanol and ethanol because efecte of viscosity and dielectric constant at different temperatures. The Lee-Wheaton equation was applied to the compelex solution described above , where the equivalent continuity was calculation program after it announced the electrical conductivity of all studied fixed cell concentration (0.5cm) ,density (0.99707gm/cm3) , the data including concentration and equivalent conductivity values,were analyzed using aspecial analysis software after giving information on both absolute temperature(T), viscosity of solution (0.0089pois) and dielectric constant (78.3D). after completing the analysis of the data it was confirmed that these solution were weak electrolytes. Tables 2(a-c) show the results of the analysis compelexes at different temperatures. where each table show the association constant (KA) and the equivalent conductance (Λ), the(R) values (distance parameter) and the best fit data standard deviation σs(Λ).

Table 2a. the values at constant Ka, Λ,the distance between R(A°) and σΛ of $[Mn(C_5H_7NO_4)_3]Cl_2$ at different temperatures in water

T (K)	Ka	Λ° (Ohm^{-1} . $equive^{-1}.cm^2$)	R (A°)	бΛ
288.16	210	92	50	0.048
293.16	260	80	4.0	0.019
298.16	310	64	7.9	0.069
303.16	360	42	4.5	0.036
308.16	420	36	5.0	0.072
313.16	470	30	4.0	0.070

Table 2b. the values at constant Ka, Λ,the distance between R(A°) and σΛ of $[Mn(C_5H_7NO_4)_3]Cl_2$ at different temperatures in methanol

T (K)	Ka	Λ° (Ohm^{-1} . $equive^{-1}.cm^2$)	R (A°)	бΛ
288.16	100	18	6.0	0.009
293.16	130	15	5.0	0.010
298.16	150	12	8.0	0.027
303.16	170	11	5.0	0.026
308.16	210	10	5.0	0.033
313.16	260	6	7.9	0.035

Table 2c. the values at constant Ka, Λ,the distance between R(A°) and σΛ of $[Mn(C_5H_7NO_4)_3]Cl_2$ at different temperatures in ethanol

T (K)	Ka	Λ° (Ohm- 1 . equive-1.cm2)	R (A°)	бΛ
288.16	31	16	9.5	0.045
293.16	61	14	8.4	0.042
298.16	80	12	5.4	0.041
303.16	110	10	5.5	0.037
308.16	130	8	5.0	0.036
313.16	160	6	9.4	0.034

We also note the Ka value of complexes because the electronic density of the solvent decrease associations with decrease that the solvent molecules will be attracted and thus ion association increase , The results of distance parameter R show that complexes electrolytes form solvent separated ion pairs (R is between4-8) these high values of R indicated that cations and anions are separated by many solvent molecules since the association was high with increase temperatures.The values of σΛ give an indication of good best-fit values (Akrawi,et al, 2008).

Calculation of the Thermodynamic Parameters (ΔH, ΔG, ΔS)

The values of ΔH were calculated by the relation between lnKA against 1/T illustrated by Vant-Hoff equation (Eggers et al., 1964).

$$\ln Ka = \frac{\Delta H}{RT} + C$$

The relation gives a straight line for complex solutions, and ΔG from the equation : ΔG = – R T lnKA
While ΔS values were calculated from the equation : ΔG = ΔH – T ΔS
From the tables below, the values of ΔH (enthalpy of association) were negative which show that the operation was hydration ,while ΔG (Gibbs free energy) has a negative values which depends upon the kind of ions and in agreement with the relation: ΔG = – RTLnKA which means that the reaction was spontaneous towards association , and the values of ΔS were small positiv due to the negative values of ΔH which leads to the ordering of the system as a result of association under the influence of solvation and columbic effect in spontaneous continuum media.

Table 3a. Thermodynamic parameters of $[Mn(C_5H_7NO_4)_3]Cl_2$ at different temperatures in water

T (K)	ΔS (J.mol-1.K-1)	-ΔG (KJ.mol-1)	-ΔH (KJ.mol-1)	Ln ka
288.16	39.2	12.80	24.1	5.34
293.16	360	13.55		5.56
298.16	33.2	14.21		5.73
303.16	30.6	14.83		5.88
308.16	28.0	15.47		6.04
313.16	25.9	16.01		6.15

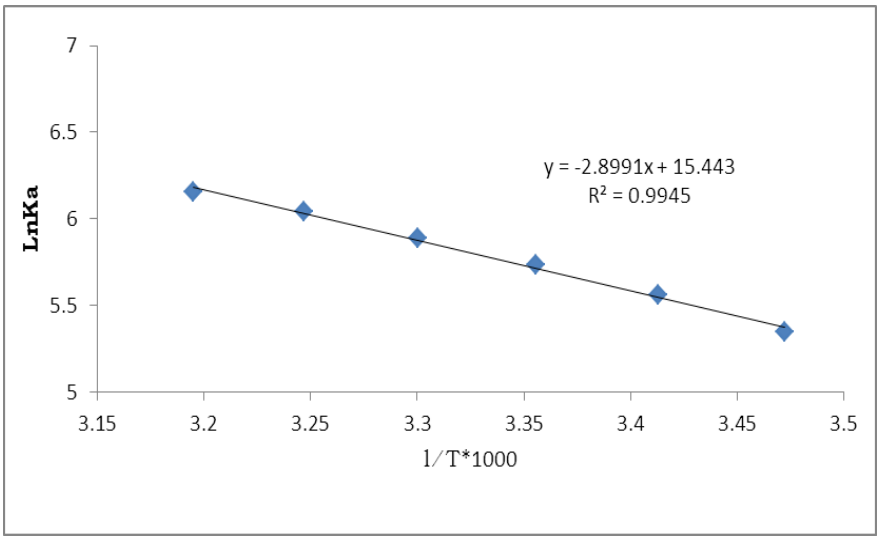

Figure 2a. The relation between the Ln ka &1/T of $[Mn(C_5H_7NO_4)_3]Cl_2$ in water

Table 3b. Thermodynamic parameters of $[Mn(C_5H_7NO_4)_3]Cl_2$at different temperatures in methanol

T (K)	ΔS (J.mol-1.K-1)	-ΔG (KJ.mol-1)	-ΔH (KJ.mol-1)	Ln ka
288.16	132.56	11.03	27.15	4.60
293.16	133.13	11.86		4.88
298.16	132.77	12.41		5.11
303.16	132.70	12.94		5.13
308.16	132.60	13.69		5.37
313.16	132.97	14.47		5.56

In water, the values of ΔH° are negative and ΔS° are positive, this will ascribed to specific short-range interaction such as hydrogen bonding. the values of ΔS° and in methanol are positive and ΔH° are negative may mean that the temperature dependence of D,

$$\Delta H°_{eq.} = -bRT_2(T^{-1} + \partial \ln D/\partial T)\,(d\ln K_A/db)$$

∂lnD/∂T represent how much the ion salvation is weakened by ion association. The positive value of ΔS° in Table 3 has been considered as due to the decreasd orientation of solvent molecules when the ion pair performed.

In ethanol the value of ΔH° is negative and ΔS° positive because of the low value of the dielectric constant of ethanol which leads to ion solvent interaction, and the high value of association constants leads to very low value of Λ° of $[Mn(glu)_3]^{2}$ ion and more orientation due to ion solvent interaction.

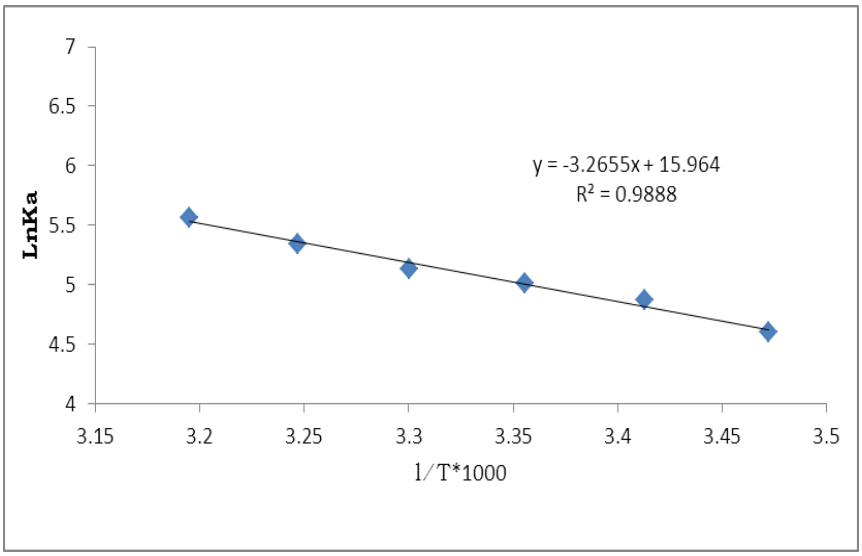

Figure 2b. The relation between the Ln ka &1/T of $[Mn(C_5H_7NO_4)_3]Cl_2$ in methanol

Table 3c. Thermodynamic parameters of $[Mn(C_5H_7NO_4)_3]Cl_2$ at different temperatures in ethanol

T (K)	ΔS (J.mol-1.K-1)	-ΔG (KJ.mol-1)	-ΔH (KJ.mol-1)	Ln ka
288.16	198.95	8.22	46.48	3.43
293.16	192.82	10.01		4.11
298.16	192.41	10.86		4.38
303.16	192.49	11.84		4.70
308.16	191.39	12.47		4.86
313.16	190.70	13.21		5.07

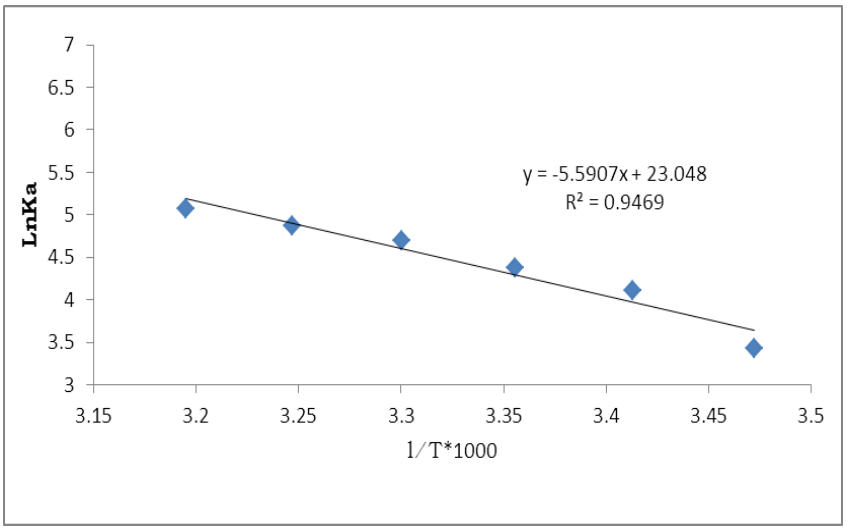

Figure 2c. The relation between the Ln ka &1/T of $[Mn(C_5H_7NO_4)_3]Cl_2$ in ethanol

Walden product

The walden product ($\Lambda_o\eta$)for studied complexes have been calculated in water, methanol and ethanol were obtained by multiplying each values of Λ from Table2 by the appropriate viscosity in the temperature range 283.15 - 313.15 K (Al-Healy & Hameed, 2020). We can show the effect of viscosity and dencety from solvent to other at different temperature. All results are listed in Table 4.

Table 4. The walden product ($\Lambda_o\eta$) parameters of $[Mn(C_5H_7NO_4)_3]Cl_2$ İn water, methanol and ethanol at different temperatures

T(K)	($\Lambda_o\eta$)		
	$[Mn(C_5H_7NO_4)_3]Cl_2$ in water	$[Mn(C_5H_7NO_4)_3]Cl_2$ in methanol	$[Mn(C_5H_7NO_4)_3]Cl_2$ in ethanol
288.16	0.6108	0.1110	0.2160
293.16	0.5104	0.0862	0.1680
298.16	0.3916	0.0645	0.1320
303.16	0.2461	0.0554	0.1003
308.16	0.2016	0.0474	0.0720
313.16	0.1620	0.0268	0.0498

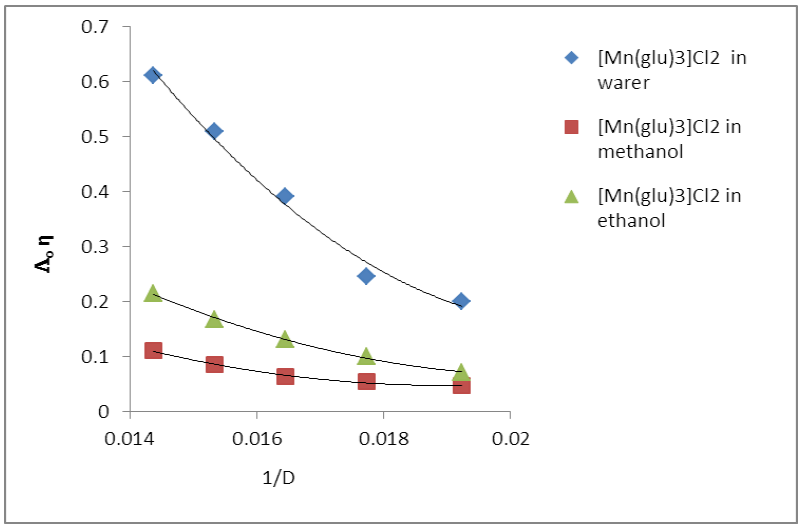

Figure 3. The walden product ($\Lambda\eta$) parameters of $[Mn(C_5H_7NO_4)_3]Cl_2$ in water, methanol and ethanol at different temperatures

Walden product ($\Lambda_o\eta$)of the compelex at different temperature against 1/D is shown in Figure(3). It is clear that ($\Lambda_o\eta$) decrease with decreasing D. The increase of D of the solvent will increase the solvating power of that solvent. This causes that the ion will move with only the primary solvation shell in the solvent and the effect of the secondary solvation appears to be very small (Doe and Kitagaw, 1985)[19]. Thus the size of the primary solvated ion is expected to be smaller in the order: MeOH < EtOH < H_2O . The ion association constant KA (1) increase with decreasing D of the solvent due to the multiplestep association process with solvation and desolvation of [Mn(glu)] (Vesna, S. et al., 2008)[20].

Conclusion

The present work reports conductivity data for the low concentration glutamic acid with Mn solutions in water,methanol and ethanol at different temperature. Lee-Wheaton equation at the best fit values of standard deviled ($\sigma\ \Lambda$) for analyzing the data of unsymmetrical electrolytes including: The conductivity parameters, the association constant KA and the distance parameter R . The values differ from solvent to another depending on dielectric constant and viscosity and interactions in solution the effect of electrophoretic effect or asymmetric effect.

Recommendations

The Lee-Wheaton equation is very important, it be used to determination of any ionic compound at very low concentration, with any solvent at different temperatures and give information about association constant KA , equivalent conductivity at infinity dillution $\Lambda°$ and the distance parameter R,Which is very important constant in Thermodynamic.Thermodynamic parameters can be calculated by using Vant-Hoff equation from association constant.

References

Abdel –Rahman, H.A. (2007). *An Electrical Conductometric Study of Some Amino Acids and Their Complexes with Some Metals in Aqueous Medium at Different Temperatures* . ;M.Sc.Thesis, Mosul University.

Al-Allaf, Y.O.; Al-Tamer, M.Y., Abdulfattah, M.N. (2013). Conductometric Studies for Association Reaction of some Amino Acid complexes in Water. *Raf. J. Sci., 24*(6), pp. 45-60.

Al-Healy, F. & Hamed, Y. (2019). Electrochemical and thermodinamic study of tyrosine and its complexes in aqueous solution by conductivity measurement. *The Eurasia Proceedings of Science, Technology, Engineering & Mathematics (EPSTEM),7*, 48-57.

Al-Healy, F. (2020).*Conductemetric Study for the Ionic Association of Some Transition Metals Complexes with Some Amino Acids in Different Solvents*. (Doctoral dissertation) , University of Mosul (College of Science).

Al-Healy,F., & Hameed, Y. (2020). Measurement of the Electrical Conductivity of Equivalent A number of Aspartic Acid Complexes in Different Percentages of Water Mixture with Methanol at 310 Absolute Temperature. *Raf. J. Sci., 29*(1), 80-94.

Chernozhak, T. & Kalugin, O. (2016). Conductivity and interparticle interactions in the solutions of 1-1 electrolytes in propylene carbonat in the wide range of temperatures. *Chemistry & Chemical Technologe ,10*, No:1, 9-18.

Dabbagh, A.M., & Akrawi, B.A. (1992). *Kinetics and Electrochemistry*. Dar Alkutub for Printing and Publishing, Mosul, pp. 323-405.

Doe, H. & Kitagawa, T. (1985). Conductometric Study of Co(II), Ni(II), Cu(II) and Zn(II) Perchlorates in Methanol-Ethylene Glycol Mixtures. *Bull. Chem. Soc. Jpn.,58*, pp.2975-2980.

Eggers, D.F., Gregory, N.W., Halsey, G.D., & Rabinovitch, B.S. (1964). *Physical Chemistry*. John Wiley and Sons, Inc. New York, 198.

Flickinger, M. C. (2010).*Encyclopedia of industrial Biotechnology:Bioprocess,Bioseparation, and Cell Technology*, Vol.7,Wiley.ISBN.978-471-79930-6.

Hummodat, M. Z., & Mustafa, I. (2013). *Synthsis and Characterization of Mixed ligand Complexes of Nikal(II) Copper(II) Palladium(II) Platinum(IV) and Gold(III) with Some Amino Acid and Dithiocarbamates or Dithiophosphat in Thetriphenylphosphine Adducts with some of the Nickal(II) Complexes* , Ph.D., University of Mosul ,College of Science:53.

Lee, W.H. & Wheaton, R.J. (1978). Conductance of symmetrical, unsymmetrical and mixed electrolytes. *J. Chem. Soc.,74*, 743-766.

Lee, W. H., & Wheaton, R. H. (1979). The conductivity of dilute aqueous magnesium chloride at 25◦ C. *J. Chem. Soc, 75*, 1128.

Okubo,Y., Sekiya, H., Namiki,S., Sakamoto,H., Linuma,S., Yamasaki,M., Watanabe,M., Hirose,K., Lion, M. (2010). Imaging extrasynaptic glutamate dynamics in the brain. *Proceedings of the National Academy of Scienes, 107*(14), 6526–6531.

Palmer, W.G. (1954). *Experimental Physical Chemistry.* Cambridge at the University Press, London, 186.

Rabindra, R.P., Radhika, M., & Manjula, P. (2005*).* Synthesis and characterization of mixed liqand complexes of Zn(II) and Co(II) with Amino Acid: Relevance to Zinc binding sites in Zing fingers . *J. Chem. Sci., 117*(3), 239-246.

Vesna, S., Renato, T., Ivo, T. (2008). Thermodynamics of the association reaction of RbBr in binary mixtures of 2-Butanol and water from 288. 15 to 308.15 K. *Acta Chem. Slov., 55*, 308-314.

Wagner, H. (2012) .Influence of temperature on electrical conductivity of diluted aequas solution. *Power Plant Chemistery Journal*, Special Edition. 1438-5325

William M. H., (2016). Handbook of chemistry and physics, 97th ed.:5-89. CRC Press.

Author Information

Fanar Al-Healy
Mosul University
Department of Chemistry College of Science,Mosul
University Mosul/Iraq
Contact E-mail:Fm.alhealy*@gmail.com*

The Eurasia Proceedings of Science, Technology, Engineering & Mathematics (EPSTEM)
ISSN: 2602-3199

The Eurasia Proceedings of Science, Technology, Engineering & Mathematics (EPSTEM), 2020

Volume 11, Pages 29-32

IConTES 2020: International Conference on Technology, Engineering and Science

Effect of Co Content on the Electrochemical Properties of (MgCoNiZnLi)O Based High Entropy Oxides for Li-Ion Batteries

Ersu LOKCU
Eskisehir Osmangazi University

Resat Can OZDEN
Eskisehir Osmangazi University

Mustafa ANIK
Eskisehir Osmangazi University

Abstract: High entropy oxides (HEOs) are attractive as a negative electrode material for lithium-ion batteries (LIBs), because of the high specific capacities and cycling stabilities. Moreover, they offer a wide range of compositional variation to reach the desired electrochemical performances. In this study, we synthesized the $Co_5(MgNiZnLi)_{95}O$ and $Co_{35}(MgNiZnLi)_{65}O$ high entropy oxides using conventional solid state reaction technique and examined their electrochemical properties in lithium-ion cells as anode material. The structural properties of as-synthesized high entropy oxides were investigated using X-ray diffraction (XRD) technique, which showed that all the oxides have single-phase rock-salt structure. The increase in the Co content from 5% to 35%, the high entropy oxide based anodes resulted in improved discharge capacity due to the different oxidation states in Co ions. This work indicates that the compositional and elemental valences are very crucial to design and achieve novel high performance high entropy oxide based anode materials for lithium-ion batteries.

Keywords: Conversion type anode, Li-ion battery, High entropy oxide

Introduction

As promising energy storage devices, lithium-ion batteries (LIBs) have attracted much attention due to their high energy density and long cycle life properties. However, to meet the increasing energy and performance expectations in applications such as electric vehicles, energy densities of LIBs should be increased (Puthusseri et al., 2018; Yuan et al., 2014). Thus, the developing high-voltage cathodes and high-capacity anodes is the easiest way to achieve these expectations. Conversion-reaction-based anode materials, especially transition metal oxides are very promising because of their high theoretical capacity and low cost (Yu et al., 2018; Lu et al., 2018).

Since the day it was discovered, the concept of high entropy materials (HEMs) has led to the designing of many new compounds such as high entropy carbides, nitrides, borides, sulfides and oxides. The key concept of HEMs is to use multiple constituents (usually five or more with the concentration of each constituent being between 5 and 35 at. %), in order to maximize the configurational entropy ($S_{config} \geq 1.5R$) to achieve a single phase solid solution structure (Rost et al., 2015). The configurational entropy can be calculated using the following equation:

$$S_{config} = -R\left[\left(\sum_{i=1}^{N} x_i \ln x_i\right)_{cation\ site} + \left(\sum_{j=1}^{N} x_j \ln x_j\right)_{anion\ site}\right]$$

- Selection and peer-review under responsibility of the Organizing Committee of the Conference

where, x_i and x_j represent the mole fractions of ions present in the cation and anion sites, respectively, and R is the gas constant (Sarkar et al., 2018).

It is reported that the entropy stabilization results in improved cycling capability in (MgCoNiCuZn)O anode (Sarkar et al., 2018). Furthermore, the specific capacity value of 920 mA h g^{-1} was reached after 300 cycles upon synthesis of HEO based anode in the form of nanoparticles (Qiu et al., 2019). In another study, $(MgCoNiZn)_{1-x}Li_xO$ HEOs were synthesized and their electrochemical performances were investigated as anode material in LIBs. The increase in the lithium cation concentration causes generation of more oxygen vacancies, which greatly affected the electrochemical performance of $(MgCoNiZn)_{1-x}Li_xO$ HEO based anodes, on the structure. They reported the $(MgCoNiZn)_{0.65}Li_{0.35}O$ anode had 1930 mA h g^{-1} initial and 610 mA h g^{-1} stable discharge capacities (Lökçü et al., 2020). These results were very promising for the use of HEOs as anode material in LIBs. Herein, we synthesized the $Co_x(MgNiZnLi)_{100-x}O$ high entropy oxides to further investigation of their electrochemical properties related to the different presence of Co in the structure.

Materials & Methods

MgO, CoO, NiO, ZnO and Li_2O were mixed homogeneously in the determined molar ratios to get $Co_5(MgNiZnLi)_{95}O$ and $Co_{35}(MgNiZnLi)_{65}O$ stoichiometry and they milled at 300 rpm for 2 h by using the planetary ball mill (Fritsch Pulverisette 7 Premium Line). The obtained oxide mixtures were then unaxially pressed at 300 MPa. Finally, the oxide pellets were sintered at 1000ºC for 12 h prior to the air quenching. The sintered pellets were re-milled at 200 rpm for 1 h to prepare electrodes.

The phase structures of the as-synthesized $Co_5(MgNiZnLi)_{95}O$ and $Co_{35}(MgNiZnLi)_{65}O$ HEOs were examined by XRD (PANalytical Empyrean) technique using Cu Kα radiation (λ = 0.154 nm). The HEO based anodes were prepared by mixing 75 wt% active material, 15 wt% carbon black (Super P) and 10 wt% polyvinylidene fluoride (PVDF) in N-methyl pyrrolidinone (NMP) to form a homogeneous slurry. Then the slurry was coated onto Cu foil and dried in a vacuum oven at 80ºC for 12 h.

The coin cells were assembled in an argon-filled glove box with H_2O and O_2 levels less than 1.0 ppm. Lithium metal was used as the counter and reference electrodes and the glass microfiber filter as a separator. 1 M Lithium hexafluorophosphate ($LiPF_6$) in ethylene carbonate and dimethyl carbonate (EC:DMC) in a 1:1 ratio by volume was used as electrolyte. The charge-discharge tests were performed galvanostatically in a potential range change between 0.01 V and 3.00 V (vs. Li^+/Li) at 100 mA g^{-1} current density.

Results and Discussion

The XRD patterns of $Co_5(MgNiZnLi)_{95}O$ and $Co_{35}(MgNiZnLi)_{65}O$ samples, which are prepared by the conventional solid state method, reveal that all the samples have a single phase rock-salt crystal structure. As shown in Figure 1, The diffraction peaks at 2θ values ~36. 92˚, 42. 89˚, 62. 29˚, 74. 63˚ and 78. 56˚, are corresponding to the (111), (200), (220), (311) and (222), planes of the rock-salt crystal structure, respectively.

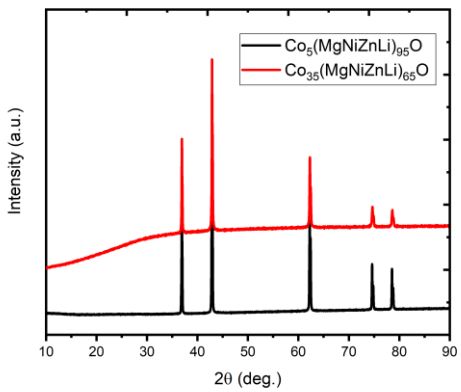

Figure 1. XRD patterns of the as-synthesized $Co_5(MgNiZnLi)_{95}O$ and $Co_{35}(MgNiZnLi)_{65}O$ HEOs.

Figure 2 shows the galvanostatic initial discharge (Li insertion) voltage profiles of the HEO based anodes at a current density of 100 mA g^{-1} in the voltage window of open circuit voltage (OCV)- 0.01 V. The initial discharge capacities of $Co_5(MgNiZnLi)_{95}O$ and $Co_{35}(MgNiZnLi)_{65}O$ are 1725 mA h g^{-1} and 1587 mA h g^{-1}, respectively. The discharge plateaus of anodes located around 0.45 V.

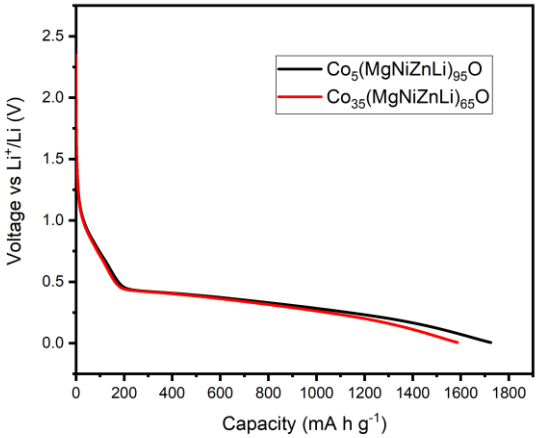

Figure 2. Initial discharge curves of $Co_5(MgNiZnLi)_{95}O$ and $Co_{35}(MgNiZnLi)_{65}O$ anodes at a current density of 100 mA g^{-1}

The charge-discharge cycles from the 2nd to 5th are given in Figure 3. The discharge voltages of the anodes look slightly increased and the discharge reaction occurs over a potential range of ~1.50-0.01 V with an inclined single slope. After the first cycle, the significant capacity loss is observed because of the formation of the SEI layer at the interface of the electrode surface and the electrolyte and initial lithium loss, mainly due to anode conversion.

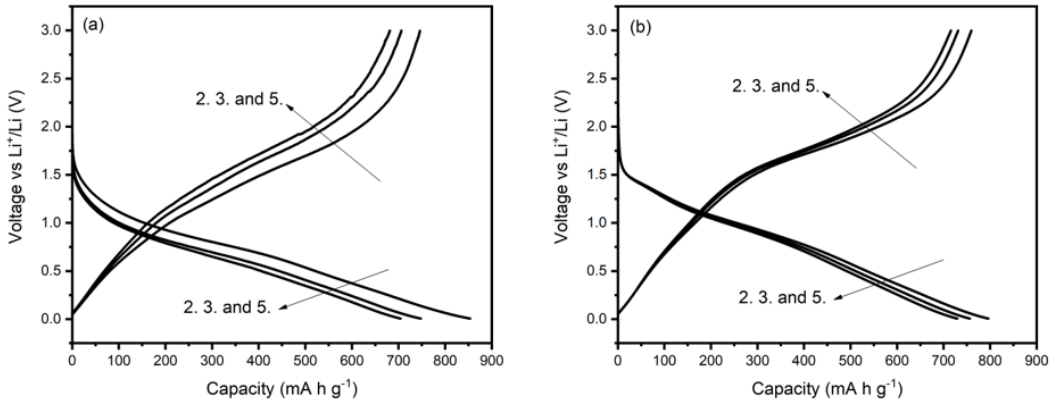

Figure 3. Discharge-charge curves of (a) $Co_5(MgNiZnLi)_{95}O$ and (b) $Co_{35}(MgNiZnLi)_{65}O$ anodes for the 2nd, 3rd and 5th cycles in the voltage range of 0.01-3.00 V at a current density of 100 mA g^{-1}.

The discharge capacities of the $Co_5(MgNiZnLi)_{95}O$ and $Co_{35}(MgNiZnLi)_{65}O$ anodes are 704 mA h g^{-1} and 729 mA h g^{-1}, respectively at the end of 5th cycle. The cycling stability of $Co_{35}(MgNiZnLi)_{65}O$ anode is relatively better than $Co_5(MgNiZnLi)_{95}O$ anode. Between the 2nd and 5th cycles, the capacity retention of $Co_5(MgNiZnLi)_{95}O$ and $Co_{35}(MgNiZnLi)_{65}O$ anodes are 82% and 91%, respectively. Therefore, these results evidence that the electrochemical performances of HEO based anodes can be improved by simply changing the cation contents in the structure.

Conclusion

In this work, $Co_5(MgNiZnLi)_{95}O$ and $Co_{35}(MgNiZnLi)_{65}O$ anodes were synthesized with a single-phase rocksalt crystal structure by the conventional solid-state method and their electrochemical performances were observed in the LIB. The results prove that Co content plays an important role in the HEO structure, which affects the

electrochemical performances of anodes. The electrochemical performance of high Co content anode is very satisfactory and promising for the future LIB applications.

Acknowledgements or Notes

This research was supported by the Scientific and Technological Research Council of Turkey under the project number 119M807.

References

Lökçü, E., Toparli, Ç., & Anik, M. (2020). Electrochemical performance of $(MgCoNiZn)_{1-x}Li_xO$ high-entropy oxides in lithium-ion batteries. *ACS Applied Materials & Interfaces, 12*, 23860-23866.

Lu, J., Chen, Z., Pan, F., Cui, Y., & Amine, K. (2018). High-performance anode materials for rechargeable lithium-ion batteries. *Electrochemical Energy Reviews, 1*, 35−53.

Puthusseri, D., Wahid, M., & Ogale, S. (2018). Conversion-type anode materials for alkali-ion batteries: State of the art and possible research directions. *ACS Omega, 3*, 4591−4601.

Rost, C. M., Sachet, E., Borman, T., Moballegh, A., Dickey, E. C., Hou, D., Jones, J. L., Curtarolo, S., & Maria, J.-P. (2015). Entropy-stabilized oxides. *Nature Communications, 6*, 1−8.

Sarkar, A., Velasco, L., Wang, D., Wang, Q., Talasila, G., de Biasi, L., Kübel, C., Brezesinski, T., Bhattacharya, S. S., Hahn, H., & Breitung, B. (2018). High entropy oxides for reversible energy storage. *Nature Communications, 9*(3400), 1-9.

Qiu, N., Chen, H., Yang, Z., Sun, S., Wang, Y., & Cui, Y. (2019). A high entropy oxide (Mg0.2Co0.2Ni0.2Cu0.2Zn0.2O) with superior lithium storage performance. *Journal of Alloys and Compounds, 777*, 767−774.

Yu, S.-H., Feng, X., Zhang, N., Seok, J., & Abruña, H. D. (2018). Understanding conversion-type electrodes for lithium rechargeable batteries. *Accounts of Chemical Research, 51*, 273−281.

Yuan, C., Wu, H. B., Xie, Y.;, & Lou, X. W. D. (2014). Mixed transition- metal oxides: Design, synthesis, and energy-related applications. *Angewandte Chemie International Edition, 53*, 1488−1504.

Author Information

Ersu Lökçü
Eskisehir Osmangazi University
Department of Metallurgical and Materials Engineering,
26040, Eskisehir, Turkey

Reşat Can Özden
Eskisehir Osmangazi University
Department of Metallurgical and Materials Engineering,
26040, Eskisehir, Turkey
rcanozden@ogu.edu.tr

Mustafa Anik
Eskisehir Osmangazi University
Department of Metallurgical and Materials Engineering,
26040, Eskisehir, Turkey

The Eurasia Proceedings of Science, Technology, Engineering & Mathematics (EPSTEM)
ISSN: 2602-3199

The Eurasia Proceedings of Science, Technology, Engineering & Mathematics (EPSTEM), 2020

Volume 11, Pages 33-40

IConTES 2020: International Conference on Technology, Engineering and Science

Investigation of the Effect of Varying Laser Scribe Sizes on the Adhesion Performance of the Aa2024-T3/Cfrp Joints Depending on the Number of Laser Scan Repeats

Seda AYBALIK
Kocaeli University

Onur COBAN
Kocaeli University

Mustafa Ozgur BORA
Kocaeli University

Erhan AKMAN
Kocaeli University

Belgin GENC OZTOPRAK
Kocaeli University

Abstract: One of the laser surface treatment parameters of "scan repeat number" was optimized for the adhesion performance of AA2024-T3/CFRP joints according to the variation of laser scribe sizes. Laser surface structuring was performed with previously optimized laser machine parameters from 1 to 9 "scan repeat number". After laser surface treatments with the increased scan repeat number, the characterization of the substrate was established by surface morphology and the dimensions of laser scribes. The adhesive bonding of laser-treated AA2024-T3 and untreated CFRP was applied and single-lap shear tests were then performed. The fracture surfaces of substrates were observed and analyzed to determine failure modes. The results indicated that laser scribe geometrical parameters have a significant effect on the adhesion performance of AA2024-T3/CFRP joints. The adhesive bonding strength was enhanced and the maximum value was 26.48 MPa (with 5 scan repetition) increasing by 39% compared to the adhesive joints without surface treatment of AA2024-T3 adherend. The observed failure modes on both the adherend surfaces have demonstrated that the mechanical interlocking mechanism between the adhesive and laser textured aluminum adherend with optimized scan repeat number has been well-worked.

Keywords: Laser treatment, Adhesive bonding, AA2024-T3, CFRP, Mechanical interlocking

Introduction

In order to benefit from the advantages of using composite materials widely used in aviation with light metal materials, a bonding method is developed instead of traditional (rivet and bolt) methods. There are two dominant mechanisms in adhesive bonding: the chemical adhesion mechanism between the bonding surfaces with covalent or weak van der Waals forces, and the mechanical locking mechanism where adhesion is achieved by the rough surface. Advances are being made in the field of surface engineering as these two mechanisms work together to improve adhesion strength.

Mechanical interlocking adhesion theory is defined by the fact that good adhesion occurs only when an adhesive enters the pores, holes, cracks, and other irregularities of a substrate surface and mechanically locks into the substrate (Singh, 2004). Generally, the most common methods applied for preparing surfaces are mechanical (sanding, sandblasting, brushing, etc.), chemical (chromic-sulfuric acid etching or conversion coating, etc.), electrochemical (chromic or phosphoric acid anodization, etc.), and adhesion enhancing coating agents (silane

and sol-gel, etc.) (Kwakernaak, 2012). Besides, methods such as plasma and laser processing, which are much newer, controlled, reproducible, low labor, and less harmful to health and the environment, are also used. Mechanical and chemical methods applied to surfaces are harmful to human health and the environment to varying degrees. Another method that eliminates the disadvantages of existing traditional effective methods and continues to be researched is the laser surface treatment method. The changes caused by laser radiation locally in the crystal structure, chemistry, and morphology of the material cause changes in the application behavior of the material (Sugioka et al., 2010). Also, the laser's ability to transfer large amounts of energy to the material in a region close to the surface, within specified limits and in a very short time allows the properties of the material to change locally and superficially (Sugioka et al., 2010). Studies using laser processing technique in the modification of surfaces to increase the adhesion strength between aluminum alloys and structural adhesives are much less than cleaning, melting, and alloying alloys using the same laser devices.

The effect of laser parameters on surface treatments has been the subject of many studies. Wu et al. (2020) reported that the pores formed on the surface of the 5052-Al alloy as a result of laser surface treatment with different laser power are small as a result of low laser power, but the pores become narrow and long with increasing laser processing power. Feng et al. (2020), examined the effects of single-shot energy, number of pits per square millimeter, and laser surface treatment (hitting the surface) angle parameters as laser processing parameters for the adhesion strength of 30CrMnSiA steel. They concluded that increasing the adhesion surface area can be achieved by increasing the diameter and depth of the pit formed due to the increase of laser pulse energy or by increasing the density of the marks on the surface. Vidal et al. (2014) investigated the change of bond strength depending on different depths, widths and proportions opened to the steel surface in the hybrid joining of steel metal with 30% glass fiber reinforced PA6 composite. In this study, which focused on the number of pulses sent to the surface, they found that the depth, which increased with the number of pulses, increases the bond strength.

Wunderling et al. (2020), processed the surface with circular oscillations using a continuous pulsed laser in to increase the bonding surface area of the steel material. It has been concluded that the microstructures created by changing the groove spacing are highly dependent on the bond strength value. Alfano et al. (2012), examined the effect of power, scanning speed, and line spacing on the bonding strength as an example showing laser surface treatment in epoxy bonding with AA6082-T6 aluminum alloy. It was emphasized that the mechanical locking mechanism, which also increases the adhesion strength thanks to the grooved structures obtained as a result of the relevant processes, provides interface toughness by preventing energy absorption and crack propagation.

As a result of the literature review, it is concluded that the depth, width, depth/width ratio of the groove type traces, which determine the density in the adhesion area and especially activate the mechanical locking mechanism, must be investigated for adhesion performance of AA2024-T3/CFRP joints. These parameters have been studied mostly for steel materials in the literature and were chosen to fill the gap in the literature in terms of their effects on aluminum alloy and CFRP adhesion strength.

Materials and Methods

The materials selected to be bonded for this study are AA2024-T3 aluminum alloy 1.6 mm thick and unidirectional carbon fiber reinforced epoxy (CFRP) $[0]_8$-layer composite with a thickness of 2.3 mm. Each sample was cut in dimensions (t x 25.4 x 101.6 mm^3) specified in the ASTM D5868-01 standard and the samples were made ready for laser processing.

Two-component Loctite EA 9396 AERO (A-epoxy-based, B-amine-based), which is widely used in joining aviation materials, was used as an adhesive in the bonding process of AA2024-T3 and CFRP specimens. This adhesive, which has low viscosity (liquid form) and curing at room conditions, also exhibits the best strength properties in the temperature range of -55 C to 177 ºC.

For laser processing of the aluminum sample surfaces, a pulsed fiber laser with a maximum power of 50 W was used. This laser operates at 1064 nm wavelength with a 100 ns pulse duration and a repetition rate range of 20 to 80 kHz. To process the desired surface area on the samples, a galvanometric system that provides a computer-controlled movement of the laser beam to the desired area is used with a 160 mm focal length F-Theta lens to focus the laser beam. Only aluminum surfaces were laser treated, CFRP samples were used as manufactured surfaces to investigate especially laser treatment process effect on the aluminum surface.

It was determined that the process took place without sufficient time for the laser in the parameter combination where the scanning speed, which is the most effective parameter, the highest (1500 mm/s), and the laser power the lowest (20 W). Therefore, a shallow scan forms on the material. The microstructure formed due to the lowest scanning speed (100 mm/s) and a medium level of power (35 W) has been observed to be formed as "chaotic" in the literature. It has been determined that with sufficient energy and time in terms of laser-material interaction, the permit that occurs due to the falling of another spot on the surface of the material is heterogeneous indentations rather than grooves. It has been determined that the laser scanning speed is 800 mm/s, the laser power is 50 W and the laser frequency is much deeper (30 µm) after the 80 kHz process parameters. As a result of laser processing, marks that could be effective in terms of mechanical locking were made with a single pass laser process. According to the range of these laser process parameters in our previous study Bora et. al (2020) optimized the laser process parameters in order to obtain optimum effective laser groove with single-pass as shown in Table 1.

Table 1. Pre-optimized laser processing parameters for one pass

Scanning Speed (mm/s)	800
Laser Power (W)	50
Frequency (kHz)	80

Aluminum samples were processed with pre-optimized laser parameters from 1 to 9 "scan repetitions" to create grooves with different depths and widths. However, considering the laser effect area in terms of processing, the distance between the grooves is greater than 60 µm, thus allowing the geometric structure of the groove to be examined much more clearly. For this purpose, the distance between the grooves was accepted as 120 µm, and 208 grooves were processed along the width for the laser processing area of 25 x 25 mm^2 (Fig. 1-a). Depending on the increase in the laser scan repetition, the cross-sectional images of the modified AA2024-T3 surfaces were taken and given in Fig. 1-b. From these images, geometric parameters such as depth and width of the formed grooves were examined and dimensional changes were recorded.

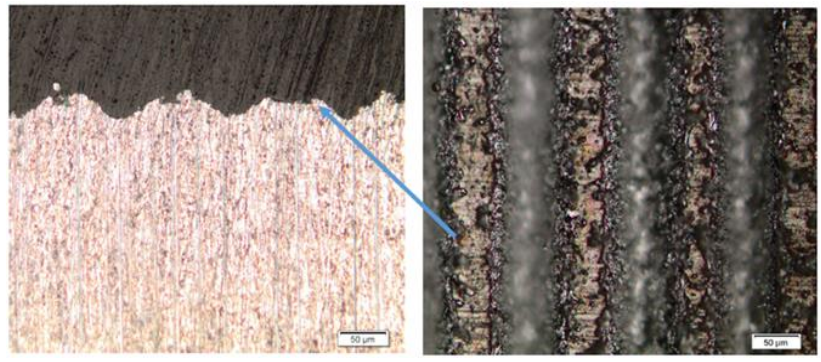

(a)

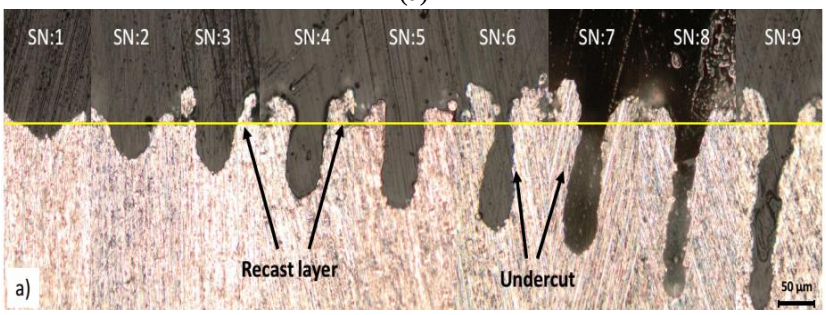

(b)

Figure 1. (a) Top view of the grooves processed with 120 µm intervals with single-pass laser treatment (b) cross-sectional views of the grooves formed depending laser scan repetition

Zwick universal test machine was used which had a capacity of 30 kN at TUBITAK-MAM for determining the adhesive shear strength of CFRP/Al adhesive joints. The single-lap test speed was selected as 13 mm/min according to ASTM D5868-01 standard. By adding the grips (Fig. 2) on both sides of the test sample, the load transferred along the bondline region.

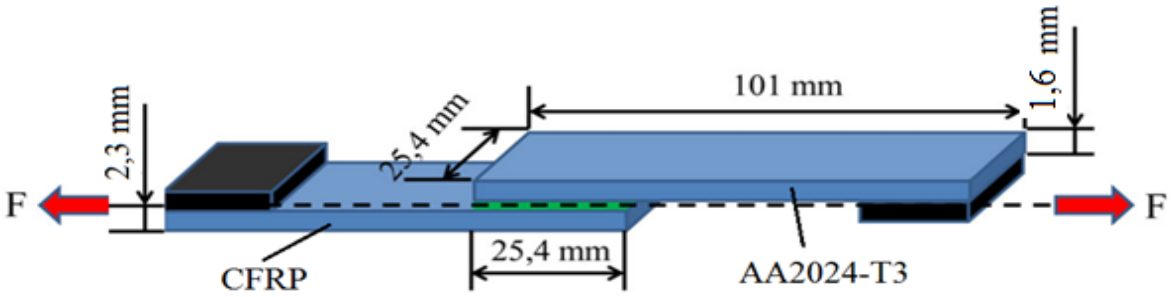

Figure 2. Dimension of single lap joint of Al/CFRP adhesive joint [Bora et. al (2020)]

Results and Discussion

The geometric parameters of the obtained grooves are measured as schematized in Fig. 3-a, and their state of change is plotted graphically and shown in Fig. 3-b and c. As seen in Fig. 1 and Fig. 3, as the laser scan repetition was increased, the depth increased linearly from approximately 25 µm to 200 µm. Contrary to increasing the depth, as the laser scan repetition increased, the width decreased up to 6 repetitions, albeit slowly, and then increased again. As it is seen in Fig 1, until the 5th laser transition, the groove went deeper in the same width without creating an under-cut ratio. In the 6th laser transition, it is seen that the lower part of the cut ratio is formed after a narrow entrance as a result of a significant decrease in the entrance width of the groove. After the 7th laser transition, it was determined that both the width and the depth continued to increase significantly. If it is added, it is seen that in the 8th scan repetition the groove depth increased while the wall becomes more indented and protruding.

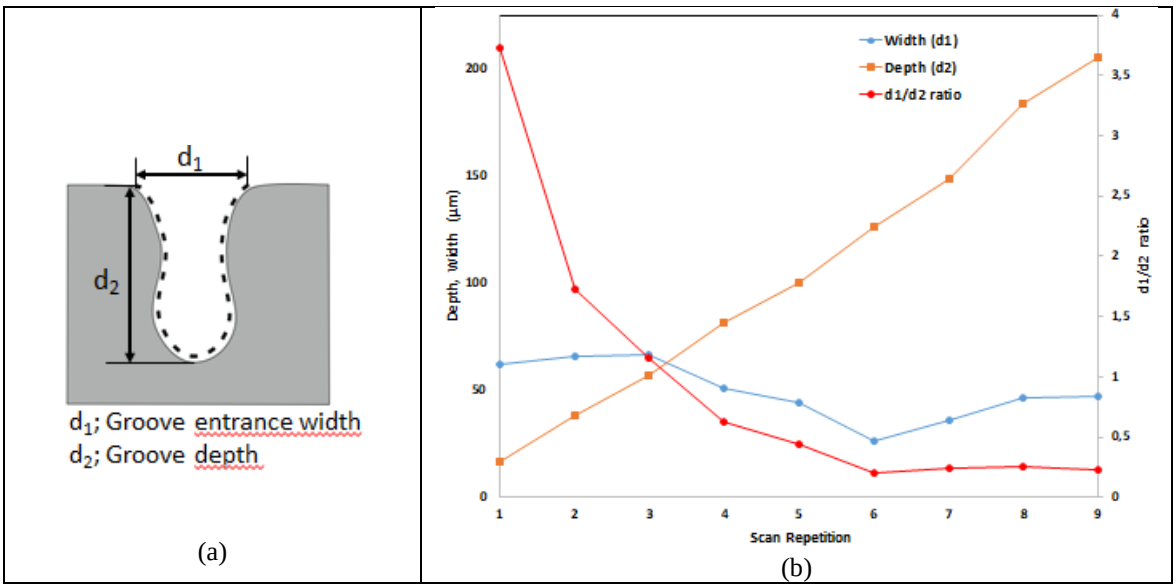

Figure 3. Schematic representation of the geometric dimensions of the groove formed by increasing the laser scan repetition of the single-scan laser processing process (a), the change of geometric parameters (b)

To evaluate the adhesion shear strength not only according to the roughness that occurs depending on the depth of the formed grooves but also in terms of the spreading ability of the adhesive, the contact angle measurements of the laser scan repetition samples were made. Very low contact angle values were obtained in single repeat processed samples. This situation supports the achievement of higher bond shear strength results than the untreated sample. Contact angle measurements were carried out to examine the effect of the laser scan repetition on the contact angle and adhesive spreading performance in the samples processed with 120 µm spaced grooves with the laser scan repetition process. While it was observed that pure water spread very rapidly by dropping it on the surface of the sample, shown by the red circle in Fig. 4; therefore, a photograph that could analyze the contact angle could not be recorded. While the situation was the same for all the laser scan repetition, the contact angles were accepted as ≈0° and it was determined that the surfaces were in super hydrophilic character in this case.

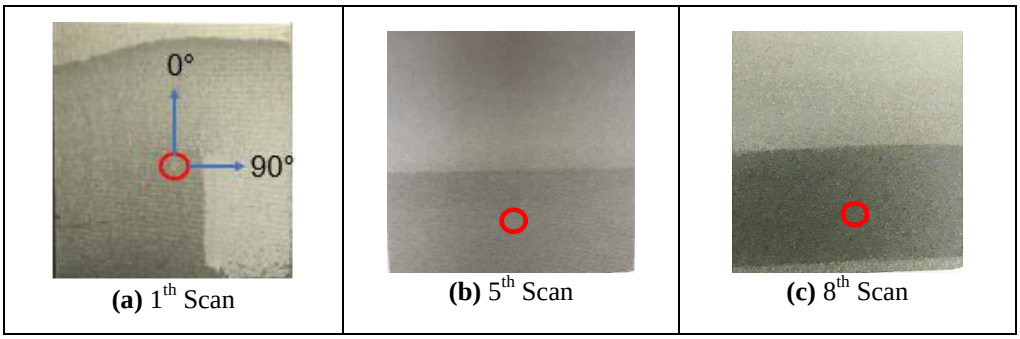

(a) 1th Scan **(b)** 5th Scan **(c)** 8th Scan

Figure 4. Contact angle results depending on the laser scan repetition

Fig. 5 shows that AA2024-T3 / CFRP adhesion shear strength was obtained as 19.03 MPa for a single repeat of the laser process. As the laser scan repetition of the same laser processing process was increased, the highest bond strength value was obtained in the 5th repeat as 26.48 MPa. This increase in adhesion shear strength has been attributed to the increase in depth, despite the slight decrease in width.

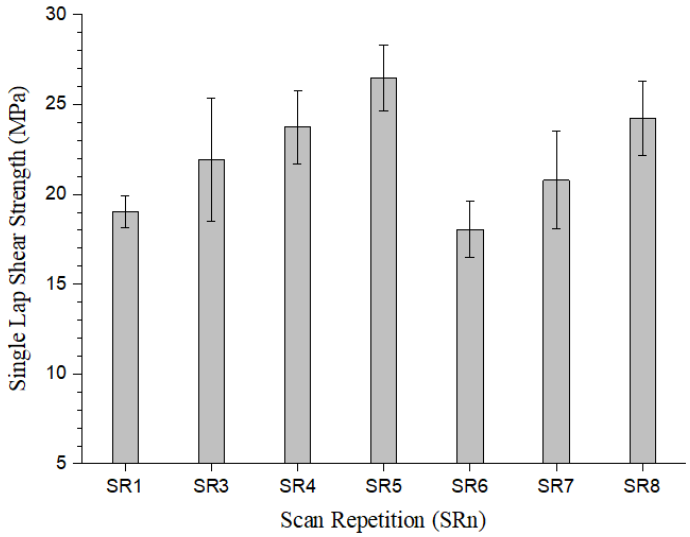

Figure 5. Single lap shear strength depending on the laser scan repetition

While the gradual increment in adhesion strength after each repetition, it is noteworthy that there is a significant decrease of 18.04 MPa in the 6th repeat. While the significant decrease seen here can be attributed to the inability of the adhesive to fill the inside of the groove, it is seen that the adhesive fills the grooves well after each repeat as seen in Fig 1-b. The reason for the decrease in adhesion shear strength was attributed to the very narrow groove width and the naturally short cross-section length of the adhesive section carrying the load in the shear direction. With the passages after the 6th repeat, it has been determined that the width of this entrance section continues to increase again, albeit slowly, and the adhesion shear strength has also begun to increase again.

Wu et al. (2020) noted that the groove depth has a negative effect on the adhesion shear strength. In this case, the viscosity of the polymer that will fill the groove is important. The researchers stated that while bonding 5052-Al alloy and polyamide 6 based CFRTP materials, the PA6 polymer in the composite structure is thermoplastic-based and melted under heat and cannot penetrate the rough structure, the depth of which increases from 120 µm to 240 µm on the aluminum alloy side, and that a gaped connection is provided and the strength is reduced. Considering this situation, the adhesive used in the study has been provided with a low viscosity considering that it will serve the target of the research better and it is seen in the section photographs in Fig. 1-b that the grooves fill the groove according to the decreasing width and increasing depth.

The CFRP material was adhesively bonded with AA2024-T3 alloy, which has been treated with different laser scan repetitions and then subjected to individual lap slip tests to determine the adhesion performance. Photographs of the broken coupon sample pairs were taken to examine the damage modes of the broken connections after the mechanical tests and are given in Fig. 6. The damage types of the joints are given in comparison to the untreated AA2024-T3 / CFRP bond joints. In Fig. 6, it is determined that the types of damage

according to the untreated AA2024-T3 / CFRP bonding joints change from adhesive damage on the aluminum surface (Fig. 6-a) to adhesive damage and fiber rupture on the CFRP surface (Fig. 6-b-e). As stated in Ebnesajjad (2014) study, if the adhesive does not fully wet the bonded surface, optimum adhesion cannot be achieved. In this context, damage to the untreated AA2024-T3 / CFRP connections occurred at the aluminum / adhesive interface. It has been determined that all laser scan repetition processes performed with the fiber laser process increase the adhesion of the adhesive and aluminum material and the damages caused by mechanical tests in the bonding joint have shifted to the surface of the CFRP material without any front surface treatment. Especially, as seen in the single lap shear test results, when the laser scan repetition is 5 and 8, the shear strength values reach the highest values. From the digital images given in Fig. 6-d and e, it is obvious that fiber tear damage is at the forefront. The presence of grooves of different depths and widths created with different laser scan repetition on the aluminum material surface increased the aluminum / adhesive adhesion by providing the interlocking mechanism. It has been determined that fiber rupture damage comes to the fore as the main damage type due to the depth and adhesion width of the grooves obtained in the laser scan repetition specified in Fig. 6-d and e.

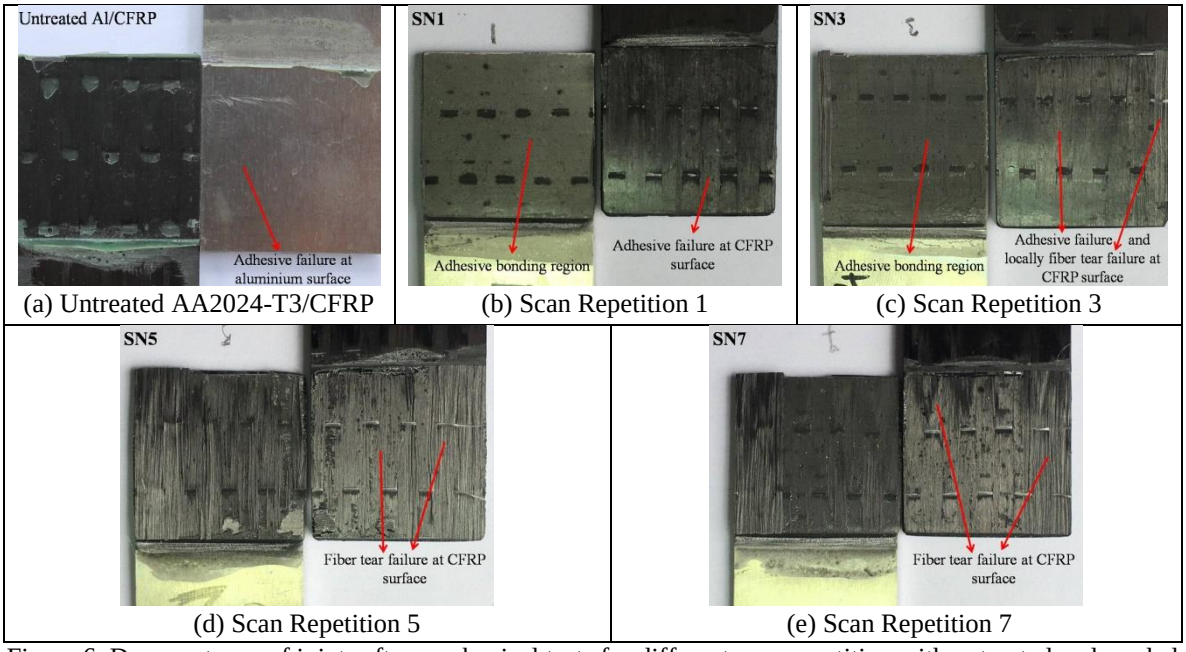

(a) Untreated AA2024-T3/CFRP (b) Scan Repetition 1 (c) Scan Repetition 3

(d) Scan Repetition 5 (e) Scan Repetition 7

Figure 6. Damage types of joints after mechanical tests for different scan repetition with untreated and sanded AA2024-T3 / CFRP bonding joints

To support the types of damage that are compatible with the literature, it was thought that fiber tear damage due to good adhesion also affected the results of the single lap shear tests. For this reason, force-elongation curves obtained in mechanical tests are drawn comparatively and given in Fig. 7. It was determined that the elongation values were also high for the transition numbers where the adhesion was high, that is, the adhesion shear force was high. Especially for the 5^{th} and 7^{th} repetition where fiber tearing damage was observed, the elongation amounts were also high. Complementing these two results with each other supports the high adhesion shear strength.

Conclusions

In this study, the laser repetitions effect on both the groove geometric parameters and the adhesion strength of AA2024-T3 / CFRP materials were investigated. The results obtained are as follows:

- By examining the effect of the laser scan repetition on the contact angle and adhesive spreading performance, it was seen that all the laser-treated aluminum surfaces exhibited nearly super hydrophilic characteristics.
- Laser groove geometric parameters have a significant and relevant effect on the adhesion strength of AA2024-T3/CFRP joints.
- This effect could be optimized for varying adherent materials by using the laser scan repetition technique.

- After the 5th laser repetition, the highest adhesion strength value was increased from 19.03 MPa to 26.48 MPa.
- This adhesion strength increment was supported with different failure modes obtained on both the adherent surfaces that especially for 5th repetition significant amount of fiber tear failure could be seen on the aluminum surface.

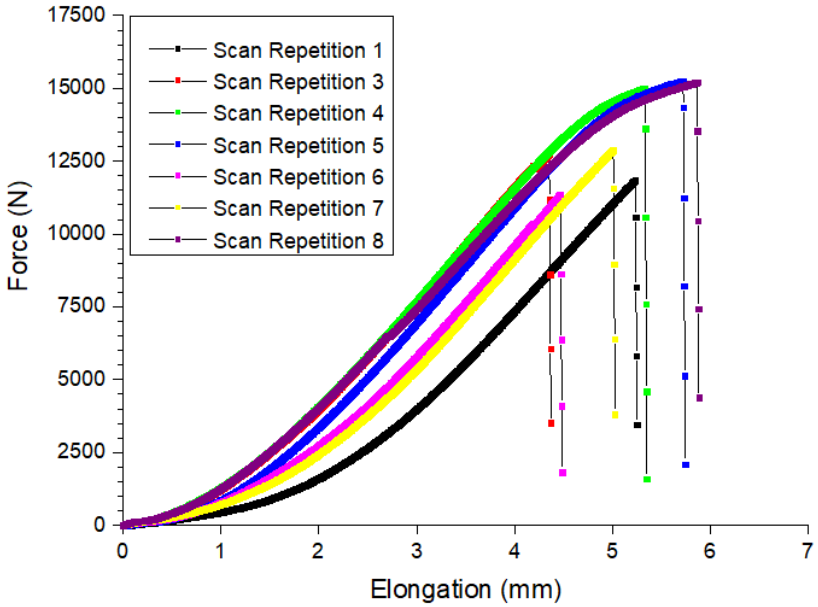

Figure 7. Individual lap shear test graphs based on the laser scan repetition

Acknowledgment

This work was supported by the TUBITAK, "The Scientific and Technological Research Supporting Program 1001" [grant number 118M280].

References

Alfano, M. Lubineau G., Furgiuele F., Paulino G.H. (2012). Study on the role of laser surface irradiation on damage and decohesion of Al/Epoxy joints. *International Journal of Adhesion and Adhesives, 39*, 33–41.

Bora, M.O., Çoban, O., Akman, E., Genc Oztoprak, B., Kutluk, T., (2020). Comparison of novel surface treatments of Al 2024 alloy for Al/CFRP adhesive bonded joints. *International Journal of Adhesion and Adhesives, 103*, 102721.

Ebnesajjad S. (2014). *Surface treatment of materials for adhesive bonding* (Second Edition), Elsevier, Chapter 5. ISBN: 978-0-323-26435-8, USA.

Feng Z., Zhao H., Tan C., Chen B., Song X., Feng J. (2020). Influence of laser process parameters on the characteristic of 30crmnsia steel substrate and adhesively bonded joints. *Optics and Laser Technology, 123*, 105920.

Kwakernaak, A. (2012). *Improvements in bonding metals for aerospace and other applications*. Woodhead Publishing Limited.

Rodríguez-Vidal, E., Lambarri J., Soriano C., Sanz C., Verhaeghe G. (2014). A combined experimental and numerical approach to the laser joining of hybrid polymer – Metal parts. *Physics Procedia, 56*, 835 – 844.

Singh, H.K., (2004). Determining interfecial adhesion performance and realiability for microelectronic applications using a wedge test method. Master's Thesis, Virgina Polytechnic Institute And State University,

Sugioka, K., Meunier, M., Pique, A. (2010). *Laser Precision Microfabrication, 135*, New York: Springer.

Wu, L.H., Xiao B.L., Nagatsuka K., Nakataa K., &v Ma Z.Y. (2020). Achieving strong friction lap joints of carbon-fiber reinforced plastic and metals by modifying metal surface structure via laser-processing pretreatment. *Composite Structures, 242,* 112167.

Author Information

Seda Aybalik
Kocaeli University
Faculty of Aeronautics and Astronautics, 41285, Kocaeli, Turkey Address: Kocaeli University, Arslanbey Campus, Faculty of Aeronautics and Astronautics, 41285, Kartepe/Kocaeli, Turkey

Onur Çoban
Kocaeli University
Faculty of Aeronautics and Astronautics, 41285, Kocaeli, Turkey Address: Kocaeli University, Arslanbey Campus, Faculty of Aeronautics and Astronautics, 41285, Kartepe/Kocaeli, Turkey

Mustafa Özgur Bora
Kocaeli University
Faculty of Aeronautics and Astronautics, 41285, Kocaeli, Turkey Address: Kocaeli University, Arslanbey Campus, Faculty of Aeronautics and Astronautics, 41285, Kartepe/Kocaeli, Turkey

Erhan Akman
Kocaeli University
Faculty of Aeronautics and Astronautics, 41285, Kocaeli, Turkey Address: Kocaeli University, Arslanbey Campus, Faculty of Aeronautics and Astronautics, 41285, Kartepe/Kocaeli, Turkey

Belgin Genç Öztoprak
Kocaeli University
Faculty of Aeronautics and Astronautics, 41285, Kocaeli, Turkey Address: Kocaeli University, Arslanbey Campus, Faculty of Aeronautics and Astronautics, 41285, Kartepe/Kocaeli, Turkey

The Eurasia Proceedings of Science, Technology, Engineering & Mathematics (EPSTEM)
ISSN: 2602-3199

The Eurasia Proceedings of Science, Technology, Engineering & Mathematics (EPSTEM), 2020

Volume 11, Pages 41-47

IConTES 2020: International Conference on Technology, Engineering and Science

Possibility of Testing the Compressive Strength of Concrete on the Halves of Prisms Specimens

Ana ROMIĆ
University of Split

Sandra JURADIN
University of Split

Nives OSTOJIĆ-ŠKOMRLJ
University of Split

Marko BERETIN
University of Split

Abstract: Compressive strength, as the main mechanical property of the building materials, depends on geometrical characteristics of the tested specimens: cube, cylinder or prism. Unlike concrete strength tests, where different specimens are used to determine compressive and flexural strength, those values are tested on the same prism specimens for the cement mortar. The purpose of this study is to investigate the possible correlation between values of compressive strength obtained on half concrete prism (10 cmx10 cmx40 cm) after flexural test with compressive strength on standardized 15 cm and 10 cm cubes. Three concrete mixtures have been tested and every mixture had a different maximum grain size of aggregate, namely 8 mm, 16 mm and 31,5 mm. Same type and quantity of the cement are used in all mixtures with the same water/cement ratio. The workability of the fresh concrete was examined by using the slump-flow method. Nine specimens are prepared for each concrete mixture; three for every dimension. According to the obtained results, it can be assumed that there is a significant level of connection of compressive strength values between half-prism and both 10 cm and 15 cm cube specimens. Results showed there is a possibility of using half-prism concrete specimens after the flexural test for the evaluation of compressive strength. This would reduce the number of test samples and the problem of sample disposal after the test.

Keywords: Concrete, Compressive strength, Flexural strength, Size of the test specimen

Introduction

The basic quality indicator for both cement and concrete is the compressive strength. The main difference between testing concrete and hardened cement mortar is in the number of required specimens: cement mortars flexural and compressive strength tests can be performed on the same specimens (HRN EN 196-1, 2016). After the flexural test, prisms are divided into two approximately equal parts and can be used to determine compressive strength. To perform a compressive test, concrete specimens were prepared following defined requirements (HRN EN 12390-1, 2012). Concrete parts of a prism tested in flexure sometimes can be used for determination of compressive strength. This experiment is called “equivalent cube test” and can be obtained by applying the load through square steel plates on the half prism. The compressive strength on half prism is approximately the same as the strength of a standard cube of the same size or due to test conditions, the strength of a modified cube can be, on average, 5 per cent higher than that of a cast cube of the same size (Neville, 1995).

- Selection and peer-review under responsibility of the Organizing Committee of the Conference

Compressive strength is the least susceptible to change when high and diameter ratio (h/d) is 2. After the ratio exceeds 4, the geometrical characteristic no longer affects strength. In lager samples possibility of the weakest link appearance is much higher (Matulić et al., 2016).

The wide-ranging research works (Matulić et al. 2016; Sabnis and Mirza, 1979; Zabihi and Eren, 2014; Kumari, 2015; Del Viso, et al., 2007; Day, 1994a and Day 1994b) carried out results for different concrete types, curing and storage processes. It has been determined that average compressive strength and standard deviation (Sabnis and Mirza, 1979) decrease with increasing of specimens dimensions. According to Matulić et al. (2016), measured dynamic modulus of elasticity can significantly correlate with compressive strength obtained by the destructive method in functional dependence of of the test specimen's dimensions. However, precautions must be taken when determining compressive strength based on values of dynamic modulus of elasticity, because a small error in measurement results drastically changes in compressive strength value. Encountering a defect, smaller specimens have shown higher sensitivity in reduction of dynamic modulus of elasticity, and this model can be used as a rough approximation.

To rationalize material consumption and reduce the problem of sample disposal after testing, the purpose of this study is to determine if there is a possibility of concrete compressive strength assessment based on half-prism compressive strength results and comparison with results obtained on standard 10 cm and 15 cm cubes. It should be noted that such results cannot be used for determination compressive strength class.

Experimental part

Materials and preparation of test specimens

For the testing purpose, three mixtures were made. The same type of cement (CEM II/B-W 42.5 N) was used for all mixtures and with equal quantities. The mass of cement was selected to be 350 kg and the w/c ratio was selected to be 0.55 for all concrete mixtures. The fractions of the crushed limestone aggregate used for preparation of concrete mixture were 0/4 mm, 4/8 mm, 8/16 mm, and 16/31,5 mm, with a grain size distribution curves as shown in Figure 1.

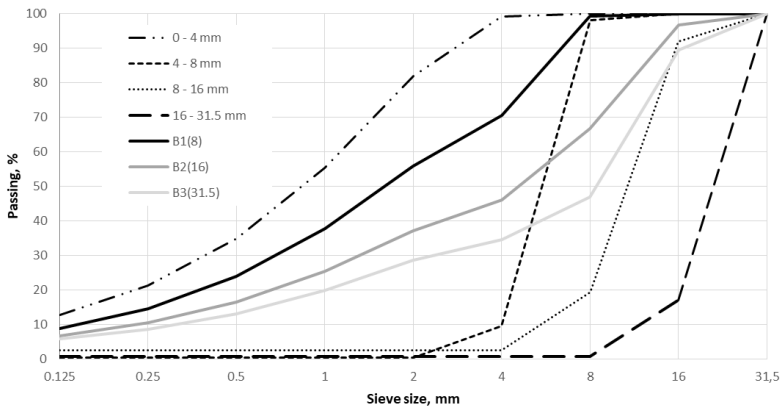

Figure 1. Grain-size distribution curves of aggregate fractions and concretes

Every mixture has a different maximum grain size of aggregate, namely 8 mm, 16 mm and 31, 5 mm. In this study, the ratios of different aggregate fractions were determined to make the granulometric curve of the combined aggregate batch to come closest to target Fuller curve (B curve), Figure 1.
Table 1 shows the concrete compositions. The mixture label contains the maximum grain size.

. Table 1. Concrete mix designs

Mix	Cement (kg)	Water (l)	w/c	Aggregate			
				0-4 mm	4-8 mm	8-16 mm	16-31.5 mm
B1 (8)	350	192.5	0.55	1326.72	490.70	0	0
B2 (16)	350	192.5	0.55	952.08	292.95	585.89	0
B3 (31.5)	350	192.5	0.55	627.10	166.00	959.10	92.22

All concrete components were weighed and placed into the moistened automatic concrete mixer. Dry components were mixed for 1 minute, and 5 more minutes with added water. The mixtures were cast into prism mold with dimensions of 10x10x40cm, and cubic molds with a length of 10 cm and 15 cm, while vibrated during casting. Nine specimens for each concrete mixture were tested, i.e. three per every dimension. After 24 h, the specimens were removed from the molds and cured in water at room temperature around 21 °C and 95% relative humidity until testing, according to EN 12390-2 (2019). Compressive strength, flexural strength, ultrasonic pulse velocity (UPV) and mass of the specimens were measured 28 days after sample preparation. The flatness of all surfaces of the tested specimens was insured according to HRN EN 12390-1 (2012).

Test results of fresh concrete

Fresh concrete was tested by using the slump- method (Figure 2) according to HRN EN 12350-2 (2019) and placed into the slump class, shown in Table 2. The obtained results are following Haktanir et al. (2012):

> Workability in the fresh phase and strength in the hardened form of structural concrete are, to a great extent, dependent on the gradation of the combined aggregate batch, and the proportioning of different size aggregate groups is a crucial step in concrete mix design.

Table 2. Results of the slump-flow test

Mixture	Slump-flow (mm)	Class
B1(8)	40	S1
B2(16)	170	S4
B3(31,5)	185	S4

As can be seen in Table 2 and Figure 2, by increasing the maximum grain size, the proportion of the fine fraction is smaller and workability of concrete is better.

Figure 2. Measuring slump on mixtures B1(8), B2(16) and B3(31.5) (Beretin, 2020)

Results and Discussion

The tests of hardened concrete

Flexural strength

According to HRN EN 12390-5 (2019), testing of concrete flexural strength is performed on 10x10x40 cm prisms by loading them with a constant rate of 0.05 MPa/s. Half of the prism should be leaning on the central

parts of the upper plate of the hydraulic press, and the lower part of the plate is spaced 30 cm apart, leaving a space of 5 cm on each side of the prism (Figure 3.)

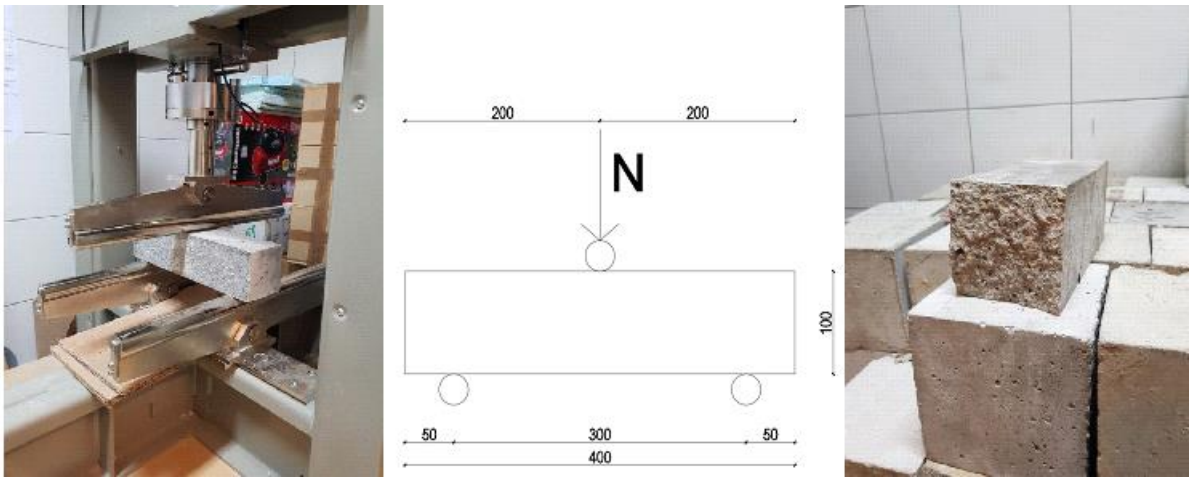

Figure 3. Testing flexural strength of concrete on prisms (Beretin, 2020)

Flexural concrete strength was calculated according to the (1) and showed in Figure 3, where N represents specimen breaking force, L is the length of the specimen, b is the specimen edge length and h is the specimen high:

$$f_t = \frac{3}{2} \cdot \frac{N \cdot L}{b \cdot h^2} \quad (1)$$

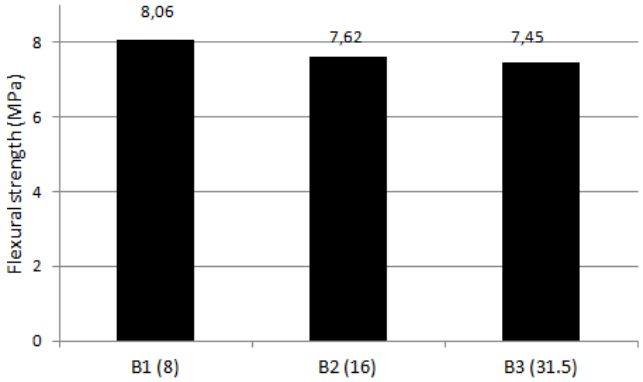

Figure 4. Flexural strength

Test results have shown a decreasing trend of flexural strength with an increased maximum grain size of aggregate. The relation is approximately linear in range of 0.5 MPa. The maximum standard deviation value (0.63 MPa) of the same mixture and dimension of specimens showed mixture with maximum grain aggregate of 16 mm.

Compressive strength

At the 28th day, the compressive strength of the hardened concrete specimens was tested on cube specimens of 10 and15 cm edge length with a loading rate of 0.6 ± 0.4 MPa/s according to EN 12390-3 (2019). After the flexural test on prism specimens has been preformed, both half fragment of the same prism were tested for compressive strength. Prism testing was conducted with 10x10 cm steel plates whose thickness was 4 mm. By placing the steel plates on both sides of the machine interaction plates before testing, it is ensured that the test on the concrete prism corresponds to the test conditions on the prisms of the standard cement mortar.

The mean values of compressive strength on tested specimens are shown in Figure 5. It was noticed that the compressive strength of every concrete mixture decrease with the decrement of specimens' dimensions, not

conforming to different previous abovementioned studies (Matulić et al., 2016). The highest value (47.09 MPa) of compressive strength gave mixture B1 (8 mm max grain of aggregate) on 15 cm cube. The same trend of compressive strength behavior was noticed on 10 cm cubes, but this specific specimen's dimension is the most susceptible to maximum grain size. The relationship between sample size and maximum aggregate grain (l_{min}/D_{max}) should be taken into account when interpreting the results of the concrete properties (Śliwiński and Duży, 2020). Results of compressive strength are in the same range for 10 cm and 15 cm cubes and B1 (8 mm) and B2 (16 mm) mixtures. The largest deviation from average compressive strength at the mixture level gave a geometric shape of the prism (around 1.5 MPa) for mixture B3. Comparing all three concrete mixtures based on cube dimension, the highest standard deviation had the mix B1 in 15 cm cube (0.67 MPa), and mixture B3 for 10 cm cube (1.4 MPa).

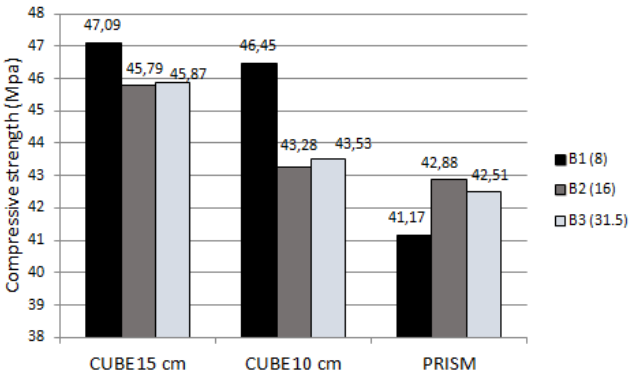

Figure 5. Compressive strength of concrete

The correlation analysis between compressive strength on 10 cm and 15 cm cubes versus prism was carried out to determine the possibility of estimation of compressive strength based on before-flexural-tested prisms. Correlation test is shown in Figure 6.

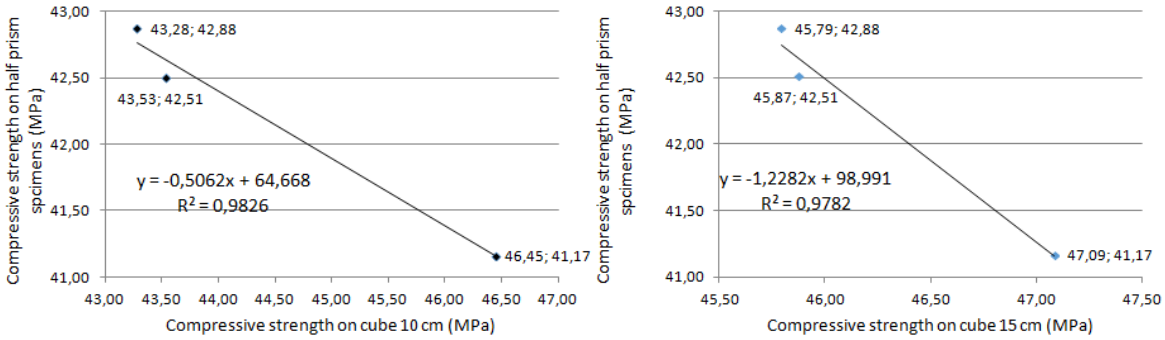

Figure 6. Correlation between compressive strength specimens

The connection between both conducted tests is significant, and in rage around 0.99. According to the obtained results, it can be assumed that there is a possibility of using prism specimens after the flexural test.

Dynamic modulus of elasticity

Before the flexural and compressive test was carried out, mass and the ultrasonic pulse velocity (UPV) of every specimen was measured in order to determine the dynamic modulus of elasticity, according to HRN EN 12504-4 (2004) and expression:

$$E_{din} = \frac{v^2 \rho (1+\mu)(1-2\mu)}{1-\mu} \quad (2)$$

where: v is mean ultrasonic wave velocity (m/s), ρ is concrete density (kg/m^3) and μ is the Poisson coefficient. Dynamic modulus of elasticity (Figure 7) showed inverse behavior in comparison with compressive strength results. The highest modulus of elasticity has mixture B3 on prism (53.62 GPa), and 15 cm cube followed the same trend of behavior with maximum values for the same mix. Mixture with 16 mm maximum grain of

aggregate (B2) has the highest modulus of elasticity on 10 cm cubes. Generally, if the shape and dimensions of specimens are observed, the lowest value was obtained on 10 cm cubes. The mixture type B1, where the maximum grain of aggregate is 8mm, gave the lowest dynamic modulus of elasticity irrespective of the size of the tested specimens. Deviation in dynamic modulus of elasticity is more variable compared to compressive strength: mixture B2 gave the highest deviation for 10 cm cubes (1.3 GPa), while mixture B3 gave the maximum deviation of 0.95 GPa for 15 cm cubes. The mixture with 16 mm maximum grain of aggregate (B2) gave a maximum deviation of 1.2 GPa for the prism specimens. The similar trend in deviation of dynamic modulus of elasticity was shown in both mixtures B1 and B2.

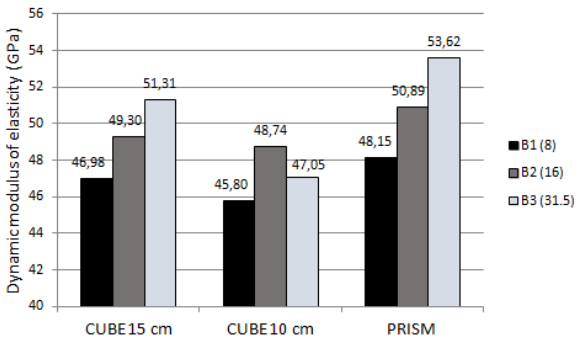

Figure 7. The dynamic modulus of elasticity

Coefficient of correlation for dynamical modulus of elasticity between 15 cm cube and prism is high (0.99). Meanwhile, the same test with 10 cm cube gave a significantly lower value of coefficient: 0.43. (Fig 8.) Possible cause of lower correlation can be found in the above-mentioned relationship between the minimum sample size l_{min} and the maximum aggregate grain D_{max}. The authors in (Śliwiński and Duży, 2020) recommend that relationship l_{min}/D_{max} is in range < 5.0; 10.0 > and for the cube with 10 cm edge, these values for maximum grains 8 mm and 31.5 mm are outside the recommended interval. Also, EN 12390-1 (2012) specifies that a specimen shall have a minimum cross-section size of $l_{min}/D_{max} > 3.5$, which for $D_{max} = 31.5$ mm is not met. There is also "wall effect", according to which: *If the maximum size of aggregate is large in relation to the size of the mould, the compaction of concrete and the uniformity of distribution of the large particles of aggregate are affected*, (Neville, 1995). A clear conclusion cannot be given based on a small number of specimens.

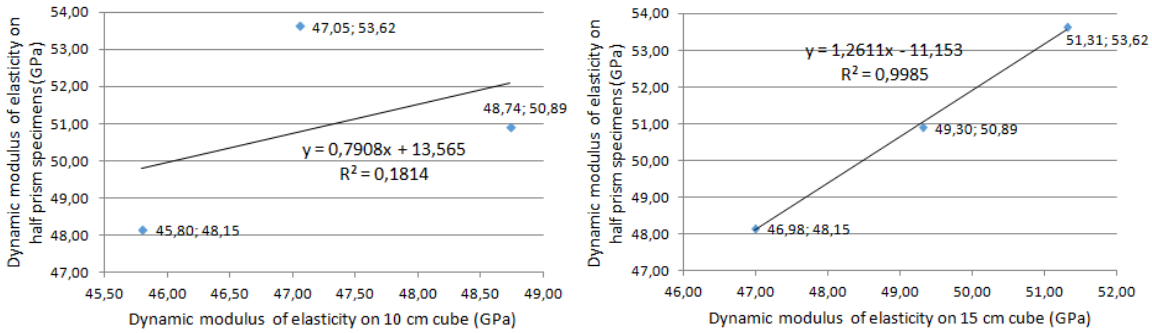

Figure 8. Correlation between dynamic modulus of elasticity of specimens

Conclusion

The sample size can significantly affect the assessment of properties that are sensitive to the composition of concrete. Although the basic cube dimension for the testing is 150 mm, the possibility of using the half prism specimens after flexural test to determine the compressive strength of the concrete was carried out in this paper. Three concrete mixtures with three different maximum grain size of aggregate (8 mm. 16 mm and 31.5 mm) were prepared and tested. Values of compressive strength were determined for each specimen's dimension: half concrete prism and 15 cm and 10 cm cubes, while the values of the dynamic modulus of elasticity were determined on concrete prism (10cmx10cmx40cm) and on both dimensions of the cube.

The relationship between the compressive strength of the 10 cm and 15 cm cubes and compressive strength of half of the prism specimens is significant, with R = 0.99. Coefficient of correlation for dynamical modulus of

elasticity between 15 cm cube and prism indicates a strong relationship (R = 0.999), but the relationship between 10 cm cube and prism is weak. The reason for this result can be an unfavorable cross-section size of l_{min}/D_{max} for a mixture with D_{max} = 31.5 mm and/or wall effect and/or a small number of tested specimens.

According to obtained results and correlation on 15 cm cubes, same prism specimens (10x10x40cm) divided in half after flexural test and then tested under a pressure can be used to determine estimated compressive strength, although they are not the same size in cross-section. This test is not scheduled for determining or evaluating the class of concrete. For a much stronger correlation between the above mentioned compressive strengths, more extensive research should be performed with a larger number of specimens. Testing half of the prisms after the flexural strength test would reduce the number of test specimens as well as the problem of construction waste disposal.

References

Beretin, M. (2020). *Utjecaj veličine ispitnog tijela i maksimalnog zrna agregata na mehaničke karakteristike očvrslog betona*, Diploma work, Faculty of Civil Engineering, Architecture and Geodesy, University of Split, Croatia (in Croatian)

Day, R.L. (1994a). Strength Mesurement of concrete using different cylinder sizes: A statistical analysis, *Cement, Concrete and Aggregates*, *16*, 21-30.

Day, R.L. (1994b). The effect of mold size and mold material on compressive strength mesurement using concrete cylinders, *Cement, Concrete and Aggregates*, *16*, 159-166.

Del Viso, J.R., Carmona, J.R., Ruiz G. (2008). Shape and size effects on the compressive strength of high-strength concrete, *Cement and Concrete Research*, *38*(3): 386-395.

Haktanir T., Karaboga D., Akay B. (2012). Mix Proportioning of aggregates for concrete by three different approaches. *Journal of Materials in Civil Engineering, 24*(5):529-537.

HRN EN 12350-2 (2019). Testing fresh concrete -- Part 2: Slump-test

HRN EN 12390-1 (2012). Testing hardened concrete -- Part 1: Shape, dimensions and other requirements for specimens and moulds

HRN EN 12390-2 (2019). Testing hardened concrete -- Part 2: Making and curing specimens for strength tests

HRN EN 12390-3 (2019). Testing hardened concrete -- Part 3: Compressive strength of test specimens

HRN EN 12390-5 (2019). Testing hardened concrete -- Part 5: Flexural strength of test specimens

HRN EN 196-1 (2016). Methods of testing cement -- Part 1: Determination of strength

HRNEN 12504-4 (2004). Testing concrete -- Part 4: Determination of ultrasonic pulse velocity

Kumari, R. (2015). Review paper based on the relation between the strength of concrete cubes and cylinders, *International Journal of Engineering Research and Applications, 5*(8): 52-54.

Matulić, P., Juradin, S., Marušić, E., Domazet, A. (2016). Effect of test specimen size on mechanical properties of shotcrete, *Građevinar. 68*(4): 301-309.

Neville, A.M. (1995). *Properties of concrete*, Pearson Education Limited, England.

Sabnis, G.M., Mirza, S.M. (1979). Size effect in Model Concretes. *Journal of the Structural Division, 105*, 1007-1020.

Śliwiński J., Duży P. (2020). Impact of sample size and maximum aggregate grain on the representativeness of concrete samples, *Energies, 13*, 3358.

Zabihi, N., & Eren O. (2014). Compressive strength conversion factors of concrete as affected by specimen shape and size, *Research Journal of Applied Sciences, Engineering and Technology, 7*(20):4251-4257.

Author Information

Romić Ana
University of Split
Faculty of Civil Engineering, Architecture and Geodesy,
University of Split, Croatia
Matice hrvatske 15, 21000 Split
Contact e-mail: *ana.romic93@gmail.com*

Sandra Juradin
University of Split
Faculty of Civil Engineering, Architecture and Geodesy,
University of Split, Croatia
Matice hrvatske 15, 21000 Split

Nives Ostojić-Škomrlj
University of Split
Faculty of Civil Engineering, Architecture and Geodesy,
University of Split, Croatia
Matice hrvatske 15, 21000 Split

Marko Beretin
University of Split
Faculty of Civil Engineering, Architecture and Geodesy,
University of Split, Croatia
Matice hrvatske 15, 21000 Split

The Eurasia Proceedings of Science, Technology, Engineering & Mathematics (EPSTEM)
ISSN: 2602-3199

The Eurasia Proceedings of Science, Technology, Engineering & Mathematics (EPSTEM), 2020

Volume 11, Pages 48-52

IConTES 2020: International Conference on Technology, Engineering and Science

Effects of Deep Cryogenic Treatment on the Mechanical Properties of Medium Carbon Spring Steels

Resat Can OZDEN
Eskişehir Osmangazi University

Ersu LOKCU
Eskişehir Osmangazi University

Mustafa ANIK
Eskişehir Osmangazi University

Abstract: The cryogenic treatment is a method frequently used in the development of the wear resistance of alloy steels due to the increase in their hardness driven by the mechanisms such as the conversion of retained austenite to martensite and the formation of secondary carbides. In recent studies, it has been reported that besides the hardening mechanisms, the cryogenic treatment can also improve the mechanical properties of the alloys by reducing the residual stresses and modifying the microstructure. This research aims to investigate the impact of deep cryogenic process (-196°C) on the microstructures of medium carbon spring steels contain various alloying elements. The conventional heat treatment (CHT) and the deep cryogenic treatment (DCT) procedures were applied to the spring steels which have various alloying elements. Hardness, tensile and notch toughness tests were performed to determine the mechanical properties. Consequently, the aim is to determine the applicability of the cryogenic treatment in the improvement of the mechanical properties of medium carbon spring steels.

Keywords: Steels, Cryogenic Treatment, Mechanical Properties, Alloying

Introduction

Medium carbon steels contain between 0.25% and 0.60% carbon by weight. This steel group is generally used in tempered martensite structure due to high strength requirements. Conventionally the steel is tempered right after the quenching process, thus achieving optimum values in hardness and toughness. Improving the mechanical properties of the spring steel produced by the conventional forming and heat treatment process can only be achieved by modification of the material microstructure. The cryogenic process, which triggers mechanisms such as the reduction of residual stress and retained austenite structure, homogenization of the grain structure, and finally the formation of secondary carbide structures, is a heat treatment process that has been successfully applied for many product groups for years (Baldissera & Delprete, 2008).

In the conventional heat treatment process (CHT), a significant amount of compressive stress occurs in the material as a result of the quenching process. After the tempering process, it is seen that the samples lose these compressive stresses to a great extent (Bensely et al., 2008). This reduction can be attributed to the precipitation of nano-fine carbides in the structure and the removal of tetragonal supersaturated martensite (Preciado & Pellizzari, 2014). The transformation of austenite to martensite at cryogenic temperatures creates internal stresses and causes crystalline defects such as dislocation and twinnings. Cryogenic process restricts the movement of dislocations by the increase in the density of crystal defects and nano-cluster carbides. Thanks to this mechanism, the compression stress in the samples is relatively preserved (Villa et al., 2014). Carbide forming elements, such as molybdenum, play an important role in preventing grain growth in the primary carbide structure. In addition, they contribute to the protection of compressive stresses in the structure by triggering the precipitation of secondary carbide structures (Michaud et al., 2007). Since spring steels work

under varying loads, it is highly desirable to maintain these compression stresses in the structure. (Myeong & Yamabayashi, 1997). Besides, the mechanisms of performance increase caused by the cryogenic process, especially for medium carbon steels, have not been fully revealed. Scientific explanations regarding the microstructural changes, process conditions and the structure-property relationship observed as a result of the process are still under development.

In this study, deep cryogenic process (DCT) was applied to medium carbon spring steels such as 55Cr3, 51CrV4, 52CrMoV4. As a result of the application of the cryogenic process to these steels containing different alloying elements, it was aimed to improve the mechanical properties of steels. The change in the efficiency of the cryogenic process with the effect of alloying elements such as Cr, Mo, V was also investigated.

Method

Three spring steels with different alloys were selected in the study. The average chemical compositions of spring steels are given in Table 1. Conventional heat treatment (CHT) and deep cryogenic process (DCT) at -196 ° C were applied to steels and the effect of the cryogenic process on mechanical properties was investigated. Details on experimental variables are given in Table 2.

Table 1. Average chemical compositions of spring steels

Material	%C	%Si	%Mn	%Cr	%V	%Mo
55Cr3	0,57	0,30	0,85	0,80	-	-
51CrV4	0,50	0,25	0,90	1,10	0,12	-
52CrMoV4	0,50	0,25	0,90	1,10	0,10	0,25

The tensile strengths of the steel samples were measured with a 250kN capacity Shimadzu tensile device using ASTM E8 / E8M-13 standard to determine the mechanical properties that change due to cryogenic processing. Notch toughnesses were measured using the ASTM A370 standard based on the Charpy method. MFL Systeme device was used in the measurements. Hardness measurements were carried out by Shimadzu HMV-2000 microhardness tester. The measurements were obtained by applying a 300 grf load for 10 seconds.

Table 2. Experimental variables and coding

Procedure	Code
Quenching (850°C (Oil)) Tempering (500°C;1 Hour)	CHT
Quenching (850°C (Oil)) Cryogenic Process (-196°C; 24 Hours) Tempering (500°C;1 Hour)	DCT

Results and Discussion

First, the microhardness of samples was measured on the Vickers hardness scale. The average hardness of the steel groups for the base and heat-treated samples are presented in Table 3.

Table 3. Average hardness values of the samples (HVickers, 300 grf – 10 seconds)

Sample	52CrMoV4	51CrV4	55Cr3
Base	351,6	328,3	332,2
CHT	401,7	393,0	390,8
DCT	432,4	410,3	406,3

As expected, a result has emerged that varies proportionally to the alloy quantity of steels. The relatively high alloyed steel group has recorded a more significant hardness increase compared to the other two steel groups with its higher carbide-forming ingenuity and increased hardenability. The mechanical strength of the samples was also measured by tensile and notch impact tests. Accordingly, the notch impact toughness of steels was measured using the ASTM A370 standard based on the Charpy method. The results are listed in Table 4.

Table 4. Average notch toughness values of the samples (Charpy, J(Joule))

Sample	52CrMoV4	51CrV4	55Cr3
Base	10	11	13
CHT	32	24	26
DCT	46	37	34

In the literature, hardness values and notch toughness values show linearity and are generally interpreted together. The main influence for notch toughness is alterations of microstructure. Changes in notch toughness after cryogenic processing are associated with carbide precipitation. Primary carbides deposited in inter-dendritic regions are particularly important for notch toughness values in steel materials. The interface interactions of these carbide structures with the matrix are determinant in notch toughness mechanism (Das et al., 2010). As a result of the notch impact tests, the relatively high alloyed steel group was distinguished from the other steel groups, just like the hardness values. The increase in this steel group was much more noticeable (44%).

As the final mechanical test, the effects of cryogenic processes on the tensile strength and elongation of steels were examined. There is an intense discussion in the literature in interpreting the results of tensile strength. In addition to the existence of scientists who reported an increase in toughness as well as gain in mechanical values with cryogenic process (Ghasemi-Nanesa & Jahazi, 2014; Vahdat et al., 2013); some scientists report a decrease in toughness as a result of the increase in mechanical strength with cryogenic treatment (Senthilkumar et al., 2011; Zhirafar et al., 2007).

Graphs of maximum tensile strength and elongation at break for all steel groups are given in Figure 1a-b. The stress/strain graph of the relatively alloyed 52CrMoV4 sample is shown in Figure 2.

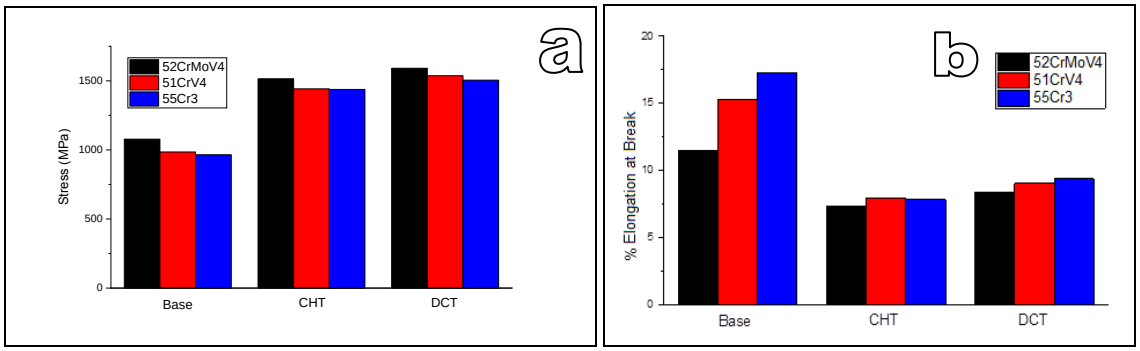

Figure 1. Graph of (a) maximum tensile strength (b) elongation at break for steels

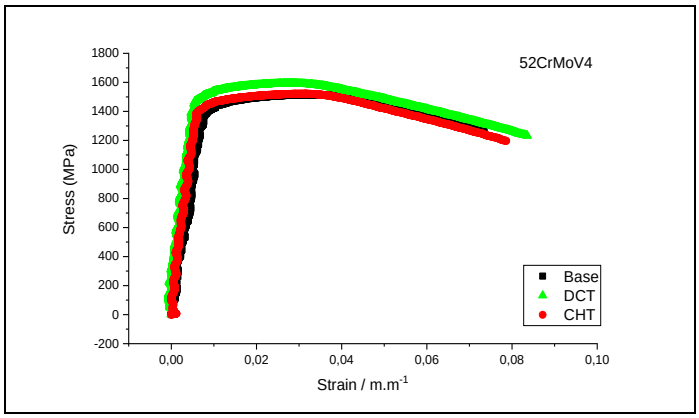

Figure 2. Stress-strain plot of 52CrMoV4 sample

As can be seen in Figure 1, an increase in static toughness values was observed in all steel groups as a result of the cryogenic process. This increase can be seen much more comfortably when the 52CrMoV4 data, which is the relatively most alloyed steel group, is traditionally plotted. As seen in Figure 2, there has been a significant increase in the static toughness of the material as a result of the significant increase in the elongation at break despite the minimal increase in tensile strength. This increase was calculated as 19.43% by calculating the area below the chart line. As seen in Table 4, this increase has also found its correspondence in notch toughness values. The main reason for this increase is reported as high-density second carbide precipitates. Although the

cryogenic process triggered carbide formation, it was possible to gain toughness without losing tensile strength by delaying the coarse kinetics of carbides (Özden & Anik, 2020; Vahdat et al., 2013).

Conclusion

- As a result, an increase was observed in the microhardness, notch impact toughness and tensile strength of the samples treated with the cryogenic process compared to the samples treated with conventional heat treatment.
- The amount of increase increased with the alloying level of steel.
- Accordingly, cryogenic treatment can be presented as an effective method for improving the mechanical properties of medium carbon spring steels.

Acknowledgment

Financial assistance from Eskisehir Osmangazi University Research Fund is gratefully acknowledged (Project No: 201615A230). The authors wish to thank MMD Mechanical and Materials Technologies R&D Consulting Engineering Services Industry and Trade Limited Company for the deep cryogenic treatments.

References

Baldissera, P., & Delprete, C. (2008). Deep cryogenic treatment: A bibliographic review. *The Open Mechanical Engineering Journal*, *2*(1), 1–11. https://doi.org/10.2174/1874155X00802010001

Bensely, A., Venkatesh, S., Mohan Lal, D., Nagarajan, G., Rajadurai, A., & Junik, K. (2008). Effect of cryogenic treatment on distribution of residual stress in case carburized En 353 steel. *Materials Science and Engineering A*, *479*(1–2), 229–235. https://doi.org/10.1016/j.msea.2007.07.035

Das, D., Sarkar, R., Dutta, A. K., & Ray, K. K. (2010). Influence of sub-zero treatments on fracture toughness of AISI D2 steel. *Materials Science and Engineering A*, *528*(2), 589–603. https://doi.org/10.1016/j.msea.2010.09.057

Ghasemi-Nanesa, H., & Jahazi, M. (2014). Simultaneous enhancement of strength and ductility in cryogenically treated AISI D2 tool steel. *Materials Science and Engineering A*, *598*, 413–419. https://doi.org/10.1016/j.msea.2014.01.065

Michaud, P., Delagnes, D., Lamesle, P., Mathon, M. H., & Levaillant, C. (2007). The effect of the addition of alloying elements on carbide precipitation and mechanical properties in 5% chromium martensitic steels. *Acta Materialia*, *55*(14), 4877–4889. https://doi.org/10.1016/j.actamat.2007.05.004

Myeong, T., & Yamabayashi, Y. (1997). A new life extension method for high cycle fatigue using micro-martensitic transformation in an austenitic stainless steel. *Journal of Fatigue*, *19*(1), 69–73. https://doi.org/10.1016/S0142-1123(97)00060-1

Özden, R., & Anik, M. (2020). Enhancement of the mechanical properties of EN52CrMoV4 spring steel by deep cryogenic treatment Verbesserung der mechanischen Eigenschaften von EN52CrMoV4 Federstahl durch Tieftemperaturbehandlung. *Materialwissenschaft Und Werkstofftechnik*, *51*, 422–431. https://doi.org/10.1002/mawe.201900122

Preciado, M., & Pellizzari, M. (2014). Influence of deep cryogenic treatment on the thermal decomposition of Fe-C martensite. *Journal of Materials Science*, *49*(23), 8183–8191. https://doi.org/10.1007/s10853-014-8527-2

Senthilkumar, D., Rajendran, I., Pellizzari, M., & Siiriainen, J. (2011). Influence of shallow and deep cryogenic treatment on the residual state of stress of 4140 steel. *Journal of Materials Processing Technology*, *211*(3), 396–401. https://doi.org/10.1016/j.jmatprotec.2010.10.018

Vahdat, S. E., Nategh, S., & Mirdamadi, S. (2013). Microstructure and tensile properties of 45WCrV7 tool steel after deep cryogenic treatment. *Materials Science & Engineering A*, *585*, 444–454. https://doi.org/10.1016/j.msea.2013.07.057

Villa, M., Pantleon, K., & Somers, M. A. J. (2014). Evolution of compressive strains in retained austenite during sub-zero Celsius martensite formation and tempering. *Acta Materialia*, *65*, 383–392. https://doi.org/10.1016/j.actamat.2013.11.007

Zhirafar, S., Rezaeian, A., & Pugh, M. (2007). Effect of cryogenic treatment on the mechanical properties of 4340 steel. *Journal of Materials Processing Technology*, *186*(1–3), 298–303. https://doi.org/10.1016/j.jmatprotec.2006.12.046

Author Information

Reşat Can Özden
Eskisehir Osmangazi University
Department of Metallurgical and Materials Engineering,
Eskisehir Osmangazi University, 26040, Eskisehir, Turkey
Contact e-mail: *rcanozden@ogu.edu.tr*

Ersu Lökçü
Eskisehir Osmangazi University
Department of Metallurgical and Materials Engineering,
Eskisehir Osmangazi University, 26040, Eskisehir, Turkey

Mustafa Anik
Eskisehir Osmangazi University
Department of Metallurgical and Materials Engineering,
Eskisehir Osmangazi University, 26040, Eskisehir, Turkey

The Eurasia Proceedings of Science, Technology, Engineering & Mathematics (EPSTEM)
ISSN: 2602-3199

The Eurasia Proceedings of Science, Technology, Engineering & Mathematics (EPSTEM), 2020

Volume 11, Pages 53-56

IConTES 2020: International Conference on Technology, Engineering and Science

Effect of Mg Content on the Electrochemical Properties of (MgCoNiZnLi)O Based High Entropy Oxides for Li-Ion Batteries

Ersu LOKCU
Eskisehir Osmangazi University

Resat Can OZDEN
Eskisehir Osmangazi University

Mustafa ANIK
Eskisehir Osmangazi University

Abstract: High entropy oxides (HEOs) are attractive as a negative electrode material for lithium-ion batteries because of the high specific capacities and cycling stabilities. Moreover, they offer a wide range of compositional variation to reach the desired electrochemical performances. In this study, we synthesized the $Mg_x(CoNiZnLi)_{100-x}O$ high entropy oxides using conventional solid state reaction technique and examined their electrochemical properties in lithium-ion cells as anode material. The structural properties of as-synthesized $Mg_5(CoNiZnLi)_{95}O$ and $Mg_{35}(CoNiZnLi)_{65}O$ HEOs were investigated using X-ray diffraction (XRD) technique, which showed that all the oxides have single-phase rock-salt structure. When tested as anode material in lithium-ion cell, $Mg_5(CoNiZnLi)_{95}O$ anode exhibits higher initial discharge capacity than $Mg_{35}(CoNiZnLi)_{65}O$ electrode. However, the $Mg_{35}(CoNiZnLi)_{65}O$ electrode shows the higher cycling stability than $Mg_5(CoNiZnLi)_{95}O$ electrode at the further cycle period. This work offers an approach to control the electrochemical properties of HEO based anodes by tuning active and inactive cation contents in the structure.

Keywords: Conversion type anode, Li-ion battery, High entropy oxide

Introduction

Recently, lithium-ion batteries (LIBs) have been regarded as the main technology for powering portable devices and consumer electronics. Commercial LIBs, based on intercalation type electrodes, such as graphite and $Li_4Ti_5O_{12}$, are generally stable, but they have low specific energy (Lu et al., 2018). Therefore, the development of new type electrode materials with high specific energy is very important and necessary. Metal oxides, such as MoO_2, Co_3O_4, MnO and $NiFe_2O_4$ etc. are alternative electrodes for LIBs that working through conversion reactions (Puthusseri et al., 2018; Fang et al., 2019). These reactions are associated with much higher energy densities than intercalation reactions. However, they often suffer from huge volume changes during charge/discharge and have poor cycling stability (Yuan et al., 2014).

Since the day it was discovered, the concept of high entropy materials (HEMs) has led to the designing of many new compounds such as high entropy carbides, nitrides, borides, sulfides and oxides. The key concept of HEMs is to use multiple constituents (usually five or more with the concentration of each constituent being between 5 and 35 at. %), in order to maximize the configurational entropy ($S_{config} \geq 1.5R$) to achieve a single phase solid solution structure (Rost et al., 2015).

Recently, designing of a high entropy oxide (HEO) to be used as an anode material is considered as one of the important developments in the LIBs. It is reported that the entropy stabilization results in improved cycling capability in (MgCoNiCuZn)O anode (Sarkar et al., 2018). The stable capacity value of 920 mA h g^{-1} was reached after 300 cycles upon synthesis of (MgCoNiCuZn)O HEO anode in the form of nanoparticles (Qiu et al., 2019). In another study, $(MgCoNiZn)_{1-x}Li_xO$ HEOs were synthesized and their electrochemical

- Selection and peer-review under responsibility of the Organizing Committee of the Conference

performances were investigated as anode material in LIBs. The increase in the lithium cation concentration causes generation of more oxygen vacancies, which greatly affected the electrochemical performance of $(MgCoNiZn)_{1-x}Li_xO$ HEO based anodes, on the structure (Lökçü et al., 2020). They reported the $(MgCoNiZn)_{0.65}Li_{0.35}O$ anode had 1930 mA h g^{-1} initial and 610 mA h g^{-1} stable discharge capacities. These results were very promising for the use of HEOs as anode material in LIBs. Herein, we synthesized the $Mg_x(CoNiZnLi)_{100-x}O$ high entropy oxides to further investigation of their electrochemical properties related to the different presence of Mg in the structure.

Materials & Methods

MgO, CoO, NiO, ZnO and Li_2O were mixed homogeneously in the determined molar ratios to get $Mg_5(CoNiZnLi)_{95}O$ and $Mg_{35}(CoNiZnLi)_{65}O$ stoichiometry and they milled at 300 rpm for 2 h by using the planetary ball mill (Fritsch Pulverisette 7 Premium Line). The obtained oxide mixtures were then unaxially pressed at 300 MPa. Finally, the oxide pellets were sintered at 1000ºC for 12 h prior to the air quenching. The sintered pellets were re-milled at 200 rpm for 1 h to prepare electrodes.

The phase structures of the as-synthesized $Mg_5(CoNiZnLi)_{95}O$ and $Mg_{35}(CoNiZnLi)_{65}O$ HEOs were examined by XRD (PANalytical Empyrean) technique using Cu Kα radiation ($\lambda = 0.154$ nm). The HEO based anodes were prepared by mixing 75 wt% active material, 15 wt% carbon black (Super P) and 10 wt% polyvinylidene fluoride (PVDF) in N-methyl pyrrolidinone (NMP) to form a homogeneous slurry. Then the slurry was coated onto Cu foil and dried in a vacuum oven at 80ºC for 12 h. The coin cells were assembled in an argon-filled glove box with H_2O and O_2 levels less than 1.0 ppm. Lithium metal was used as the counter and reference electrodes and the glass microfiber filter as a separator. 1 M Lithium hexafluorophosphate ($LiPF_6$) in ethylene carbonate and dimethyl carbonate (EC:DMC) in a 1:1 ratio by volume was used as electrolyte. The charge-discharge tests were performed galvanostatically in a potential range change between 0.01 V and 3.00 V (vs. Li^+/Li) at 100 mA g^{-1} current density.

Results and Discussion

The XRD patterns of $Mg_5(CoNiZnLi)_{95}O$ and $Mg_{35}(CoNiZnLi)_{65}O$ samples, which are prepared by the conventional solid state method, reveal that all the samples have a single phase rock-salt crystal structure and no impurity peaks are detected in Figure 1.

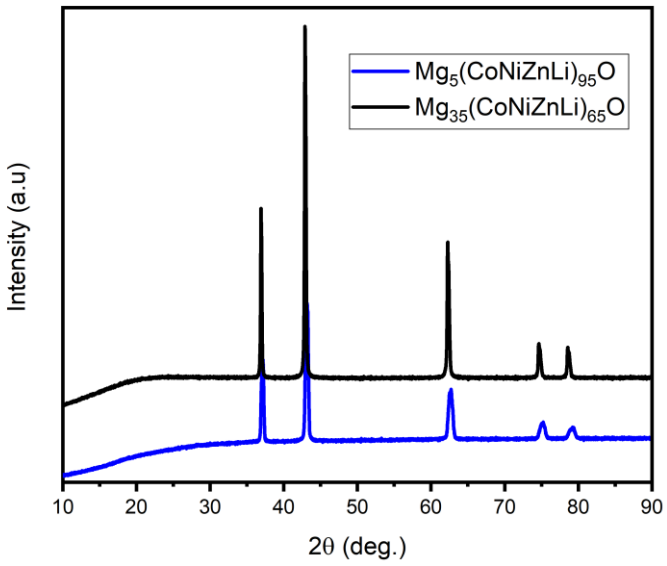

Figure 1. XRD patterns of the as-synthesized $Mg_5(CoNiZnLi)_{95}O$ and $Mg_{35}(CoNiZnLi)_{65}O$ HEOs.

As the amount of Mg increases in the HEO structure, the X-ray diffraction peaks shifts towards lower angle. The shift in XRD peaks is a result of a change in the lattice parameters due to the presence of different amount cations in the HEO structure. Ionic radii of the cations in the rock-salt crystal structure are given in Table 1.

Table 1. Ionic crystal radii of the elements in the rock-salt crystal structure.

Cations	Radius (nm)
Mg^{2+}	0.072
Ni^{2+}	0.069
Co^{2+}	0.075
Co^{3+}	0.055
Zn^{2+}	0.074
Li^{1+}	0.076

The initial discharge capacities of $Mg_5(CoNiZnLi)_{95}O$ and $Mg_{35}(CoNiZnLi)_{65}O$ are 1459 mA h g^{-1} and 1222 mA h g^{-1}, respectively. For the initial discharge process, the voltages dropped to a plateau of 0.75 V and 0.32 from the open circuit potential and then decreased to 0.01 V for the $Mg_5(CoNiZnLi)_{95}O$ and $Mg_{35}(CoNiZnLi)_{65}O$ anodes, respectively. Following the initial discharge curves in Figure 2, the charge-discharge cycles from the 2nd to 5th are given in Figure 3. The discharge voltages of the anodes look slightly increased and the discharge reaction occurs over a potential range of ~1.38-0.01 V with an inclined single slope. After the first cycle, the significant capacity loss is observed because of the formation of SEI layer at the interface of the electrode surface and the electrolyte and initial lithium loss, mainly due to anode conversion.

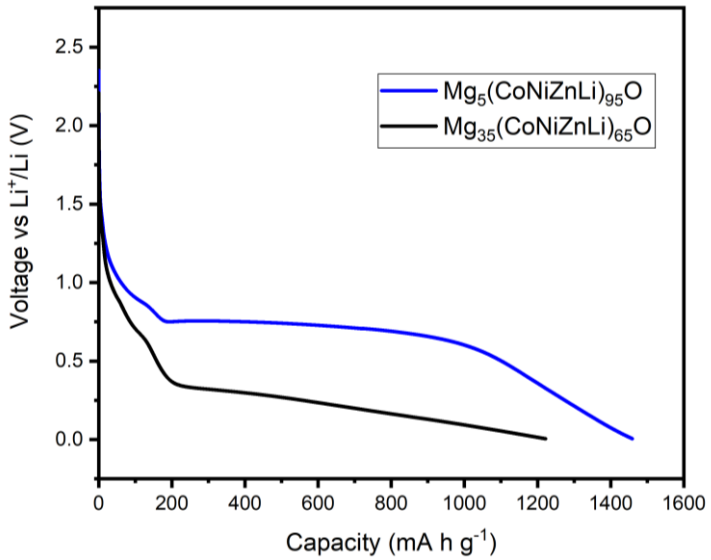

Figure 2. Initial discharge curves of $Mg_5(CoNiZnLi)_{95}O$ and $Mg_{35}(CoNiZnLi)_{65}O$ anodes at a current density of 100 mA g^{-1}.

The discharge capacities of the $Mg_5(CoNiZnLi)_{95}O$ and $Mg_{35}(CoNiZnLi)_{65}O$ anodes are 168 mA h g^{-1} and 576 mA h g^{-1}, respectively at the end of 5th cycle. The results clearly indicated that increasing content of inactive MgO in the HEO structure promoted the cyling stability of electrode. However, the point to be considered here is that the homogeneous distribution of Mg cation in HEO structure and preserves the rock-salt phase during the charge-discharge process. Otherwise, the mechanical mixture of metal oxides, especially MgO, will not positively contribute to cycling stability of the electrodes.

Conclusion

$Mg_5(CoNiZnLi)_{95}O$ and $Mg_{35}(CoNiZnLi)_{65}O$ HEO anodes were synthesized with a single-phase rocksalt crystal structure by the conventional solid-state method and their electrochemical performances were observed in the LIB. The HEO based $Mg_{35}(CoNiZnLi)_{65}O$ anode showed excellent cycling stability compared to the $Mg_5(CoNiZnLi)_{95}O$ anode. Therefore, these results evidence that the electrochemical performances of HEO based anodes can be improved by simply changing the active/inactive cation contents in the structure.

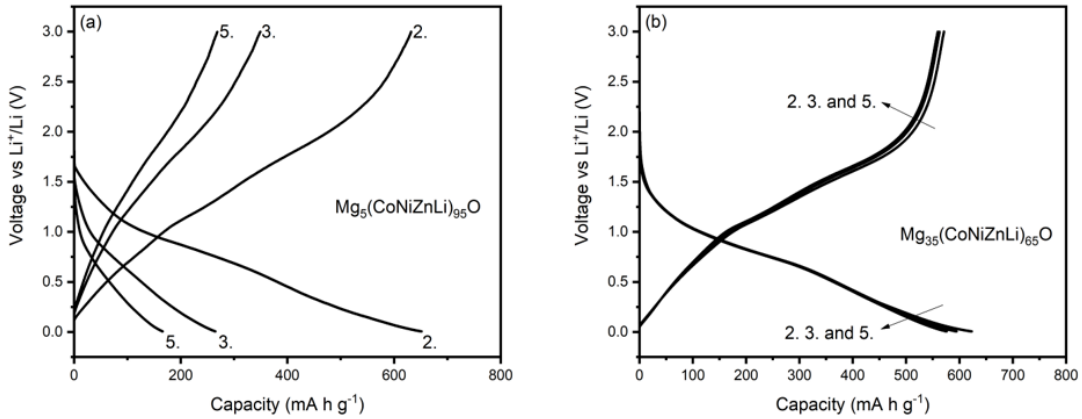

Figure 3. Discharge-charge curves of (a) $Mg_5(CoNiZnLi)_{95}O$ and (b) $Mg_{35}(CoNiZnLi)_{65}O$ anodes for the 2nd, 3rd and 5th cycles in the voltage range of 0.01-3.00 V at a current density of 100 mA g^{-1}.

Acknowledgements or Notes

This research was supported by the Scientific and Technological Research Council of Turkey under the project number 119M807.

References

Fang, S., Bresser, D., & Passerini, S. (2019). Transition metal oxide anodes for electrochemical energy storage in lithium- and sodium- ion batteries. *Advanced Energy Materials, 10*, 1902485.

Lökçü, E., Toparli, Ç., & Anik, M. (2020). Electrochemical performance of $(MgCoNiZn)_{1-x}Li_xO$ high-entropy oxides in lithium-ion batteries. *ACS Applied Materials & Interfaces, 12*, 23860-23866.

Lu, J., Chen, Z., Pan, F., Cui, Y., & Amine, K. (2018). High-performance anode materials for rechargeable lithium-ion batteries. *Electrochemical Energy Reviews, 1*, 35−53.

Puthusseri, D., Wahid, M., & Ogale, S. (2018). Conversion-type anode materials for alkali-ion batteries: State of the art and possible research directions. *ACS Omega, 3*, 4591−4601.

Rost, C. M., Sachet, E., Borman, T., Moballegh, A., Dickey, E. C., Hou, D., Jones, J. L., Curtarolo, S., & Maria, J.-P. (2015). Entropy-stabilized oxides. *Nature Communications, 6*, 1−8.

Sarkar, A., Velasco, L., Wang, D., Wang, Q., Talasila, G., de Biasi, L., Kübel, C., Brezesinski, T., Bhattacharya, S. S., Hahn, H., & Breitung, B. (2018). High entropy oxides for reversible energy storage. *Nature Communications, 9*(3400), 1-9.

Qiu, N., Chen, H., Yang, Z., Sun, S., Wang, Y., & Cui, Y. (2019). A high entropy oxide (Mg0.2Co0.2Ni0.2Cu0.2Zn0.2O) with superior lithium storage performance. *Journal of Alloys and Compounds, 777*, 767−774.

Yuan, C., Wu, H. B., Xie, Y.;, & Lou, X. W. D. (2014). Mixed transition- metal oxides: Design, synthesis, and energy-related applications. *Angewandte Chemie International Edition, 53*, 1488−1504.

Author Information

Ersu Lökçü
Eskisehir Osmangazi University
Department of Metallurgical and Materials Engineering,
26040, Eskisehir, Turkey
elokcu@ogu.edu.tr

Reşat Can Özden
Eskisehir Osmangazi University
Department of Metallurgical and Materials Engineering,
26040, Eskisehir, Turkey

Mustafa Anik
Eskisehir Osmangazi University
Department of Metallurgical and Materials Engineering,
26040, Eskisehir, Turkey

The Eurasia Proceedings of Science, Technology, Engineering & Mathematics (EPSTEM)
ISSN: 2602-3199

The Eurasia Proceedings of Science, Technology, Engineering & Mathematics (EPSTEM), 2020

Volume 11, Pages 57-63

IConTES 2020: International Conference on Technology, Engineering and Science

Microstructural Evolution and Mechanical Properties of Mg Added ZA-12 Alloy

Ibrahim CELIKYUREK
Eskişehir Osmangazi University

Bedri BAKSAN
Eskişehir Osmangazi University

Osman TORUN
Afyon Kocatepe University

Abstract: A ZA-12 Zinc-based alloy was melted in an induction melting furnace, and cast in a graphite mold. Different amount of Mg was added for examining the microstructural evolution and mechanical properties of ZA-12 alloy. All alloys were annealed at 350oC for 22 hours to research the effect of heat treatment on the properties of ZA-12 alloy. The microstructure examinations revealed that while ZA-12 alloy has a dendritic microstructure with fine grains, with the Mg addition the distance between dendrite arms was getting larger. The hardness of alloys was increased with an increase in Mg content. The hardness of all alloys was increased slightly with the annealing also. Compression tests were performed to determine the mechanical properties. These tests showed that the yield strength and elongation are increased with increasing Mg amount for as casted alloys. The annealing heat treatment decreased the yield strength of alloys. A brittleness was observed for as-cast alloys containing more than 2.0wt.% Mg. The brittleness was still existing after heat treatment for alloy including 4.0 wt.% Mg while the alloy containing 2.0 wt.% of Mg became ductile.

Keywords: Zinc-based alloys, microstructure, hardness, compression strength.

Introduction

Zinc based alloys are very attractive engineering materials due to their low density, very good castability, low energy consumption for shaping, low cost and intermediate strength and hardness, etc. (Prasad et al. 1996, Pürçek et al. 2002). The commercial zinc-based alloys called ZAMAK, ALZEN, and ZA are binary Zn-Al alloys and include small amounts of Cu. These alloys are based on Zn-Al eutectic, eutectoid, or monotectoid composition. (Savaşkan et al. 2004).

Although their poor strength and hardness the Zn-Al alloys have been used widely in a variety of industries due to their excellent fluidity. With these alloys, very thin-walled and complex shaped parts can be cast using gravity or pressure die casting with/without heating the mold (Hanna et al. 1997). In recent years some works have been made intend to improve the strength and hardness of Zn-Al alloys. In these studies, some authors suggested the alloying of Zn based alloys (Prasad et al. 1996, Savaşkan et al. 2004, Pürçek et al. 2002, Hanna et al. 1997, Şevik 2014), whereas some of them suggested reinforcing the alloy with particulates or fibers (Pola et al. 2016, Li et al. 2001, Tao et al. 1995, Xu et al. 2014, Alaneme et al. 2017, Madronero et al. 1997, Almomani et al. 2016, Liu et al. 2009).

In addition to low strength and hardness low using temperature compared to other metallic materials limits the use of Zinc based alloys. Besides these properties, the Zn based alloys are an alternative material to bronzes which are used in tribological applications. It is reported that Zn based bearings have good wear and seizure resistance, and a lower coefficient of friction than bronzes under heavy load and slow to medium friction speed conditions. (Prasad et al. 1996).

Further studies have been focused on increasing the hardness, strength, and wear resistance of zinc-based alloys. Abou El-Khair et al. (2004) investigated the effects of Al content on the properties of the Zn-Al binary alloys. They reported that hardness, strength, and wear resistance of the alloy is increased with increasing Al content, however ductility was degreased. Furthermore, the strength is decreased and ductility is increased with increasing temperature for Zn-Al binary alloys. A higher strength at elevated temperature was also observed with increasing Al content.

Türk et al. (2007) modified the ZA8 commercial alloy with Pb, Sn, and Cd. The samples were subjected to the wear tests and the results were compared with commercial SAE 660 bearing bronze. They found that ZA8 and modified ZA8 alloys have higher wear resistance, but also a higher coefficient of friction than bearing bronze.

On the other hand, Savaşkan et al. (2014) investigated the effects of Cu and Si on the Zn-Al alloys. They increased the Si and Cu content systemically while the Al content was 15%. They found that the hardness, tensile, and compressive strength are increased whereas the elongation and impact energy was decreased with increasing Copper content for Zn-Al-Cu ternary alloys. For Zn-Al-Cu-Si quaternary alloys, the hardness and compressive strength were increased while the tensile strength, elongation, and impact energy were decreased with increasing Si content.

In this study, ZA-12 alloy was produced by casting and heat treatment was applied to the alloy. The effects of the applied heat treatment on the microstructure and mechanical properties of the alloy were investigated. Also, Mg was added to the alloy systematically at increasing rates and heat treatment was applied to these alloys.

Method

Zinc alloy ZA-12 and Mg added alloys (Table 1) were produced in an induction melting furnace at the nominal composition of 88%Zn, 11.0%Al, and 1.0%Cu (wt%). First, Zn was melted and then Al and Cu were added. Also, ZA-12 alloys modified with Mg by adding increasing amounts of Mg were produced in the same way. The melted alloy was poured into a graphite mold and allowed for cooling. In this way, samples of 10 mm diameter and 100 mm length were obtained by casting. All cast alloys were annealed at 350 C for 22 hours and quenched by throwing into the water.

Mechanical characterization of cast and annealed specimens was done by axial compression tests and hardness measurements. Compression test specimens are formed by machining. Compression tests were conducted at room temperature and a jaw speed of 10mmmin^{-1}. Hardness measurements were made by applying the Vickers tip for 10 seconds with a 1kgf load. A light optical microscope (LOM) was used to examine the changes in microstructure.

Table 1. The nominal compositions of the alloys (wt.%)

Alloy	Zn	Al	Cu	Mg
ZA-12	88.0	11.0	1.0	0
ZA-12+0.5Mg	87.5	11.0	1.0	0.5
ZA-12+1Mg	87	11.0	1.0	1.0
ZA-12+2Mg	86	11.0	1.0	2.0
ZA-12+4Mg	85	11.0	1.0	4.0

Results and Discussion

The Zn-Al phase diagram and the annealing temperature corresponding to the alloy composition are shown in Figure 1. The crystal structures of the phases are seen in the figure. According to the Zn-Al phase diagram, the Zn alloy containing 11 wt.% Al contains phases α and η at room temperature. At 350 ^{o}C there are β and η phases. In practice, the phase β can be found in addition to α and η at room temperature depending on the solidification conditions.

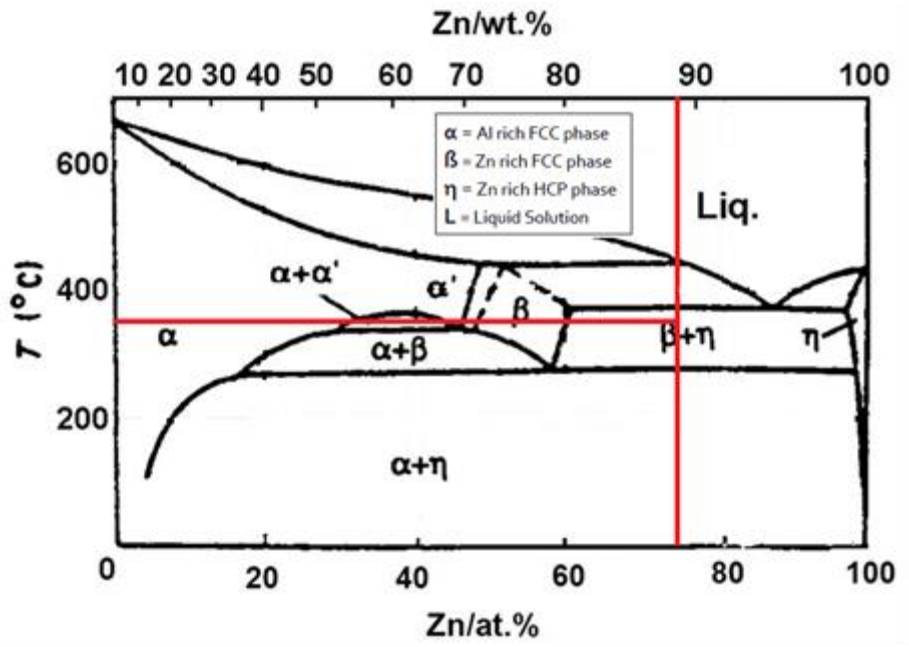

Figure 1. The binary phase diagram of the Al-Zn system.

Microstructure

The microstructures of the cast and annealed alloys obtained from the optical microscope are shown in Figure 2. All microstructure photos were taken at the same magnification. In the figure, it is seen that the ZA-12 alloy has a dendritic structure with very small fine particles. It is seen that the dendritic structure is preserved and the η phase expands after annealing (Figure 2a, b). When Mg is added to ZA-12 alloy in as-cast form, the dendritic structure deteriorates as the amount of Mg increases (Figure 2 c, e, g, i). In the ZA-12 alloy containing 4 wt.%Mg, the η phase appears to have a rosette-like growth. Also, a new phase appears in gray. In the literature, it is recommended to keep the amount of Mg low in Zinc-based alloys. Because Mg makes the alloy brittle. After the Mg containing alloys are annealed, it is seen that the dendritic structure is destroyed and the grains become coaxial. After the heat treatment, the new phase formed together with the α phase dispersed at the boundaries of the η phase became prominent. The particle size of the η phase decreases with increasing Mg amount.

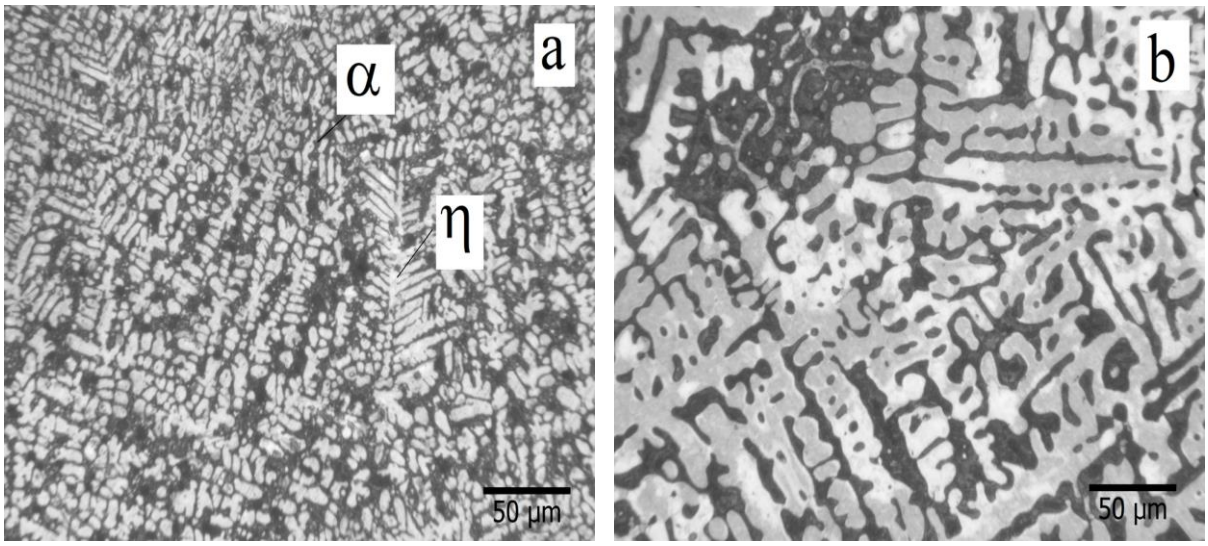

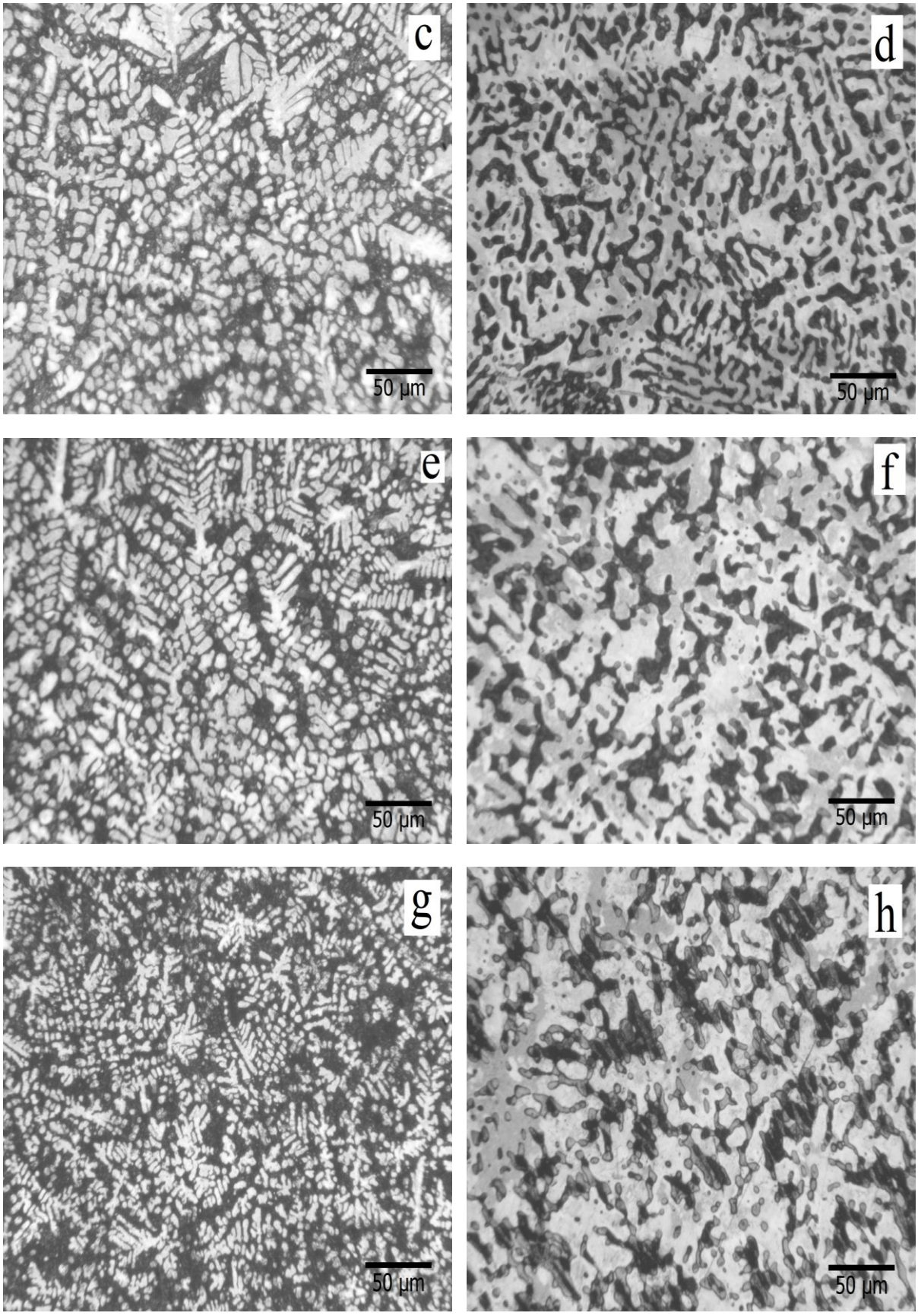
c
50 µm
d
50 µm
e
50 µm
f
50 µm
g
50 µm
h
50 µm

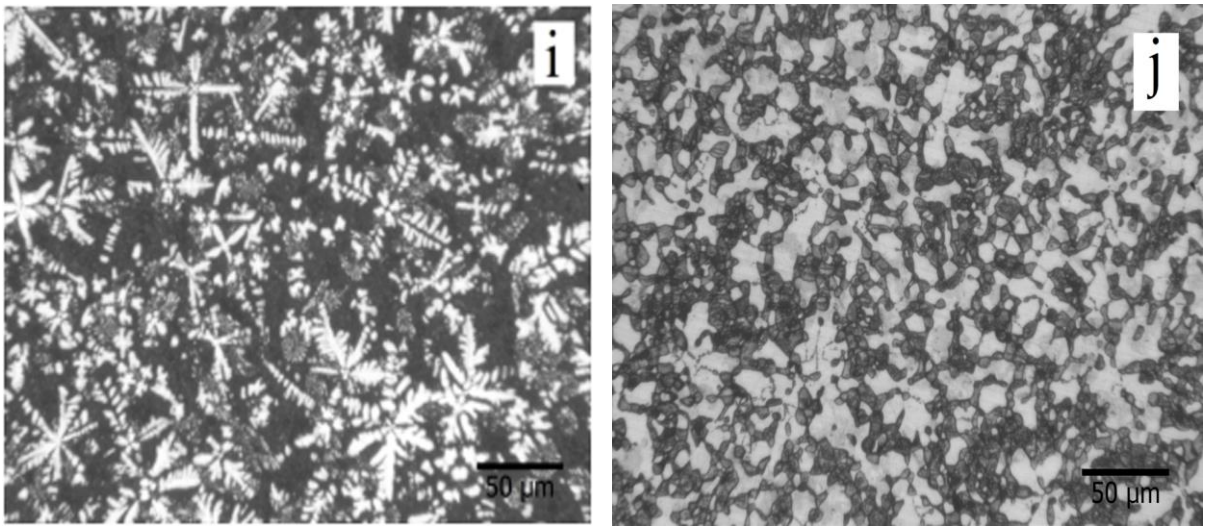

Figure 2. The LOM micrographs of the as-cast and annealed alloys. a) ZA-12 as-cast, b) ZA-12 annealed, c) ZA-12+0.5Mg as-cast, d) ZA-12+0.5Mg annealed, e) ZA-12+1Mg as-cast, f) ZA-12+1Mg annealed, g) ZA-12+2Mg as-cast, h) ZA-12+2Mg annealed, i) ZA-12+4Mg as-cast, j) ZA-12+4Mg annealed

Compression Strength and Hardness

The compression test results and hardness values are summarized in Table 2. The methods used in the determination of mechanical properties are shown on the stress-strain curve obtained as an example of the compression test of the ZA-12 cast alloy given in Figure 3. All alloys, except the brittle alloys, behaved similarly to figure 3. The stress-strain curve of a brittle alloy is given in Figure 4.

Table 2. The mechanical properties of the alloys in as-cast and annealed form.

	As-cast							Annealed						
	%0.2 Yp		Consatant plastic deformation rate		εp	H	E	%0.2 Yp		Consatant plastic deformation rate		εp	H	E
Alloy	σ,MPa	ε,%	σ,MPa	ε,%	%	HV	MPa	σ,MPa	ε,%	σ,MPa	ε,%	%	HV	MPa
ZA12	495	2.35	990	49.64	62	128	226	530	2.66	860	38.38	57	144	228
ZA12+0.5Mg	551	2.43	896	39.52	58	134	240	580	2.58	792	32.60	56	153	246
ZA12+1Mg	602	2.72	850	32.57	58	146	244	634	2.56	764	29.50	53	154	258
ZA12+2Mg	650	2.72				175	221	668	2.55	797	28.40	58	170	241
ZA12+4Mg	759	2.76				199	306	678	2.56				183	279

As can be seen from the table, when the amount of Mg addition to the cast alloy increased, the yield strength and strain, hardness, and Elasticity Modulus increase. But, the stress and strain values at the limit of constant plastic deformation rate and the plastic deformation limit (εp) are decreased. While cast alloys containing up to 1wt.% Mg show ductile behavior, alloys containing more than 1wt.% Mg was quite brittle. Interestingly, the alloy containing 2wt.%Mg, which was brittle in its cast form, gained ductile character at the end of the annealing process, while the alloy containing 4wt. %Mg remained brittle.

The annealing heat treatment affects the mechanical properties of alloy ZA-12 and alloys modified with Mg. In the case of annealing at 350 ^{o}C and rapid cooling in the alloy without Mg addition, the yield strength and elongation, hardness, and elastic modulus increase, while the strength and elongation at the constant plastic deformation rate limit and the plastic deformation limit decrease. The increase in the amount of β phase in the alloy may have caused this result. While the yield strength increased with increasing Mg addition in annealed alloys, 0.5wt.% Mg addition increased the yield elongation but adding more Mg resulted in a decrease in yield elongation. Hardness and Elasticity Modules of annealed alloys are higher than cast alloys. Annealing has also reduced the plastic deformation limits of all alloys.

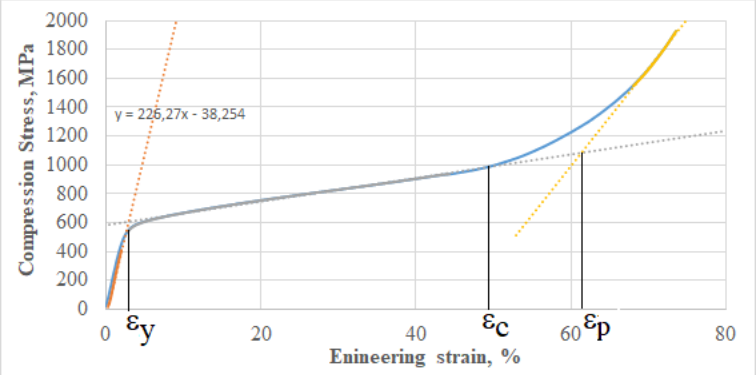

Figure 3. The stress-strain curve of as-cast ZA-12 alloy.

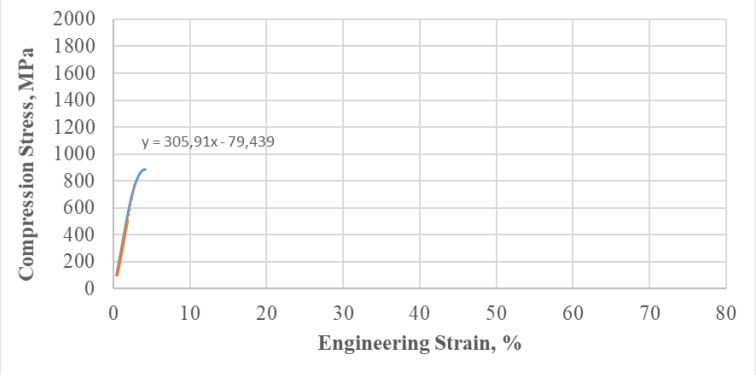

Figure 4. The stress-strain curve of as-cast ZA-12 alloy including 4 wt. % Mg

Conclusion

Increasing amounts of Mg were added to the commercial ZA-12 zinc alloy and the effect of Mg addition on the microstructure and mechanical properties of the ZA-12 alloy was investigated. ZA zinc alloys are only considered as-cast alloys. However, it is known that the microstructure and mechanical properties of many metal alloys can be changed by heat treatment. This study revealed that the microstructure and mechanical properties of the ZA-12 alloy and the Mg modified alloys changed. It was observed that the mechanical properties of ZA-12 alloy improved only with solution heat treatment. The Mg-added alloy, which was evaluated as brittle, could be made ductile by heat treatment.

Recommendations

Advanced studies such as SEM-EDS and XRD are required to determine the phases in the alloy microstructure.

References

Abou El-Khair M.T., Daoud A., Ismail A. (2004). Effect of different Al contents on the microstructure, tensile, and wear properties of Zn-based alloy. *Materials Letters, 58*, 1754-1760.

Alaneme K.K., Ajayi O.J. (2017). Microstructure and mechanical behavior of stir-cast Zn-27Al based composites reinforced with rice husk ash, silicon carbide, and graphite. *Journal of King Saud University-Engineering Sciences, 29*, 172-177.

Almomani M., Hayajneh M.T., Draidi M. (2016). Tribological investigation of Zamak alloys reinforced with alumina (Al2O3) and fly ash. *Particulate Science and Technology, 34*, 317-323.

Hanna M.D., Carter J.T., Rashid M.S. (1997). Sliding wear and friction characteristics of six Zn-based die-casting alloys. *Wear, 203-204*, 11-21.

Li Z.Q., Zhang S.Y., Wu B.Y. (2001). Solidification and microstructure of ZA27/SiCp composite fabricated by mechanical – electromagnetic combination stirring process. *Materials Science and technology, 17*, 465-472.

Liu J., Yu S., Zhu X, Wei M., Luo Y., Liu Y. (2009). Correlation between ceramic additions and compressive properties of Zn-22Al matrix composite foams. *Journal of Alloys and Compounds, 476*, 220-225.

Madronero A., Cruz J., Foruria C., Coleto J. (1997). Rheocasting a Zn-Al Composite reinforced with Coke dust. *Journal of Minerals, Metals and Materials Society, 49*, 46-49.

Narimannezhad A., Aashuri H., Kokabi A.H., Khosravani A. (2009). Microstructural evolution and mechanical properties of semisolid stir welded zinc AG40A die cast alloy. *Journal of Materials Processing Technology, 209*, 4112-4121.

Pola A., Montesano L., Gelfi M., La Vecchia G.M. (2016). Comparison of the sliding wear of a novel Zn alloy with that of two commercial Zn alloys against bearing steel and leaded brass. *Wear, 368-369*, 445-452.

Prasad B.K., Patwardhan A.K., Yegneswaran A.H. (1996). Dry sliding wear characteristic of some zinc-aluminium alloys: a comparative study with a conventional bearing bronze at a low speed. *Wear, 199*, 142-151.

Pürçek G., Savaşkan T., Küçükömeroğlu T., Murphy S. (2002). Dry sliding friction and wear properties of zinc-based alloys. *Wear, 252*, 894-901.

Savaşkan T, Hekimoğlu A.P., Pürçek G. (2004). Effect of copper content on the mechanical and sliding wear properties of monotectoid-based zinc-aluminium-copper alloys. *Tribology International, 37*, 45-50.

Savaşkan T., Hekimoğlu A.P. (2014). Microstructure and mechanical properties of Zn-15Al-based ternary and quaternary alloys. *Materials Science and Engineering A, 603*, 52-57.

Şevik H. (2014). The effect of silver on wear behavior of zinc-aluminium-based ZA-12 alloy produced by gravity casting. *Materials Characrterization, 89*, 81-87.

Tao L., Dellis M.A., Boland F., Delannay F. (1995). Comparison of fibres for creep strengthening of zinc-aluminium foundry alloys. *Composites, 26*, 611-617.

Türk A., Kurnaz C., Çevik H. (2007). Comparison of the wear properties of modified ZA-8 alloys and conventional bearing bronze. *Materials and Design, 28*, 1889-1897.

Xu Z., Ma L., Yan J, Chen W., Yang S. (2014). Solidification microstructure of SiC particulate reinforced Zn-Al composites under ultrasonic exposure. *Materials Chemistry and Physics, 148*, 824-832.

Author Information

İbrahim Çelikyürek
Eskişehir Osmangazi University
Faculty of Eng. And Arc. Metallurgical and Materials Eng Dept.Eskişehir, TURKEY
Contact e-mail: cibrahim*@ogu.edu.tr*

Bedri Baksan
Eskişehir Osmangazi University
Faculty of Eng. And Arc. Metallurgical and Materials Eng Dept.Eskişehir, TURKEY

Osman Torun
Afyonkocatepe University
Ahmet Necdet Sezer Kampüsü, Gazlıgöl Yolu, 03200,
Afyonkarahisar, TURKEY

The Eurasia Proceedings of Science, Technology, Engineering & Mathematics (EPSTEM)
ISSN: 2602-3199

The Eurasia Proceedings of Science, Technology, Engineering & Mathematics (EPSTEM), 2020

Volume 11, Pages 64-68

IConTES 2020: International Conference on Technology, Engineering, and Science

Boriding of Ni40Al

Osman TORUN
Afyon Kocatepe University

Ibrahim CELIKYUREK
Eskişehir Osmangazi University

Bedri BAKSAN
Eskişehir Osmangazi University

Abstract: Boriding has been one of the thermochemical processes that have been developed and used recently in industries. The main advantages of this technique are leading to the high strength of abrasion wear and high oxidation resistance compared with other conventional surface treatments Ni-Al alloy is a new material that offers improved high-temperature properties over traditional ferrous and nickel based hot work die materials. In this study, Ni and Ni-40Al alloys were borided. Ni40Al at. % alloy was prepared by vacuum arc melting under argon atmosphere. Boriding of Ni and Ni-Al alloys was carried out with Ekabor–Ni powders at 875 C for 2, 4, and 6 h. The characterization of the boride layer formed on the surface of nickel aluminide substrates was identified by optical microscopy. Microhardness and thickness of boride layers were measured. Its hardness was found to be higher than the cast Ni-40Al alloy. The thickness and of boriding layers were found to be different depending on the boriding time.

Keywords: Hardness, boriding, Ni-Al

Introduction

Excellent high-temperature strength properties of intermetallics, occurring in relatively narrow compositional ranges around simple stoichiometric ratios, have long been recognized and attributed to long-range ordered superlattices. Aluminides are an important group of materials in this class. Alloy design work has been centered primarily on aluminides of nickel, iron, and titanium. Nickel aluminides are an important group of intermetallics have been used for since long as a base for alloy developments for high-temperature applications because of many attractive chemicals (e.g. high resistance to oxidation and corrosion), physical (e.g. high melting point), and mechanical (e.g. positive temperature dependence of flow strength) properties. However, they tend to be brittle, especially at low temperatures. Recently, considerable efforts have been devoted to improving the ductility of nickel aluminides at ambient temperatures by controlling microstructure and alloy additions (Matuschka, 1980; Cahn and Deevi, 1997; Kim, 1998).

Ni_3Al alloy is a new material that offers improved high-temperature properties over traditional ferrous and nickel-based hot-work die materials. Conventional hot-work die steels are based on the family of Cr–Mo–V tool steel, typical grades H1 and H13. The problem with these materials is that they rapidly lose strength and hardness at above 811 K and cannot sustain prolonged die surface contact during the hot forging of metals heated to 1089–1533 K. Nickel aluminide alloys provide improved strength, oxidation resistance, and thermal stability at these temperatures (Orth, 1997).

Boronizing is a thermochemical surface-hardening process in which boron atoms diffuse into a metal surface to form metal borides. The surface hardness of the resulting boride layer can exceed 2000 HV and has good resistance to abrasive and adhesive wear. In particular, surface hardening of steels by boriding treatments has found wide applications in industries (Matuschka, 1980; Tsipas. 1987; Palombariniand. 1993; Kim. 1998).

- Selection and peer-review under responsibility of the Organizing Committee of the Conference

Boronizing can be carried out in numerous ways, including gas boronizing, molten salt boronizing, with and without electrolysis, and pack boronizing (Tsipas,1987). Surface hardening treatments such as carburizing and nitriding of pure nickel is difficult because pure nickel has a very low solubility for carbon and nitrogen in the solid-state. The nickel alloys, which contain the nitride-forming elements such as Cr and Mo, are nitrided but the thickness of the nitrided layer is thin. On the other hand, boriding is appropriate for Ni because Ni can be easily borided and the boride layer is thick. The authors have reported their findings of boriding Ni using the fluidized bed method and powder pack method (Özbek et al., 2000; Ueda et Al., 2000; Anthymidis et al., 2002). Although studies have been done on the boriding of Ni, no investigation has been reported on the boriding of nickel aluminides. Alloying elements such as carbon, silicon, nickel, chromium, and manganese can influence the morphology, thickness, and nature of the boride layers consisting of either Fe2B or FeB or sometimes both formed in iron-based alloys (Keown and Pickering 1977; Tsipas, 1987). All these alloying elements, depending on their amounts, reduce the boride layer thickness and flatten the tooth-like morphology generally observed in ferrous alloys. There is little data available for the effect of alloying with aluminum on the properties of the boride layer. It has been reported that increasing aluminum content in steels decreases the boride layer thickness (Tsipas, 1987).

Method

The alloy Ni-40Al was prepared by electrical arc melting under argon atmosphere from nickel and aluminum of 99.9 and 99.7% purity, respectively (Fig.1). The samples were cast into molds with a nominal diameter of 8 mm. Surfaces of samples were ground with 1200 grit grinding paper and polished with 1 μm diamond paste before boriding process. Boriding was carried out in a solid medium consisting of Ekabor–Ni powders at 875 ^{o}C for periods of 2, 4, and 6 h.

The characterization of the boride layers formed on the Ni-Al substrates was confirmed by optical microscopy. Microhardness measurements of the boride layer were made to the center from surfaces of borided samples utilizing Vickers indenter with a load of 50 g. Averages of ten measurements were taken for each sample.

Figure 1. Vacuum arc melting furnace.

Results and Discussion

Optical microscopy cross-sectional examinations of the borided Ni and Ni-40Al samples showed that boride layers formed on the substrates had smooth morphology (Fig. 2). This morphology is different from the tooth-shaped form of carbon steels and low-alloy steels. In the previous works, it was reported that the tooth-like boride layer has strong bond to the base metal (Üçışık and Bindal, 1997; Yu et Al., 2002). During the boriding process, the majority of aluminum atoms diffused away from the surface into the matrix (Çelikyürek et Al., 2006). According to Ni-Al–B ternary phase diagram, up to 7–8 at. % aluminum dissolves in the boride phases. With increasing the amount of aluminum, Ni-Al–B compounds form (Villars, 995). In this situation, the boride layer and Ni-Al–B compound formed on the surfaces of the borided samples.

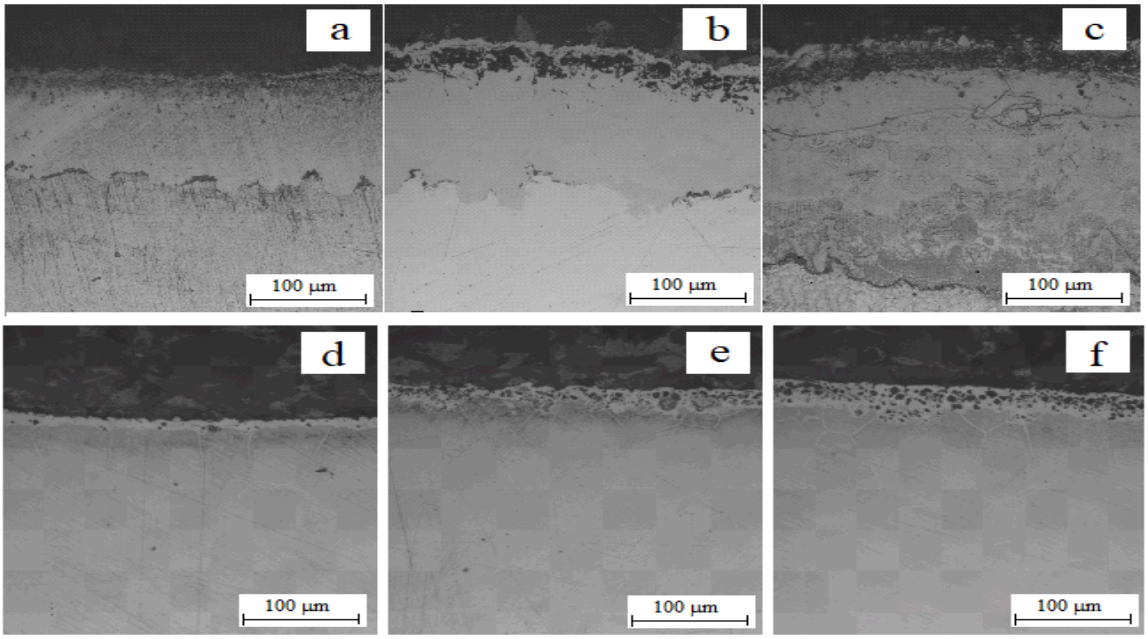

Figure 2. Optical micrographs of borided samples a) Ni-120 min. b) Ni-240 min. c) Ni-360 min. d) Ni40Al-120 min e) Ni40Al-240 min f) Ni40Al-360 min

The boride layer thicknesses of the borided samples were given in Fig 3. The boride layer thickness increased with increasing the boriding time. While the boride layer thickness was 120 µm for Ni at 2 hours, it was 245 µm at 6 hours. While the boride layer thickness was 13 µm for Ni40Al at 2 hours, it was 25 µm at 6 hours. Besides, the increase in boride layer thickness showed a parabolic tendency. The boride layer thicknesses were found to be decreasing sharply with the Al content increasing to 40Al for all boriding times. The diffusion of Boron atoms into Ni was more difficult due to an increase in Al content because Nickel boride has a limited solubility of Al atoms.

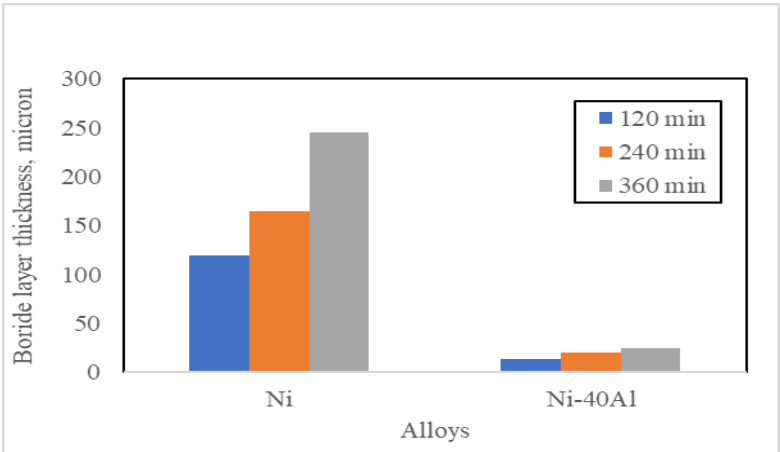

Figure 3. Boride layer thicknesses of the borided samples

In Figure 4a hardness values were shown for Nickel substrate, in Fig.4b the Ni-40Al substrates' microhardness values were given. From the figure it can be clearly seen that the hardness of boride layers formed on the surface of the borided samples was fairly high. The results of microhardness measurements showed that the microhardness values of boride layers were slightly increased with increase boriding time. Higher microhardness values were measured by Ni40Al alloy. The microhardness values were found 1235 HV for Ni and 1315 HV for Ni40Al. The reason for the increase in surface hardness is related to the B content in the Ni-B phase. If the quantity of Boron in Ni-B phases increases, the hardness of boride layer increases.

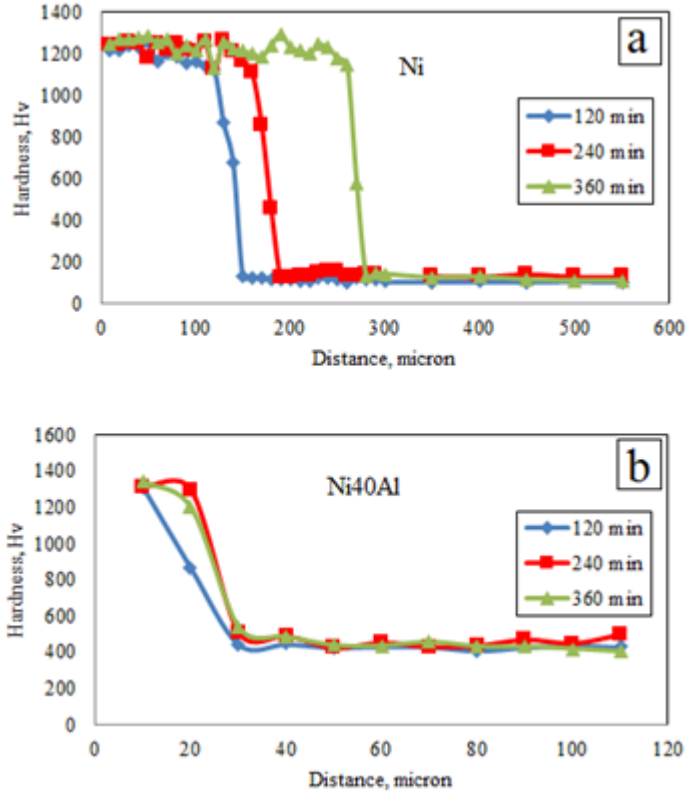

Figure 4. Microhardness values to the center from the borided samples. a) Ni b) Ni40Al

Conclusion

In this study, boriding of pure Ni and various Ni40Al alloys was carried out with Ekabor–Ni powders at 875 ^{o}C for various times. Depending on boriding time and alloy composition, the hardness of borides formed on borided nickel aluminide is between 1070 and 1315 HV while unborided Ni substrate is 380 HV. When the hardness of boride layer is compared with substrates, boride layer hardness is much higher than substrates. Compared with pure nickel, the diffusion of boron atoms into nickel aluminide is more difficult because of by significant migration of aluminum atoms into the substrate. As a result of this situation according to pure nickel, the thickness of boride layer formed on the surface of Ni-40Al alloy is much lower for all boriding times.

References

Anthymidis, K. G., Zinoviadis, P., Roussos, D., & Tsipas, D. N. (2002). Boriding of Nickel in a Fluidized Bed Reactor, *Mater. Res. Bull., 37*, 515-522.

Cahn, RW. In: Deevi, SC, S. V., & Maziasz, P.J. (1997). *International Symposium on Nickel and Iron Aluminides: Processing, Properties, and Applications: Proceedings from Materials Week'96,* 7-9 October 1996, Cincinnati Convention Center, Cincinnati, Ohio. ASM International (OH).

Çelikyürek, İ., Baksan, B., Torun, O., & Gürler, R. (2006). Boronizing of iron aluminide Fe72Al28, *Intermetallics 14*, 136-141.

Keown, S.R., & Pickering, F.B. (1977). Some aspects of the occurrence of boron in alloy steels. *Metal Science, 11*(7), 225-234.

Kim, YS, K. Y. (1998). Sliding wear behavior of Fe3Al-based alloys. *Mater Sci Eng A 258*, 319-324.

Matuschka, A.G.V., (1980). *Boronizing*. München, Wien: Hanser, p 100.

Ueda, N.,Mizukoshi, T., Demizu, K., Sone, T., Ikenaga, A., & Kawamoto, M., (2000). Boriding of nickel by the powder-packmethod, *Surface and Coatings Technology126* 25-30.

Orth, J.E., Maddox, C. C., G., Horax, D., Orillion, M.T., & Pyle, J. (1997*). Proceedings of materials week '96 on nickel and iron aluminides: Processing, properties, and applications*, Ohio, 7–9 October 1996, ASM International, USA, 1997, p. 377.

Özbek, I., Akbulut, H., Zeytin, S., & Bindal, C. (2000). The characterization of borided 99.5% purity nickel, *Surface and Coatings Technology*, *126*, 2–3, 166-170.

Palombariniand G, C. M. (1993). Influence of carbon on the chromium redistribution when boriding iron alloys. *J Mater Sci Lett.12*(11), 797-798.

Tsipas, D.N., & Rus, J. (1987). Boronizing of alloy-steels, *J Mater Sci Lett*, *6*(1), 118-120.

Ueda, N., Mizukoshi, T., Demizu, K., Sone, T., Ikenaga, A., & Kawamoto, M. (2000). Boriding of nickel by the powder-pack method, *Surface and Coatings Technology*, *126*, 25-30.

Üçışık, A.H., Bindal, C. (1997) Fracture Toughness of Boride Formed on Low-. Alloy Steels, *Surface Coatings*, and *Technology*, *94-95*, 561-565.

Villars, P. (1995). *Handbook of ternary alloy phase diagrams*, ASM International, Materials Park, OH. USA.

Yu, L.G, Khor, K.A, & Sundararajan, G. (2006). Boride layer growth kinetics during boriding of molybdenum by the Spark Plasma Sintering (SPS) technology, *Surface and Coatings Technology*, *157*, 2849-2853.

Author Information

Osman Torun
Afyon Kocatepe University
Technology Faculty, Department of Mechatronic Engineering
otorun@aku.edu.tr

İbrahim Çelikyürek
Eskişehir Osmangazi University
Department of Metallurgy and Materials Engineering

Bedri Baksan
Eskişehir Osmangazi University
Department of Metallurgy and Materials Engineering

The Eurasia Proceedings of Science, Technology, Engineering & Mathematics (EPSTEM)
ISSN: 2602-3199

The Eurasia Proceedings of Science, Technology, Engineering & Mathematics (EPSTEM), 2020

Volume 11, Pages 69-76

IConTES 2020: International Conference on Technology, Engineering and Science

Analysis of the Methods Used in Documentation of Historical Structures with Examples

Filiz KARAKUS
Yıldırım Beyazıt University

Abstract: It is of great importance to pass on the cultural and architectural heritage, which is an important link between us and the past, to future generations. It is very important to carry out documentation studies with correct and appropriate methods in order to carry out the repair and restoration of cultural assets in accordance with their original. In this study, the documentation methods of cultural heritage and the importance of the documentation process are emphasized. In the documentation phase and in determining the interventions to be made to the building, what studies were done and what kind of path was followed were tried to be explained with examples. Documentation of cultural and architectural heritage has different components and characteristics from urban scale to single building scale. Within the scope of this paper, the studies conducted on a single building scale were discussed. Before starting the restoration work of historical buildings, it is necessary to determine the current state of the building, that is to document it. The characteristics of the structure, whether there are cracks in the structure, the presence of a sign indicating that there is ground movement, material deterioration, and determination of previous restorations are of great importance in terms of documenting the structure. With this study, it is aimed to guide the experts working in the field of conservation.

Keywords: Cultural heritage, documentation, survey

Introduction

It has been acknowledged that cultural and architectural heritage should be preserved and documented in order to be passed on to future generations and to ensure its continuity. The success of the studies to be made and the intervention decisions to be made on conservation depends on the sensitivity of the documentation. As a result of the efforts to obtain the healthiest and most accurate information for the building or building groups during the documentation, important developments have been experienced in the documentation methods.

Significant progress has been made with the efforts made in the field of scientific and technology in the methods and techniques used in the documentation studies to be carried out to create a basis for the projects to be prepared for the restoration of registered immovable cultural assets. Along with the developing technology, contemporary documentation techniques have progressed quite rapidly. With these techniques, documentation of historical artifacts can be done more precisely and quickly.

The documentation phase of cultural assets should include the current state of the building, the carrier system and deterioration as well as material analysis. Research on the building should also include the repairs and interventions the building has undergone over time (Tucci: 2009). During the documentation phase, the information needed about the building can be obtained from old photographs, old projects, engravings, archaeological research and travel notes (Kuban: 2000).

In this study, first of all, the definition of the documentation was made and a research was made on the methods used in the documentation. Before making the decision to intervene in a building that qualifies as an immovable cultural property, the documentation studies that were made to form a basis for the restoration projects were examined with different examples and the preparation processes of the survey were discussed. The deterioration sheets of the investigated structures were examined, and the studies carried out while determining the problems and deteriorations in the structure were discussed.

Definition and Methods of Documentation

Documentation is the physical definition of a building, and the first step of this definition is the survey and photographic work. The analytical survey, which constitutes the second stage, includes the studies carried out to determine the structure of the building and the changes it has undergone, as well as the measurement of the building (Kuban: 2000). Documentation studies provide a basis for the preparation of restitution and restoration projects and are the first and most important step before intervention decisions are made.

Before starting the restoration of cultural assets, it is very important to determine the current state of the building. Historical research constitutes the first step of the determination phase regarding the building. At this stage, literature and archive research related to the historical structure is made, written and visual documents are used. Another step of the determination phase is the preparation of the survey projects. These projects consist of the site plan, floor plans, section, facade and architectural elements in 1/100, 1/50, 1/20 and 1/5 scales according to the characteristics of the building. During the preparation of the survey projects, it is also necessary and important to prepare reports containing the architectural and art history features of the building. It is preferred to carry out photographic examination together with the survey drawings, it is important to mark the place and directions of the photographs on the plan.

As part of the survey projects, structural and material deterioration and originality analyzes should also be made. During the examination of the bearing system and the deterioration of the structure, issues such as plumb line deviation, settlement, collapse are an important part of the examination. If the movement in the structure is still continuing, it is necessary to follow the changes, movements and deformations in the cracks within a certain period (Croci: 1998). It is extremely important to determine the mechanical, physical and chemical properties of the materials such as stone, brick, wood, mortar, plaster that make up the structure in order to determine the interventions to be made.

Documentation is a process in which experts from many disciplines can work together and contribute. It is important that the people in this team have sufficient knowledge and awareness of the methods to be applied. The people in the team should be in cooperation and harmony, they should work together in the development of the methods used in the implementation process (Bohler: 2005).

In the survey measurements, traditional techniques and methods can be used as well as advanced documentation methods. When traditional methods such as triangulation, vertical coordinates and grids are used, instruments such as tape measure, plumb line, compass, range pole, mira, leveling instrument and theodolite are used. In advanced documentation methods, tacheometric and laser measuring instruments (laser meters, protractors, advanced levels, advanced theodolites, total station), GPS, laser scanning and photogrammetry are used (Uluçpakben: 2013). With the developments in the field of technology, traditional methods leave their place to modern methods in the acquisition of survey measurements. It is faster and easier to take measurements and make drawings with modern methods. In addition, more accurate and more precise information can be obtained with these methods. Since traditional methods are not sufficient in the certification stage of large-scale and complex functional buildings suc h as castles, palaces and inns, advanced documentation methods are preferred and sometimes different techniques are used together.

With the development and widespread use of computer technology, the use of local photogrammetry in the architectural field has increased. With this method, it is aimed to obtain information about the visual data of an architectural object, geometric definition of this object, the size, shape, texture properties of this object and also its planar properties by using photographs (Güleç:2007; Korkmaz:2011). Terrestrial photogrammetry is a method that enables the creation of two-dimensional drawings and three-dimensional models after the necessary procedures from photographs taken with the aid of a camera from close or far distances (Güleç: 2007).

Laser scanners provide more accurate results than many photogrammetric methods (Almagro: 2007). Two methods are used to obtain three-dimensional modeling from the point cloud obtained by laser scanners. In the first method, geometric shapes in the point cloud are automatically corrected and modeled. In this method, the data occupies less space and is a less costly method. In the second method, mesh models of more complex geometry shapes in the point cloud are created. In this method, the data take up more space and it is a more costly method (Chevrier, 2008).

In this method, the system converts the three-dimensional point coordinates obtained by laser beams sent to the object to be measured into digital data. These data are transferred to the drawing environment on the computer, and the point cloud records obtained with 360 ° rotating camera angles are transferred to microstation and

similar programs and the point data is transformed into digital data. Then these data are transferred to the CAD environment to be drawn in the technical drawing environment. With the help of the views obtained through photographic pictures recorded in digital environment, floor plans, facade and sections of the building can be obtained (Uzun, 2019).

Examination of the Documentation Phase on the Examples

The terrestrial photogrammetry method is used for the surveys of detailed and embroidered sections, especially in historical buildings. Within the scope of this study, applications in the process of documentation of immovable cultural property buildings are discussed.

Çankırı Buğdaypazarı Mosque

The Buğdaypazarı Mosque, located in the Center of Çankırı, is located in the same courtyard with the Buğdaypazarı Madrasa. The survey, restitution and restoration projects of the mosque were drawn by Mithat Zafer Architecture Office. For documentation, FARO FOCUS X330 laser scanner with NIKON D80 camera, GPS, Altimeter, Inclinometer, compass sensors and capable of measuring 122,000, 244,000, 488,000 or 976,000 points per second was used. For the drawing of the details, sketches were made and the measurements were taken on site with a tape measure and profile comb. 2056 photographs were taken to cover all points of the building. Laser scanning was done in color and black and white at 120 points and processed and combined with FARO SCENE software.

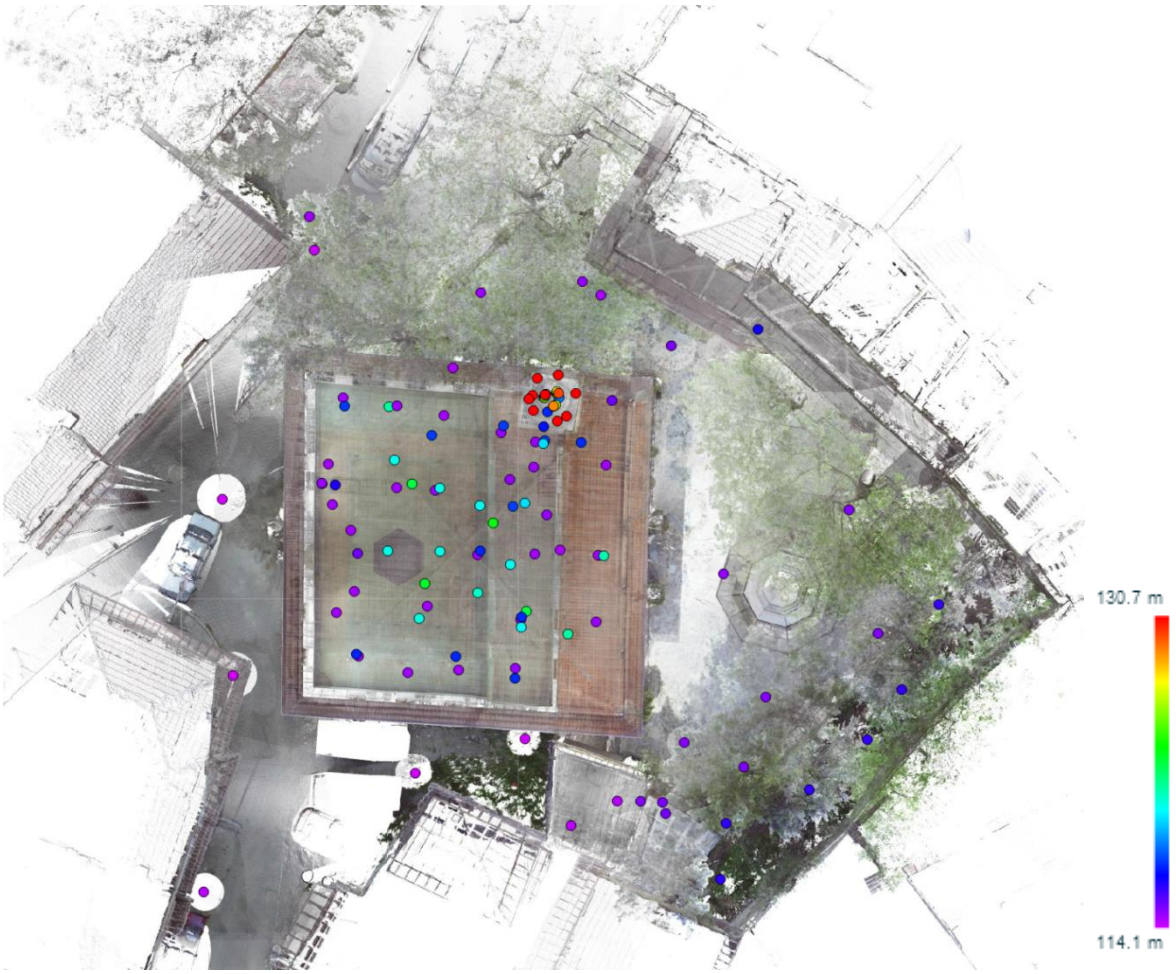

Figure 1. Points read with a laser scanner

The combined point clouds were transformed into drawings in Autocad. For the decorations on the ceiling, orthographic photographs were obtained by wearing photographs on the point cloud and detailed drawings were

made on them. Among the photographs taken, the ones to be used in the album are numbered and shown on the key plan together with the shooting directions. At the stage where the measurements were taken and the drawings of the building were made, written and visual documents related to the building were reached and archive research was conducted. Based on these, an art history report of the building was prepared.

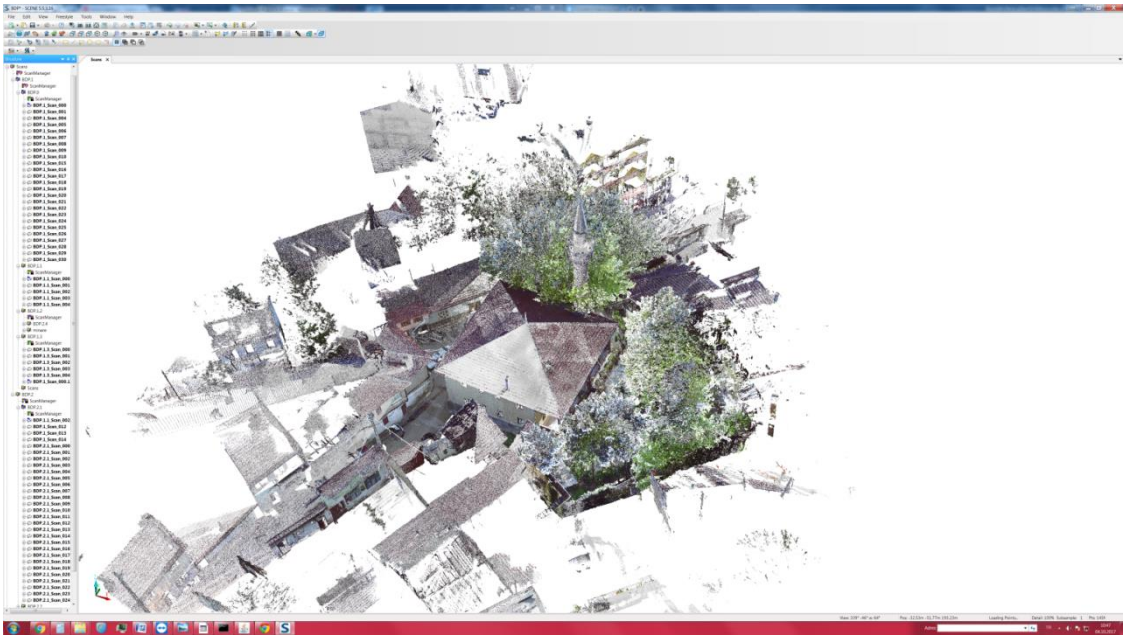

Figure 2. The combined point clouds are transformed into drawing

The deterioration and damage in the building; Structural Distortions, Material Distortions, Color Changes and Unqualified Interventions were examined and worked on the Survey Distortion Sheet. Types of deterioration in the building are determined as "Plaster Crack", "Deflection", "Fibrillation", "Planting", "Oil Paint Applications", "Cement Based Material Use", "Incompatible Material Use" and "Repairs Made with Current Materials". The interventions to be made to the building in line with the detected deteriorations and problems were determined and accordingly, restoration projects were prepared.

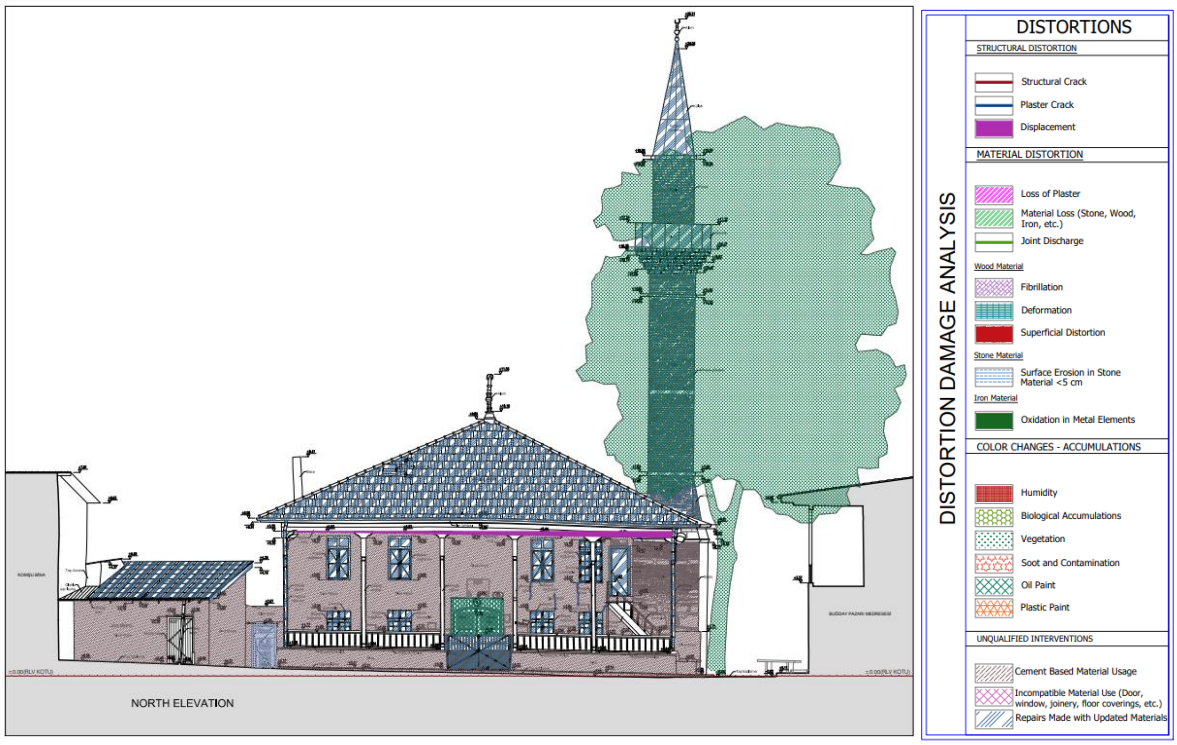

Figure 3. Layouts prepared in line with the detected deterioration and problems for Buğdaypazarı Mosque

Ankara- Altındağ Arslanhane Mosque

Arslanhane Mosque, located in Altındağ District of Ankara, is one of the most magnificent examples of the Anatolian Seljuk Period mosques with wooden posts and wooden ceilings. The walls of Arslanhane Mosque were built with a masonry system and the wooden ceiling is carried by 24 wooden columns. Rubble stone, spolia material, bricks and wooden beams were used in the main walls of the building. The survey, restitution and restoration projects of the mosque were drawn by ANB Mimarlık İnşaat ve Ticaret Limited Şirketi. During the documentation phase, advanced documentation methods and traditional methods were used together. Historical research reports were prepared in coordination with the measurements. When the building was measured with a laser scanner and the survey drawings were made, it was determined that the columns carrying the roof were offset by 10-30 cm in the vertical axis and deflection in the ceiling beams. In addition, it has been observed that the moisture problem arising from the rain water that cannot be evacuated on the roof and the materials used in old dated repairs also cause problems in the building. In order to detect these problems, Infrared Thermal Imaging and Mortar and Plaster Analyzes regarding the superstructure were carried out by the METU Material Protection Laboratory. Infrared thermal images clearly show damp areas caused by faults in the roof drain assembly. In the infrared thermal images, the humidity problem rising from the bottom to the top of the building walls is also clearly seen.

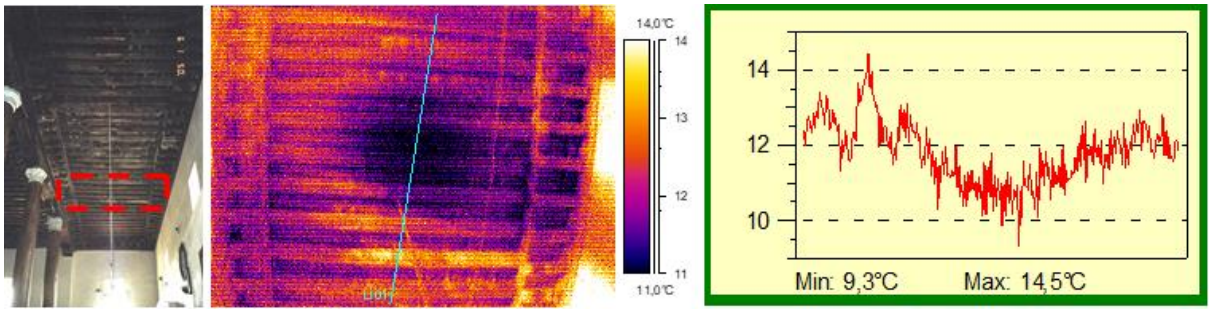

Figure 4. Wooden ceiling infrared thermal image and wood temperature curve

From the temperature curve showing the infrared thermal image of the area in the frame and the heat distribution on the wooden ceiling, we see that the temperature difference on the wooden ceiling surface reaches up to 5 C. This indicates that the cold area is wet and there are moisture problems in the ceiling caused by problems in the roof drainage system (Saltık:2008). For the definition of historical building materials, physical properties of unit weight and porosity are determined. As a result, it has been observed that the mortars have high porosity (31% - 60%) and low unit weight (1.16 g / cm3 - 1.42 g / cm3). Thin sections of some mortar and plaster samples taken from Arslanhane Mosque were prepared; mineralogical and petrographic definitions of aggregates and properties of binder materials.

Figure 5. Lime mortar between wood and bricks on the steps of the minaret (left)

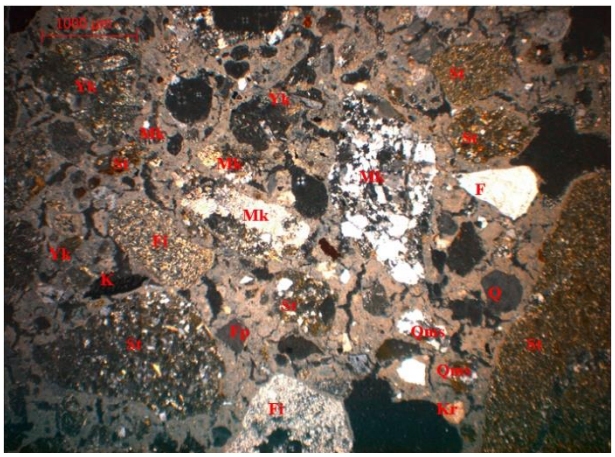

Figure 6. Thin section view of the inter-brick mortar sample (AC12) from the minaret F: Feldspar, Yk: Surface Rock Fragment, Mk: Metamorphic Rock Fragment, St: Siltstone, K: Coal fragment, Qms: Quartz-mica-schist, Fi: Fillite, Q: Quartz, Fp: Plagioclase feldspar, Kr: Limestone.

As a result of these analyzes and examinations, the problems in the structure were determined more accurately and solution suggestions were made. In addition, the content of mortars and plasters to be used in repairs was determined in line with the material analysis made. Based on these documentation studies, intervention decisions were made and restoration projects were prepared accordingly.

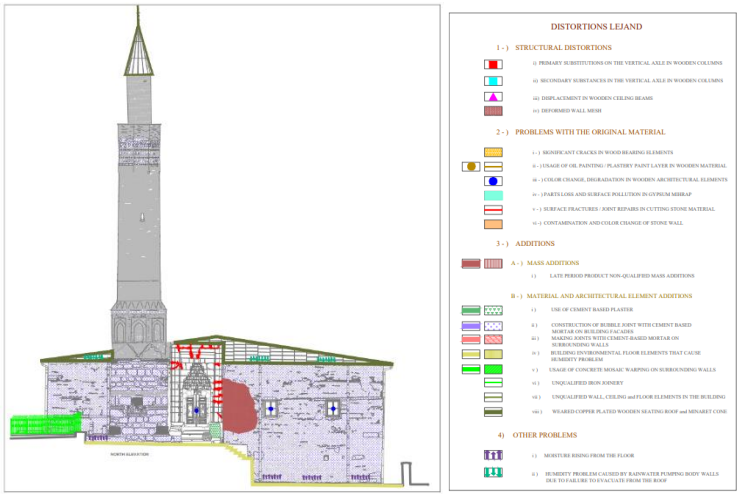

Figure 7. Layouts prepared in line with the detected deterioration and problems for Arslanhane Mosque[1]

Bolu-Gerede Aşağıovacık Village Mosque

Located in Bolu Province, Gerede District, Aşağıovacık Village Mosque was built by Sultan Abdulhamid II in H. 1309 / AD 1891-1892. It was understood that Hacı Habib Efendi, who was the chief carpenter of Sultan Abdülhamid, was built as a gift in his village upon his superior services and request. In a document dated 1903 in the Archives of the General Directorate of Foundations, it is seen that the name of the building is "Hamidiye Câmi-i Şerif". The survey, restitution and restoration projects of the mosque were drawn by Erk Architecture Office. Studies to document the current state of the building were carried out in two different digital media, namely “laser scanner and photo-video shooting”. The current state of the building, its material and structural features, problems in the structure (types and reasons of material deterioration, structural problem, etc.) and the interventions of the building have been determined. Studies for the documentation of the current situation were completed as a result of the work of a team consisting of architects, art historians, civil engineers and restoration experts. Every bit of information obtained during the survey, restitution and restoration works formed the data (basis) of the next stage. In order for the project to achieve its goals, it was concluded by following the method of completing all phases in a healthy way and transferring the information between the phases correctly.

Conclusion

Keeping the cultural and historical values that make up the historical environment alive and transferring them to the next generations with their unique characteristics is one of the most important problems in the field of conservation. In our country, which carries the traces of various civilizations, it is very important to protect and restore the rich architectural heritage that has survived until today. For this reason, it is necessary to document this heritage and to use the correct methods during the documentation phase. With the developing technology, many advanced documentation methods and devices have started to be used apart from traditional methods. It is of great importance to select the appropriate ones among these methods and to work together from different disciplines on the subject. The correctness of the work done during the documentation phase ensures that the intervention decisions are healthy.

It has been observed that the use of the terrestrial photogrammetry method, whose area of use has expanded and become widespread with the developing technology, is a more economical and easy method in terms of time to make survey measurements, and it is more accurate and accurate results can be achieved compared to other methods.

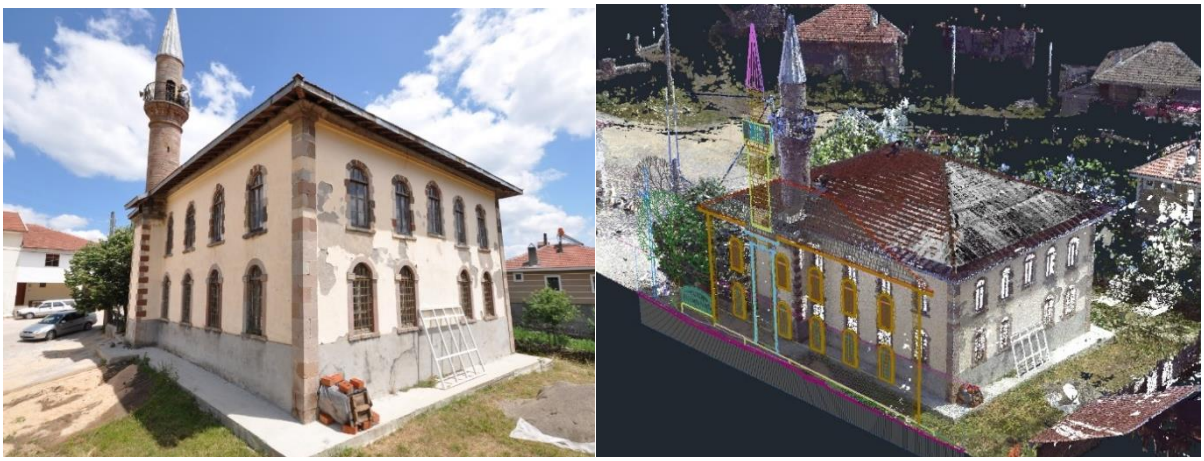

Figure 8. Hamidiye Mosque, northwest view and orthophoto view

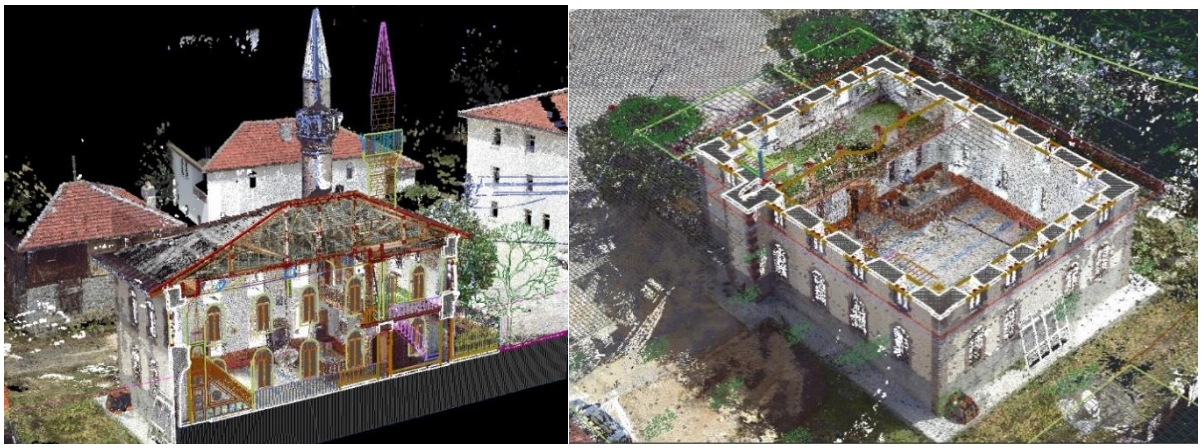

Figure 9. Hamidiye Mosque, section and plan orthophoto views

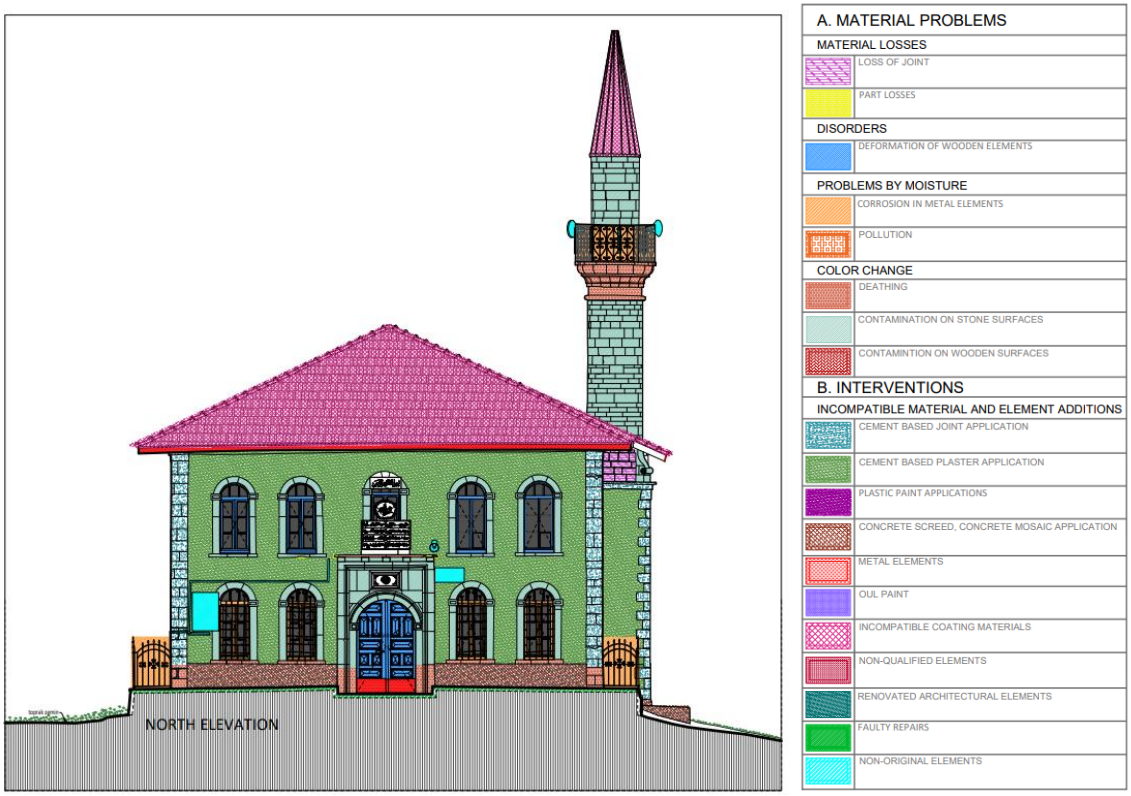

Figure 10. Layouts prepared in line with the detected deterioration and problems for Hamidiye Mosque

References

Almagro A., Vidal, A., (2007, October 01-06). Traditional Drawings versus New Representation Techniques, *XXI International CIPA Symposium* , Athens, Greece.

Boehler, W., (2005, May 22-27). Comparison of 3D scanning and other 3D measurement techniques, Proc. *International Workshop on Recording, Modeling and Visualization of Cultural Heritage*, (Centro Stefano Franscini, Monte Verità, Ascona, Switzerland.

Chevrier C. , Perrin J.P., (2008). Laser Range Data, Photographs and Architectural Components, *Commission V,WG V/2 The International Archives of the Photogrammetry, Remote Sensing and Spatial Information Sciences*, Vol. 37. Part B5. Beijing.

Croci, G., (1998). *The Conservation and Structural Restoration of Architectural Heritage*, UK and Boston, USA, Computational Mechanics Inc.

Güleç, S., A., (2007). *Yersel Fotogrametri Yöntemi ile Rölöve Alım Tekniğinin Taç Kapılarda Uygulanışı Konya Örnekleri*, (Yayınlanmamış Yüksek Lisans Tezi), Selçuk Üniversitesi, Fen Bilimleri Enstitüsü, Mimarlık Ana Bilim Dalı, Konya.

Korumaz, G., A., & Dülgerler, O., N., (2011). Kültürel Mirasın Belgelenmesinde Dijital Yaklaşımlar, *S.Ü. Mühendislik-Mimarlık Fakültesi Dergisi, 26*(3), p.67-83.

Kuban, D. (2000). *Tarihi Çevre Koruma ve Onarımın Mimarlık Boyutu Kuram ve Uygulama*, İstanbul, Yapı Endüstri Merkezi.

Pakben, U., (2013). *Tarihi Yapıların Rölöve ve Analizlerinde Kullanılan İleri Belgeleme Teknikleri*, (Yayınlanmamış Yüksek Lisans Tezi), Dokuz Eylül Üniversitesi, Fen Bilimleri Enstitüsü, Mimarlık Anabilim Dalı, İzmir.

Saltık, E. C., Tavukçuoğlu, A., & Akoğlu, K. G., (2008). Aslanhane Camii Kızılötesi Isıl Görüntüleme ve Harç ve Sıva Analizleri Ön Çalışmaları, *ODTÜ Malzeme Koruma Laboratuarı, Ankara Vakıflar Bölge Müdürlüğü Arşivi*, 5-12.

Tucci, G., Bonora, V., Crocetto, N., Nobile, A., (2009, October 11-15). New Technologies for Surveying Building Ruins, *CIPA 2009 XXII International Symposium, Digital Documentation, Interpretation & Presentation of Cultural Heritage*, Kyoto, Japan.

Uzun, T., İ., Spor, Y. (2019). Yersel Lazer (Nokta Bulut) Tarama Yöntemi ile Rölöve-Restitüsyon-Restorasyon Projesi Hazırlama Süreci ve Bir Örnek: Elazığ Harput Kale Hamamı, *Tasarım Kuram*, *15*(28):1-26.

Author Information

Filiz Karakuş
Yıldırım Beyazıt University
Esenboğa Külliyesi Mimarlık Fakültesi D Blok Çubuk
ANKARA
Contact e-mail: *ferdemir06@gmail.com*

The Eurasia Proceedings of Science, Technology, Engineering & Mathematics (EPSTEM)
ISSN: 2602-3199

The Eurasia Proceedings of Science, Technology, Engineering & Mathematics (EPSTEM), 2020

Volume 11, Pages 77-88

IConTES 2020: International Conference on Technology, Engineering and Science

Evidence of Combined Site Effects and Foundatıon-Soil-Structure Interaction Effects on Seismic Response of Rc Buildings

Mohamed BENELDJOUZI
University of Science and Technology Houari Boumediene

Mohamed HADID
National High School of Public Works

Nasser LAOUAMI
Earthquake Engineering Applied Research Centre

Abstract: The seismic excitation experienced by structures is a function of earthquake source effects, travel path effects, local site effects, and soil-structure interaction (SSI) effects. SSI effects related to variation of the structural behavior recently became a common practice in structural seismic design. Building seismic codes usually consider site effects through site factors, which reflect amplification of seismic waves due to the change in the geological contrast. For seismic structural analysis purposes, however, they consider the assumption of a fixed base, where, the input motion at the base of the structure is taken as equal to the free field ground motion. This paper investigates, in a rational way, the influence of kinematic and inertial SSI effects combined to local soil conditions effects on RC multistory buildings, resting on different design sites, through a global explicit transfer function for lateral component of the response. It comes from the combination of the transfer functions of structure, foundation and soil. It was found that the approach allows capturing the realistic physical fluctuations of the rock input motion before it excites the superstructure.

Keywords: Soil-structure interaction, Site effects, Transfer function, RC buildings

Introduction

Most civil engineering structures involve direct contact with the ground. When subjected to earthquake ground motions, structures responses and ground displacements are dependent of each other. The seismic waves excite the structure, which in turn, modifies the input (free field) ground motion. This difference in ground motion is due to interaction between the foundation, geological backgrounds underlying and surrounding the foundation and the superstructure.

The seismic excitation experienced by structures is a function of earthquake source effects, propagating path effects, local site effects, and soil-structure interaction (SSI) effects. The latter result due to the presence of the foundation and its flexible supports. In seismic structural design, it is usually needed to provide engineers by effective input motion which refer to rock acceleration records. However, because of its extremely high stiffness, firm-to-rock soils underlying the ground surface constrain the rock motion to be very close to the free field motion. Structures founded on soils of such a nature are considered as having a fixed base, conversely, in the case of soft soil deposits, the foundation motion will usually deviate from the free field motion. This deviation is governed by the transfer function (TF) of the soil deposits and foundation system.

SSI effects produce kinematic interaction effects related to the inability of foundation to follow ground motion due to its greater stiffness, and inertial interaction effects caused by the existence of structural and foundation masses. Almost, all proposed SSI modeling approaches deal separately with kinematic and inertial interaction. Wu (1992) analysed distinctly the effects of kinematic and inertial interaction effects for simple structures supported by rigid rectangular foundations and excited by representative earthquake ground motions.

- Selection and peer-review under responsibility of the Organizing Committee of the Conference

Zania and Tsompanakis (2009) studied the effects of soil conditions and inertial SSI on dynamic response and stability of earth structures. Recently, Sayyadpour and Behnamfar (2016) investigated the inertial SSI effects on non-linear response of steel buildings built on different soil conditions. Several other studies (Lin and Miranda, 2008; Karapetrou *et al*., 2015) dealing with SSI effects adopted the same approach, which is unable to consider the combined effect of both phenomena, as it happens in real cases.

In this study, the problem of site effects combined to both kinematic and inertial SSI effects and their influence on reinforced concrete (RC) buildings is addressed through a global TF. The TF is a mathematical mean governing the input/output relationship of a physical system in the frequency domain. The global TF results from a simple multiplication in the frequency domain of site, foundation and structure TFs. The expected roof-level structural response could, therefore be captured through the combination of the rock motion with the global TF. The study will conducted on typical multistory buildings founded on sites classified according to the Algerian Seismic Resisting Rules (RPA99, ver 2003, simply referred below by RPA99). Appropriate selection of building types relative to their weight and stiffness properties may well highlight combined kinematic and inertial SSI effects.

RPA99 SSI Effects and Site Effects Consideration

The northern part of Algeria is a moderate to strong seismic region, as evidenced by recent seismic risk studies (Benouar 1994, Bouhadad and Laouami 2002), where, many sites show geotechnical, topographic and geological conditions leading to the appearance of local effects (Laouami et al., 2006, Laouami and Slimani, 2013). In RPA99, the amplification phenomenon is indirectly considered through normalized response spectra corresponding to four soil categories (Table 1). For site and SSI effects consideration, RPA99 simply recommend specific and additional investigations. Beneldjouzi and Laouami (2015) proposed a novel method for modelling site effects based on a mean TF for each RPA99 site class. The proposed TFs can be used to make an appropriate site classification and reasonable estimation of site amplification potential (fig. 1).

Study purpose

For seismic structural design purposes, most building seismic codes assume the hypothesis of a fixed base corresponding to a rock site. They also provide mean site factors associated with average design response spectra. Site factors (Beneldjouzi and Laouami, 2015; Beneldjouzi et al., 2017) reflect the amplification of seismic waves due to the change in the geological contrast between the bedrock and sedimentary material deposits. In the case of loose soil deposits, this amplification is partially reduced by the SSI effects. Indeed, because of presence of the foundation rigid bodies, retransmission of a part of the seismic energy from the structure to the ground is produced due to radiative damping at the soil-foundation interface. The nature of soil deposits will affect the dynamic properties of the soil-foundation-structure system because of additional flexibility.

Contemporary seismic codes (IBC 2012, ASCE 7-16, Eurocode8...) propose formulas for period and damping ratio lengthening in the case of a flexible base, but the latter do not allow capturing the effective properties of the seismic motion at the base of the structure. A good assessment of soil motion should implicate understanding all fluctuations to a suitable level of detail, in order to identify the expected structural response and the associated seismic damage.

The objective of this study is to highlight the combined site effects and SSI effects on the response of typical RC buildings founded on regulatory sites. Algerian regulatory considerations about site conditions are mainly pointed in this study. To this purpose, the methodology proposed by Beneldjouzi and Laouami (2015) is considered. Following this methodology, an average transfer function performed over a wide sample of 1-D soil profiles has been proposed for each soil type, based on a stochastic simulation approach. A probabilistic model using the random field theory allowed generating the bounded SW velocity values in each layer of any profile, in agreement with RPA99 requirements. The same 1-D profile simulation results are used in this study, with the only difference that they deal with the corresponding equivalent one layer soil profiles, obtained through the average SW velocity from the multi-layer profiles over a depth of 30 m. Only equivalent linear TFs are used herein to emphasize seismic behavior of the considered RC buildings.

Building Types and modeling

To ensure an adequate lateral load carrying capacity, resisting moment frames associated with bidirectional RC shear wall systems are an effective solution for multi-story RC buildings introduced within the revised RPA99. Currently, that is the most common construction system in Algeria, recognized economically viable and technically easy. The studied buildings are within that construction system and are of substantially symmetrical geometry. To meet requirements of RPA99, the buildings are of mixed structural system (shear wall associated with moment frames), with RC stairs and fillings of hollow brick masonry (fig. 2). They stay on raft foundation and have one basement floor, ground floor plus three floors (R+3) and seven floors (R+7), respectively. Floors and roof are of two-way solid RC flat slab. The basement floor's and floor's highs are of 3m and 3.06 m, respectively. This choice reflects the wish to target a specific natural frequency values characterizing buildings ranging from rigid to flexible. The dimensions of the structural elements in both directions are given in Table 3. It is well established that SSI effects are particularly strong for a rigid building based on a flexible support, whereas they are less obvious when the soil loses flexibility and becomes stiffer. Several authors, (Stewart et al., 1999, among others), consider that structures of multi-story buildings having predominant fundamental mode can be studied as a 1 degree of freedom (D.O.F) systems with the properties (mass, stiffness, frequency and eigen mode) of the first mode (fig. 5). A fixed base modal analysis allowed extracting the properties of the fundamental mode for the studied buildings (Table 4), to be used in flexible base buildings analysis.

.

Table 1. RPA99 site categories

Site type	Geotechnical description	Mean value of V_s (m/s)
S1	Rock site:	
	Rock or other similar geological formation	$V_s \geq 800$
S2	Stiff site:	
	Deposits of dense sand, gravel and/or over consolidated clay with 10 to 20 m thickness	$V_s \geq 400$ From 10 m depth
S3	Soft site:	
	Deep deposits of medium dense sand, gravel or medium raid clay	$V_s \geq 200$ From deep of 10 m
S4	Very soft site:	
	Deposits of releases sand with/without presence of soft clay layers	$V_s \geq 200$ In the firsts 20 m

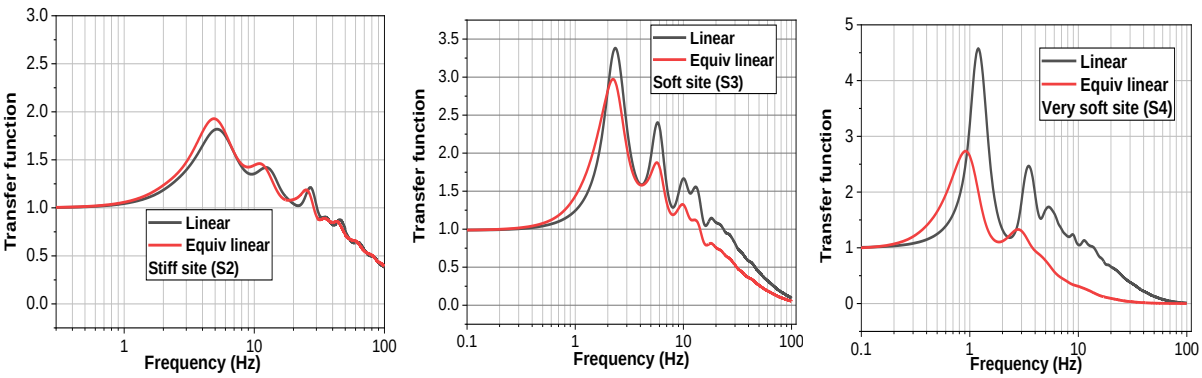

Figure 1. Mean transfer functions for RPA99 seismic site classes from Beneldjouzi and Laouami (2015). Mean transfer functions were performed for linear and equivalent linear cases. In this study, we deal with equivalent linear transfer functions to emphasize seismic behavior of RC buildings.

Methodology

The simulated multilayer soil profile are all representative of RPA99 site classes in terms of average V_s values and thicknesses of the different soil layers. Except for the S1 site representing the rock site (Table 1), the deterministic TF is calculated for the equivalent one layer profile in the linear case. To agree with requirements of the seismic design, soil nonlinearity should be considered, since it is commonly accepted that soil deposits behave non-linearly under strong seismic motions near the soil surface. The mechanical properties associated with dynamic loading are the SW velocity, V_s (or the shear modulus, G), the damping ratio, β and the Poisson's coefficient, v. The variation of dynamic properties (mainly G and β) is governed by intermediate to high

deformation levels (10^{-2} ~ 5%), which generally originate as a result of medium to high seismic stresses. In this study, the dissipative character is considered as an approximation of the soil nonlinear response.

Figure 2. 3D FE models of the studied buildings made with CSi SAP2000 ver 15

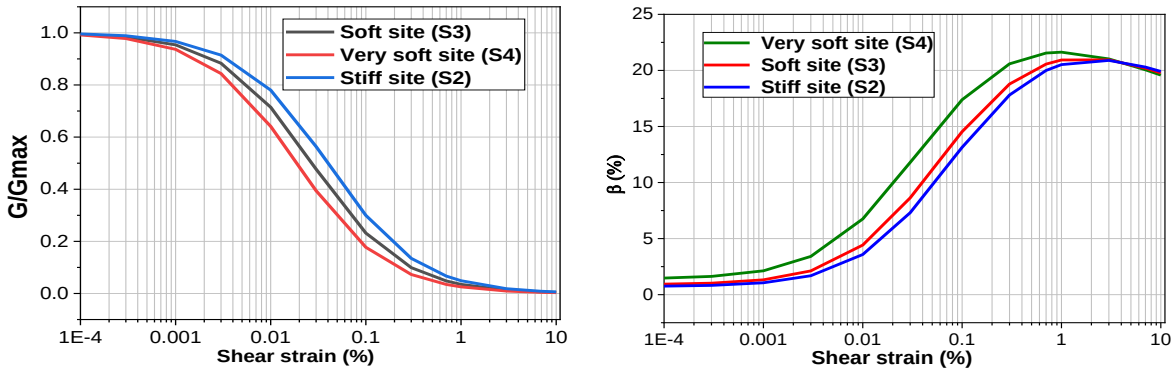

Figure 3. Small strain shear modulus reduction curve and damping ratio increasing curve of sites considered in this study performed according to Seed and Idriss (1970)

1-D equivalent linear analysis conducted by a developed computer program led to modified G and β values, based on decreased G and increased β reduction curves selected to this end (fig. 3). G and β reduction curves (Fig. 3) were made following the Seed and Idriss (1970) variation curves, as no data on G and β variations are available for the regulatory sites. These reduction curves were taken from the literature (Seed and Sun, 1989) and were selected according to the dissipation level which varies following the soil mechanical properties of the considered sites.

Following the Allison et al., (1994) methodology (eqts. 3-9), the equivalent linear TF of each soil profile is combined first to the structure's TF, then, the resulting one is combined to inertial effect TF and, finally, to inertial and appropriate kinematic TF to obtain global TF including site effects and both kinematic and inertial SSI effects. In all cases, a mean TF for lateral response is obtained by averaging combined TF of the simulated soil profiles over the whole considered frequency range.

Foundation stiffness and damping

Impedance functions represent the frequency-dependent stiffness and damping characteristics of soil-foundation system. Solutions for the complex impedance function proposed by Pais and Kausel (1988) are used:

$$K_j^d = K_{j/e}^s (k + ia_0 c) \tag{1}$$

$$K_{j/e}^s = K_j^0 \alpha_j \eta_j \tag{2}$$

where, K_j^d, is the dynamic impedance function for *j* mode; $K_{j/e}^s$, is the static impedance along *j* direction for a circular foundation of *R* radius and with *e* embedment, resting on an homogenous soil layer of h_f depth. $K_{j/e}^s$ is a function of the static stiffness K_j^0, for a rigid foundation on a semi finite medium. k, is a term of static stiffness depending on the dimensionless frequency: $a_0=\omega R/V_s$; with ω, the circular frequency; V_s, the SW velocity in the soil layer and *R*, the foundation radius. *c*, is the damping factor. α_j and η_j are the stiffness modifiers referring, respectively, to dynamic effect and embedment foundation. Elsabee and Morray (1977) and Kausel (1974) proposed solutions for static stiffness modifiers as given in the table 3, where, *G* is the complex shear modulus: $G=G_0(1+2i\beta)$, where, G_0 stands for the reduced small strain shear modulus with increasing shear strain. *e* is the foundation embedment depth and *v*, the soil Poisson's ratio.

Table 2. Dimensions in Cm of building's structural element

		R+3	R+7	
Element		stories 1-4	stories 1-4	stories 5-8
Column	C1 (*axb*)	40x40		40x40
	C2 (*axb*)		50x50	
	C3 (*axb*)			
Beam	b (*bxh*)	30x40	30x40	30x40
Slab	D (*e*)	16	16	
Wall	W (a_w)	20	20	
E(MPA)	32000			
ν	0.3			
ρ_c(t/m^3)	2.5			

Seismic Response of Multistory RC Buildings Considering Soil-Foundation-Structure Interaction

Unlike buildings on fixed base, flexible base has an obvious effect on the buildings seismic behavior and offers a prominent reduction in the internal forces produced within the superstructure. The equations of the dynamic equilibrium of the above 1DOF representative system are written as follows:

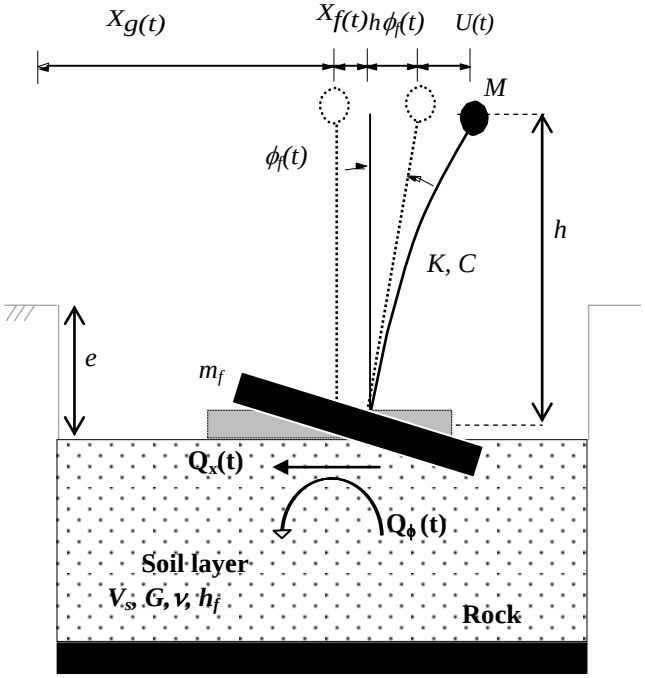

Figure 4. Simplified modelling of coupled dynamic soil foundation–structure system for horizontal and rocking motions with characteristics *K, C, M* and *h* of the first mode. V_s, *G*, ν and h_f stand, respectively, for SW velocity, shear modulus, Poisson's ratio and thickness of the soil layer. Q_x and Q_ϕ are, respectively, the shear force and the overturning moment at foundation-soil interface. *e*, is the foundation embedment.

Table 3. Static stiffness formulas with the corresponding dynamic modifiers from Kausel (1974) and Elsabee and Morray

Degree of freedom	Static stiffness	Soil stiffness modifire	Embedment stiffness modifire	Radiation damping
Translation along x axis	$K_x^0 = \frac{8GR}{(2-\nu)}$	$\alpha_x = (1+\frac{1}{2}\frac{R}{h_f})$	$\eta_x = (1+\frac{2}{3}\frac{e}{R})(1+\frac{5}{4}\frac{e}{h_f})$	$c_x = \begin{cases} \frac{0.65\beta_s\xi}{1-(1-2\beta_s)\xi^2} \text{ if } \xi = \frac{a_0}{a_{01}} \le 1 \\ c_x' \text{ if } a_0 > a_{01} = \left(\frac{\pi}{2}\right)\left(\frac{R}{h_f}\right) \end{cases}$ $c'_x = \frac{\pi\left(1+(1+\alpha)\frac{e}{R}\right)}{K^s_{x/e}/GR}$ $\alpha = \frac{V_P}{V_S} = \sqrt{\frac{2(1-\nu)}{1-2\nu}}$; $k_x=1$
Rocking about y axis	$K_\phi^0 = \frac{8GR^3}{3(1-\nu)}$	$\alpha_\phi = (1+\frac{1}{6}\frac{R}{h_f})$	$\eta_\phi = (1+2\frac{e}{R})(1+0.7\frac{e}{h_f})$	$c_\phi = \begin{cases} \frac{0.5\beta_s\xi}{1-(1-2\beta_s)\xi^2} \text{ if } \xi = \frac{a_0}{a_{01}} \le 1 \\ c_\phi' \text{ if } a_0 > a_{02} = a_{01}\frac{V_P}{V_S} \end{cases}$ $c'_\phi = \frac{\pi\left(\frac{\alpha}{4}+\frac{e}{R}+\frac{(1+\alpha)}{3}\left(\frac{e}{R}\right)^3\right)\frac{a_0^2}{b+a_0^2} + 0.84(1+\alpha)\left(\frac{e}{R}\right)^{2.5}\frac{b}{b+a_0^2}}{K^s_{\phi/e}/GR^3}$ $k_\phi = 1-\frac{0.35a_0^2}{1+a_0^2}$ $b = \frac{2}{1+e/R}$

$$\ddot{U} + 2\xi\omega_0\dot{U} + \omega_0^2 U = -(\ddot{X}_f + h\ddot{\phi}_f)$$

$$(3)\, m_f\ddot{X}_f + M(\ddot{X}_f + h\ddot{\phi}_f + \ddot{U}) + Q_x(t) = 0 \tag{4}$$

$$I_f\ddot{\phi} + Mh(\ddot{X}_f + h\ddot{\phi}_f + \ddot{U}) + Q_\phi(t) = 0 \tag{5}$$

where, M and m_f are the masses of the superstructure and the foundation, respectively, I_f, is the moment of inertia of the foundation with respect to its horizontal axis, $Q_x(t)$ and $Q_\phi(t)$ are the Shear force and the overturning moment at the soil-foundation interface. $\omega_0 = \sqrt{K/M}$, is the fundamental circular frequency of the structure, $\xi = C/2M\omega_0$, is the damping ratio of the structure. Assuming that the excitation and the responses induced by the sol-foundation-structure system are harmonic, the dynamic equilibrium of the system can be rewritten as (Prasad, 1989):

$$\begin{bmatrix} M(TR)_x + m_f & Mh(TR)_x \\ Mh(TR)_x & I_f + Mh^2(TR)_x \end{bmatrix}\begin{Bmatrix} \ddot{X}_f \\ \ddot{\phi}_f \end{Bmatrix} - \frac{1}{\omega^2}[K_f]\begin{Bmatrix} \ddot{X}_f \\ \ddot{\phi}_f \end{Bmatrix} = \frac{1}{\omega^2}[K_f]\begin{Bmatrix} \ddot{X}_g \\ \ddot{\phi}_g \end{Bmatrix} \tag{6}$$

where $[K_f]$ is the impedance matrix of the foundation. $(TR)_x = 1 - \omega^2 H(\omega)$, in which, $H(\omega)$, is the transfer function of the 1DOF oscillator:

$$H(\omega) = -\frac{1}{(\omega_0^2 - \omega^2) + i2\xi\omega_0\omega} \tag{7}$$

Assuming that the absolute rotation of the soil is insignificant, $(\ddot{\phi}_g = 0)$, the solution of this system is given in the following form:

$$U = H_u T_u \ddot{X}_g \tag{8}$$

and

$$\ddot{U} = -\omega^2 H_u T_u \ddot{X}_g \tag{9}$$

where, U, is the response of the system, H_u , is the TF of the oscillator, T_u, is a dimensionless factor evaluating the effect of inertial interaction:

$$T_u = \frac{B_3}{B_1 a_0^4 - B_2 a_0^2 + B_3}; \qquad B_1 = (\varepsilon_i + \varepsilon_m)(\mathrm{TR})_x + \varepsilon_i \varepsilon_m \quad ; \; B_2 = (k_x + k_\phi)(\mathrm{TR})_x + \varepsilon_m k_\phi \; ; \; B_3 = k_x(k_\phi + \varepsilon_i a_0^2)$$

$\varepsilon_i = I_f / Mh^2$, $\varepsilon_m = m_f / M$, $k_x = K_x R^2/(MV_s^2)$, $k_\phi = K_\phi R^2/(Mh^2 V_s^2)$

and

$$\ddot{X}_g = -\omega^2 X_g \,.\, R,$$

is the equivalent radius of the foundation. The response accounting for the soil-structure interaction and site effects may be obtained by the equation below:

$$\ddot{U}(\omega) = -\omega^2 H_u T_u T F_S \ddot{X}_g(\omega) \tag{10}$$

where, TF_s, is the soil's TF.

Table 4. Data required for the soil-structure interaction analysis related to the superstructures and foundations of the studied buildings

		R+3	R+7	Designation
h (m)		19.5	23.3	Superstructure high related to the first mode
b (m)		15.3	15.3	Fondation's width
L (m)		29	29	Fondation's length
e (m)		3	3	Foundation embedment depth
h_f (m)		30	30	Soil layer high
e_f (m)		0.8	0.8	Fondation's thickness
ξ_0 (%)		5	5	Modal structural damping
M (t)		1428.5	3297.2	Modal structural mass
m_f (t)		768	768	Foundation's mass
f (Hz)		4.3	1.22	Building's fundamental frequency
v_s	S2	0.3		Poisson's ratio
	S3	0.35		
	S4	0.4		

Results and discussion

R+3 building

Figure 5a shows the TF of the structure with fixed base on S2 site which reveals a well noticeable amplification peak, compared to that corresponding to structure with fixed and rigid base. The latter reflects the dominance of site effects, in accordance with the rigid nature of the structure having a natural frequency lying around the soil dominant frequency. The TF of combined site and SSI effects prevails at the same level of amplification and remains overhead of that corresponding to a fixed base and rigid foundation. This explains the site effects control the response of the superstructure rather than SSI effects. The inertial interaction did not have a dominant effect and remembers presence of rigid structure on firm soil.

For the S3 site (fig. 5b), the amplification peak caused by the site effects due to change in the stiffness contrast near the surface is slightly reduced to a level up to that corresponding to rigid foundation. The inertial interaction effects are generated by an increase in the flexibility of the system and leads to a somewhat more damped response of the superstructure. The two amplification peaks appear at a frequency corresponding to the structure's fundamental frequency, but which is in shift with the ground's dominant frequency, located upstream of the latter. Once again, it is well showed that site effects have a dominant control of the structural response because of the weak additional flexibility inherent in soft site, leading to moderately damped superstructure seismic response.

For that reason, the very soft nature of the S4 site led to an amplification markedly lower than that corresponding to a rigid foundation (fig. 5c). SSI effects are very well evidenced, due to the important additional flexibility, brought by the weak stiffness of S4 site. Both site and SSI effects had a downward trend around the natural frequency of the structure and led to a considerably more damped response of the superstructure, dominated jointly by the two effects. A slight bump also appears around the soil's dominant frequency, but remains without influence on the overall trend of amplification.

R+7 building

The TFs of figure 6a show amplification peaks having close amplitudes, with a slight dominance of the case of fixed base on S2 site. The response of the superstructure is governed rather by the site effects, in the same way as the R+3 building. It is easily seen that inertial effects are not influent with a value approaching the unity around the dominant structural frequency and one can speak of absence of SSI effects. Nevertheless, two other peaks dominated by site effects appear at, respectively, the soil's natural frequency and at around 10 Hz, although they remain at relatively lower level. On the other hand, the figure 6b points out that for the S3 site, the response is dominated by inertial interaction effects whose TF has a slightly lower peak than one corresponding to a fixed base on S3 site. The two TFs have a remarkably high level of amplification due to a large amplification, occurring at the natural frequency of the structure.

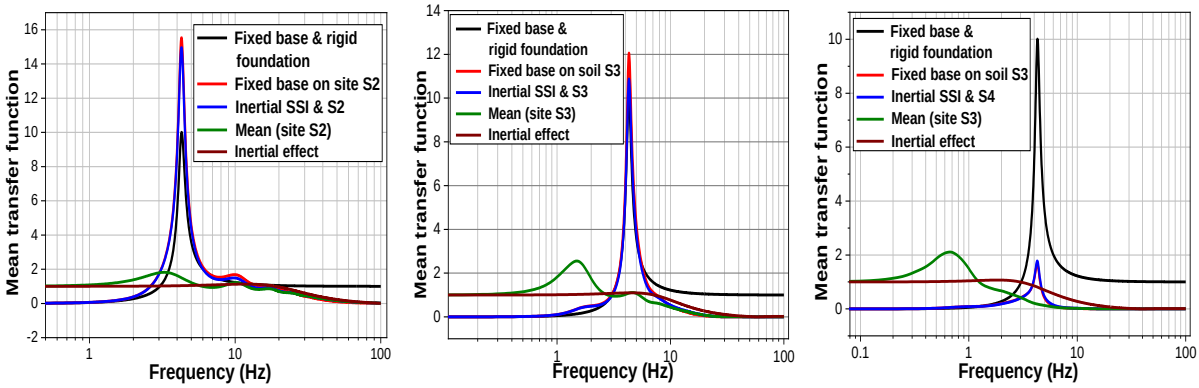

Figure 5. Mean transfer functions of the R+3 building's structure with a fixed base combined to that of site S2, S3 and S4. The transfer functions of the sites and inertial effects are also separately represented, in addition to transfer functions of that combined effects. Site transfer functions designate herein the mean transfer functions calculated over the whole sample of the simulated soil profiles.

The response of the superstructure is then dominated by the effect of inertial interaction, which is significant compared to the case of fixed base and rigid foundation. Because of passage to very loose medium from rigid formation in the case of S4 site leading to important damping effect (fig. 6c), the TF of the structure exhibits a significant amplification peak, compared to the case of fixed-base structure on rigid foundation.

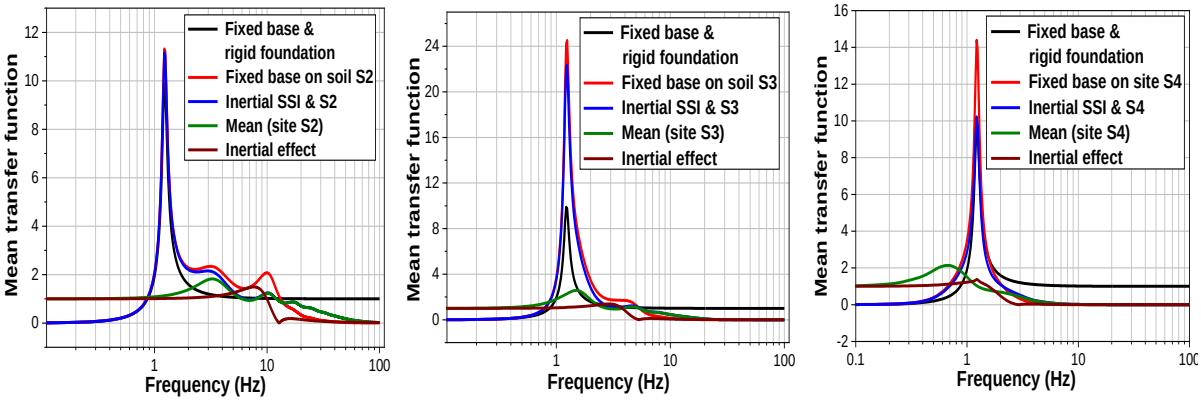

Figure 6. Transfer functions of the R+7 building's structure with a fixed base combined to that of site S2, S3 and S4. The transfer functions of the sites and inertial effects are also separately represented, in addition to transfer functions of that combined effects. Site transfer functions designate herein the mean transfer functions calculated over the whole sample of the simulated soil profiles

In fact, site effects pushed the amplification at a level clearly highest than those of fixed base and rigid foundation around the structure's fundamental frequency, even though the soil's natural frequency places upstream of the structure's fundamental peak. The response of the structure remains dominated by the inertial interaction, which allowed reducing the amplification exhorted by the nature of the site. The very soft nature of the S4 site enables the advent of SSI effects when dealing with a stiff structure, which is in agreement with what occurs in real cases.

Effect of Kinematic Interaction

Kinematic interaction effects are caused by the inability of foundation to follow ground motion due to the greater foundation stiffness compared to the ground. The presence of foundation rigid bodies gives rise to a base slab averaging effect when the foundation dimensions are in the same order of magnitude as the wavelength (Clough & Penzien, 1993) and, a wave scattering effects at the corners of the foundation will result. The mathematical transformation from the free field motion to the foundation input motion could be performed by a specific frequency dependent TF. It represents the ratio of the foundation motion to the free field motion:

$$H_k = \frac{u_F}{u_g} \tag{10}$$

where, u_F, is the foundation motion and u_g, is the ground motion. For embedded shallow foundation, seismic motion at the foundation level is further reduced because of reduction of ground motion with depth. The model used in this study is the Kausel *et al*., (1978) model's, adapted for rectangular shaped foundations from embedded rigid cylinder solution subjected to vertically propagating shear waves, for translational and rocking modes (Table 5).

Table 5. Kinematic transfer functions used in this study from Kausel et al., 1978

Degree of freedom	Kinematic transfer function
Translation along *x* axis	$H_{kx} = \cos\left(\frac{D\omega}{V_s}\right) \quad for \ \frac{D\omega}{V_s} < 1.1$
Rocking about *y* axis	$H_{k\phi} = 0.26\left[1 - \cos\left(\frac{D\omega}{V_s}\right)\right] \quad for \ \frac{D\omega}{V_s} < \frac{\pi}{2}$

D, is the embedment depth (*e*), ω, is the circular frequency and V_s, is the SW velocity value of the soil layer. The solution considers the response of the foundation embedded in the actual soil and subjected to the seismic environment defined in the free field at the soil structure interface before the soil has been excavated. The investigation of figures 7a to 8c shows that, except for the case of the R+3 building on S4 site (fig. 7c), the kinematic interaction has no effect on the structural response compared to that of the inertial interaction effects.

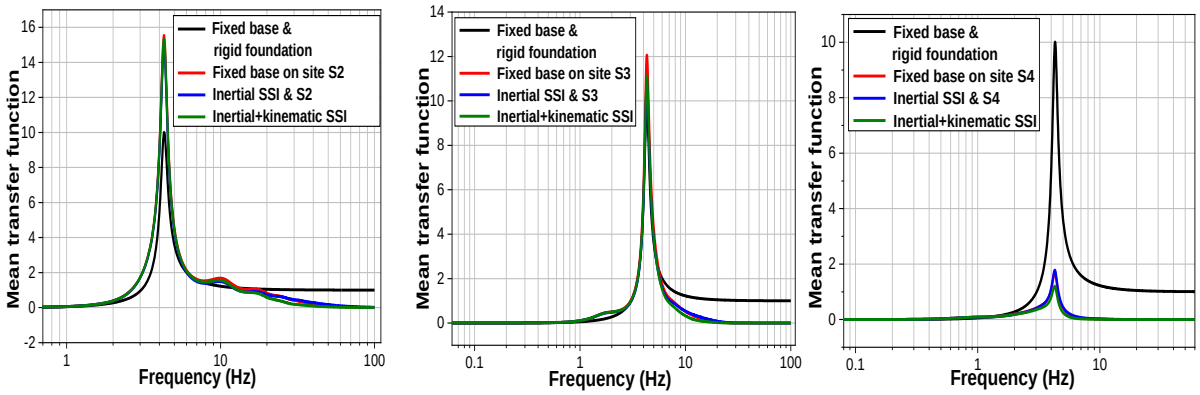

Figure 7. Transfer functions of the R+3 building's structure with a fixed and with a fixed base combined to that of site soils. The figure also shows transfer functions of inertial SSI effects combined to site effects in addition to inertial and kinematic interaction effects combined to soil effects

This could be due to the kinematic TF, which does not have a frequency preference in reducing structural response over the whole frequency considered range. Kinematic interaction, on the other hand, is influent compared to the case of a fixed base and rigid foundation, and follows fluctuations of the site effects. Except for the R+3 building on S4 site, TF of combined kinematic, inertial and soil effects clearly has a overall trend to follow site effects TF in all other cases (figs. 7a, 7b and 8a to 8c). In the case of the R+3 building on S4 site, the response of the superstructure is widely influenced by the effects of kinematic interaction, which has allowed reducing the amplification level caused by soil and inertial interaction effects. In the other cases, the response of the superstructure remains slightly dominated by the combined soil and inertial interaction effects, compared to soil effects alone and absence of kinematic interaction effects is due likewise to weakness of dimensions ratio of the foundation and embedment encountered in these common buildings.

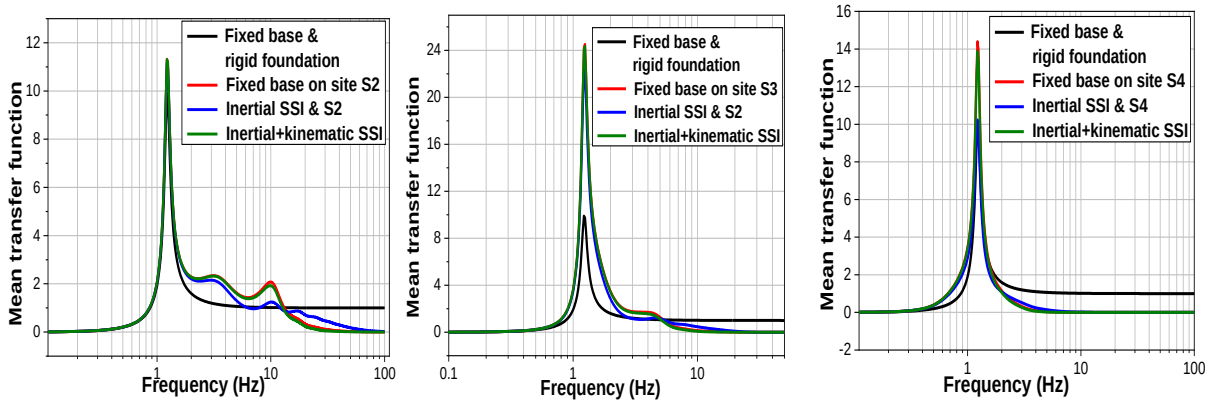

(a) (b) (c)

Figure 8. Transfer functions of the R+7 building's structure with a fixed and with a fixed base combined to that of site soils. The figure also shows transfer functions of inertial SSI effects combined to site effects in addition to inertial and kinematic interaction effects combined to soil effects

Conclusion

The influence of kinematic and inertial SSI effects combined to local site effects on typical RC multistory buildings was analyzed in this study, based on a global explicit TF modeling the soil-foundation-structure system. It comes from a simple combination, in the frequency domain, of the TFs of structure, foundation and soil. Site effects are modeled by TFs made following the Beneldjouzi and Laouami methodology according to RPA99 requirements.

For the R+3 building, the TF of the fixed-base structure on S2 site reveals a noticeable amplification peak, appeared around the fundamental structural frequency. In that case, inertial interaction effects has no influence on the structural response since it has not made any change to soil effects. As well, a clear trend to follow soil effects is observed for S3 site, where, combined soil and inertial effects lightly control the response of the superstructure.

Because of important change in stiffness contrast near the soil surface, the amplification peak related to the S4 site reduced to a level widely below that corresponding to rigid foundation, and allows the appearance of broad inertial interaction effects, generated by an increase in the flexibility of the system, and leads to a more damped response of the superstructure. The very soft nature of the S4 site led to an amplification markedly lower than that corresponding to a rigid foundation.

For the R+7 building on, respectively, S2 and S3 sites, the TFs show amplification peaks having similar amplitudes. The structure has not broadly reacted to the soil-structure interaction due to the nature of the R+7 building and the foundation supports, due to their comparable flexibilities. Soil effects lightly govern the response of the superstructure and one can speak of absence of soil-structure interaction effects. In the case of S4 site, inertial interaction effects whose TF has a widely lower peak than one corresponding to soil-structure TF dominate the structural response.

In all cases, however, it is clearly showed that, except for the case of the R+3 building on S4 site, the kinematic interaction has no effect on the structural response compared to that of the inertial interaction effects, and has an overall trend to follow soil effects.

References

Allison, S.H., Wu, W.H., & Borja, R.I., (1194). Structural control considering soil-structure interaction effects. *Earthquake Engineering And Structural Dynamics*, *23*, 609-626.

Beneldjouzi, M., & Laouami, N., (2015). Stochastic based approach for a new site classification method: application to the Algerian seismic code. *Earthquake Engineering and Engineering Vibration*, *14*, 663-681.

Beneldjouzi, M., Laouami, N., & Slimani, A., (2017). Numerical and random simulation procedure for a preliminary local site characterization and site factor assessing. *Earthquake and Structures*, *13*(1) 79-87.

Benouar, D., (1994). The seismicity of Algeria and adjacent regions. *Annali Di Geofisica*, *37*, 459–862.

Bouhadad, Y., & Laouami, N., (2002). Earthquake Hazard assessment in the Oran region (northwest Algeria). *Natural hazards*, *26*, 227–243.

Elsabee, F., & Morray, J.P., (1977). Dynamic behavior of embedded foundations. *Rep. No. R77-33*, Dept. of Civ. Eng, MIT, Cambridge, Mass.

Karapetrou, S.T., Fotopoulou, S.D., & Pitilakis, K.D., (2015). Seismic vulnerability assessment of high-rise non-ductile RC buildings considering soil–structure interaction effects. *Soil Dynamics and Earthquake Engineering*, *73*:42–57.

Kausel, E., (1974). Forced vibrations of circular foundations on layered media. *Rep. No. R74-11*, Dept. of Civ. Engrg., MIT, Cambridge, Mass.

Kausel, E., Whitman, A., Murray, J., & Elsabee, F., (1978) The spring method for embedded foundations. *Nuclear Engineering and Design*, *48*, 377-392.

Laouami, N., & Slimani. A., (2013). Earthquake induced site effect in the Algiers–Boumerdes Region: Relation between Spectral Ratios Higher Peaks and observed damage during the May 21st Mw 6.8 Boumerdes earthquake (Algeria). *Pure and Applied Geophysics*, *170*(11), 1785-1801.DOI 10.1007/s00024-012-0612-3.

Lin, Y.Y., & Miranda, E., (2008). Kinematic soil-structure interaction effects on maximum inelastic displacement demands of SDOF systems. *Bull Earthquake Eng.6*, 241–259.

Prasad, A.M., (1989). *Studies of soil structure and fluid structure interaction*. *Ph D* Thesis, Rice University, Houston, Texas.

RPA99, (2003 version). Règles Parasismiques Algériennes. D.T.R. –B.C. 2.48. *Centre National de Recherche appliquée en génie parasismique* (CGS), *Rue Kaddour Rahim, BP 252, Hussein Dey*, Alger, Algerie. Imprimé par l'Office Nationale des Publications Universitaires (OPU). ISBN 9961-923-13-8.

Sayyadpour, H., Behnamfar, F. & Hesham El Naggar, M., (2016). The near-field method: a modified equivalent linear method for dynamic soil–structure interaction analysis. Part II: verification and example application. *Bull Earthquake Eng.*, *14*, 2385–2404.DOI 10.1007/s10518-016-9871-1.

Seed, H.B., & Idriss, I.M., (1970). Soil moduli and damping factors for dynamic response analyses. earthquake engineering research center, *Report N°. EERC 70-10*, University of California, Berkeley, California.

Seed, H.B., & Sun, J.H., (1989) Implication of Site Effects in the Mexico City Earthquake of September 19, 1985 for Earthquake-resistance-design Criteria in the San Francisco Bay Area of California. *Report N°. UCB/EERC-89/03*, University of California, Berkeley, California.

Stewart, J.P., Seed, R.B. & Fenves, G.L., (1999a). Seismic soil-structure interaction in buildings I: Analytical aspects. *Journal Geotechnical and Geo environmental Engineering*, *125*, 26-37.

Wong, H.L., & Luco, J.E., (1985). Dynamic interaction between rigid foundations in a layered half space. *Earthquake Engineering and Structural Dynamics*, *5*, 3, 149-158.

Wu, W.H., (1992). *Soil-structure interaction effects of simple structures supported on rectangular foundations*. Master of Science thesis, Rice University, Huston, Texas.

Zania, & Tsompanakis, (2009). The effect of soil-structure interaction and site effects on dynamic response and stability of earth structures. *Proceedings of the NATO Advanced Research Workshop on Coupled Site and soil-structure Interaction Effects with Application to Seismic Risk Mitigation*, Borovets, Bulgaria, 30 August – 3 September 2008, ISBN 978-90-481-2 - (e-book).

Author Information

Mohamed Beneldjouzi
University Of Science and Technology Houari Boumediene
Faculty of Civil Engineering, University
Of Science and Technology Houari Boumediene
B.P 32 El Alia Bab Ezzouar , Alger, 16111, Algeria
mbeneldjouzi@*usthb.dz*

Nasser Laouami
Earthquake Engineering Applied Research Centre
Rue Kaddour Rahim, BP 252, Hussein Dey, Alger, 16040,
Algeria

Mohamed Hadid
National High School of Public Works,
1, Rue Sidi Garidi, Vieux Kouba, Alger, 16051, Algeria

The Eurasia Proceedings of Science, Technology, Engineering & Mathematics (EPSTEM)
ISSN: 2602-3199

The Eurasia Proceedings of Science, Technology, Engineering & Mathematics (EPSTEM), 2020

Volume 11, Pages 89-97

IConTES 2020: International Conference on Technology, Engineering and Science

Effect of Thermal Cycles on Flexural Behavior of Al/Al Honeycomb Sandwich Structures

Emre KURT
Turkish National Defence University

Mustafa Ozgur BORA
Kocaeli University

Sedat SUSLER
Kocaeli University

Halit Suleyman TURKMEN
Istanbul Technical University

Eyup AKAGUNDUZ
Tubitak MAM

Abstract: The main attractiveness of honeycomb sandwich structures lies in their high stiffness/weight and strength/weight ratios, which makes them suitable for primary structural aerospace parts such as aileron, elevator and rudder where weight reduction is a primary concern. Honeycomb cores, including nomex and aluminum honeycombs, have been used in the aerospace industry where bending, buckling, impact resistance and fire retardation are required, for example in some primary structural applications like wings and stabilizers. During flight time period, structural parts of an aircraft can be subject to thousands of such thermal cycles. Due to these environmental effects, damages can be occurred, especially at the interface region of core/face sheet. From literature surveys on evaluation of honeycomb sandwich structure flexural properties, it is not easy to find an article about sandwich behaviors under the effects thermal cycling. The information probably exists, as it is used on aircrafts that are submitted to a rigorous certification process to guarantee that they operate under safe conditions. However, this information may be restricted by confidentiality because of military or commercial concerns. In this study, AA3005-H19 aluminum alloy core/AA5754-H22 aluminum alloy face sheet (Al/Al) honeycomb sandwich structures are subjected to thermal cycles (0, 50, 150 and 300 cycles) in a full function environmental test chamber at temperature ranges -30 ^{o}C to +40 ^{o}C for 120 minutes. This paper deals with the determination of flexural properties such as ultimate core shear stress, facing stress, flexural stiffness, transverse shear rigidity and core shear modulus of various thermal cycled Al/Al honeycomb sandwich structures. Three-point bending tests are performed and flexural properties are calculated according to ASTM C393/C393M-16 and ASTM D7250/D7250M-16. After three-point bending tests, damage mechanisms which are occurring in the honeycomb sandwich structures are detected by digital camera images.

Keywords: Honeycomb sandwich structures, Three-point bending tests, Thermal cycles, Damage modes

Introduction

With the development of new materials technology, honeycomb sandwich structures are increasingly used in the aerospace, civil engineering and other fields because of its good performance in lightweight, high strength and stiffness, resistance of fatigue (Ley & Godinez, 2013, pp. 309-336). Due to its outstanding absorbed energy properties, impact resistance and lightweight characteristic with high in-plane and flexural stiffness, honeycomb sandwich structures are widely used on aircraft flight control surfaces such as rudder, aileron, spoiler, and flap. (Bruffey & Shiu, 2016; Han et al., 2020; Lu & Yu, 2003; Zhang, Lu, Ruan, Fei & Duan, 2019).

- Selection and peer-review under responsibility of the Organizing Committee of the Conference

Face sheets of honeycomb sandwich structures are made from stainless steel, aluminum alloy, titanium alloy or typically thin composite laminates. On the other hand, the core of the sandwich is mostly honeycomb cell walls and made of nomex, fiberglass or aluminum alloy (Wei, Wu, Gao, & Xiong, 2020; Xie, Jing, Zhou, & Liu, 2020). Aluminium/aluminium (Al/Al) structures are especially preferred in the use of structural parts of the aircraft due to their performance against environmental conditions such as high G forces and high fatigue strength (Jen & Chang, 2008). 5xxx and 3xxx aluminum alloys are preferred as the face sheet and core material in honeycomb sandwich structures for aircraft structural parts due to resistant of atmospheric corrosion. When the literature studies on the mechanical properties of Al/Al honeycomb sandwich structures are investigated, some previous studies are found. Palomba, Crupi & Epasto (2019) performed three-point bending tests at different bending test speeds to determine the flexural properties of AA5754/AA5052 honeycomb sandwich structures. It was determined that the bending moment values of Al/Al honeycomb sandwich structures did not change significantly according to the bending test speed. In addition to this result, it was stated that the highest bending moment value (83 kNm) was obtained in tests with 2 mm/min bending speed. Sun, Huo, Chen & Li (2017) applied three-point bending tests on samples (AA5052/AA3003 honeycomb sandwich structures) with different core thickness (0.04 mm, 0.07 mm and 0.1 mm) in order to examine the effect of core thickness on the flexural properties of honeycomb sandwich structures. The results showed that the increase in core thickness had been increased the maximum force applied to the material and had been consequently improved the strength of the material. Maximum force is about 2000 N at 0.1 mm and about 1000 N at 0.04 mm. In another study, Crupi, Epasto & Guglielmino (2012) investigated the effect of different lower support span distance (55 mm, 70 mm, 80 mm, 125 mm) on the flexural properties of the AA5754/AA5052 honeycomb sandwich structures. It was found that the maximum force (2800 N) had been achieved at the smallest support span distance (55 mm). As the support range increased, the load acting on the support points increased so at longer support distances and more deflection could be applied to the material with less force. Belouettar, Abbadi, Azari, Belouettar & Freres (2009) used the bending test to examine the maximum load-deflection effects of Al/Al honeycomb sandwich structures with different core densities. AA5754 aluminum alloy was used as the face sheet material in the sample, and an aluminum alloy having different densities (55 kg/m^3 and 82 kg/m^3) was used as the core material. It was determined that an increase in core density had increased the hardness of aluminum honeycomb sandwich structures. As a result, the increase in core density made the damage load value of the material higher.

Thermal cycling (TC) is a very important phenomenon in aviation. Aircraft structural components are exposed to different temperature due to changes in the altitude. There are a few studies on the thermal cycles of Al/Al honeycomb sandwich structures in the literature. Zaoutsos (2019) aimed to determine the mechanical properties of honeycomb sandwich structures exposed to bending loading in low temperature applications. They applied four different temperatures of 23 °C, 0 °C, -40 °C and -70 °C to honeycomb sandwiches having face material aluminum 3000 series and core material aluminum 3003 alloy. Three-point bending tests were carried out on specimens made of aluminum sandwich panels according to ASTM C-393 in order to study the bending behavior of the sandwich panel. Ultimate tensile strength and yield strength are not affected from changes of temperature; while in the case of compression loading the respective values of strength seem to be decreased as temperature decreases. Bending strength is concerned by the values of ultimate strength and yield strength are not affected by the temperature. The experimental data can be used for the selection of lighter and stiffer combination of sandwich panels according to the temperatures and loading conditions. Due to limited studies in literature, it is necessary to investigate the bending behavior of such honeycomb composites used in structural parts especially in the aviation industry by also concerning the effect of thermal aging. In all mission profiles of an aircraft including taxi, flexural loading occurs in the moving parts of the aircraft due to environmental conditions. This situation is also an issue that needs to be investigated.

In this study, flexural behaviors of Al/Al honeycomb sandwich structures subjected to different thermal cycles (0, 50, 150 and 300 cycles) are investigated. Ultimate core shear stress, facing stress, flexural stiffness, transverse shear rigidity and core shear modulus of AA5754-H22/AA3005-H19 honeycomb sandwich structures are investigated by applying three-point bending test. After mechanical tests, failure modes which were occurred in the material are visualized with digital camera.

Materials and Methods

Materials

Honeycomb sandwich panels used in this study are made of aluminum alloy face sheet (5754-H22) and honeycomb core (3005-H19), which were bonded together using the double layer polyurethane. The layup including aluminum based face sheets, polyurethane adhesive and the aluminum based honeycomb core was co-

cured under atmospheric pressure at the recommended cure temperature of 80 ^{o}C for 15 min. The dimensions of test specimens (200 mm x 28.7 mm x 14.5 mm) were cut from the manufactured sandwich panel for three-point bending tests according to the ASTM C393/C393M standard (American Society for Testing and Materials [ASTM], 2016). L is the total length of the sandwich panel (200 mm) and W is the total width of the sandwich panel (28.7 mm). The schematic views of honeycomb sandwich structures are given in Fig. 1 where H is the total thickness of the sandwich panel (14.5 mm), b is the cell size (6.78 mm), d1 and d2 are upper and lower face sheet thickness (0.5 mm). In addition, the material properties of core and face sheet are given in Table 1.

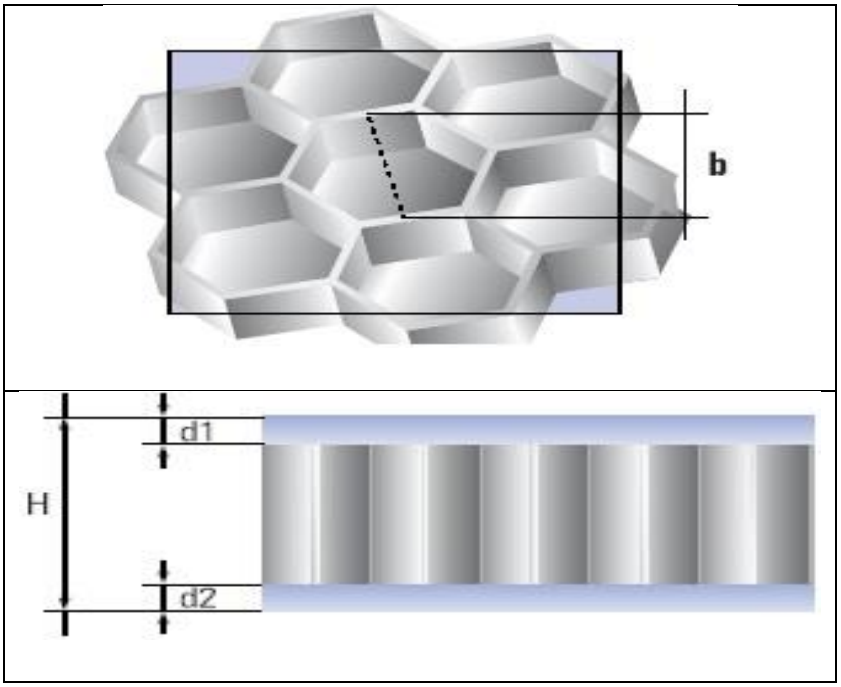

Figure 1. The geometry of honeycomb sandwich structures

Table 1. The properties of core and face sheet material

Properties	Core material (3005-H19)	Face sheet material (5754-H22)
Density	2.8 g/cm^3	2.66 g/cm³
Modulus of Elasticity	70 GPa	70.3GPa
Ultimate Tensile Strength	270 MPa	245 MPa
Shear Modulus	26 GPa	25.9 GPa
Shear Strength	150 MPa	150 MPa
Poisson's Ratio	0.33	0.33

Thermal Cycle Condition

For accelerated thermal cycle process, Atlas SC 600 Solar Simulator environmental chamber which is facilitated in TÜBİTAK-MAM was operated. Al/Al honeycomb sandwich structures were subjected to the thermal cycles (0, 50, 150 and 300 cycles) in a full function environmental chamber at a temperature ranges -30 ^{o}C to +40 ^{o}C for 120 minutes. 300 thermal cycles corresponds to typical check interval for military fighter jet F-16C/D maintenance programs. Samples were subjected to cyclic environments with the following controlled factors: the relative humidity (RH) and the surrounding temperature (T). After thermal cycle process, honeycomb sandwich structures were removed from the climatic chamber. Fig.2 illustrates the applied temperature changes during the thermal cycling process. In Fig. 2, one cycle of thermal aging process is 120 minutes according to a flight of a military fighter jet which is serviced routine daily operational flight. In addition, RH was only applied between 0 ^{o}C and +40 ^{o}C. Accelerated thermal cycles imposed on samples at a temperature range of -30 to +40 ^{o}C with 98% RH.

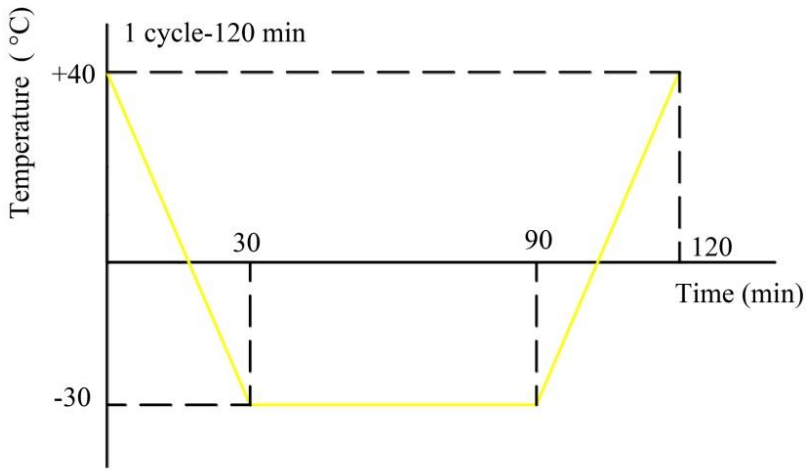

Figure 2. The temperature variations imposed during the accelerated thermal cycling test of honeycomb sandwich structures

Three-Point Bending Tests

After thermal cycling process, three-point bending tests were applied to various thermally aged honeycomb sandwich structures by the guidance of ASTM C393/C393M-16 (ASTM, 2016). MTS universal testing machine and three-point bending apparatus which are facilitated in Composites & Structures Laboratory at Istanbul Technical University was operated for three-point bending tests. Support span length was chosen as 150 mm. Rigid rollers which were used for loading and supporting tools had a diameter of 10 mm. In addition, for preventing the local core damage at support and loading locations of the honeycomb sandwich structures, 25 mm x 30 mm wide flat steel loading blocks which have 4 mm thickness are used between the sandwich surfaces and rigid rollers. Sufficient samples of honeycomb sandwich structures to get significant flexural data were tested with the speed of 4 mm/min for cross head displacement. The load-displacement curves were obtained by using the load and displacement data which were stored by MTS universal testing machine. The flexural properties such as ultimate core shear stress, facing stress, flexural stiffness, transverse shear rigidity and core shear modulus of various thermally aged honeycomb sandwich structures were determined. Average values of tested honeycomb sandwich structures were given. The ultimate core shear stress and facing stress are calculated from the load-displacement curve based on the formulas in ASTM C393/C393M-16 (Eq. 1 and Eq. 2) (ASTM, 2016). The flexural stiffness, transverse shear rigidity and core shear modulus of sandwich structures are obtained by using the formulas and the method of two loading configurations on the same test specimens described in ASTM D7250/D7250M-16 (Eqs. 3-5) (ASTM, 2016). In this method, the data in elastic region of load-displacement curves were used. The support span length for the second loading configuration was described as 120 mm. The flexural stiffness, transverse shear rigidity and core shear modulus of the honeycomb sandwich structures can also be obtained using simple bending theory (ASTM, 2016). However, the effects of thermal cycles and humidity on material properties of face sheet, core and adhesive were not able to be determined. For determining the flexural properties of honeycomb sandwich structures, the formulas of flexural properties are shown in Eqs. 1–5, respectively;

$$F_s^{ult} = \frac{P_{max}}{(d+c)b} \tag{1}$$

$$\sigma = \frac{P_{max} S}{2t(d+c)b} \tag{2}$$

$$D = \frac{P_1 S_1^3 (1-S_2^2/S_1^2)}{48\Delta_1 (1-P_1 S_1 \Delta_2 / P_2 S_2 \Delta_1} \tag{3}$$

$$U = \frac{P_1 S_1 (S_1^2/S_2^2-1)}{4\Delta_1 \left((P_1 S_1^3 \Delta_2 / P_2 S_2^3 \Delta_1)-1 \right)} \tag{4}$$

$$G = \frac{U(d-2t)}{(d-t)^2 b} \tag{5}$$

where P_{max} is maximum load prior to failure (N), d is sandwich thickness (mm), c is core thickness (mm), b is sandwich width (mm), S is support span length (mm), t is face thickness (mm), Δ is mid-span deflection(mm), F_s^{ult} is core shear ultimate strength (MPa), σ is facing stress (MPa), D is sandwich flexural stiffness (Nmm^2), U is transverse shear rigidity (N), G is core shear modulus (MPa). After three-point bending tests, damage mechanisms which are occurring in the honeycomb sandwich structures are detected by digital camera images.

Results and Discussions

The load-displacement curves of various thermally aged honeycomb sandwich structures were obtained to investigate the effect of the thermal cycle numbers on the flexural behavior of the samples. Obtained load-displacement curves of various thermally aged honeycomb sandwich structures and conventional unaged load-displacement curve are given. Damage process of honeycomb sandwich structures under three-point bending test were illustrated in Fig. 3.

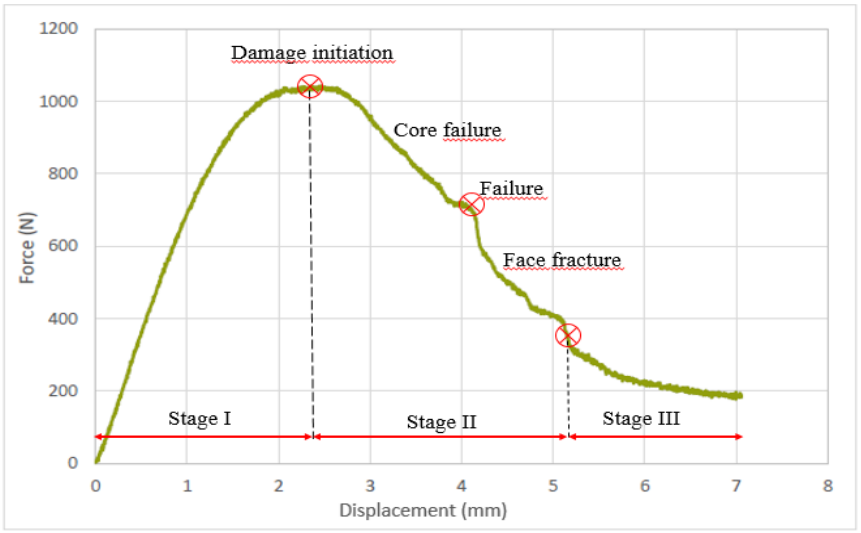

(a) Typical force-displacement curve and damage process of honeycomb sandwich structures under three-point bending test (He et al., 2019).

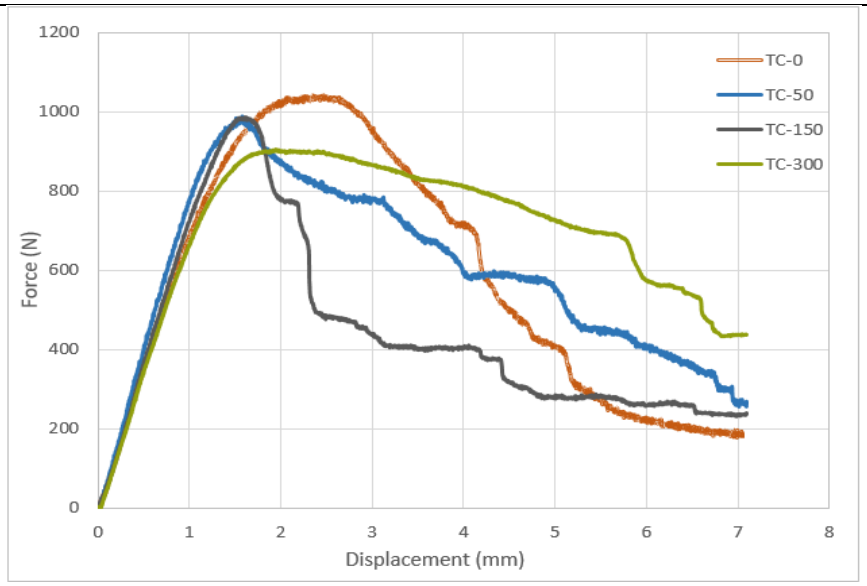

(b) Force-displacement curves of various thermally aged honeycomb sandwich structures

Figure 3. (a) Typical force-displacement curve and damage process of honeycomb sandwich structures under three-point bending test (He et al., 2019), (b) Load-displacement curves of various thermally aged honeycomb sandwich structures

From Fig.3(a), depending on the drop points the load-displacement curves can be divided into three distinct stages: the initial elastic stage (Stage I), the core or face sheet failure stage (Stage II), and global failure stage (Stage III). In Stage I, the specimen deforms elastically in the initial phase of bending and the corresponding load value has a nearly linear increase almost up to the peak load. However, for the core failure case, there is a little non-linearity in the load-displacement curve prior to peak load, indicating some plastic buckling of the core occurring under the indenter. In Stage II, there are two main damage modes (core failure and face sheet failure), and the trend change is closely associated with the competing failure patterns of sandwich panel. After the top face sheet complete fracture, there is a relative stable load plateau until the final rupture of the panel in Stage III.

In this stage, the prominent failure patterns are core crushing under the indenter and further delamination of the fracture section in the top face sheet (He et al., 2019). From Fig. 3(b), it was determined that all of the thermally aged honeycomb sandwich structures exhibited a similar general trend in the load–displacement curve. First of all, damage initiation occurred at maximum load values, after this point core failure and face sheet failure determined for all thermally aged honeycomb sandwich structures. It was easily determined that displacement values at maximum load also sharply decreased with the increment of thermal cycle numbers. At last, catastrophic damages occurred as core crushing and delamination at all thermally aged honeycomb sandwich structures. Average values of maximum load, core shear ultimate stress, facing stress, flexural stiffness, transverse shear rigidity and core shear modulus for all cases are shown in Table 2.

Table 2. Obtained flexural properties of various thermally aged honeycomb sandwich structures from load-displacement curves

Sample Codes	Maximum Load (N)	Core Shear Ultimate Stress (MPa)	Facing Stress (MPa)	Flexural Stiffness (Nm2)	Core Shear Modulus (MPa)	Transverse Shear Rigidity (kN)
TC-0	1042,49	1,296	194,46	105,92	123,22	51,4
TC-50	989,84	1,232	184,76	209,34	100,72	41,97
TC-150	984,59	1,226	183,91	224,2	89,48	34,85
TC-300	905,26	1,129	169,33	157,13	83,70	37,21

The results of the three-point bending test show a clear reduction trend in the flexural properties such as core shear ultimate stress, facing stress and core shear modulus values as the number of thermal cycles increased (Table 2). Core shear ultimate stress, facing stress and core shear modulus values of thermally aged honeycomb sandwich structures (TC-300) decreased approximately %13, %13 and %32 according to the original honeycomb sandwich structures (TC-0), respectively. At this point, there is a sharp decrement at core shear modulus values for thermally aged honeycomb sandwich structures with 300 thermal cycles. This trend was observed due to the effects of the shear stresses occurring on the fracture of the core during loading. The high value of the shear stress caused deformation and fracture of the core in a shear mode. In the three-point bending test, crack propagation in the core was significant along the neutral axis, which caused the strength of the core to play an important role in determining the mechanical properties of the honeycomb sandwich structures. The fracture of the core relieved the local stress in the material as similar to Ref. (Antony Arul Prakash, Jagannatha Guptha, Sharma, & Mohan 2012).

At higher support span length (≥ 70 mm), the collapse mode was different because it was accompanied the mid-plane and by the formation of a plastic hinge also in the tensioned face. By this way, at higher deflections boardened peak occured (Fig. 3-b) as similar to Ref. (Crupi et al.,(2012). For the transverse shear rigidity as a flexural property shown in Table 2, a similar reduction trend with other properties above observed as the number of thermal cycles increased from 0 to 150 cycles. No significant reduction in 300 cycles detected according to 150 cycles. Lastly, a regular reduction pattern was not observed for flexural stiffness while the thermal cycles were increased. It has an increased trend except for 300 cycles. This can be because of flexural stiffness is generally related to strength of face sheets while the others are related to shear performance of core and adhesive. It is possible that the thermal cycle effect could be increase the strength of the face sheets as so-called heat treatment effect on a metallic material.

Failure modes of various thermally aged honeycomb sandwich structures after three-point bending tests were given in Fig.4. The between face sheet and core which were strong enough to bear the bending and shear load result in the adhesive delamination mode.

(a) the original honeycomb sandwich structures- TC-0

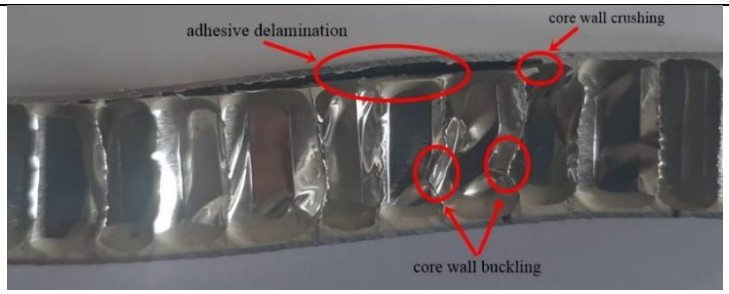

(b) thermally aged honeycomb sandwich structures -TC-50

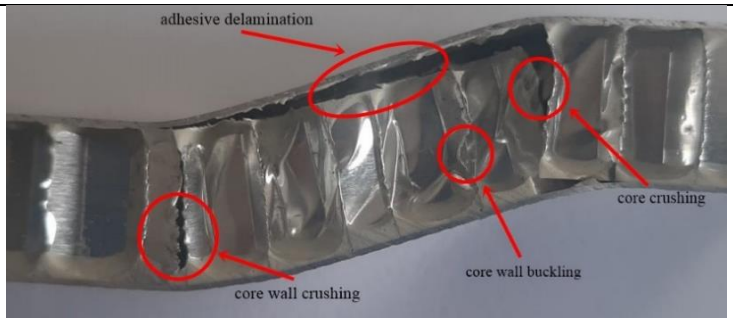

(c) thermally aged honeycomb sandwich structures- TC-150

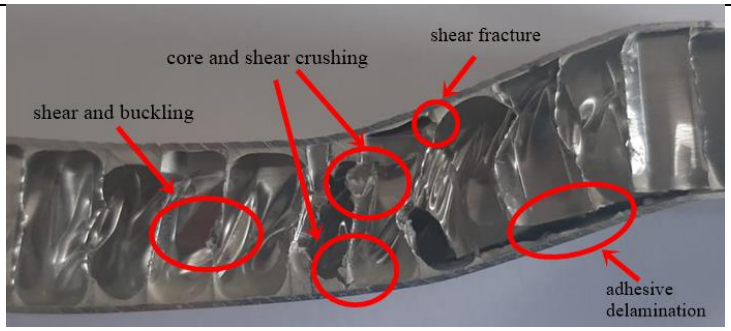

(d) thermally aged honeycomb sandwich structures- TC-300

Figure 4. Failure modes of various thermally aged honeycomb sandwich structures after three-point bending tests

This situation observed as damage with each thermal cycle tested. Fig. 4(a) shows that the main failure mode observed is face sheet indentation and adhesive delamination. However, adhesive delamination collapse mode observed is between core and face sheet (Jen & Lin, 2013). In Figure 4 (b-c), no different from each other collapse modes detected. In addition to the original sample, core wall fracture and buckling were observed. When the load reaches the peak value, the core under the face sheet is began to crush. In Fig 4(d), five competing failure modes were observed, including shear buckling, shear fracture, adhesive delamination, core crushing and core buckling. Significant core and shear crushing is observed in thermal cycle followed by fracture of core walls. This sample is after the core failed by shear fracture, debonding occurred as the cracks propagated in the adhesive layer. The reason for this is the more deformation of the sample due to the increase in thermal cycling. The decrease in flexural properties such as core shear ultimate stress, exposure stress and core shear modulus values was also observed in digital images (Anandan, Dhaliwal, Ganguly & Chandrashekhara, 2020; Wang et al, 2018).

Conclusions

In this study, flexural behaviors of Al/Al honeycomb sandwich structures subjected to different thermal cycles were investigated. From the obtained experimental results, it was possible to draw some conclusions on the behaviour of investigated honeycomb sandwich structures:

1. Maximum load, core shear ultimate stress, facing stress and core shear modulus values of thermally aged honeycomb sandwich structures (TC-300) decreased approximately %14, %13, %13 and %32 according to the original honeycomb sandwich structures (TC-0), respectively.
2. Flexural stiffness of values of thermally aged honeycomb sandwich structures (TC-300) increased approximately %50 according to the original honeycomb sandwich structures (TC-0).
3. Transverse shear rigidity values of thermally aged honeycomb sandwich structures (TC-300) decreased approximately %27 according to the original honeycomb sandwich structures (TC-0).
4. Failure of cell walls due to local buckling was observed in the honeycomb sandwich structures due to the thermal cycles.
5. Differently shear fracture, core and shear crushing, shear and buckling of thermally aged honeycomb sandwich structures (TC-300) were observed according to the original honeycomb sandwich structures (TC-0).

As a result, the decrease due to thermal cycles in flexural properties such as core shear ultimate stress, exposure stress and core shear modulus values was observed.

References

Anandan, S., Dhaliwal, G., Ganguly, S., & Chandrashekhara, K. (2020). Investigation of sandwich composite failure under three-point bending: Simulation and experimental validation. *Journal of Sandwich Structures & Materials*, *22*(6), 1838-1858.

Antony Arul Prakash, M. D., Jagannatha Guptha, V. L., Sharma, R. S., & Mohan, B. (2012). Influence of cell size on the core shear properties of FRP honeycomb sandwich panels. *Materials and Manufacturing Processes*, *27*(2), 169-176.

ASTM International C393/C393M-16. (2016). *Standard test method for core shear properties of sandwich constructions by beam flexure*. ASTM International.

ASTM International D7250/D7250M-16. (2016). *Standard test method for core shear properties of sandwich constructions by beam flexure*. ASTM International.

Belouettar, S., Abbadi, A., Azari, Z., Belouettar, R., & Freres, P. (2009). Experimental investigation of static and fatigue behaviour of composites honeycomb materials using four point bending tests. *Composite Structures*, *87*(3), 265-273.

Bruffey, N., & Shiu, W. (2016). Predicting Flexural Strength of Composite Honeycomb Core Sandwich Panels Using Mechanical Models of Face Sheet Compressive Strength.

Crupi, V., Epasto, G., & Guglielmino, E. (2012). Collapse modes in aluminium honeycomb sandwich panels under bending and impact loading. *International Journal of Impact Engineering*, *43*, 6-15.

Han, Q., Qin, H., Liu, Z., Han, Z., Zhang, J., Niu, S., ... & Shi, S. (2020). Experimental investigation on impact and bending properties of a novel dactyl-inspired sandwich honeycomb with carbon fiber. *Construction and Building Materials*, *253*, 119161.

He, W., Lu, S., Yi, K., Wang, S., Sun, G., & Hu, Z. (2019). Residual flexural properties of CFRP sandwich structures with aluminum honeycomb cores after low-velocity impact. *International Journal of Mechanical Sciences*, *161*, 105026.

Jen, Y. M., & Chang, L. Y. (2008). Evaluating bending fatigue strength of aluminum honeycomb sandwich beams using local parameters. *International Journal of Fatigue*, *30*(6), 1103-1114.

Jen, Y. M., & Lin, H. B. (2013). Temperature-dependent monotonic and fatigue bending strengths of adhesively bonded aluminum honeycomb sandwich beams. *Materials & Design*, *45*, 393-406.

Ley, O., & Godinez, V. (2013). Non-destructive evaluation (NDE) of aerospace composites: application of infrared (IR) thermography. In *Non-Destructive Evaluation (NDE) of Polymer Matrix Composites* (pp. 309-336e). Woodhead Publishing.

Lu, G., & Yu, T. X. (2003). *Energy absorption of structures and materials*. Elsevier.

Palomba, G., Crupi, V., & Epasto, G. (2019). Collapse modes of aluminium honeycomb sandwich structures under fatigue bending loading. *Thin-Walled Structures*, *145*, 106363.

Sun, G., Huo, X., Chen, D., & Li, Q. (2017). Experimental and numerical study on honeycomb sandwich panels under bending and in-panel compression. *Materials & Design*, *133*, 154-168.

Wang, P., Zhang, Y., Chen, H., Zhou, Y., Jin, F., & Fan, H. (2018). Broadband radar absorption and mechanical behaviors of bendable over-expanded honeycomb panels. *Composites Science and Technology*, *162*, 33-48.

Wei, X., Wu, Q., Gao, Y., & Xiong, J. (2020). Bending characteristics of all-composite hexagon honeycomb sandwich beams: experimental tests and a three-dimensional failure mechanism map. *Mechanics of Materials*, 103401.

Xie, S., Jing, K., Zhou, H., & Liu, X. (2020). Mechanical properties of Nomex honeycomb sandwich panels under dynamic impact. *Composite Structures*, *235*, 111814.

Zaoutsos, S. P. (2019, November). Mechanical behavior of aluminum honeycomb sandwich structures under extreme low temperature conditions. In *IOP Conference Series: Materials Science and Engineering* (Vol. 700, No. 1, p. 012017). IOP Publishing.

Zhang, D., Lu, G., Ruan, D., Fei, Q., & Duan, W. (2019). Quasi-static combined compression-shear crushing of honeycombs: An experimental study. *Materials & Design*, *167*, 107632.

Author Information

Emre KURT
Turkish National Defence University
Air NCO Higher Vocational School, 35415, Gaziemir, Izmir,Turkey
Contact e-mail: *emrekurt012@gmail.com*

Mustafa Ozgur BORA
Kocaeli University
Faculty of Aeronautics and Astronautics, 41380, Kartepe, Kocaeli, Turkey

Sedat SUSLER
Kocaeli University,
Faculty of Aeronautics and Astronautics, 41380, Kartepe, Kocaeli, Turkey

Halit Süleyman TÜRKMEN
Istanbul Technical University
Faculty of Aeronautics and Astronautics, 34469, Maslak, Istanbul, Turkey

Eyüp AKAGÜNDÜZ
TUBITAK-MAM
Materials Institute, 41470, Gebze, Kocaeli**,** Turkey

The Eurasia Proceedings of Science, Technology, Engineering & Mathematics (EPSTEM)
ISSN: 2602-3199

The Eurasia Proceedings of Science, Technology, Engineering & Mathematics (EPSTEM), 2020

Volume 11, Pages 98-105

IConTES 2020: International Conference on Technology, Engineering and Science

Design and Analysis of Thermoplastic Prepreg Based Heavy Commercial Vehicle Seat

Serkan BIRCICEK
Kocaeli University

Mustafa Ozgur BORA
Kocaeli University

Erman ARKIN
Assan Hanil Industry and Trade Inc

Bunyamin YAKAR
Assan Hanil Industry and Trade Inc

Ersan ERTURK
Assan Hanil Industry and Trade Inc

Emre GODEK
Assan Hanil Industry and Trade Inc

Abstract: Combining two or more reinforcing elements into the matrix to compose a new material with enhanced properties is called hybrid composite. By favor of related method; prime advantages such as lightening the vehicles and reducing the process steps are obtained and it is aimed to bring the parts production costs to a competitive point depending on the appropriate part selection and design optimizations. In this regard, it is essential to integrate hybrid composite and advanced molding technologies and to produce certain structural components associated with using this technology. Within the scope of this study, the metal part (S420 MC) used in the truck seat structure was modelled along with the finite element method of the continuous glass fiber reinforced composite material that will be used to produce with composite technology. Part design studies and ECE R14 regulation analysis applied to composite production of the relevant seat part have been realized. In this work, heavy commercial vehicle passenger seat backrest was chosen as the study product. The backrest of the existing weight is 3200 gr and the related backrest was welded from S420 MC tube. Based on this, weight reduced to 1700 gr by performing over-molding method under favor of using polypropylene / GF 40 (P40B01) raw material on Epoxy Resin based (OM10) prepreg material and weight reduction have successfully substantiated. Mechanical properties of the materials used as the acceptance criteria of the models were determined as the relevant acceptance ranges. Within the scope of the analysis studies, design that encounters the mechanical limits of the material for all the scenarios was determined as the accepted design. There is a static loading condition for ECE-R14 analysis. In the designs, ribs were added to the areas above the mechanical limits of the material, revisions were made in the thickness of the material.

Keywords: Thermoplastic Composite, Over-Molding, Composite Design, Finite element analysis

Introduction

Composite materials which have gained rapid development over the last 50 years, widely used in aeronautical, marine, subsea, automotive and artificial legs and arms, due to their excellent mechanical properties, low density, unique mechanical characteristics, light weight, corrosion resistance and ease of manufacture (Gaikwad, 2018). Especially in the automotive sector, the trend is towards weight reduction due to the new regulations

- Selection and peer-review under responsibility of the Organizing Committee of the Conference

created to reduce CO_2 emissions. This has led the automobile industry to develop new technology for lighter parts (Schijve and Kulkarni, 2016). In addition, many automotive manufacturers stated that they will be on the market with lighter vehicles after 2021 (Schijve and Kulkarni, 2016). For this reason, it has gained importance to use polymer-based materials instead of metal parts that make up about 90% of the vehicles by weight. However, meeting the current regulation requirements of these polymer-based materials, which are intended to be used instead of metals, stands out as one of the most important issues to be considered. Due to this reasons, composite technologies are one of the most important fields of study when it comes to using polymer-based materials instead of metals. On the other hand, the composite technology must meet the competitive conditions in the automotive industry and must be designed to be suitable for mass production of parts. From this point of view, the technologies such as chopped glass fiber reinforced thermoplastic composites (GMT, Glass Mat Thermoplastics) and hybrid thermoplastic composite parts production with injection molding are shown as the most up-to-date composite part production methods, which are suitable for mass production and meet regulation requirements. Thermoplastic composites are very popular today, especially in high-volume production industries, due to the fast and environmentally friendly production processes. As an intermediate product in the production of thermoplastic composites, thermoplastic prepregs with continuous fiber additive are expected to be used more in the upcoming periods due to their lack of a special storage condition, recyclability and unlimited shelf life (European Environment Agency, 2014).

Hybrid thermoplastic composite production technology; Multiple molding finds place in the world automotive industry as an important method that enables continuous fiber reinforced composites to replace parts formed by injection molding and metal components used in vehicles (European Environment Agency, 2014). For instance this technology, battery carrier, oil tank, air conditioner carrier, bumper carrier system, seat chassis parts and so on. Many structural parts are produced with composite materials and find a place in the sector. Examples of these studies are the oil tank project produced in cooperation with NIFCO and Dupont, the composite seat study produced by Faurecia and CETIM companies, and the seat project developed by Faurecia and ZF, which was introduced in 2018 (Tian Tuo Machinery, 2018). The most important point that stands out is that the relevant composite parts are designed correctly to ensure the specified regulation. At this point, designing composite parts with computer support and verifying the regulatory requirements of the part with computer aided analysis (CAE) is one of the first and most important stages of the composite part design and production process as in other design studies. In this direction, an important step was taken about the analysis of a part that is aimed to be produced by injection method with the method of finite element analysis, and a significant contribution was made to the literature in terms of the gradual realization of the composite part design (Carello et al, 2017). As an example of studies conducted with these methods, Karpat et al. (Karpat et al, 2014) focused on the design and analysis results of the seats used in buses for weight reduction and they achieved 20% weight reduction in this study. In another study Ning et al. (Ning, Pillay, Vaidya, 2009) focused an air conditioning cover roof door. They changed material aluminum to composite and they achieved %39 weight savings and reduction of free-standing deflection of 42% (Ning, Pillay, Vaidya, 2009). Within the scope of the study, it was mentioned that composite materials can be an alternative to traditional materials.

Finite element analysis is used for progressive damage characterization in composite material analysis. In the relevant analysis method, the material properties are assigned to the mesh that forms the composite structure when the model is created. With this method, the stress and strain values calculated in the element due to the load applied to any finite element network are calculated at the integration points of the relevant element. Therefore, it is assumed that the material properties are assigned to these integration points with this method. The elements created on the model represent composite plates formed by the combination of layers (Guney, 2019; Banerjee, Sankar, 2014). In addition to this, Hypermesh program is utilized in related analysis and supports wide variety of CAD and solver interfaces making it a perfect solution for most industry verticals and domains. With its advanced geometry and meshing capabilities Hypermesh provides an environment for rapid model generation (Ferruh, 2017). Overmolding is the injection molding process where one material (usually TPE) is molded into a second material (typically a rigid plastic). Regarding overmolding, process conditions permit high mechanical properties along with good stiffness for complex parts. During the related process; one of both materials is in molten condition with low viscosity. Besides, overmolding process have many advantages such as high level of function integration and large series in production cycle and that's why it has become popular in recent years (Akkerman, Bouwman, Wijskamp, 2020). The literature studies carried out so far have been examined and it’s determined that a product at the level required by the driver's seat regulation for heavy commercial vehicles has not been observed. With this study, it is aimed to meet the ECE R14 regulation conditions required for the heavy commercial driver's seat. Based on this, the materials have been modeled using Catia V5 program, then the appropriate design is produced by using innovative overmolding technology. In addition, it is aimed to weight gain by using composite material and to shorten the part production time with the use of over-molding technology.

Materials

In this study, twill 2/2 balanced glass fiber reinforced polypropylene (PP) matrix prepreg material (OM10) was supplied from Kordsa. The technical properties of the OM10 are given in Table 1.

Table 1. Technical properties of prepreg material

Polymer type	High crystalline polypropylene (PP)
Fiber type	PP compatible 1200 tex roving glass
Fiber volume	45% by volume
Density	1,6 g/cm^3
Fabric areal weight	600 gsm
Fabric type	Twill 2/2 balanced
Melt temperature	167°C
Glass Transition Temperature	-7°C
Processing Temperature	195-215°C
Tensile strength (ISO 527-4)	385 MPa
Tensile modulus (ISO 527-4)	18,5 GPa
Thickness	3mm

During the plastic injection; Polytron P40B001 which had 40 vol.% long glass fiber reinforced PP, was used as raw material. Technical properties of related raw material are given in Table 2.

Table 2. Technical properties of polytron P40B01 material

Density	1.22 g/cm^3
Flexural Modulus (ISO 178)	9000 MPa
Flexural Strength (ISO 178)	190 MPa
Tensile Modulus (ISO 527-2/1A)	10000 MPa
Tensile Strength (ISO 527-2/1A)	125 MPa
Notched Charpy Impact @-40°C Edgewise (ISO 179-1/1eA)	18 kJ/m^2
Notched Charpy Impact Edgewise (ISO 179-1/1eA)	20 kJ/m^2
Un Notched Charpy Impact @-40°C Edgewise (ISO 179-1/1eA)	45 kJ/m^2
Un Notched Charpy Impact Edgewise (ISO 179-1/1eA)	55 kJ/m^2

Over Molding Process

Before the over molding, epoxy resin based (OM10) prepreg material was reheated at 180^{o}C for 30 seconds at industrial type infrared furnaces. After the OM10 prepreg material was activated, material was inserted to the industrial type mold with robotic arm. There after mold was closed and PP GF40 (P40B001) material was injected onto the prepreg material between 15-30 seconds. Injection process parameters are given in Table 3.

Table 3: Injection process parameters

Insert Raw Material	Epoxy Resin based (OM10) prepreg
Injection Raw Material	Polytron P40B001 PP GF40
Injection Pressure	1000 TON
Mold Temperature	60 ^{o}C
Injection Speed	50 mm/sn
Holding Pressure	80 bar
Holding Time	7 sn

Finite Element Modelling

In this study, Catia V5 program was used as design program for the vehicle seat backrest and the Hypermesh program was used for finite element analysis (FEA). The reference methodology was given in Fig.1. In order to perform FEA of overmolded thermoplastic matrix based composite material, coupon samples were prepared from the relevant materials in accordance with ISO 517-4 standards. Instron 5982 model tensile test machine was used at a speed of 2 mm/min. Tensile tests were carried out on test samples in order to create a material database and to obtain the material data required for simulations at the desired scale.

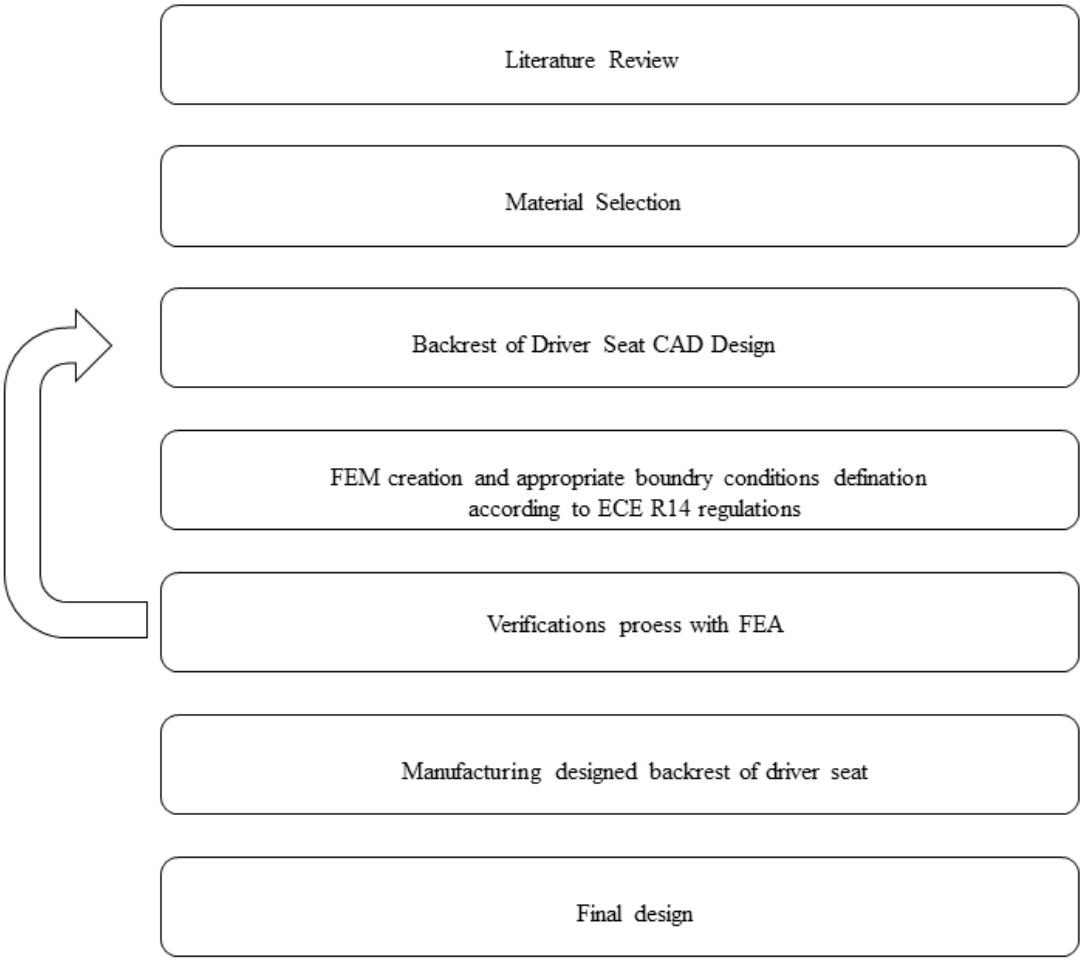

Figure 1. Flowchart of the backrest of driver seat design and analysis

As a result of the mechanical tests, various mechanical properties were obtained such as young's modulus, ultimate tensile strength and poisson ratio values. The obtained data were modelled in the Hypermesh program and solved in Radioss. Composite material's data was supported by the FEA, and a material card was created in the analysis program of the composite material. Finite element model test sample is shown in Fig. 2. Where h is the thickness of the composite material (2 mm), L_3 is the total length of the material (250 mm), L is unclamp total length (150 mm), b_1 is the width of the composite material (25 mm), L_0 is test length zone (approximately 50 mm), D is optional centering holes (5 mm).

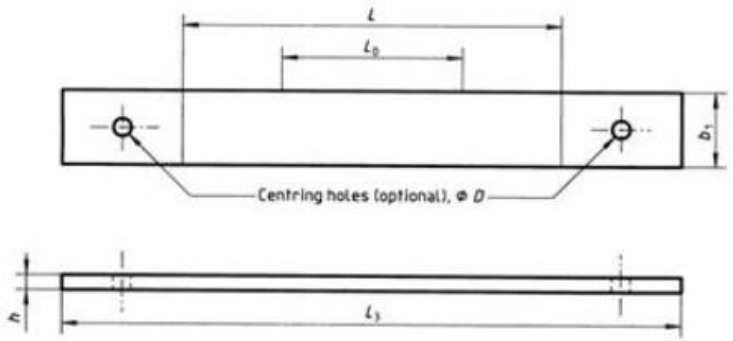

Figure 2. Finite element model test sample

After creating the material card, the model setup was done in the Hypermesh program. After removing middle surfaces of the entire structure, it was modelled using the shell element option. The element size was determined

as 5 mm considering the time and model flatness. The element properties were determined by using P1_shell and QEPH24, and the number of integration points was determined as 5. All components in the seat structure were modelled with this method. OM10 and Polytron P40B001 materials in the structure were combined using the node to node merge feature. The connection between the designed composite seat back and the body was provided with mechanical joints as bolts. Defined spring element modeling was used to model the used bolts.

Composite seat-backrest part design studies were carried out in 3 revisions (code of revisions rev1, rev2, rev3) in a computer-aided environment using the Catia V5 program. According to the ECE R14 regulation requirement, the applied load was shown in Fig. 3. According to this regulation, seat belt anchorage points and seat vehicle anchorage points should maintain their structural integrity, should not exceed the maximum displacement amount given in the regulation. There should not be any sharp corners on the seat that may cause injury.

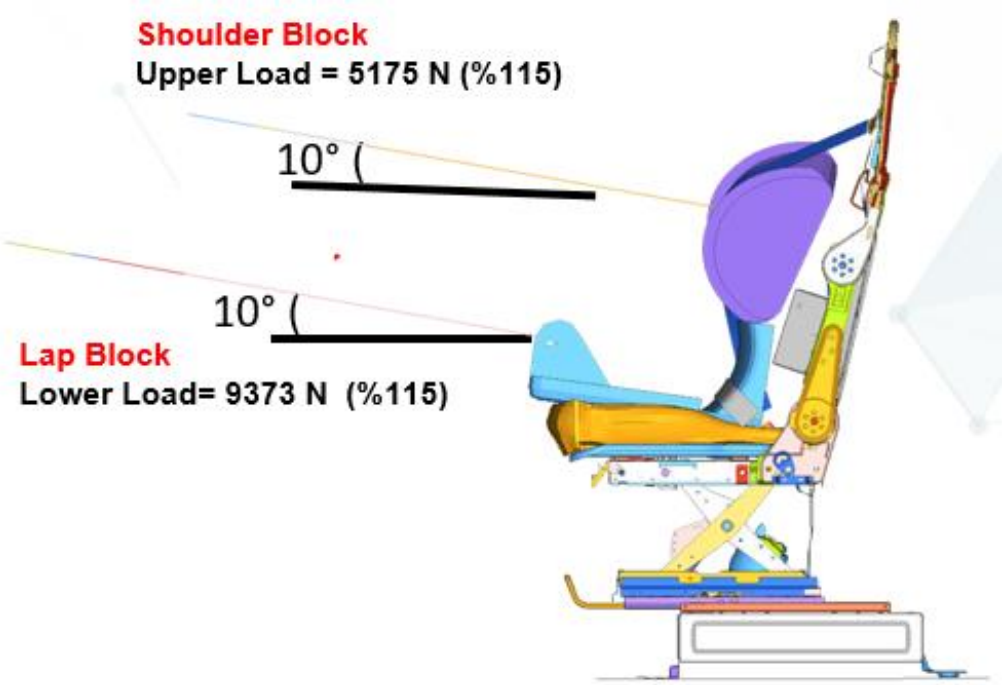

Figure 3. ECE R14 regulation virtual analysis model

Result and Discussion

The main purpose of performing virtual analysis modeling study on thermoplastic prepreg material is the finite element method modeling of (0°/90°) layered glass fiber reinforced PP matrix composite sample that mechanical properties are determined by the tensile tests and the use of this model in virtual analysis studies. In this direction, the material data used in the virtual analysis modeling studies of the relevant composite material and obtained from the tensile tests are given in Table 4

Table 4. Tensile test results of thermoplastic prepreg (OM10)

Pull Test - 0 ° (ISO 527-4)	Tensile Strength (MPa) - Xt	437,00
	Young's Modulus (GPa) - E1	20,90
	Basic (Major) Poisson's Ratio	0,06
Pull Test - 90 ° (ISO 527-4)	Tensile Strength (MPa) - Xt	417,00
	Young's Modulus (GPa) – E2	19,90
	Basic (Major) Poisson's Ratio	0,08

Xt: X direction, E1:1. Module of Elasticity, E2: 2. Module of Elasticity

Stress-strain curve of tested thermoplastic prepreg sample was given in Fig.4 compared to the simulation curve data. As can be seen in Fig.4, both obtained stress-strain curves of the sample had similar characteristics. In the analysis studies, it was observed that the maximum tensile strength value was 15 % higher than the mechanical test result.

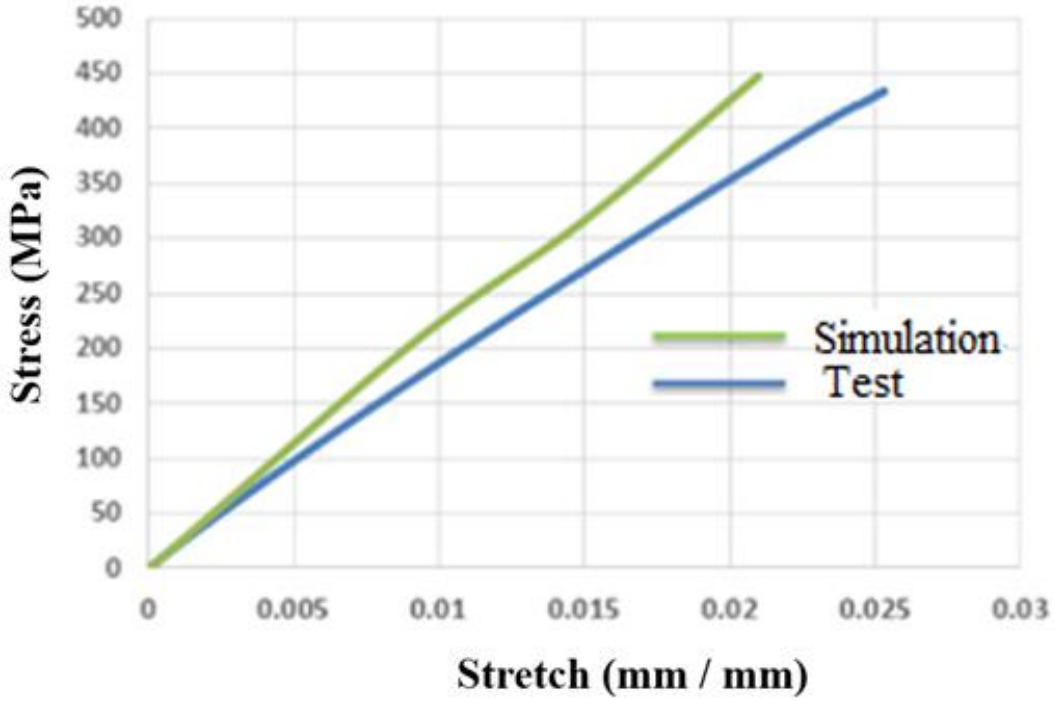

Figure 4. Stress-strain curve of tested thermoplastic prepreg sample compared to the simulation curve data

Technical information about the design studies is given in Table 5. In the Rev1 design, a U-shaped rib design was made and the effect of the stresses on the design during the ECE R14 simulation was analyzed. With the benchmark studies carried out in the Rev 2 design, the rib design in U form was canceled and a 45 ^{o} angle rib design was applied. ECE R 14 analysis results showed an improvement of approximately 13% according to Rev1. The Rev3 design, opposing 45 ^{o} angled rib designs were added to cross with previously designed 45 ^{o} angled ribs, and additional rib designs were added to the back of the seat. According to Rev 2 Approximately 45% improvement was observed in the ECE R 14 analysis results and the design studies were frozen.4

Table 5. Technical information about the design studies

Design of Rev1	
Main Material Thickness (Polytron P40B001)	3 mm
Type of Rib	U Type
Prepreg (OM10) Material Thickness	2 mm
Prepreg (OM10) Length / Width	300 mm / 100 mm
Design of Rev2	
Main Material Thickness (Polytron P40B001)	3 mm
Type of Rib / Rib Thickness	45 ^{o} angular / 1,5 mm
Prepreg (OM10) Material Thickness	2 mm
Prepreg (OM10) Length / Width	300 mm / 100 mm
Design of Rev3	
Main Material Thickness (Polytron P40B001)	3 mm
Type of Rib / Rib Thickness	45 ^{o} angular / 3 mm
Prepreg (OM10) Material Thickness	3 mm
Prepreg (OM10) Length / Width	300 mm / 100 mm

Various designs were realized depending on the examination of the metal structure in the reference seat and the research studies. Related designs are named as Rev 1-3. Criticalities were determined with the analysis made within the framework of the relevant designs, the sections in the design were changed according to these implications, and suitable load paths were created to transfer the load to other parts. In addition, design changes and improvements were made by taking the maximum stress and plastic elongation values as reference Fig. 5.

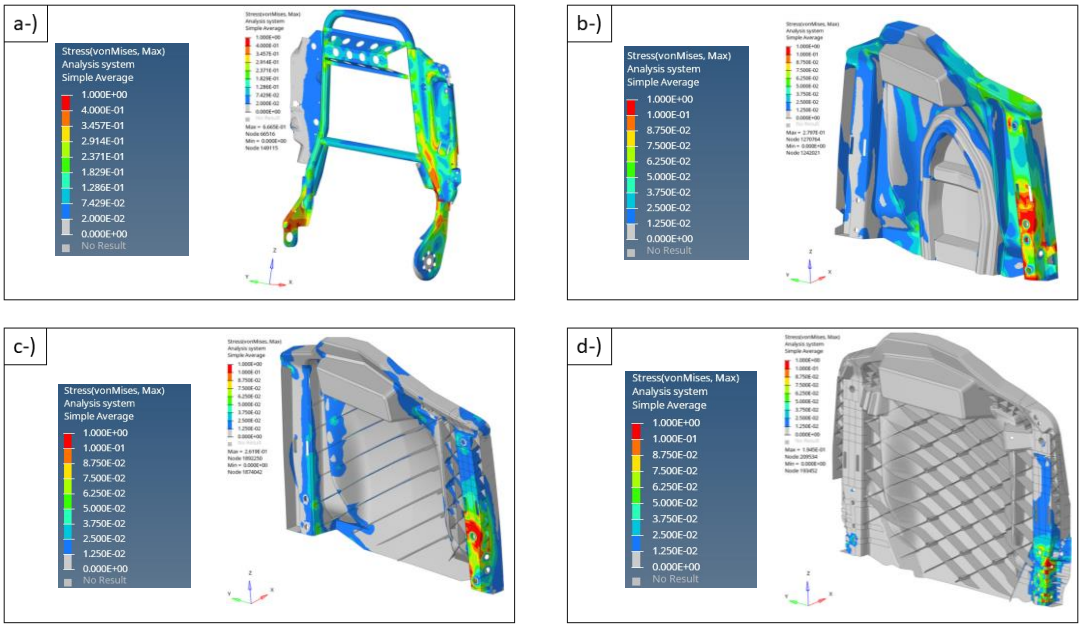

Figure 5. a-) Reference Seat Backrest(Metal), b-) Design of Rev1, c-) Design of Rev2, d-) Design of Rev3

Glass fiber reinforced polymer material was used as the material in the first phase of the design studies. Related studies were started with the reference model (metal backrest), which was carried out based on the investigation of the metal structure in the reference seat and the research studies. In this design, the structural tests applied on the metal seat frame were simulated in computer environment and the critical regions were determined by numerical analysis on a draft plastic body. ECE R14 loading results applied to various designs is given in Table 6.

Table 6. Results of maximum resultant stress on composite seat (axial and shear stress)

Reference Seat (Metal)	0,567 MPa
Design of Rev1	0,289 MPa
Design of Rev2	0,251 MPa
Design of Rev3	0,184 MPa

Conclusions

As a result of this study, sample modeling was made for finite element analysis of prepreg material with continuous glass fiber reinforced woven-based thermoplastic PP matrix, and the model correlation was achieved with the physical tests performed on the relevant sample. Then, using the material data, a finite element model was created and numerical analyzes were made on the seat.

Considering the analysis results, the design was developed and Rev3 design; It has been determined to be the best design within the scope of composite part optimization and analysis studies. Accordingly, the design phase was frozen in Rev3. The current version of the design is within the desired limit values within the ECE R14 regulation conditions

With the displacement of the metal and the composite structure, which is the main purpose of the study, a structure similar to metal in performance but lighter than metal was achieved. In this context, 1500 gr weight reduction has been achieved and success has been achieved regarding the related project target.

Acknowledgement

This study was supported by TUBITAK within the scope of TUBİTAK 1511 Priority Areas Research Technology Development and Innovation Program (Project number: 1160352).

We thankt to Assan Hanil Otomotiv San. ve Tic. A.Ş., for the design and analysis support. We thankt to Kordsa Teknik Tekstil A.S., for the technical support on prepreg material. We thankt to Karel Kalıp San. A.Ş., For the production and support of the overmolding plastic injection mold

References

Akkerman, R., Bouwman, M., & Wijskamp, S. (2020). Analysis of the thermoplastic composite overmolding process: interface strength. *Frontiers in Materials, 7*, 27.

Banerjee, S., & Sankar, B. V. (2014). Mechanical properties of hybrid composites using finite element method based micromechanics. *Composites Part B: Engineering, 58*, 318-327.

Carello. M, Amirth, N., Airale A.G., Monti, M., Romeo, A. (2017). Building block approach' for structural analysis of thermoplastic composite components for automotive applications. *Applied Composite Materials, 24*, 1309–1320.

European Environment Agency (2014). Monitoring CO_2 emissions from new passenger cars and vans in 2014. Retrieved from https://www.eea.europa.eu/publications/monitoring-emissions-cars-and-vans.

Ferruh D. (2017). Comparison of mechanical effect of different material usage in automotive passenger seat bearing with finite element method and tests. Master Dissertation. Uludağ University Graduate School of Natural and Applied Sciences Department of Automotive Engineering, Bursa.

Ning, H. Pillay, S., & Vaidya, U.K (2009). Design and development of thermoplastic composite roof door for mass transit bus. *Mater. Des., 30*, 983–991.

Prashik Sunil Gaikwad (2018), *Comprasion of steel and composite leaf springs using FEA*. Master Thesis https://rc.library.uta.edu/uta-ir/bitstream/handle/10106/27447/GAIKWAD-THESIS 2018.pdf?sequence=1&isAllowed=y

Schijve, W., Kulkarni, S. (2016) *New Thermoplastic composite solutions present viable options for automotıve lightweighting*, Sabic Innovation Plastics.

Tian Tuo Machinery (2018). Retrieved from https://frptitan.com/automotive-composite-column-vizilon-thermoplastic-composite-oil-pan/

Yuce C., Karpat F., Yavuz N., & Sendeniz G., (2014). A case study: Designing for sustainability and reliability in an automotive seat structure. *Sustainability, 6*, 4608-4631.

Author Information

Serkan Birçiçek
Kocaeli University
Institute of Science Polymer Science and Technologies, Umuttepe Campus, Kocaeli/Turkey
Contact e-mail: *serkanbircicek@gmail.com*

Mustafa Özgür Bora
Kocaeli University
Aviation Material Research and Development Laboratory, Faculty of Aeronautics and Astronautics, Kocaeli/Turkey

Erman Arkin
Assan Hanil Industry and Trade Inc
Kocaeli/Turkey

Bünyamin Yakar
Assan Hanil Industry and Trade Inc
Kocaeli/Turkey

Ersan Ertürk
Assan Hanil Industry and Trade Inc
Kocaeli/Turkey

Emre Gödek
Assan Hanil Industry and Trade Inc
Kocaeli/Turkey

The Eurasia Proceedings of Science, Technology, Engineering & Mathematics (EPSTEM)
ISSN: 2602-3199

The Eurasia Proceedings of Science, Technology, Engineering & Mathematics (EPSTEM), 2020

Volume 11, Pages 106-112

IConTES 2020: International Conference on Technology, Engineering and Science

Effect of Geometric Characteristics of Empty Metal Tanks on the Critical Dynamic Buckling Load

Mokhtar TOUATI
University of Science and Technology

Mohamed CHABAAT
University of Science and Technology

Abstract: We investigate a parametric study on dynamic buckling of empty steel tanks, anchored at the bottom and with open top. The study attempts to estimate the critical load (Pcr), which induces the elastic buckling at the top of the cylindrical shell under a suddenly applied concentrated load with infinite duration in the horizontal direction through transient dynamics analysis (including geometric non-linearity) using the finite element shell of the library of commercial software ANSYS while applying the criterion of Budiansky-Roth and checking by the plan-phase, and subsequently obtain the stabilization level of the critical buckling load versus the geometric characteristics of the tanks in question which led to their design. This study deals three types of tanks with heights (H) of 10m, 20m and 30m, each type has height-radius ratio (H/R) of 1/3, 2/3, 3/3, 4/3 and 5/3, giving fifteen tanks of the same thickness (t). It is reported that the effects of imperfections and damping was not considered. The investigation showed that the studied parameters have a pronounced effect on the buckling load of the tanks and the results are discussed in this study.

Keywords: Dynamic buckling, Critical load, Tanks

Introduction

Damage of metal tanks are usually recorded (Hamdan, 2000 and Seisme du 21 MAI, 2003) ALGERIE, with the existence of liquid, but rarely for the tanks empty, most of the work done in this context consider the instability of the tanks caused by major earthquakes (Fukuyama et al., 2001). A strong wind and turbulent may also lead to instability of the tanks and cause damage in its transitional phase (during its execution).

The area of instability "dynamic" structures is the subject of numerous studies over the past 40 years (Sahu and Datta, 2007) after a good mastery of the static analysis of thin shells (Touati, 2008). Similarly to the analysis of non-linearity of the problem (Moussaoui and Benamar, 2002). The choice of stability criteria is an essential element.

Lagrange in (1788) proposed a criterion, called from "energy criterion", which presents a potential energy minimum for a stable equilibrium. If this energy is maximum, the equilibrium is unstable. As for Mathieu-Hill (Budiansky, 1965), his theorem was used to identify areas of instability. The first observation of parametric resonance is attributed to Faraday in (1831), studies were conducted on the parametric resonance of cylindrical thin shells by Yao (1963, 1965).

A second type of dynamic instability for structures with post-critical behavior unstable type snap-trough, subjected to loads very fast (explosion, crash ...). The dynamic instability appears when realizes a slight disturbance on a structure under dynamic loading, the latter initiates a major shift from the original position undisturbed, this phenomenon is characterized by a jump more or less important from an initial state stable and a stable final state for a finite jump or even unstable for an infinite jump.

The application of the finite element method in the analysis of dynamic buckling of shells began in the 70s of last century. Experimentally, Ari-Gur et al. (1982) and Yaffe and Abramovich (2003) have undertaken a series of Work at the Haifa Institute of Aerospace, which struck first simple structures (columns) before spreading then more complex structures. Nagazawa et al. (1995) studied experimentally the behavior of thin cylindrical shells under seismic loading biaxial. Ren et al. (1983) conducted an experiment on the influence of impact velocities on the dynamic buckling of cylindrical shell. Michel, Limam and Jullien (2000) and Michel, Combescure and Jullien (2000) have designed an experiment to study the dynamic buckling under shear loading, then validated numerically.

Lundquist (1935) was the first to investigate the buckling of circular cylindrical shells under transverse shear. Clough and Wilson (1971) addressed the case of thin shells in the broader context of nonlinear dynamics. Recently Karagiozov and Jones (2000, 2001, 2002, 2004) have examined the dynamic elastic buckling of elastoplastic cylindrical shells (tubes) using a discrete method called "Buckward Differentiation Formula BDF". The effect of certain phenomena on the dynamic buckling were investigated but still so disparate, thus Petry and Fahlbush (2000) and others have studied the effect of imperfections, Simitis (1983) showed the effect of a static preload on the critical force.

Parametric studies were also held in this area, Virella et al. (2003) conducted a comparison of natural frequencies of cylindrical shells under the effect of different roof shapes, they have treated also three types of tanks with differents height-diameter ratios (H/D) by comparing modes of fundamental tank-liquid systems (Virella et al., 2006) and peak ground accelerations (PGA) relating to each type of tank (Virella et al., 2006). Regarding recommendations for the calculation of the efforts of various codes, a study was conducted by Barros (2008) by comparing the basal moments and basal shear of the various cylindrical tanks by varying the ratio of height-radius (H/R) one hand and the radius-thickness ratio (R/t) on the other hand. By cons Cao (2010) has treated the buckling of various tanks varying H/R and R/t under harmonic loading, and a recent parametric study of vibrations of different cylindrical shells under the effect of geometrics deformations took place (Kochurov and Avramov, 2011).

Characteristics of tanks and modeling of walls

The tanks to study are empty (under construction), with one end clamped and the other one free, schematically by elastic, thin, circular cylindrical shells. The metallic walled material is assumed to be homogeneous, isotropic, and linearly elastic with physical properties supposed to be Young's modulus $E= 210.10^6$ *KPa*, Poisson's ratio $\nu=0.3$ and density $\rho = 7.7\ t/m^3$.Fifteen tanks are studied, of same thickness ($t=1cm$) and different heights *H=10m, H=20m* and *H=30m* (Figure 1), each height contains five types of height-radius ratio (H/R) *1/3, 2/3, 3/3, 4/3* and *5/3* (Barros, 2010).

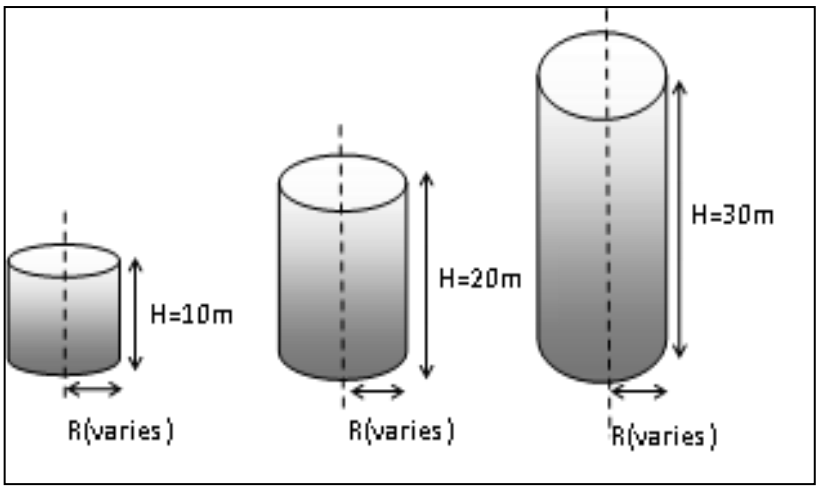

Figure 1. Characteristics of tanks with varying radius (R).

For modeling the thin-walled structures, a quadrilateral shell element, SHELL63 from the ANSYS element library (ANSYS 11 ,2004, Structural Analysis Guide), were used. These are four nodes, 3D elastic shells with both bending and membrane capabilities. The SHELL63 element has 6 DOFs at each node: 3 translations in the nodal x, y and z directions and 3 rotations about the nodal x, y and z axes. Convergence tests were conducted

using a series of different meshes: 10, 16, 24, 30 and 60 divisions along the shell axis, until obtaining the values of neighboring loads with deviations of less than 3%.

Methodology

Criteria for Dynamic Critical Conditions

Several approaches are used to calculate the instability conditions for this type of problem (Huyan, 1996). In this paper, the dynamic buckling critical load is determined by the approach of Budiansky-Roth (1962). In this criterion, the response is calculated for different loading parameters from the numerical solution of equations of motion. By drawing the curve of displacement versus time while varying the intensity of the applied load, a jump of the curve is found from the curves drawn for neighbouring values. A particular value of the load causing this remarkable leap corresponds to the critical value of dynamic buckling (Figure 2).

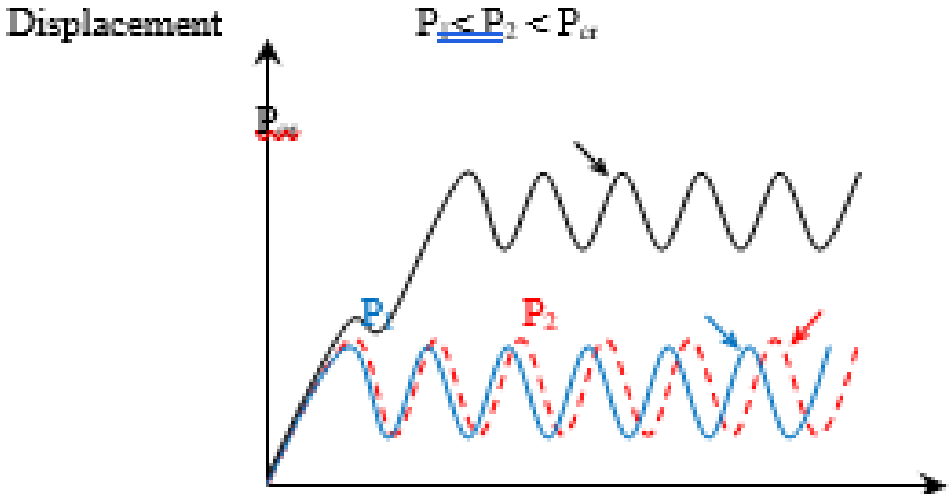

Figure 2. Detection of the critical load by criterion of Budiansky.

Once the buckling load is determined, the latter is verified by the phase plane (Hoff and Bruce, 1954), wich is plotted in a coordinate system (displacement, *x* and velocity, *dx/dt*). As the loading parameters are small, then stable movements describing paths closed are limited and focused around the solution of a static equilibrium in Figure 3a. On the other side, if the loading factor increases, a value is reached at which a movement gets away from the pole without any oscillation around him. In this case, the system is in the condition of instability having a critical value (Figure 3b).

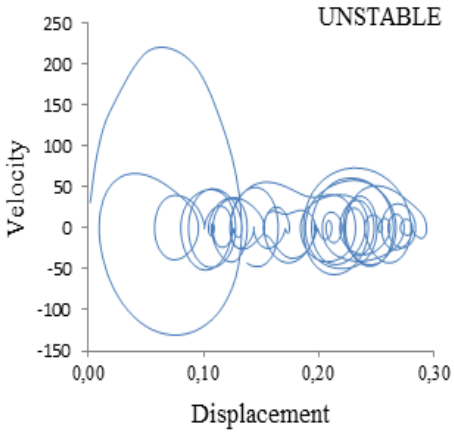

Figure 3.a. Phase-plane, stable motion.

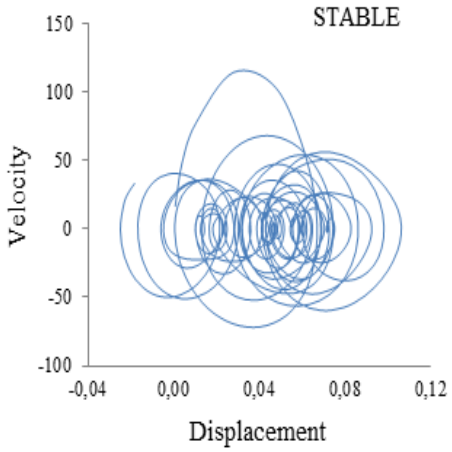

Figure3.b. Phase-plane,unstable motion.

Calculation Procedures

The calculation is achieved by a commercial software ANSYS (2004), solving the general equation of motion obtained by the different principles used in structural dynamics (Lagrange, Hamilton or virtual work)

$$M\ddot{x}(t) + C\dot{x}(t) + Kx(t) = P(t) \tag{1}$$

Where *M* is the mass matrix, *C* is damping matrix, *K* is the stiffness matrix, $\ddot{x}(t)$ is the acceleration vector, $\dot{x}(t)$ is the velocity vector, *x(t)* is the horizontal displacement vector and *P(t)* is the transient external dynamic load vector, concentrated horizontally at the top of the tank (Figure 4). This form of excitation is insensitive to the effects of imperfections relatively to the axial compression. The dynamic load is suddenly applied with constant magnitude and infinite duration which reflects the case of wind.

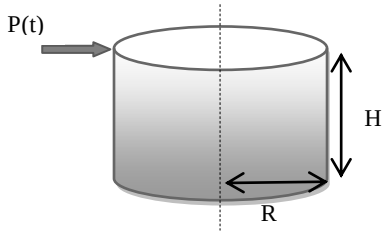

Figure 4. Tanks subjected to a concentrated load at the top.

To obtain answers on the displacement, velocity and accelerations, a transient analysis was used by solving the Equation 1 by direct integration method (step by step) often given by Newmark scheme (Newmark, 1959), displacement and velocity are developed at time n+1 by the Taylor formula (Equations 2 and Equation 3), β_s *and* γ_s are specific to the Newmark scheme and are chosen to control stability and accuracy.

$$x_{n+1} = x_n + \Delta t\dot{x}_n + \Delta t^2(1 - 2\beta_s)\frac{\ddot{x}_n}{2} \tag{2}$$

$$\dot{x}_{n+1} = \dot{x}_n + \Delta t(1 - \gamma_s)\ddot{x}_n \tag{3}$$

The expressions of Equation 2 and equation 3 are injected into the dynamic equilibrium Equation 1 to calculate the acceleration at n+1, Δt is chosen so that $\Delta t \leq 1/(20.f)$, *f* is the fundamental frequency of the structure.

If:

$$S = (M + \Delta tC + \Delta t^2K) \tag{4}$$

We obtain:

$$S\ddot{x}_{n+1} = P_{n+1} - C\dot{x}_{n+1} - Kx_{n+1} \tag{5}$$

S and the second member are fully known, the resolution of linear system (5) evaluates the acceleration at n+1. The displacement and velocity are finally obtained by injecting the value of this acceleration in expressions 2 and 3.

Numerical Results

The results of tanks of *H=10m* for different ratios of height-radius *H/R=1/3, 2/3, 3/3, 4/3* and *5/3* are shown in Figure 5, those tanks *H=20m* in the Figure 6 and for tanks of *H=30m*, the critical load values are shown in Figure 7.

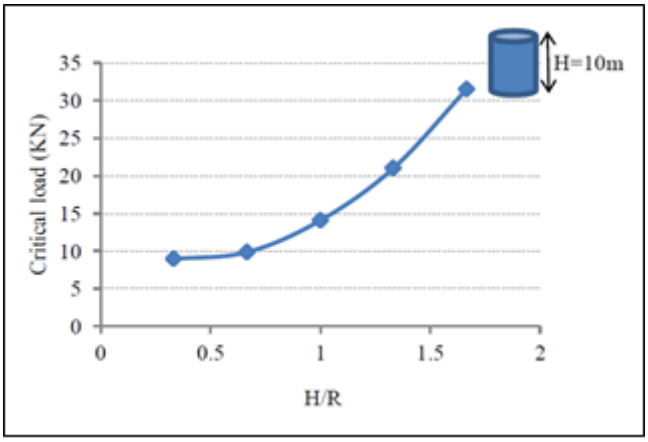

Figure 5. Variation of critical load versus h/r of tank h=10 m.

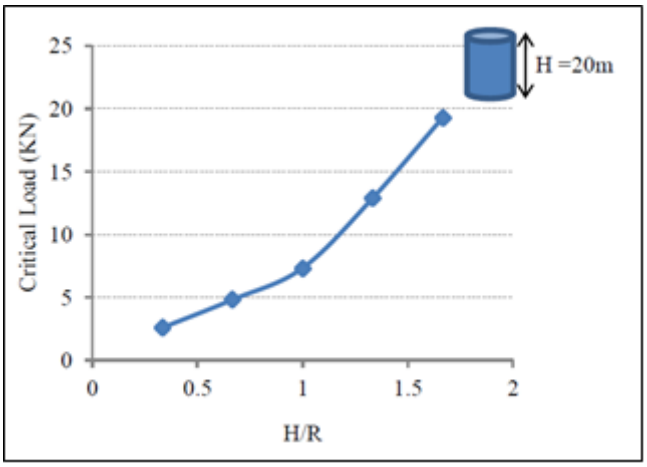

Figure 6. Variation of critical load versus h/r of tank h=20 m.

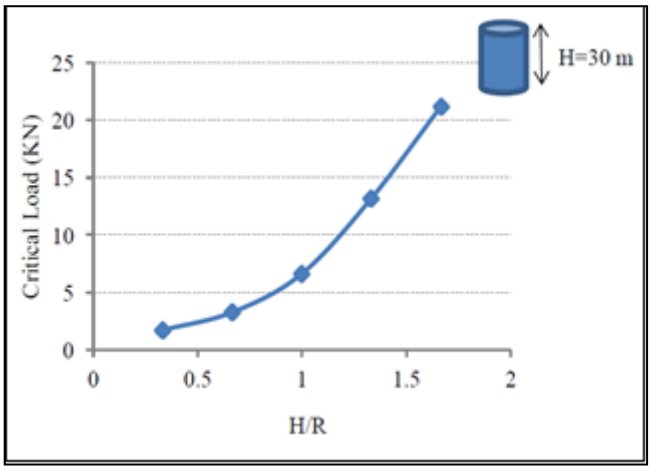

Figure 7. Variation of critical load versus h/r of tank h=30 m.

Conclusion

The results of the tank with constant thickness and radius-height ratios (H/R) variables, the dynamic buckling critical load increases with the increase of the ratio (H/R), this increase is considerable From R=H. while the stabilization of this charge appears to below R=3H, Similarly we can determine the optimum size of heights and radius of these tanks with H/R < 1 / 3.

References

ANSYS (2004) *Structural Analysis Guide*. ANSYS, Inc., Houston

Ari-Gur J., Weller T., & Singer J. (1982) Experimental and theoretical structures of columns under axial impact. *Int. Journ. Solids and Structures*, 18, 619-641.

Barros R. C. (2010) On the Comparative Seismic Design of Anchored Bottom Supported Tanks, In: *The 14th European Conference on Earthquake Engineering*, Ohrid – Macedonia.

Barros R. C. (2008) Parametric study of the seismic response of anchored metallic tanks by international design codes, In: *The 14th WCEE*, Beijing, China, (pp. 12-17).

Budiansky B. & Roth R. S. (1962) Axisymmetric dynamic buckling of clamped shallow spherical shells. Collected papers on instability of shell structures, *NASA TN D 1510* , Washington, (pp. 597-606).

Budiansky B. (1965) Dynamic buckling of elastic structures, Criteria and estimates, *Proceeding of an International Conference on Dynamic stability of structures*, North-western University, Evanston, Illinois, (pp. 83-106).

Cao Q. S. & Zhao Y. (2010) Buckling strength of cylindrical steel tanks under harmonic settlement, *Thin-Walled Structures, 48*, 391-400.

Clough R. W. & Wilson E. I. (1971) Dynamic finite element analysis of arbitrary thin shells, *Computers and Structures, 1*, 33-56.

Fukuyama M., Nakagawa M., Yashiro T., Toyoda Y. & Akiyama H. (2001) Seismic design method of clamped-free thin cylindrical shells immersed in fluid, *Nuclear Engineering and Design, 207*, 147–162.

Hamdan F. H. (2000) Seismic behaviour of cylindrical steel liquid storage tanks, *Journal of Constructional Steel Research, 53*, 307–333.

Hoff N. J. & Bruce V. C. (1954) Dynamic analysis of the buckling of laterally loaded flat arches, *J. Math. Phys, 32*, 276-288.

Huyan X. (1996) Dynamic stability of cylindrical shells of various constructions, *Ph.D. Thesis*, University of Cincinnati, USA.

Kochurov R. E. & Avramov K. V. (2011) Parametric vibrations of cylindrical shells subject to geometrically nonlinear deformation: multimode models, *International Applied Mechanics, 46*(9), 50-59.

Lundquist E. E. (1935) Strenght tests of thin-walled duralumin cylinders in combined transverse shear and bending, *NACA Report 523, National Advisory Committee for Aeronautics*, Washington.

Michel G., Combescure A. & Jullien J. F. (2000) Finite element simulation of dynamic buckling of cylinders to periodic shear, *Thin-Walled Structures, 36*, 111-135.

Michel G., Limam A. & Jullien J. F. (2000) Buckling of cylindrical shells under static and dynamic shear loading, *Engineering Structures, 22*, 535-543.

Moussaoui F., Benamar R. (2002) Non-linear vibrations of shell-type structures, a review with bibliography, *Journal of Sound and Vibration, 255*(1), 161-184.

Nakagawa P., Fukuyama M., Ishihama K., Ikeuch H., Hagiwara Y. & Akiyama H. (1995) Pseudo-Dynamic buckling experiments on thin cylindrical shells under biaxial seismic loads, *Nuclear Engineering and Design, 157*, 27-36.

Newmark N. M. (1959) A method of computation for structural dynamics, *Jour Eng Mech Div ASCE, 85*, 67–94.

Petry, D. & Fahlbush, G. (2000). Dynamic buckling of thin isotropic plates subjected to in plane impact. *Thin-Walled Structures, 38*, 267-283.

Ren, W., Zhuping, H. & Qingshum, Y. (1983) An experimental study of the dynamic axial plastic buckling of cylindrical shells. *Intern. Impact. Engineering, 1*, 249-256.

Sahu S. K. & Datta P. K. (2007) Research advances in the dynamic stability behaviour of plates and shells for conservative system: 1987-2005, *Applied Mechanics Reviews, 60*, 65-75.

Virella, J. C., Godoy, L. A. & Su´arez, L. E. (2003) Influence of the roof on the natural periods of empty steel tanks. *Engineering and Structures, 25*, 877–887.

Virella, J. C., Godoy, L. A. & Su´arez, L. E. (2006) Dynamic buckling of anchored steel tanks subjected to horizontal earthquake excitation. *Journal of Constructional Steel Research, 62*, 521–531.

Virella, J. C., Godoy, L. A. & Su´arez, L. E. (2006). Fundamental modes of tank-liquid systems under horizontal motions. *Engineering and Structures, 28*, 1450–1461.

Yao J. C. (1965) Nonlinear elastic buckling and parametric excitation of a cylinder under axial loads, *Journ. Appl. Mech., 32*, 109-115.

Yao J. C. (1963) Dynamic stability of cylindrical shells under static and periodic axial and radial load, *AIAA Journal*, 1, 1391-1396.

Author Information

Mokhtar Touati
University of Science & Technology Houari Boumediene
LBE, Civil Engineering Faculty, University of Science & Technology Houari Boumediene (USTHB)
BP 32 El-Alia / Bab Ezzouar / Algiers, ALGERIA
Contact e-mail: *touatimokh@yahoo.fr*

Mohamed Chabaat
University of Science & Technology Houari Boumediene
LBE, Civil Engineering Faculty, University of Science & Technology Houari Boumediene (USTHB)
BP 32 El-Alia / Bab Ezzouar / Algiers, ALGERIA

The Eurasia Proceedings of Science, Technology, Engineering & Mathematics (EPSTEM)
ISSN: 2602-3199

The Eurasia Proceedings of Science, Technology, Engineering & Mathematics (EPSTEM), 2020

Volume 11, Pages 113-124

IConTES 2020: International Conference on Technology, Engineering and Science

On Flying-Handling Qualities of B747-100 Longitudinal Flight based on Gain Scheduling Control

Ezzeddin ELARBIA
The University of Tripoli

Abdulhamid GHMMAM
The University of Tripoli

Saad ISSA
The University of Tripoli

Abstract: This paper evaluates flying handling qualities (FHQ) for the Boeing 747-100 (B747-100) in longitudinal flight. A genuine control has been realized using the spline gain-scheduling approach and full-state feedback linear quadratic regulator (FSFLQR). Converged steady-state responses have been shown for longitudinal states over Mach number and altitude ranging from 0.2 to 0.9 and sea-level to 12190m respectively. However, the FHQ verifications of such gain-scheduling control design are done using control anticipation parameter (CAP), normalised parameters of pitch rate and Cstar (combination effects of pitch rate, pitch and normal acceleration responses). The controller has been identified at which those conditions to be reformulated so that all the FHQ criteria are being satisfied. The CAP criterion well respects the level I of FHQ boundaries. However, some spectra of normalised pitch rate and Cstar with respect to their steady states slightly infringe the FHQ boundaries. This study has shown such a successful implementation of the gain-scheduling controller in terms of converged normal accelerations as well.

Keywords: Flying handling quality, Tracking longitudinal responses, Gain scheduling, Pitch rate criterion, CAP criterion, Cstar criterion, Normal acceleration

Introduction

As being revealed by Cooper and Harper (Etkins, 1994), ‘‘handling qualities are simply the ease and precision to support an aircraft flight.’’ Adequate handling qualities (HQ) would be required for successful flight performance by considering the numerical pilot rating (1-10) or the Cooper and Harper scale (CHS). For example, considering transport aircraft at low-speed longitudinal controlled flight, pilot rating is specified ten at CHS for deficiency in control performance whereas pilot rating is agreed to be one for adequate performance with tolerable pilot workload and satisfactory control characteristics (Etkins, 1994) and the intermediate ratings are gradually shown how the deficiency being improved. Primarily, the HQ criteria would be evaluated using mathematical models of the aeroplane as well as the pilot interaction control systems. The HQ depends on aircraft dynamics, control system performance, cockpit environment, outside view, and instrument display (Mclean, 1990). The development of HQ criteria has been made by the pilots’ opinions, aircrafts evaluations, in-flight simulation, and ground-based simulators (Jitendra & Jatinder, 2009). Various government agencies are complying with HQ requirements for military aircraft as well as transport aircraft which demand the safe operation rather than the manoeuvrability performance. Modern aircraft development requires full HQ evaluation for different controller modes, loadings, and various operational missions throughout the flight regimes. Flight testing would be time-wasting to cover wide-ranging conditions over the whole flight envelope.

After the 2nd World War with the increase of aircraft flying speed and altitude, the flight envelope has been enlarged a lot and the incidence time lag between the pitch rate response and the normal acceleration response may vary from 0.5s at a high speed and low altitude to 4.0s at low speed and high altitude. Several important

- Selection and peer-review under responsibility of the Organizing Committee of the Conference

evaluation criteria of aircraft's longitudinal flying handling qualities are known such as bandwidth criterion, time lag, *CAP* and *Cstar* (*C**) criteria. Bandwidth criterion characterizes the phase roll-off using a phase delay parameter whereas *CAP* clarifies that the initial pitch attitude response of the aircraft ascertains the ultimate response of the flight path (Jitendra, & Jatinder, 2009). Besides, Neal–Smith criterion evaluates the closed-loop performance based on the lead-lag compensation used by the pilot. However, the *Cstar* criterion is widely used by control system designers using a combination of the pitch rate (at low speeds) and the normal acceleration (at high speeds) responses (Jitendra, & Jatinder, 2009).

HQPACK MATLAB package was designed to predict handling qualities and pilot induced oscillation tendencies of aircraft (Shaik, & Chetty, 1998). Also, the HQ of large transport aircraft software (HQLTASW) was evaluated with the NLR's database for Fokker F28/Mk6000 aircraft (Shaik, 2005). Sample software control algorithms were developed to improve the flying qualities of general aviation aircraft and the results also rated the HQs (Rogalski, & Dołega, 2006). Flying qualities and guidance displays were evaluated for an advanced tilt-wing STOL transport aircraft in the final approach and landing (Frost, *et. el.* 2002). The aircraft, control modes, and display combination produced satisfactory flying qualities for all operations excepting that an extremely severe crosswind and wind shear. Effective relationships were found between FQ levels and 52 tests of Mach number, altitude and angle of attack for longitudinal and lateral flight of F/A-18 aircraft (Botez,& Rotaru, 2007).

Many literatures miss out evaluating FHQs of augmented flight control system, particularly for linear quadratic regulator (LQR) and classical control algorithms. For examples: Tosun controlled quadrotor position using the LQR to reach desired attitudes (Tosun, *et. al.*, 2015). LQR control was improved using an integral action for mass-related uncertainties showing the effective stabilisation of the star-shaped Octrotor vehicle (Adîr, & Stoica, 2012). Six degrees of freedom control of a small-scale quadcopter was achieved by an integral LQR for highly tracking and balancing responses (Joukhadar ,*et. el.*, 2015). The linear quadratic Gaussian (LQG) method was used to attenuate the pitching longitudinal noise of cruise aircraft (Shaji, & Aswin, 2015). LQR and LQG controllers showed the accuracy of an attitude microsatellite stabilisation comparing with feedback quaternion and proportional-integral-derivative (PID) designs (Tayebi, *et. el.*, 2017). The LQR method was applied for disturbed longitudinal flight of an unmanned aerial vehicle where the reference speed reached quickly without affecting altitude and pitch angle (Hajiye, *et. el.*, 2015). A good LQR performance was found in real-time pitching stabilisation for reference tracking as high as 55 degrees for a helicopter (Bharathi, & Kumar, 2013). A satisfactory LQR performance was also found for a SUAVE tilt-wing quadrotor during the yaw angles (Oner, *et. el.*, 2009).

This work mainly investigates the FHQ criteria over the B747-100 longitudinal flight envelope. A genuine gain-scheduling FSFLQR controller was already designed over Mach numbers (*M*) and altitudes (*H*) ranging from 0.2 to 0.9 and sea-level to 12190m respectively (Elarbi, *et. el.*, 2019). The gain-scheduling scheme was considered a continuous function of two scheduling variables (*M* and *H*). The gain scheduling methodology is a very effective way to control a nonlinear system since the 1960s (Mclean, 1990). However, gain-scheduling controllers have been widely used in industrial automated machines and aviation since the 1990s (Mclean, 1990). Here, particular attention was paid to longitudinal variables of axial velocity (u), transverse velocity (w), pitch rate (q) and pitch attitude (θ) coupling with elevator (δ_e) and throttle (δ_t). The multivariable dynamics of aircraft control was presented by a linearized state-space (LSS) model. 27 design pairs of *M* and *H* were uniformly sampled using the Latin hypercube approach for an optimised flight landscape (Elarbi, *et. el.*, 2019). A spline gain scheduling interpolation (Chapra, & Canale, 2010) was used to obtain the intermediate responses over the *M-H* ranges meeting velocities and altitudes objectives. Extensive studies related to the FHQs specification will here be undertaken, before being satisfied that the gain scheduling design is acceptable. Normalised pitch rate; *CAP* criteria; and normalised *Cstar* are evaluated over the longitudinal flight envelope. No obvious infringements the level I of FHQ boundaries are seen for the spectra of normalised pitch rate and *Cstar* responses with respect to (wrt) their steady-state values. The *CAP* criteria are well respected the level I of FHQ boundaries. Also, converged normal acceleration responses confirm the successful FSFLQR control based on the gain scheduling design over the B747-100 longitudinal flight envelope.

Analysis Method

Longitudinal Flight Model

The longitudinal flight model cross-coupled with elevator and throttle controls can be given in the LSS form by

$$\begin{bmatrix} \dot{u} \\ \dot{w} \\ \dot{q} \\ \Delta\dot{\theta} \\ \dot{h} \end{bmatrix} = A(M,H) \begin{bmatrix} u \\ w \\ q \\ \Delta\theta \\ h \end{bmatrix} + B(M,H) \begin{bmatrix} \Delta\delta_e \\ \Delta\delta_t \end{bmatrix} \quad (1)$$

where $A(M,H)$ is A/C dynamics matrix of 5×5 and $B(M,H)$ is a control design matrix of 5×2. These matrices parameters which depend on Mach number and altitude are given below

$$A(M,H) = \begin{bmatrix} X_u & X_w & 0 & -g & 0 \\ Z_u & Z_w & u_0 & 0 & 0 \\ M_{p,u} + M_{p,\dot{w}} Z_u & M_{p,w} + M_{p,\dot{w}} Z_w & M_{p,q} + M_{p,\dot{w}} u_0 & 0 & 0 \\ 0 & 0 & 1 & 0 & 0 \\ 0 & -1 & 0 & u_0 & 0 \end{bmatrix} \quad (2)$$

$$B(M,H) = \begin{bmatrix} X_{\delta_e} & X_{\delta_t} \\ Z_{\delta_e} & Z_{\delta_t} \\ M_{p,\delta_e} + M_{p,\dot{w}} Z_{\delta_e} & M_{p,\delta_t} + M_{p,\dot{w}} Z_{\delta_t} \\ 0 & 0 \\ 0 & 0 \end{bmatrix} \quad (3)$$

where the derivatives of forwarding force (X), transverse force (Z) and pitching moment (M_p) are given wrt axial velocity (u), normal velocity (w), transverse velocity derivative ($\dot{w}$), pitch rate (q), elevator deflection (δ_e) and throttle actuation (δ_t). u_0 is a steady-state velocity and g is a gravity acceleration (9.81m/sec^2). The full-states longitudinal responses can easily be obtained by regarding all the states as system outputs. Thus, the output observation matrix and the state transition matrix were taken unity and nullity matrices respectively.

FSFLQR Algorithm

A full state feedback (FSF) design is obtained by choosing a gain matrix (K (M,H)) which is a linear combination of the longitudinal states. The optimal control law is given as,

$$\begin{bmatrix} \Delta\delta_e \\ \Delta\delta_t \end{bmatrix} = -\mathrm{K}\,(M,H) \begin{bmatrix} u \\ w \\ q \\ \Delta\theta \\ h \end{bmatrix} \quad (4)$$

The LQR control law is typically used to find the optimal control gains for a multivariable large scale system. The controller can be tuned by adjusting the state and control weighting matrices. The cost function ensures that J is non-negative and zero for the optimal tracking system.

$$J = \int_0^{tf} \left[\left(\begin{bmatrix} u & w & q & \Delta\theta & h \end{bmatrix} \mathrm{Q}(M,H) \begin{bmatrix} u \\ w \\ q \\ \Delta\theta \\ h \end{bmatrix} \right) + \left(\begin{bmatrix} \Delta\delta_e & \Delta\delta_t \end{bmatrix} \mathrm{R}(M,H) \begin{bmatrix} \Delta\delta_e \\ \Delta\delta_t \end{bmatrix} \right) \right] dt \quad (5)$$

Here $\mathrm{Q} = \mathrm{Q}^{\mathrm{T}} \geq 0$ is 5×5 state weighting matrix and $\mathrm{R} = \mathrm{R}^{\mathrm{T}} > 0$ is 2×2 control weighting matrix. t_f is control time. The state feedback gain matrix in Eq. (4) can be obtained from

$$\mathrm{K}(M,H) = \mathrm{R}(M,H)^{-1} \mathrm{B}(M,H)^T \mathrm{P} \quad (6)$$

Matrix P is obtained by solving the steady-state algebraic equation below

$$-\mathrm{PA}(M,H) - \mathrm{A}(M,H)^{\mathrm{T}}\mathrm{P} + \mathrm{PB}(M,H)\mathrm{R}(M,H)^{-1}\mathrm{B}(M,H)^T\mathrm{P} - \mathrm{Q}(M,H) = 0 \quad (7)$$

Once the optimal LQR gains, K, results in swift longitudinal convergences the autopilot takes place for tracking.

Gain Scheduling Design

The interpolations of the longitudinal flight variables will be applied over the discretized flight envelope. Physical design plans are chosen as $M \in [0.2, 0.9]$ and $H \in [0, 12190]$

$$M^{(i)}, H^{(j)} = \frac{(M^{(i)}, H^{(j)}) - (M_l, H_l)}{(M_u, H_u) - (M_l, H_l)} \tag{8}$$

where M_u and M_l are the upper and lower bounds of M respectively whereas H_u and H_l are the upper and lower bounds of H respectively. The cubic splines will be used to determining intermediate responses for a group of systematic data points which can be defined as (Chapra, & Canale, 2010),

$$f(M) = f(M_i) + \frac{f(M_{i+1}) - f(M_i)}{M_{i+1} - M_i}(M - M_i) \qquad M_1 \leq M \leq M_n \tag{9}$$

$$f(H) = f(H_i) + \frac{f(H_{i+1}) - f(H_i)}{H_{i+1} - H_i}(H - H_i) \qquad H_1 \leq H \leq H_n \tag{10}$$

where data points i = 1, 2, 3 …, n and n is number of intervals. These equations are used to predict the LQR gains and state-space models at the selected intervals. The nth equations can then be employed to compute values within each interval. The scheme was implemented using built-in MATLAB functions which result in a more memory-efficient implementation than a lookup table.

FHQ Criteria

Flying handling qualities describe the easy, precise and rapid level when pilot controlling an aircraft to conduct flying tasks, such as flight refuel, landing and rolling. The MIL-F-8785 standard 'Military Specification, Flying Qualities of Piloted Airplane' based on enormous flying experience data and flight simulator tests were created by the military aeronautic organization, and the last version was released in 1980 in which aircraft is described in a linear mathematical model. Of the numerical requirements is system parameters based on aircraft's mathematical model, for example, natural frequency and damping ratio. Three important FHQ criteria used in this work are represented next

Pitch Rate Criteria

Pitch rate FHQ criterion is evaluated using the pitch rate history in the normalized form concerning the steady-state pitch rate which should be sited within specified boundaries. The steady-state pitch rate can be obtained using the final value theory as below

$$\frac{q_{ss}}{\Delta\delta} = lim_{s \to 0}\left(\frac{q(s)}{\Delta\delta}\right) \tag{11}$$

The normalized pitch rate concerning steady-state pitch rate is given by

$$\frac{q}{q_{ss}} = \frac{q}{\Delta\delta} . \frac{\Delta\delta}{q_{ss}} \tag{12}$$

CAP Criteria

Control anticipation parameter is the ratio of the initial pitch acceleration to the steady-state normal acceleration. The CAP criteria measures how the trimmed flying condition coincides with what the pilot expected. The maximum CAP boundaries indicate the manoeuvrability constraints in terms of short-term natural frequency. Large CAP value specifies sensitive and abrupt aircraft response and small CAP means sluggish and overshooting aircraft (Mclean, 1990). CAP can be expressed by the formula below (Mclean, 1990),

$$CAP = \frac{sq(\infty)}{az(0)} = \frac{{\omega_{sp}}^2}{az_{\propto}} \tag{13}$$

From the flying geometric model and ignoring the effect of gravity, normal acceleration at the aircraft centre of gravity for perturbed motion is defined as

$$\frac{az(s)}{\Delta\delta} = \frac{sw(s)}{\Delta\delta} - u_0 \frac{q(s)}{\Delta\delta} \tag{14}$$

where ω_{sp} is short period frequency. Normal load factor wrt angle of attack can be expressed as,

$$az_{\propto} = \frac{az(s)}{\Delta\delta} . \frac{\Delta\delta}{\Delta\propto(s)} = \frac{1}{g} . \frac{az}{\Delta\propto} \tag{15}$$

Cstar Criteria

The *Cstar* criteria assess the dynamic response of the aircraft longitudinal motion wrt the normal acceleration and pitch acceleration. The pitch rate of aircraft should be laid between specific *Cstar* criteria limits (Mclean, 1990). The *Cstar* criteria may be arranged so;

$$\frac{Cstar(s)}{\Delta\delta} = \frac{1}{g}\left(\frac{az(s)}{\Delta\delta} + V_c \frac{q(s)}{\Delta\delta}\right) \tag{16}$$

where V_c is a crossover velocity. The steady-state *Cstar* can be found by

$$\frac{Cstar_{ss}}{\Delta\delta} = lim_{s\to 0}\left(\frac{Cstar}{\Delta\delta}\right) \tag{17}$$

The normalized *Cstar* criteria may now be rearranged so

$$\frac{Cstar}{Cstar_{ss}} = \frac{Cstar}{\Delta\delta} . \left(\frac{Cstar_{ss}}{\Delta\delta}\right)^{-1} \tag{18}$$

Discussions of Results

Flight Envelope Discretization

A symmetric longitudinal flight manoeuvre was considered under small perturbations with almost comparable stall speed and cruise speed. The B747-100 flight envelope for the *M* range from 0.2 to 0.9 and the *H* range from sea-level to 12190m is shown in Fig. 1.

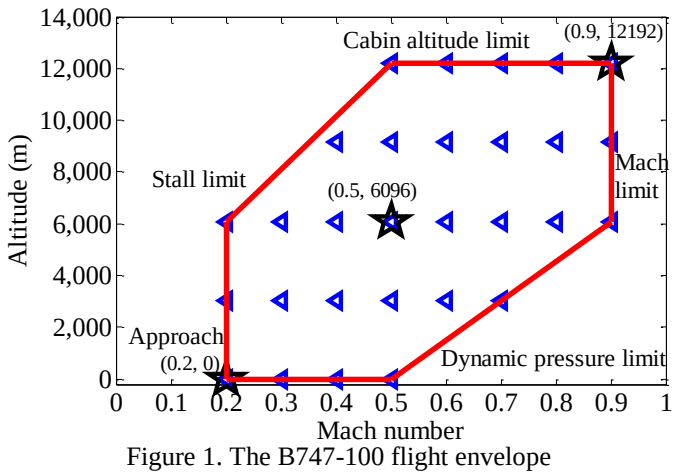

Figure 1. The B747-100 flight envelope

The Latin hypercube design (Forrester., *et. al.*, 2008) was used to select operating points for Mach number of 0.1 and altitude of 3048m. The black stars signify equilibrium points: (0.2, 0), (0.5, 6096m) and (0.9, 12190m). 27 points over the flight envelope were chosen to avoid overlapping gain scheduling, the regions of the dynamic pressure and stall limits. The spline approach was applied in connecting lower-order polynomials of subsets. Then the gain scheduling approach was used to interpolate based on the equilibrium points' simulations. Therefore, all the flight and stability derivatives were obtained to fulfil the control law of the most flight scenarios.

Pitch Rate Criteria Responses

The FHQ pitch rate time-history criterion evaluations over the *M-H* flight envelope are shown in Fig. 2. The pitch rate transfer function and the steady-state pitch rate were found over the flight envelope ($H_i = 0 - 12190$m and $M_i = 0.2 - 0.9$) below.

$$\frac{q}{\Delta\delta} = \frac{\begin{array}{c}(12.8H + 2\times10^5M + 6.39HM - 3.1\times10^5)s^4 + \\ (49.37H + 8.75\times10^5M + 25.43HM - 9.94\times10^5)s^3 + \\ (56.88H + 8.38\times10^5M + 28.03HM - 1.46\times10^6)s^2 + \\ (91.09H + 0.24\times10^5M + 1.36HM + 8.72\times10^6)s \\ (35.38H + 4.56\times10^5M + 16.96HM - 1.03\times10^6)\end{array}}{\begin{array}{c}(-1.04\times10^{-5}H + 0.219M - 2.37\times10^{-6}HM + 0.956)s^5 \\ +(1.55H + 7.2\times10^4M + 1.13HM + 5.14\times10^4)s^4 + \\ (182.53H + 5.35\times10^6M + 109.67HM + 2.41\times10^5)s^3 + \\ (-50.64H + 9.73\times10^5M - 12.26HM + 4.48\times10^6)s^2 + \\ (-90.43H - 1.16\times10^6M - 43.34HM + 2.63\times10^6)s + \\ (-231.43H - 2.89\times10^6M - 110.22HM + 6.91\times10^6)\end{array}}$$

$$\left.\frac{q_{ss}}{\Delta\delta}\right|_{\forall\,(M,H)} = \frac{(35.38H + 4.56\times10^5M + 16.96HM - 1.03\times10^6)}{(-231.43H - 2.89\times10^6M - 110.22HM + 6.91\times10^6)}$$

Table 1 valuates the steady-state pitch rate wrt the combined control inputs over the flight envelope. The "*s*" variable terms in numerator and denominator were eliminated by applying the final value theory on the transfer function terms. The steady-state pitch rate wrt one degree of control input over the flight envelope varies from -80.7×10^{-3} to -148×10^{-3} sec^{-1}. Although small pitch rates were found authorizing the steady-state longitudinal flight the negative signs indicated violent nose-down tendencies due to the reverse pitch damping.

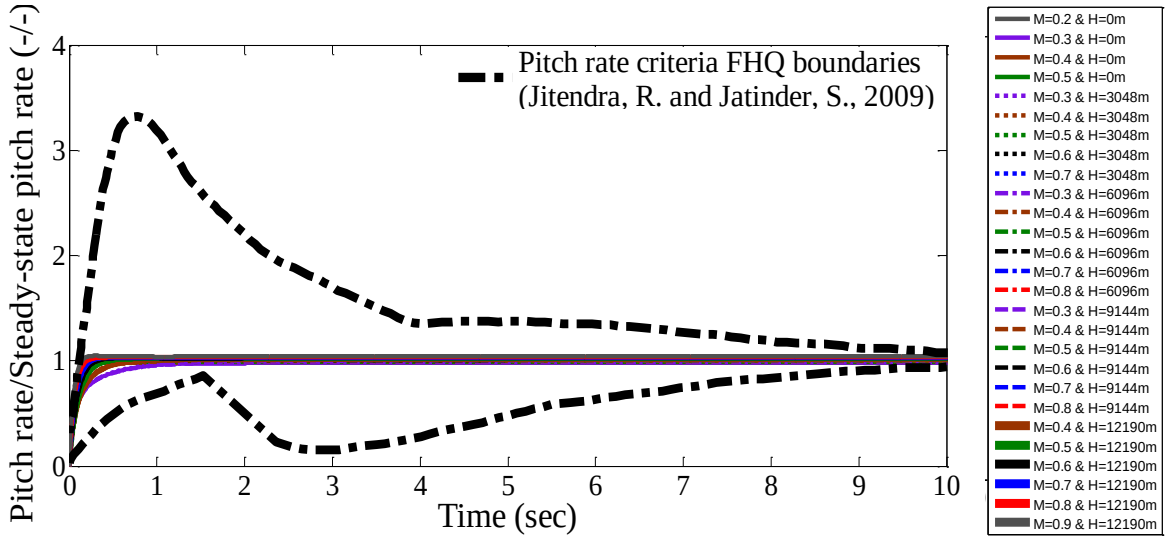

Figure 2. FHQ pitch rate criteria over the B747-100 longitudinal flight envelope

Table 1. The steady-state pitch rate over the flight envelope

M	0.2	0.3	0.4	0.5	0.3	0.4	0.5	0.6	0.7	0.3	0.4	0.5	0.6	0.7
H (m)	0	0	0	0	3048	3048	3048	3048	3048	6096	6096	6096	6096	6096
$\frac{q_{ss}}{\Delta\delta_3}$ (10^{-3}sec^{-1})	-148	-147	-147	-146	-147	-146	-145	-144	-143	-145	-144	-143	-142	-140

M	0.8	0.3	0.4	0.5	0.6	0.7	0.8	0.4	0.5	0.6	0.7	0.8	0.9
H (m)	6096	9144	9144	9144	9144	9144	9144	12190	12190	12190	12190	12190	12190
$\frac{q_{ss}}{\Delta\delta_3}$ (10^{-3}sec^{-1})	-138	-144	-142	-140	-138	-134	-129	-139	-135	-129	-119	-97.6	-80.7

The normalized pitch rate wrt steady-state pitch rate over the flight envelope $(q/q_{ss})|_{\forall\,(M,H)}$ is discussed next. The normalized parameter should lay within boundaries specified in Fig. 3. Figure 3 a) shows the close-up transient region of FHQ pitch rate criteria. All the normalized rates' settled to almost levelled responses in the range of 0.002 to -0.004 which satisfies the longitudinal trimmed merits of straight levelled flight. The responses of Mach number higher than 0.8 and altitude higher than 6096m infringed slightly the upper boundaries of the transient region. However, all the responses placed inside the lower boundaries. Figure 3 b) shows the close-up steady-state region of FHQ pitch rate criteria. All the response spectra well placed inside the boundaries.

CAP Criteria Responses

The steady state velocity was assumed equivalent to the crossover velocity of 150m/sec. The normal acceleration transfer function for ($H_i = 0 - 12190$m and $M_i = 0.2 - 0.9$) was found by Eq. (14),

$$\frac{az}{\Delta\delta} = \frac{\begin{array}{c}(67.01H + 1.024\times10^{6}M + 33.3HM - 1.65\times10^{6})s^{5} + \\ (-0.31\times10^{3}H + 0.04\times10^{7}M - 1.12\times10^{2}HM + 1.77\times10^{7})s^{4} + \\ (-2.76\times10^{3}H - 3.89\times10^{7}M - 1.35\times10^{3}HM + 7.39\times10^{7})s^{3} + \\ (-5.49\times10^{3}H - 8.96\times10^{7}M - 2.76\times10^{3}HM + 12.4\times10^{7})s^{2} + \\ (-2.94\times10^{3}H - 3.78\times10^{7}M - 1.4\times10^{3}HM + 8.5\times10^{7})s\end{array}}{\begin{array}{c}(-1.04\times10^{-5}H + 0.219M - 2.37\times10^{-6}HM + 0.956)s^{5} + \\ (1.55H + 7.2\times10^{4}M + 1.13HM + 5.14\times10^{4})s^{4} + \\ (182.53H + 5.35\times10^{6}M + 109.67HM + 2.41\times10^{5})s^{3} + \\ (-50.64H + 9.73\times10^{5}M - 12.26HM + 4.48\times10^{6})s^{2} + \\ (-90.43H - 1.16\times10^{6}M - 43.34HM + 2.63\times10^{6})s + \\ (-231.43H - 2.89\times10^{6}M - 110.22HM + 6.91\times10^{6})\end{array}}$$

Perturbed normal acceleration at the A/C centre of gravity over *M-H* flight envelope is shown in Fig. 4. Converged responses took longer to almost settle the normal acceleration in the range of 0.034 to -0.0069m/sec^2 which well agreed with the main merits of longitudinal trimmed straight levelled flight. However, these responses were tipped at 50sec to 100sec during transient regions. However, the angle of attack transfer function for ($H_i = 0 - 12190$m and $M_i = 0.2 - 0.9$) was already obtained (Elarbi, *et. el.*, 2019),

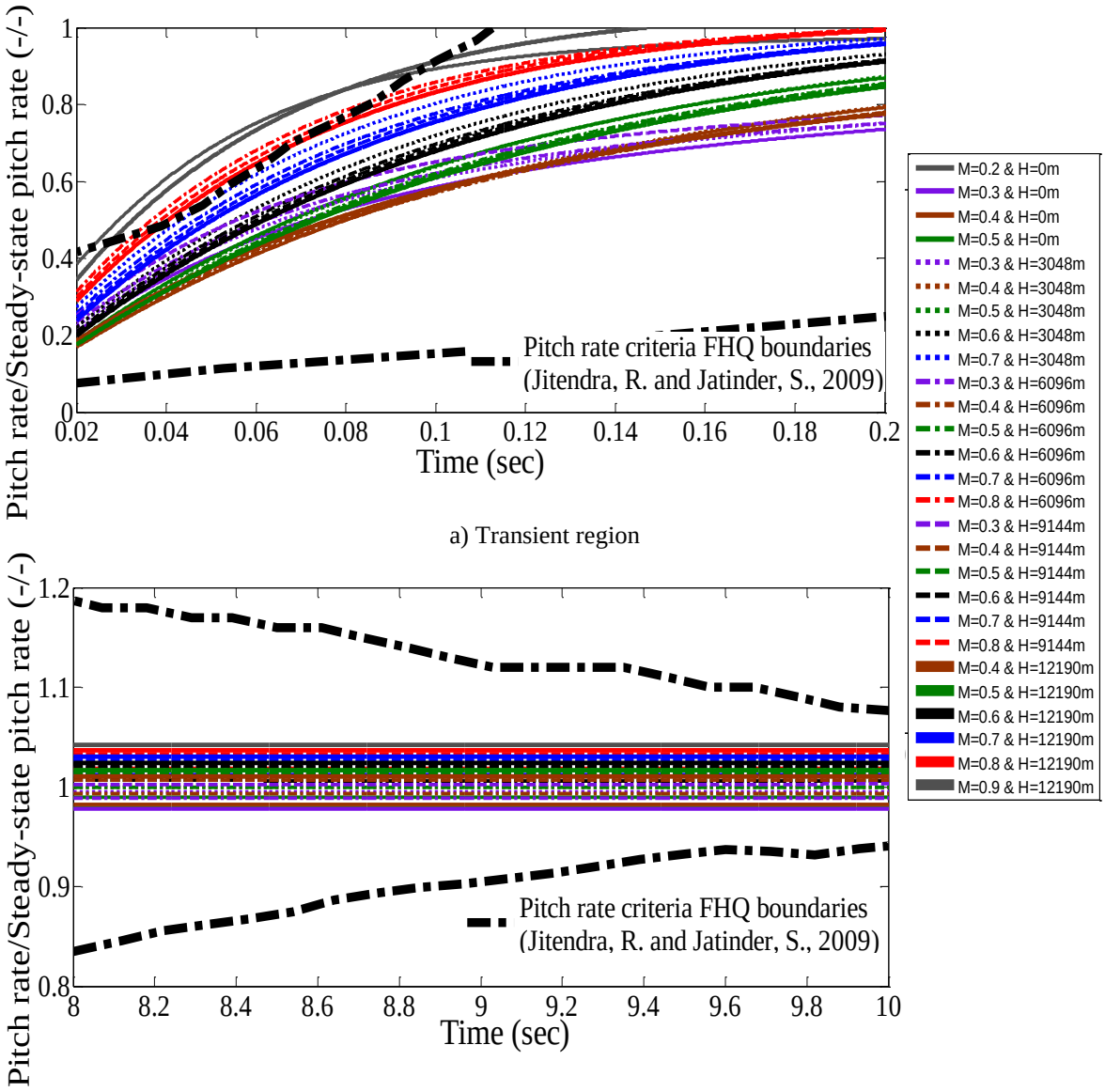

a) Transient region

b) Steady-state region

Figure 3. Close-up FHQ pitch rate criteria

$$\frac{\Delta\propto}{\Delta\delta} = \frac{\begin{array}{c}(67.01H + 1.024\times10^{6}M + 33.3HM - 1.65\times10^{6})s^{4} + \\ (1.61\times10^{3}H + 3.04\times10^{7}M + 8.41\times10^{2}HM - 2.88\times10^{7})s^{3} + \\ (4.65\times10^{3}H + 9.23\times10^{7}M + 2.47\times10^{3}HM - 7.52\times10^{7})s^{2} + \\ (3.04\times10^{3}H + 3.61\times10^{7}M + 1.44\times10^{3}HM - 9.47\times10^{7})s + \\ (2.37\times10^{3}H + 3.06\times10^{7}M + 1.14\times10^{3}HM - 6.93\times10^{7})\end{array}}{\begin{array}{c}(-8.41H - 1.15\times10^{6}M - 4.1HM + 2.32\times10^{5})s^{4} + \\ (4.18\times10^{3}H + 1.21\times10^{7}M + 250.89HM + 3.96\times10^{5})s^{3} + \\ (2.85\times10^{4}H + 7.58\times10^{8}M + 1.65\times10^{4}HM - 1.06\times10^{8})s^{2} + \\ (-3.49\times10^{3}H - 2.02\times10^{7}M - 1.49\times10^{3}HM + 1.47\times10^{8})s + \\ (-5.57\times10^{3}H - 7.11\times10^{7}M - 2.66\times10^{3}HM + 1.63\times10^{8})\end{array}}$$

The FHQ *CAP* criterion was then easily obtained using Eq. (13) and is shown over the flight envelope in Fig. 5. The upper and lower limits are straight lines, each with a slope of 0.5 on the log-log plot. The plot is defined by short-period frequency versus normal load factor per unit angle of attack. *CAP* parameter slightly passes close to the upper limit which indicates excellent dynamic response characteristics in executing flight tasks. A zooming-in view of *CAP* parameter is also shown on the upper left corner.

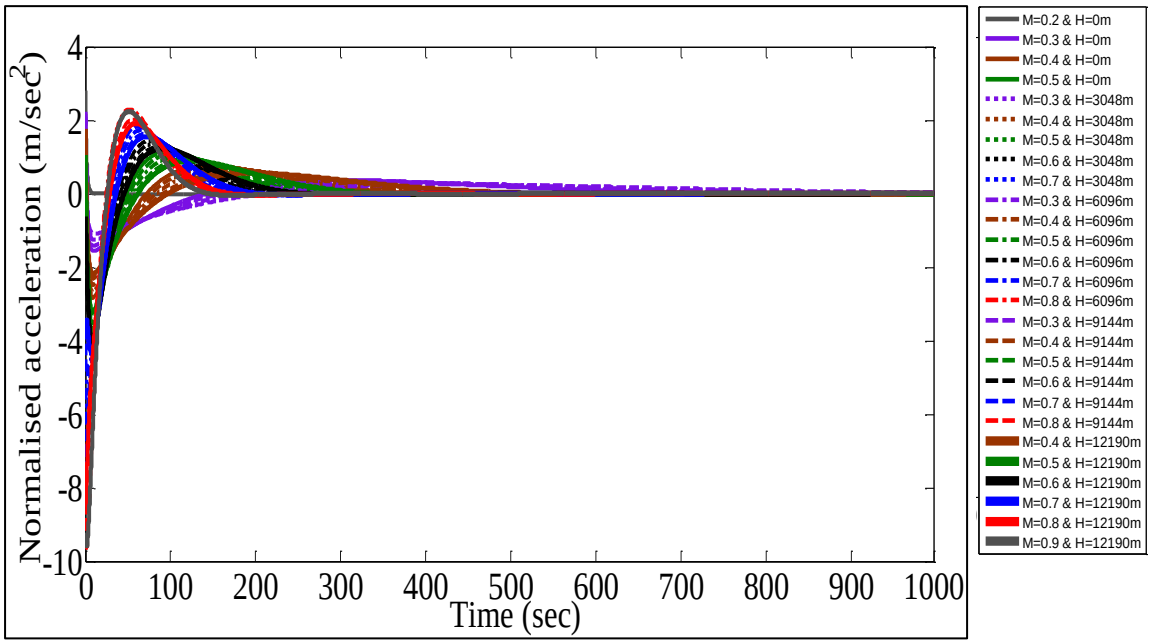

Figure 4. B747-100 normal accelerations over the longitudinal flight envelope

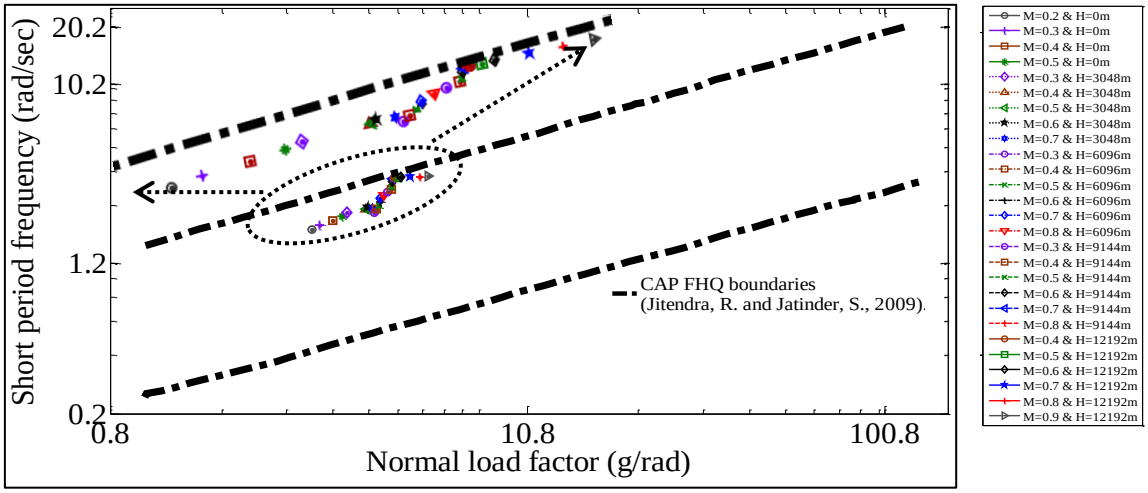

Figure 5. FHQ *CAP* criteria over the B747-100 longitudinal flight envelope

Cstar Criteria Responses

The *Cstar* criterion was obtained by Eq. (16) in terms of transfer function wrt control inputs over the flight envelope ($H_i = 0 - 12190$m and $M_i = 0.2 - 0.9$) using the assumption earlier made, i.e, V_c = 150m/sec.

$$\frac{Cstar(s)}{\Delta\delta} = \frac{\begin{array}{c}(67.01H + 1.024\times10^{6}M + 33.3HM - 1.65\times10^{6})s^{5} + \\ (-0.12\times10^{3}H + 0.35\times10^{7}M - 0.14\times10^{2}HM + 1.29\times10^{7})s^{4} + \\ (-2.01\times10^{3}H - 2.55\times10^{7}M - 0.96\times10^{3}HM + 5.87\times10^{7})s^{3} + \\ (-4.62\times10^{3}H - 7.68\times10^{7}M - 2.33\times10^{3}HM + 10.17\times10^{7})s^{2} + \\ (-2.4\times10^{3}H - 3.1\times10^{7}M - 1.4\times10^{3}HM + 5.9\times10^{7})s + \\ 0.00467\end{array}}{\begin{array}{c}(-1.04\times10^{-5}H + 0.219M - 2.37\times10^{-6}HM + 0.956)s^{5} + \\ (1.55H + 7.2\times10^{4}M + 1.13HM + 5.14\times10^{4})s^{4} + \\ (182.53H + 5.35\times10^{6}M + 109.67HM + 2.41\times10^{5})s^{3} + \\ (-50.64H + 9.73\times10^{5}M - 12.26HM + 4.48\times10^{6})s^{2} + \\ (-90.43H - 1.16\times10^{6}M - 43.34HM + 2.63\times10^{6})s + \\ (-231.43H - 2.89\times10^{6}M - 110.22HM + 6.91\times10^{6})\end{array}}$$

The normalized *Cstar* of FHQ criteria is shown in Fig. 6. Slightly infringements the upper boundaries at trainset region are obtained at low Mach numbers and altitudes. However, the steady-state region showed passable convergences in which the evaluations of normalized *Cstar* wrt steady-state *Cstar* pass well between the upper and lower boundaries. The steady-state *Cstar* and the normalized *Cstar* were obtained using Eqs. (17) and (18) respectively as below,

$$\frac{Cstar_{ss}}{\Delta\delta} = \frac{0.00467}{-231.43H - 2.89\times10^{6}M - 110.22HM + 6.91\times10^{6}}$$

$$\frac{Cstar}{Cstar_{ss}} = (-0.05H - 618.84M - 0.024HM + 1479.66)$$
$$(67.01H + 1.024\times10^{6}M + 33.3HM - 1.65\times10^{6})s^{5} +$$
$$(-0.12\times10^{3}H + 0.35\times10^{7}M - 0.14\times10^{2}HM + 1.29\times10^{7})s^{4} +$$
$$(-2.01\times10^{3}H - 2.55\times10^{7}M - 0.96\times10^{3}HM + 5.87\times10^{7})s^{3} +$$
$$(-4.62\times10^{3}H - 7.68\times10^{7}M - 2.33\times10^{3}HM + 10.17\times10^{7})s^{2} +$$
$$(-2.4\times10^{3}H - 3.1\times10^{7}M - 1.4\times10^{3}HM + 5.9\times10^{7})s +$$
$$\times10^{6}.\frac{0.00467}{(-1.04\times10^{-5}H + 0.219M - 2.37\times10^{-6}HM + 0.956)s^{5} +}$$
$$(1.55H + 7.2\times10^{4}M + 1.13HM + 5.14\times10^{4})s^{4} +$$
$$(182.53H + 5.35\times10^{6}M + 109.67HM + 2.41\times10^{5})s^{3} +$$
$$(-50.64H + 9.73\times10^{5}M - 12.26HM + 4.48\times10^{6})s^{2} +$$
$$(-90.43H - 1.16\times10^{6}M - 43.34HM + 2.63\times10^{6})s +$$
$$(-231.43H - 2.89\times10^{6}M - 110.22HM + 6.91\times10^{6})$$

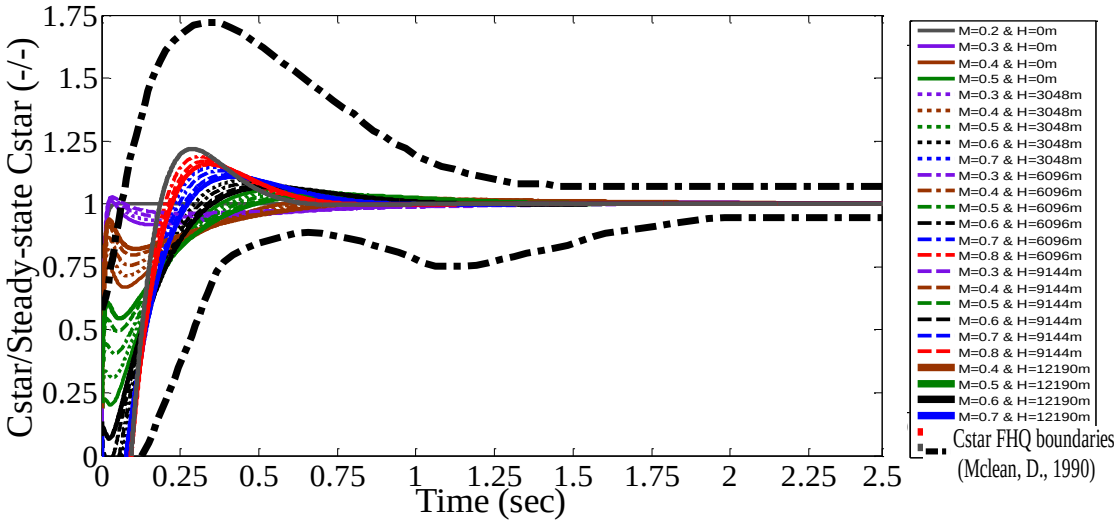

Figure 6. Normalized *Cstar* FHQ criteria over the B747-100 longitudinal flight envelope

Conclusions

Only the flying handling characteristics of the B747-100 longitudinal flight control have been taken into account through the design cycle of in-flight stressing control law authentications. The gain scheduling design has been arranged to assure acceptable flying qualities criteria within the operational envelope for a safely manoeuvrable flight from one steady-state condition to another. Local FSFLQR controllers have been scheduled at the combinations of Mach numbers and altitudes. Feasibly global control based on the combined elevator and throttle has been obtained governing the whole longitudinal flight envelope. Time responses of velocity, pitch rate, pitch attitude and altitude healthily match the performance specifications of negligible steady-state errors and swift responses of small overshoots and fast transitions. Realistic satisfactions of the FHQs' requirements are achieved based on normalized pitch rate criteria, *CAP* criteria and normalized *Cstar* criteria. No obvious infringements the FHQ limits are seen from large-scale assessments conducted within the flight envelope. In addition to the quality of gain scheduling approach being confirmed in producing a uniquely stabilizing control law, it is also shown the success in controlling the normal acceleration which is not primarily state variable.

Finally, the implementation of FSF normal acceleration control would be useful in case of altering the sensed normal accelerations of less than 1g and then to correct the aircraft nose-down attitude.

Recommendations

Further FHQ criteria should be evaluated to validate the performance of the FSFLQR gain scheduling control design. Of those criteria could be the pitch attitude bandwidth and flight-path bandwidth in the frequency domain, and Gibson's dropback criterion in the time domain.

Acknowledgements

Thanks to colleagues at Mobility and Transport Research Centre (MTRC), Coventry University, the UK for past researches. Also, thanks go to the University of Tripoli for support towards conference attendance.

References

Adîr, V. G. & Stoica, A. M. (2012). Integral LQR control of a star-shaped octorotor, *Incas Bulletin*, *4* (2), 3-18, ISSN 2066 – 8201, DOI: 10.13111/2066-8201.

Bharathi, M. & Kumar, G. (2013, April). An LQR controller design approach for pitch axis stabilisation of 3-DOF helicopter system, *International Journal of Scientific & Engineering Research (IJSER)*, *4* (4), ISSN 2229-5518.

Botez, R. M. & Rotaru, M. (2007, August). Analysis of flying qualities for an F/A-18 aircraft. www.researchgate.net/publication/270217047,

Chapra, S. C. & Canale R. P. (2010). *Numerical Methods for Engineers* (6th ed.). New York, The McGraw-Hill

Elarbi, E. M., Laila, D. S. & Horri, N. M. (2019, 26-30 August). *Neural-network bilinear gain-scheduling control for B747-100 longitudinal flight*. ICAT'19 8th International Conference on Advanced Technologies. 52-58, E-ISBN: 978-605-68537-4-6.

Etkins, B. (1994, December). *Dynamics of Flight Stability and Control*. (3rd ed.). Toronto, Canada.

Forrester, I.J.A., Sóbester, A. & Keane, A.J. (2008). *Engineering design via surrogate modelling*. University of Southampton, UK. John Wiley & Sons Ltd.

Frost, C. R., Franklin J. A. & Hardy G. H. (2002, November 5-7). Evaluation of flying qualities and guidance display for an advanced tilt-wing STOL transport aircraft in final approach and landing. *Biennial International Powered Lift Conference and Exhibit*. Williamsburg, Virginia. AIAA 2002-6016.

Hajiyev, C. Soken, E., Yenal, H. & Vural, S. (2015). *State estimation and control for low-cost unmanned aerial vehicles*. ISBN 978-3-319-16416-8, Springer International Publishing Switzerland, 176-200.

Jitendra, R. & Jatinder, S. (2009). *Flight Mechanics Modeling and Analysis*, Taylor & Francis Group, LLC

Joukhadar, A., Hasan, I., Alsabbagh, A. & Alkouzbary, M. (2015). Integral LQR-based 6DOF autonomous quadrocopter balancing system control, *International Journal of Advanced Research in Artificial Intelligence (IJARAI)*, *4* (5).

Mclean, D. (1990). *Automatic Flight Control Systems*, UK, the Prentice-Hall International

Oner, K. T., Cetinsoy, E., Sirimoglu, E., Hancer, C. Ayken, T. & Unel, M. (2009). LQR and SMC Stabilization of a new unmanned aerial vehicle. *World Academy of Science, Engineering and Technology*, *58*, 373-378.

Rogalski, T. & Dołega, B. (2006) Algorithms improving flying qualities of general aviation aircraft. ISSN 1648-7788 *Aviation*, *X*, 2, 17-28

Shaik, I. & Chetty, S. (1998, December). HQPACK User's Guide, Vols. 1, 2. PC based SW package in MATLAB for the prediction of handling qualities and pilot induced oscillation tendencies of aircraft, NAL Project document, PD-FC-9810,

Shaik, I. (2005, December). Evaluation of NLR handling qualities database for a large transport aircraft using HQPACK, Project Document FC 0519, National Aerospace Laboratories, Bangalore.

Shaji, J. & Aswin, R. B. (2015, August). Pitch control of aircraft using LQR & LQG control. *International Journal of Advanced Research in Electrical, Electronics and Instrumentation Engineering, IJAREEIE, (An ISO 3297: 2007 Certified Organisation)*, *4* (8), ISSN: 2320-3765.

Tayebi, A., Nikkhah, A. & Roshanian, J. (2017). LQR/LQG attitude stabilisation of an agile microsatellite with CMG, *An International Journal of Aircraft Engineering and Aerospace Technology*, *89* (2), 290-296, Emerald Publishing Limited [ISSN 1748-8842].

Tosun, D. C., Işık, Y. & Korul, H. (2015, Mar 15). LQR control of a quadrotor helicopter. *New Developments in Pure and Applied Mathematics.* 247-252, ISBN: 978-1-61804-287-3.

Author Information

Ezzeddin Elarbi
The University of Tripoli
Aeronautical Engineering Department
Tripoli-Libya
Contact e-mail: *ezzely5@.yahoo.com*

Abdulhamid Ghmmam
The University of Tripoli
Aeronautical Engineering Department
Tripoli-Libya

Saad Issa
The University of Tripoli
Aeronautical Engineering Department
Tripoli-Libya

The Eurasia Proceedings of Science, Technology, Engineering & Mathematics (EPSTEM)
ISSN: 2602-3199

The Eurasia Proceedings of Science, Technology, Engineering & Mathematics (EPSTEM), 2020

Volume 11, Pages 125-130

IConTES 2020: International Conference on Technology, Engineering and Science

Evaluating Stream Flow Forecasting Performance Using Adaptive Network Based Fuzzy Logic Inference System, Artificial Neural Networks with Feature Selection

Levent LATIFOGLU
Erciyes University

Abstract: Water resources are needed to maintain the human life and the management the ecologic system for many areas. The most economical use, protection and development of water resources have a great importance for hydrological studies. Variable such as stream flow data are commonly used in hydrology. Accurate stream flow estimation is very important in terms of planning and management of water resources and minimizing the effects of natural disasters such as drought and flood. Monthly river flow data obtained from the Sakarya basin on Porsuk River between 1970-2000 years were used for the estimation study. For this purpose, forecasting performance has been analyzed using Adaptive Network Based Fuzzy Logic Inference System (ANFIS) and Artificial Neural Networks (ANN) models and performances of these two models were compared. In addition, the average monthly stream flow data, standard deviation values of these data were also used in the forecasting study and applied as an input to ANFIS and ANN models. For a one ahead estimation, models have been developed with different input combinations of 1-3 past value of stream flow data and standard deviation values. In this study, mean square error (mse), mean absolute error (mae) and correlation coefficient parameters were used to evaluate the performance of the models. According to the obtained results, it is seen that the ANN model has better forecasting performance for two inputs according to mse and mae parameters and for three inputs according to R and R^2 parameters. Also, it is seen that the ANFIS model has the best performance for two inputs according to mse, mae, R and R^2 parameters. There has been some improvement in the forecast performance if the monthly average river stream flow data as well as the standard deviation data has been applied as an input to the model.

Keywords: Stream flow forecasting, Adaptive Network Based Fuzzy Logic Inference System Method (ANFIS), Artificial Neural Networks (ANN)

Introduction

In the planning of hydrological processes, river flow modeling and streamflow estimation are very important in terms of effective planning and use of water resources. Stream flow forecasting is essential for efficient operation and planning of reservoirs, sediment transport in rivers, hydropower generation, irrigation management decisions, scheduling of reservoir emissions and other hydrological applications. Accurate prediction of hydrological time series is a challenging task. This is because the dynamics of the stream flow data tends to have complex nonlinear dynamics and chaotic behaviors and nonstationary character. Increasing the predictions accuracy and reliability of non-stationary hydrological variables has been an important research topic. To date, no unique approach has been performed providing optimal stream flow estimation results. Artificial intelligence (or statistical) models are also classified as "black box" models. These models are very useful in modeling natural systems and these methods include mathematical optimization algorithms as they are used in logic, classification, statistical learning, and probability-based methods (Bayazit,, 1998; Chow et. al., 1988).

AI techniques such as Artificial Neural Networks (ANN), Support Vector Machines (SVM), Genetic programming (GP), Adaptive Network Based Fuzzy Inference System (ANFIS) have shown remarkable results

in estimating nonlinear stream flow data (Adamowski et.al. , 2010; Cigizoglu, 2005; Dehghani et.al, 2019; Hadi et. al., 2018; He et. al, 2019; Jain et. Al, 2007, Mehr et al., 2015).

In this study, estimation of the average monthly stream flow data one of hydrological time series data has been performed. By investigating the appropriate methods for the forecasting of these data which are not linear and non-stationary by nature, a forecasting study has been made with ANN and ANFIS methods. In addition, the average monthly stream flow data, standard deviation values of these data were also used in the forecasting study as input parameter and applied as inputs to ANFIS and ANN models. The rest of the paper is organized as follows. Section 2 gives information about study area and the data. Section 3 provides a brief review of the ANN and ANFIS approaches for streamflow estimation. Section 4 describes the forecasting results obtained by ANN and ANFIS models using the proposed approach and concludes the paper.

Materials and methods

Recently, artificial intelligence techniques have been used as an alternative to classical approaches for estimating hydrological data. Among them, ANN and ANFIS are common. In this paper the forecasting of stream flow models has been developed using ANN and ANFIS models.

Study Area and Data

The mean monthly stream flow in (m^3/s) data has been continuously gauged over the 30 year period, between 1970 through 2000, hence consisting of 372 successive numbers are used as the material of this study. Region where data has been gauged has been from the Porsuk River at Beşdeğirmen Station lies between 30° 02' 12" East - 39° 31' 41" North, in the Sakarya basin in the South East Marmara Region in Turkey. Drainage basin from which the data has been recorded is shown in Figure 1. This data set has been obtained from Electrical Power Resources Survey Administration (EIEI), in Turkey (as seen in Figure 2) (www.dsi.gov.tr/faaliyetler/akim-gozlem-yilliklari). The drainage area at this site is 3838.4 km^2. 260 of these elements have been used for the training phase and the rest 112 values have been used for the testing stage. All of these data are normalized.

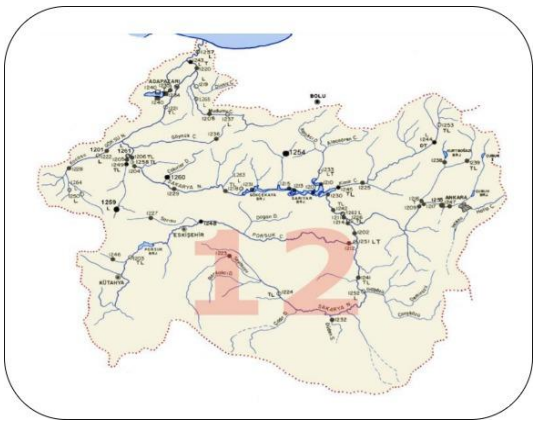

Figure 1. Basin of porsuk in turkey (www.dsi.gov.tr/faaliyetler/akim-gozlem-yilliklari)

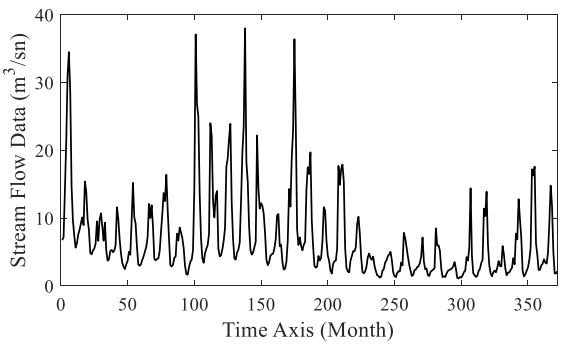

Figure 2. Streamflow data measured on porsuk river

Artificial Neural Networks

Recently, ANN has been widely used in forecasting study due to its advantages such as its ability to process nonlinear structures and its ability to process parallel and series. Just as there are nerve cells in biological neural networks, there are artificial nerve cells in ANN. Artificial nerve cells are called processor elements in engineering science. In an ANN structure, the sum and activation functions of the processor elements, the learning strategy and the learning rule are used. The topology resulting from the connection of the processor elements determines the model of the network. Artificial neurons come together to form ANNs. Neurons are not collected randomly. Generally, cells form a network of three layers called as the input, hidden and output layers, and these cells are positioned in parallel in each layer. In this study, the multi-layer perceptron (MLP) model has been used that has the input layer, one or more hidden layers, and output layer. The processor element in the input layer acts as a buffer that distributes the input signals to the processor element in the hidden layer and each one (layer) has at least one neuron. Each input is combined via the sum function of the multiplied input values (wij*ai) by the weight value (wij) that links it to the processing element.

$$y_j = f(\sum_i w_{ij} a_i + \theta) \quad (1)$$

Where, j is the neuron number, i is the input number, a_i input signal, w_{ij} weight coefficient and θ is the bias term (or threshold). These operations are repeated for all processors in the hidden layers. The processor element in the output layer also acts as a hidden layer processor element and network output values are calculated. Thus, the output of neurons in the output layer has been calculated. The backpropagation algorithm is used in the training of MLP networks commonly, because it can be proved mathematically and is easy to apply. This strategy gets its name (backpropagation) by reducing errors from output to backward input. Back propagation strategy is the most common learning strategy with a supervised learning structure and used in many applications. In this study, for forecasting of stream flow data, MLP and Back Propagation Neural Network (BPNN) feed forward network structure have been used. In the ANN, different learning algorithms are used to train the network. The Levenberg Marquardt (LM) learning algorithm, which has a computational speed advantage in the ANN, is used here for the forecasting of the hydrological time series data (Hagan et. al. 1996: Haykin, 1994).

In order to be used in time series estimation of MLP networks, the structure of the network must be determined. Number of layers of the network, number of processing elements in each layer, and transfer function to be used for these process elements are important for determination of the ANN structure. The number of output neurons is determined depending on how many periods will be forecasted. Determination of the number of neurons to be used at the input is not as easy as determination of the number of output neurons, because it is necessary to determine the data value at time t is affected by how many past observation values.

In this study, different numbers of neurons in the hidden layer, different number of layers, inputs and transfer functions have been set in the architecture of the ANN, and the optimum architecture of the model has been determined based on the resulting minimum mean square error between forecasted and stream flow data during training performance (Marquardt, 1963).

Adaptive Network Based Fuzzy Logic Inference System (ANFIS)

Various methods have been used to regulate the relationship between many variables. Some of these methods are: ANNs and fuzzy inference systems (FIS). It is a combination of neural networks and FIS known as ANFIS. The adaptive neural fuzzy inference system (ANFIS) is the Tagaki-Sugeno-Kang fuzzy inference deep fuzzy map algorithm [16]. It was developed by Jang in the early 1990s and was used in modeling nonlinear functions and forecasting chaotic time series. The ANFIS model generally uses the hybrid learning algorithm. ANFIS combined with the hybrid learning algorithm can create an input-output structure based on forecasted input-output data pairs. ANFIS takes advantage of both structures as it integrates neural networks and fuzzy logic inference methods. In order to apply the ANFIS method, a data set based on input-output is generally required. The model established depending on the number and type of membership functions selected is created using a learning algorithm. The method uses the created fuzzy if-then set of rules.

The main structure of ANFIS consists of five layers. Layer 1 is the fuzzification layer, layer 2 is the rule layer, layer 3 is the normalization layer, layer 4 is the defuzzification layer and layer 5 is the output layer. For

simplification, it is assumed that the framework of ANFIS has two inputs x; y and one output z. This framework has two rules which are the corresponding rule set with two fuzzy (if-then) rules. This set is used for a first order Sugeno fuzzy model expressed in below Equation.

Rule 1: if x is A_1 and y is B_1 then $z_1=p_1x+q_1y+r_1$
Rule 2 : if x is A2 and y is B2 then $z_2=p_2x+q_2y+r_2$ (2)

where p1; q1; r1 and p2; q2; r2 are the consequent constants. A1; B1 and A2; B2 are the linguistic labels. Adaptive (compatible) networks consist of directly attached nodes. Each node represents a unit of processing. Connections between nodes indicate an uncertain weight between them. All or some of the nodes may be adaptive. Adaptation is created by determining the outputs of these nodes with variable parameters. Learning rules determine how variable parameters should be changed to make the difference between the output of the entire network and the target value, that has to minimize the error. The basic learning rule in adaptive networks is the steepest descent method. In this study, the ANFIS parameters; the number of rules, membership functions and learning rule were chosen by trial and error, also the initial set of values has been found as in Ref. (Jang, 1993).

Training and Test Sets

The stream flow data has been splitted into two subsets before performing the model fitting. The subset of training was composed of 70% of original length. Thus, during the training, the 70% of the hydrological time series has been applied to the ANN and ANFIS model and the remaining 30% has been applied as test set to compare the quality of the k-steps-ahead forecasted values. The performance parameters to measure the trained for the k-step-ahead forecasting model are the Mean Squared Error (mse), Mean Absolute Error (mae), the correlation coefficient (R) and Coefficient of Determination (R^2). One to three numbers of inputs obtained from monthly mean of stream flow data (x(t)) and standard deviation of stream flow data (st(t)) in each month have been performed to show forecasting performance. The forecasting process has been summarized in below table.

Table 1. One to three ahead forecasting process

One Ahead Forecasting		
One input	Two inputs with std	Two inputs
$\hat{x}(t) = f(x(t-1))$	$\hat{x}(t) = f(x(t-1), st(t-1))$	$\hat{x}(t) = f(x(t-2), x(t-1))$
Three inputs	Four inputs	
$\hat{x}(t) = f(x(t-2), x(t-1), st(t-1))$	$\hat{x}(t) = f(x(t-3), x(t-2), x(t-1), st(t-1))$	

Results and Discussions

In this study, to evaluate the forecasting performance of stream flow data ANN and ANFIS models have been performed with different number of inputs and features. The obtained results have been summarized in Table 2 and 3 for one to four input ANN and ANFIS models for one step ahead forecasting. Also forecasted data using ANN and ANFIS model vs observed data can be seen in Figure 3.

Table 2. Testing performance of ANN model for one to four input

	One input	Two inputs with std	Two inputs	Three inputs	Four inputs
MSE	0.0057	0.0054	0.0065	0.0061	0.0062
MAE	0.0476	0.0466	0.0500	0.0485	0.0516
R	0.6896	0.6951	0.7051	0.7466	0.7140
R^2	0.4707	0.4784	0.4725	0.5534	0.5052

Table3. Testing performance of ANFIS model for one to four input

	One input	Two inputs with std	Two inputs	Three inputs	Four inputs
MSE	0.0069	0.0055	0.0066	0.0067	0.0065
MAE	0.0562	0.0439	0.0559	0.0565	0.0551
R	0.7267	0.7371	0.7379	0.7331	0.7377
R^2	0.4992	0.5303	0.5045	0.5196	0.5142

Obtained performance parameters showed in the Table 2 and 3 indicates that the forecasting performance of the models. As an example, ANN model performance has been better than ANFIS model for one step ahead forecasting according to mse and mae performance parameters. But the forecasting performance of the ANFIS model better than ANN model for one step ahead forecasting according to R and R^2 performance parameters. While the mse, mae, R and R^2 values have been obtained as 0.0057, 0.0476, 0.6897 and 0.8641 in the ANN method for one input one ahead forecasting, it has been obtained as 0.0069, 0.0562, 0.7267 and 0.4992 respectively in the ANFIS method. When Table 3 is examined, it is seen that the performance of the ANFIS model increases by adding the standard deviation values as input parameters of ANFIS model. It is same as also for the ANN model for three input (two of past values of the time serie with standard deviation value), as can be seen from Table 2. Also, the optimal performance has been obtained from ANFIS model using two inputs (one of time series past values, one of standard deviation values) and the optimal performance has been obtained from ANN model using three inputs.

In this study monthly streamflow data forecasting performance of ANN and ANFIS model has been analyzed and the effect of input features to the forecasting performance has been tested using the past value of the data and standard deviation values of the data. As a result, when the standard deviation value is used for the input parameters, it has been observed that the forecasting performance increases even more.

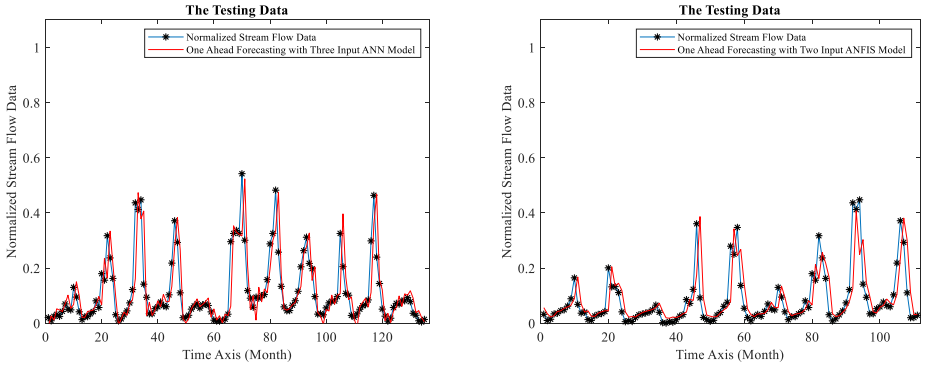

a b

Figure 3. One ahead forecasted stream flow data a- obtained from three input ANN model, b- obtained from two input ANFIS model

References

Adamowski, J., & Sun, K. (2010). Development of a coupled wavelet transform and neural network method for flow forecasting of non-perennial rivers in semi-arid watersheds. *Journal of Hydrology*, *390*, 85-91.

Bayazıt M., (1998). *Hidrolojik Modeller*, İTÜ İnşaat Fakültesi Matbaası, İstanbul.

Chow V.T., Maidment D.R. & Mays L.W., (1988). *Applied Hydrology*, McGraw-Hill, NY.

Cigizoglu, H. K. (2005). Application of generalized regression neural networks to intermittent flow forecasting and estimation. *Journal of Hydrologic Engineering*, *10*(4), 336-341.

Jain, A., & Kumar, A. M. (2007). Hybrid neural network models for hydrologic time series forecasting. *Applied Soft Computing*, *7*(2), 585-592.

Jang, J.S.R., (1993). ANFIS: adaptive-network-based fuzzy inference system, *IEEE Trans. Syst. Man Cybern*, *23*, 665-685.

Dehghani, M., Seifi A., & Riahi-Madvar H., (2019). Novel forecasting models for immediate-short-term to long-term influent flow prediction by combining ANFIS and grey wolf optimization, *Journal of Hydrology*, *576*, 698-725.

Hadi, S.J., & Tombul M., (2018), Monthly streamflow forecasting using continuous wavelet and multi-gene genetic programming combination, *Journal of Hydrology*, *561*, 674-687.

Hagan, M.T., Demuth H.B., & Beale M.H., (1996). *Neural Network Design*. Boston. MA: PWS Publishing.

Haykin, S., (1994), *Neural Networks: A Comprehensive Foundation*, Macmillan College Publishing Company Inc., New.

He, Y., Yan Y., Wang X., & Wang C., (2019). Uncertainty Forecasting for Streamflow based on Support Vector Regression Method with Fuzzy Information Granulation. *Energy Procedia*, *158*, 6189-6194.

Marquardt, DW., (1963). An algorithm for least-squares estimation of nonlinear parameters, *Journal of the Society for Industrial and Applied Mathematics*, *11*, 431-441.

Mehr, A. D., Kahya, E., Şahin, A., & Nazemosadat, M. J. (2015). Successive-station monthly streamflow prediction using different artificial neural network algorithms. *International Journal of Environmental Science and Technology*, *12*, 2191-2200.

www.dsi.gov.tr/faaliyetler/akim-gozlem-yilliklari , (accession date February, 2020)

Author Information

Levent Latifoğlu
Erciyes University
Civil Engineering Dept.
Contact e-mail: *latifoglu@erciyes.edu.tr*

The Eurasia Proceedings of Science, Technology, Engineering & Mathematics (EPSTEM)
ISSN: 2602-3199

The Eurasia Proceedings of Science, Technology, Engineering & Mathematics (EPSTEM), 2020

Volume 11, Pages 131-135

IConTES 2020: International Conference on Technology, Engineering and Science

Possibilities of Dyeing of Polyamide Fabric with Substantive Dye

Milena NIKODIJEVIĆ
University of Niš

Nemanja VUČKOVIĆ
University of Niš

Dragan ĐORĐEVIĆ
University of Niš

Abstract: The possibility of dyeing polyamide fabric with a substantive dye is studied in this paper. This type of dye most often dyes natural fibers, e.g. cotton, while polyamide belongs to the group of synthetic fibers. Due to their outstanding mechanical properties, polyamide fibers are used in the production of clothing, technical textiles and reinforcement of textile composites. Dyeing by substantive dye is performed with the aim of applying it in industrial conditions. Substantive dye can be bonded by hydrogen bridges with amide groups in a polyamide chain. 100 % polyamide 6.6 fabric was used. The samples were dyed at temperatures of 95 °C with the addition of acetic acid. Samples were dyed at a time interval of 5, 10, 20, 40, 50, and 60 minutes. The solution contained dye concentrations of 5, 10, 15, 20, 25 and 30 mg/dm^3. From the results, the degree of dye exhaustion and adsorption capacity were analyzed. At the highest applied dye concentrations and the longest dying time, the highest adsorption occurs. Increasing the concentration of dye when dyeing PA 6.6 fabric with a substantive dye reduces the degree of exhaustion, longer dyeing gives a higher degree of dye exhaustion, and this is maintained throughout the dyeing process. The adsorption capacity increases during the increase of the initial dye concentration and time, i.e. a larger amount of dye or a longer period of dyeing yield a higher amount of adsorbed dye per unit mass of polyamide fabric.

Keywords: Polyamide, Dyeing, Adsorption, Substantive dye

Introduction

The most often used polymers in the textile industry are polypropylene, polyacrylonitrile and polyamide. These fibers surpass the production of natural fibers. Advantages of the chemical fibers are strength, wear and stretch resistance, relatively low price and easy recycling. In addition to their useful properties, they also have disadvantages such as hydrophobicity, less wearing comfort, poor color fastness and a number of difficulties in finishing work (Parvinzadeh, 2012).

Due to their outstanding mechanical properties, polyamide fibers are used in the manufacture of clothing, technical textiles and reinforcement of textile composites. Polyamide fibers have a very smooth surface with a low surface area energy. Physical and chemical methods are used to improve surface properties such as humidity, biocompatibility and color sorption (Rietzler, Bechtold, & Pham, 2018). Substrate dyeing is performed in a neutral or acidic bath depending on the affinity of the dye and the depth of the shade which is to be achieved. Substrate dyes exhibit dichroism on polyamide, indicating that dye molecules are bound hydrogen bridges with amide groups in the polyamide chain (Džokić, 1989, Novaković, 1996). Substance dyes are chemically composed of sulfonated azo compounds: derived from benzidine and its derivatives or amines of the diaminostilbene type, etc. Substantive dyes are soluble in water and their solubility depends on the chemical composition, especially from the content of sulfone groups in the molecule. Solubility increases by raising the temperature of the solution, and when the temperature is lowered, a stable solution (Novaković, 1996). is obtained. Substantive colors are very popular because they have exceptional advantages such as a wide range of

- Selection and peer-review under responsibility of the Organizing Committee of the Conference

colors, low prices, excellent color penetration, short staining time, etc. However, they also have disadvantages such as poor durability washing due to hydrophilic sulfone groups in the structure of molecules (Liu, Wang, & Xu, 2010).

In this paper, new findings from the laboratory research of dyeing polyamide 6.6 fabric are presented with a selected substrate dye that has a high affinity for this fiber, in a slightly acidic bath without additives. The aim of the research is to develop a procedure for dyeing polyamide 6.6 with direct dye without the addition of any substances aqueous dye solution in laboratory conditions with a tendency to be applied in industry, given that this dyeing is not common for polyamide dyeing.

Method

In the experimental part, 100% raw polyamide 6.6 fabric was used. One measurement was performed for each of the samples. The dyeing was performed in glass conical flasks in which a sample of raw polyamide 6.6 fabric was placed in acetic acid solution and substrate dyes. The Erlenmeyers were placed on the stove and the dyeing was done in different time intervals. The ratio of the bath was 20:1. Processing time with continuous stirring was 5, 10, 20, 30, 40, 50 and 60 minutes. The dye used is Solophenyl green 5BL (Huntsman, USA). The solution in the constant amount contained dye concentrations of 5, 10, 15, 20, 25 and 30 mg/dm^3. The samples were stained at a temperature of 95 °C. Upon completion of staining, the samples were separated and washed with water.

The absorbance at the maximum wavelength was measured for color (680 nm), spectrophotometer (Cary 100 Conc UV-VIS, Varian). The absorbance of the solution was measured for making a calibration curve and determining unknown concentrations during staining.

The degree of dye exhaustion was calculated using the form:

$$\text{The degree of dye exhaustion}=\frac{C_0 - C_t}{C_0} \times 100\ (\%) \tag{1}$$

where: C_0 and C_t (mg/dm3) are initial and dye concentration at time t (Tayebi et al., 2015).

The amount of absorbed dye per unit mass of the adsorbent (absorption capacity) was obtained using the equation:

$$q_t = \frac{C_0 - C_t}{w} \times V \quad \text{and} \quad q_e = \frac{C_0 - C_e}{w} \times V \tag{2}$$

where q_t (mg/g), is mass of absorbed dye per unit mass at dye time t; q_e (mg/g), is mass of absorbed dye per unit mass in equilibrium, C_0 (mg/dm^3), is initial dye concentration; C_t (mg/dm^3),is dye concentration in solution at dye time t, C_e (mg/dm3), is equilibrium dye concentration in solution; w (g), is mass of sample and V (dm^3), is volume of staining solution (Tayebi et al., 2015).

Results and Discussion

The ability to dye polyamide 6.6 fabric with substrate dye implies knowledge of the existing dyeing mechanisms with conventional dyes, as well as creating assumptions as it would be with a new dye of a different structure. It is known that polyamide fiber usually has an average molecular weight of 10,000-12,000, and at its ends can contain an equal number of carboxyl and amino groups. In practice, it often contains free carboxyl groups and a small number of free amino groups. The presence of these end groups is of great importance and influence on the dyeing of polyamide fibers (Tayebi et al., 2015).

When considering the mechanism of dyeing polyamides with acid dyes that show a greater or lesser affinity for the fiber, it indicates that the adsorption of acid dyes for the fiber can take place in three ways depending on the nature of the dye and the pH of the dye solution. Having in mind the active sites where the dye is adsorbed, the binding of the dye can be organized in the following ways: binding to amino groups, binding to amide groups and binding to positively charged amide groups. Binding of the dye by establishing hydrogen bridges between the corresponding groups of the polyamide chain and the dye molecules is also possible in solutions at pH 2-7, but for groups of dyes showing high affinity for polyamide in neutral solutions (Tayebi et al., 2015).

The diagram in Figure 1 shows the influence of time or length of contact between the adsorbate (dye) and the adsorbent (polyamide 6.6 fabric) on the adsorption-depletion of dye during dyeing, for different initial concentrations of substrate dye. Continuity in changes over time is noticeable. At all initial concentrations, in the beginning, there is a sharp increase in color depletion, and after 30 minutes of staining, this trend is much milder by the end of staining. The linear parts of the curve reflect the diffusion in the surface layer while the parts of the plateau on the curve correspond to the diffusion in the pores.

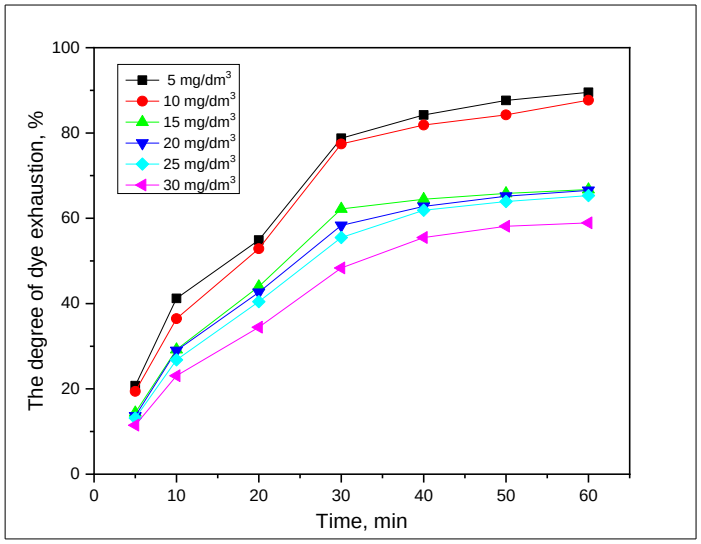

Figure 1. Change in the degree of dye exhaustion of direct dye during dyeing of polyamide 6.6 fabric for different initial dye concentrations

The influence of the initial dye concentration on the adsorption - dye depletion during standard dyeing of polyamide fabric, for different times, is given by the diagram in Figure 2. There is continuity in the changes during the growth of the initial dye concentration. As the concentration increases, the degree of color depletion decreases depending on the adsorption-staining time. At lower concentrations of paint in the solution, at the beginning there is a slightly larger drop in the percentage of exhausted paint, and at the end of painting this drop was somewhat milder. The shortest staining time (5 min.) causes the lowest depletion values, while the longest staining time (60 min.) Produces the highest depletion values.

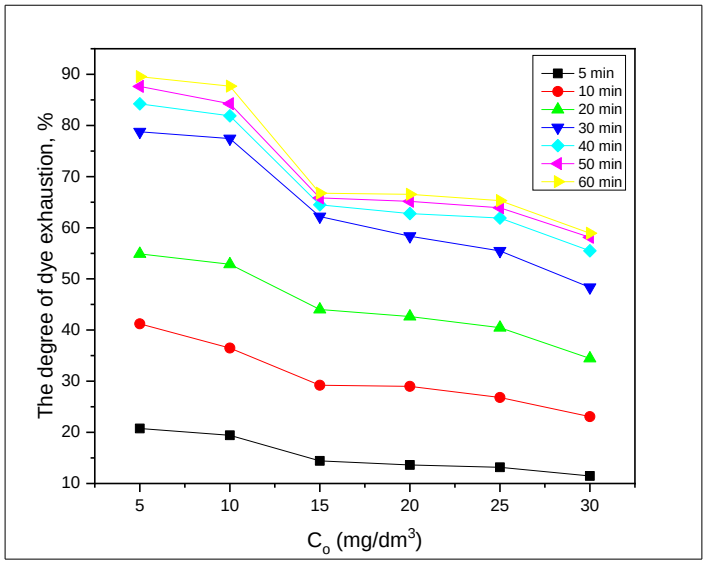

Figure 2. Influence of the initial dye concentration of direct dye on the degree of exhaustion dye

The diagram in Figure 3 shows the results of the change in the adsorbed amount of adsorbate (dye) on the adsorbent (PA 6.6 fabric) for different initial concentrations and dyeing time. With an increase in the initial dye

concentration, the dye absorption on the polyamide 6.6 fabric increases sharply, especially after 10 minutes of dyeing up to 60 minutes, where the curve is the steepest.

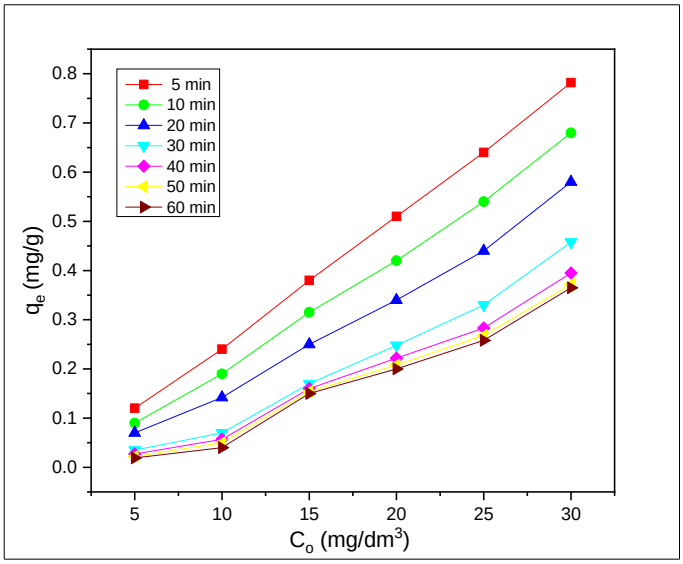

Figure 3. Adsorbed amount of direct dye per unit mass of PA 6.6 fabric in relation to the initial dye concentration for different time of dyeing

Figure 4 is a diagram showing the adsorbed amount of direct dye per unit mass of PA 6.6 fabric over time for different initial dye concentrations. As the initial dye concentration increases, the dye absorption on the polyamide 6.6 fabric increases over time, especially after 30 minutes of dyeing up to 60 minutes, where the curve is the steepest.

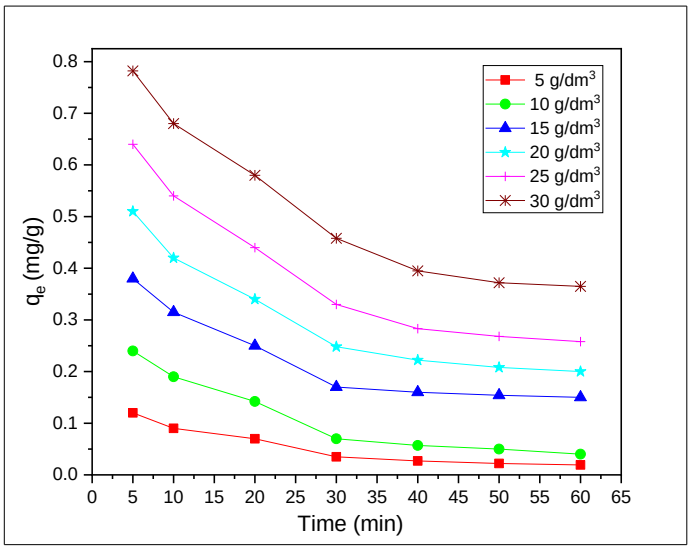

Figure 4. Adsorbed amount of direct dye per unit mass of PA 6.6 fabric in relation to time for different initial dye concentrations

Conclusion

According to the results of experiments and statistical data, dyeing of PA 6.6 fabric can also be achieved in industrial conditions, which of course requires adapting the recipes to the new space and equipment. Based on the obtained experimental results, it can be concluded: Dyeing PA 6.6 fabric with substrate dye in laboratory conditions gives excellent results at a temperature of 95 °C.

Increasing the concentration of dye when dyeing PA 6.6 fabric with substrate dye reduces the degree of depletion, longer dyeing gives a higher degree of dye depletion, and this is maintained throughout the dyeing process. The change in the adsorbed amount of adsorbate (dye) on the adsorbent (fabric), for different initial concentrations and dyeing time, increases during the increase of the initial concentration and time, ie. a greater amount of dye or a longer period of dyeing yields a greater amount of adsorbed dye per unit mass of fabric.

References

Džokić, D. (1989). *Teorija i tehnologija bojenja tekstilnog materijala*, Beograd, Zavod za grafičku tehniku – TMF.

Liu, X., Wang, W. & Xu P. (2010) Improving the Wash Fastness of Direct Dyes on Cotton by Si/Ti Composite Nanosol. *Fibres & Textiles in Eastern Europe*, *18*, 93-96.

Novaković, M. (1996). *Teorija i tehnologija oplemenjivanja tekstila bojenjem i štampanjem*, Beograd, BMG.

Parvinzadeh, M. (2012). Surface modification of synthetic fibers to improve performance: recent approaches. *Global J Phys Chem*, *3*, 1-11.

Rietzler, B., Bechtold, T., & Pham, T. (2018). Controlled surface modification of polyamide 6.6 fibres using $CaCl_2/H_2O$/EtOH solutions. *Polymers*, *10*, 207.

Tayebi, H. A., Yazdanshenas, M. E., Rashidi, A., Khajavi, R., & Montazer, M. (2015). The Isotherms, Kinetics, and Thermodynamics of Acid Dye on Nylon 6 with Different Amounts of Titania and Fiber Cross Sectional Shape. *Journal of Engineered Fibers and Fabrics*, *10*, 97-108.

Author Information

Milena & Nikodijević
University of Niš
Faculty of Technology in Leskovac
Bulevat oslobođenja 124, Leskovac 16000, Serbia
Contact e-mail: *nikmilena94@gmail.com*

Dragan & Đorđević
University of Niš
Faculty of Technology in Leskovac
Bulevat oslobođenja 124, Leskovac 16000, Serbia

Nemanja & Vučković
University of Niš
Faculty of Technology in Leskovac
Bulevat oslobođenja 124, Leskovac 16000, Serbia

The Eurasia Proceedings of Science, Technology, Engineering & Mathematics (EPSTEM)
ISSN: 2602-3199

The Eurasia Proceedings of Science, Technology, Engineering & Mathematics (EPSTEM), 2020

Volume 11, Pages 136-140

IConTES 2020: International Conference on Technology, Engineering and Science

The Anode Performance of the $Mg_{0.2}Co_{0.2}Ni_{0.2}Zn_{0.2}Li_{0.1}Cu_{0.1}O$ High Entropy Oxide for Li-Ion Batteries

Ersu LOKCU
Eskisehir Osmangazi University

Resat Can OZDEN
Eskisehir Osmangazi University

Mustafa ANIK
Eskisehir Osmangazi University

Abstract: High-entropy oxides (HEOs), which are new class of single-phase solid solution materials, have recently attracted as electrode material due to their Li-ion storage properties. In this work $Mg_{0.2}Co_{0.2}Ni_{0.2}Zn_{0.2}Li_{0.1}Cu_{0.1}O$ high entropy oxide was synthesized by conventional solid state method to evaluate its electrochemical performances as anode in the Li-ion battery. The structure of the synthesized $Mg_{0.2}Co_{0.2}Ni_{0.2}Zn_{0.2}Li_{0.1}Cu_{0.1}O$ was characterized by using X-ray diffraction and field emission - scanning electron microscope techniques. The synthesized high entropy oxide was observed to have single phase rock salt crystal structure. The electrochemical performance of the anode was evaluated by assembling CR2016 type coin cell. Galvanostatic charge/discharge tests showed that the $Mg_{0.2}Co_{0.2}Ni_{0.2}Zn_{0.2}Li_{0.1}Cu_{0.1}O$ anode delivers a high initial discharge capacity of 1668 mA h g^{-1} at a current of 200 mAg^{-1}. The capacity cyclic stability was observed as also satisfactory. These performance values show that the $Mg_{0.2}Co_{0.2}Ni_{0.2}Zn_{0.2}Li_{0.1}Cu_{0.1}O$ high entropy oxide has good potential to be used as anode in Li-ion batteries.

Keywords: Conversion type anode, Li-ion battery, High entropy oxide

Introduction

Li-ion batteries (LIBs) with high cycling stability and reversible capacity are promising energy storage devices to meet the rapid development of electric vehicles. Transition metal oxides have been intensely studied over the past decades as anode material for LIBs due to their high reversible capacity and low cost properties (Kim et al., 2019; Puthusseri et al., 2018). Investigations on the transition metal oxide anodes focus mainly on adjusting the structural properties such as morphology, size, and defect formation in order to solve their fundamental problems which are low Coulombic efficiency (CE), unstable solid electrolyte interface (SEI) film formation, large potential hysteresis, and poor cycling and rate capability (Yuan et al., 2014; Lu et al., 2018; Yu et al.,2018).

Firstly, it is reported by Sarkar et al, the entropy stabilization results in improved cycling capability in (MgCoNiCuZn)O anode (2018). Furthermore, the specific capacity value of 920 mA h g^{-1} was reached after 300 cycles upon synthesis of HEO based anode in the form of nanoparticles (Qiu et al., 2019). Moreover, the (MgCoNiCuZn)O HEO anode with the NCM111 cathode provided 300 mA h g^{-1} full cell capacity after 50 cycles (Wang et al., 2019). In another study, $(MgCoNiZn)_{1-x}Li_xO$ HEOs were synthesized and their electrochemical performances were investigated as anode material in LIBs. The increase in the lithium cation concentration causes generation of more oxygen vacancies, which greatly affected the electrochemical performance of $(MgCoNiZn)_{1-x}Li_xO$ HEO based anodes, on the structure. They reported the $(MgCoNiZn)_{0.65}Li_{0.35}O$ anode had 1930 mA h g^{-1} initial and 610 mA h g^{-1} stable discharge capacities (Lökçü et al., 2020). These results were very promising for the use of HEOs as anode material in LIBs. Besides the (MgCoNiCuZn)O rock-salt type HEO anode, spinel type $(Mg_{0.}2Ti_{0.2}Zn_{0.2}Cu_{0.2}Fe_{0.2})_3O_4$ and $(FeCoNiCrMn)_3O_4$

HEO anodes were synthesized and their electrochemical performances were investigated in LIBs (Wang et al., 2020; Chen et al., 2020). Herein, we synthesized the $Mg_{0.2}Co_{0.2}Ni_{0.2}Zn_{0.2}Li_{0.1}Cu_{0.1}O$ high entropy oxide to further investigation the effect of entropy stabilization on the electrochemical properties of HEO based anodes.

Materials & Methods

MgO, CoO, NiO, ZnO, Li_2O and CuO were mixed homogeneously in the determined molar ratios to get $Mg_{0.2}Co_{0.2}Ni_{0.2}Zn_{0.2}Li_{0.1}Cu_{0.1}O$ stoichiometry and they milled at 300 rpm for 2 h by using the planetary ball mill (Fritsch Pulverisette 7 Premium Line). The obtained oxide mixture was then unaxially pressed at 300 MPa. Finally, the oxide pellet was sintered at 1000ºC for 12 h prior to the air quenching. The sintered pellet was re-milled at 200 rpm for 1 h to prepare electrodes.

The phase structure of the as-synthesized $Mg_{0.2}Co_{0.2}Ni_{0.2}Zn_{0.2}Li_{0.1}Cu_{0.1}O$ was examined by XRD (PANalytical Empyrean) and FE-SEM techniques using Cu Kα radiation ($\lambda = 0.154$ nm). The HEO based anode was prepared by mixing 75 wt% active material, 15 wt% carbon black (Super P) and 10 wt% polyvinylidene fluoride (PVDF) in N-methyl pyrrolidinone (NMP) to form a homogeneous slurry. Then the slurry was coated onto Cu foil and dried in a vacuum oven at 80ºC for 12 h.

The coin cell was assembled in an argon-filled glove box with H_2O and O_2 levels less than 1.0 ppm. Lithium metal was used as the counter and reference electrodes and the glass microfiber filter as a separator. 1 M Lithium hexafluorophosphate ($LiPF_6$) in ethylene carbonate and dimethyl carbonate (EC:DMC) in a 1:1 ratio by volume was used as electrolyte. The charge-discharge tests were performed galvanostatically in a potential range change between 0.01 V and 3.00 V (vs. Li^+/Li) at 200 mA g^{-1} current density.

Results and Discussion

The XRD pattern of $Mg_{0.2}Co_{0.2}Ni_{0.2}Zn_{0.2}Li_{0.1}Cu_{0.1}O$, which is prepared by the conventional solid state method is given in Figure 1. The $Mg_{0.2}Co_{0.2}Ni_{0.2}Zn_{0.2}Li_{0.1}Cu_{0.1}O$ shows a typical face-centered-cubic (FCC) rock-salt type structure. Figure 2 shows the FE-SEM images of the $Mg_{0.2}Co_{0.2}Ni_{0.2}Zn_{0.2}Li_{0.1}Cu_{0.1}O$ particles, which is re-milled at 200 rpm for 1 h. As shown in Figure 2, there is no secondary phases and the $Mg_{0.2}Co_{0.2}Ni_{0.2}Zn_{0.2}Li_{0.1}Cu_{0.1}O$ sample was successfully synthesized. Moreover, the size of particles in the range of 300-400 nm can be seen in Figure 2.

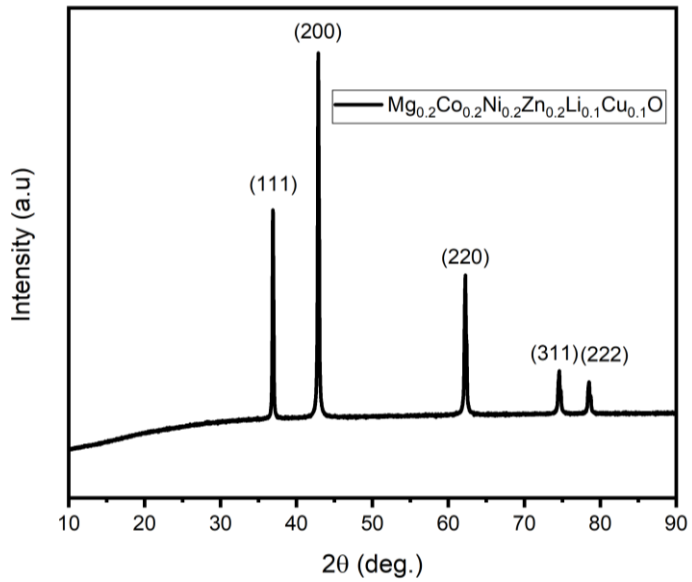

Figure 1. XRD pattern of the as-synthesized $Mg_{0.2}Co_{0.2}Ni_{0.2}Zn_{0.2}Li_{0.1}Cu_{0.1}O$.

In order to determine electrochemical properties of the $Mg_{0.2}Co_{0.2}Ni_{0.2}Zn_{0.2}Li_{0.1}Cu_{0.1}O$ anode, galvanostatic charge/discharge tests were performed between 0.01 and 3.0 V vs. Li/Li^+ (Figure 3). The initial discharge capacity of $Mg_{0.2}Co_{0.2}Ni_{0.2}Zn_{0.2}Li_{0.1}Cu_{0.1}O$ anode is 1668 mA h g^{-1}. The open circuit voltage (OCV) of the fabricated coin-cell is ~2.60 V and the discharge plateau of anode is around 0.75 V for the first cycle process.

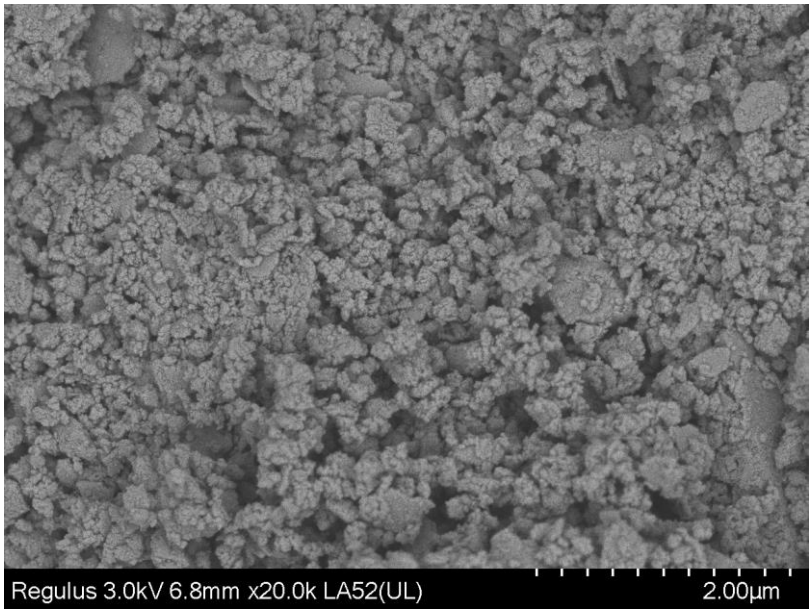

Figure 2. FE-SEM image of the as-synthesized $Mg_{0.2}Co_{0.2}Ni_{0.2}Zn_{0.2}Li_{0.1}Cu_{0.1}O$.

The following charge-discharge cycles also are given in Figure 3. The discharge voltages of the anodes look slightly increased and the discharge reaction occurs over a potential range of ~1.60-0.01 V with an inclined single slope. After the first cycle, the significant capacity loss is observed because of the formation of the SEI layer at the interface of the electrode surface and the electrolyte and initial lithium loss, mainly due to anode conversion (Lökçü et al., 2020). The discharge capacity of the $Mg_{0.2}Co_{0.2}Ni_{0.2}Zn_{0.2}Li_{0.1}Cu_{0.1}O$ anode is 724 mA h g^{-1} at the end of 5^{th} cycle.

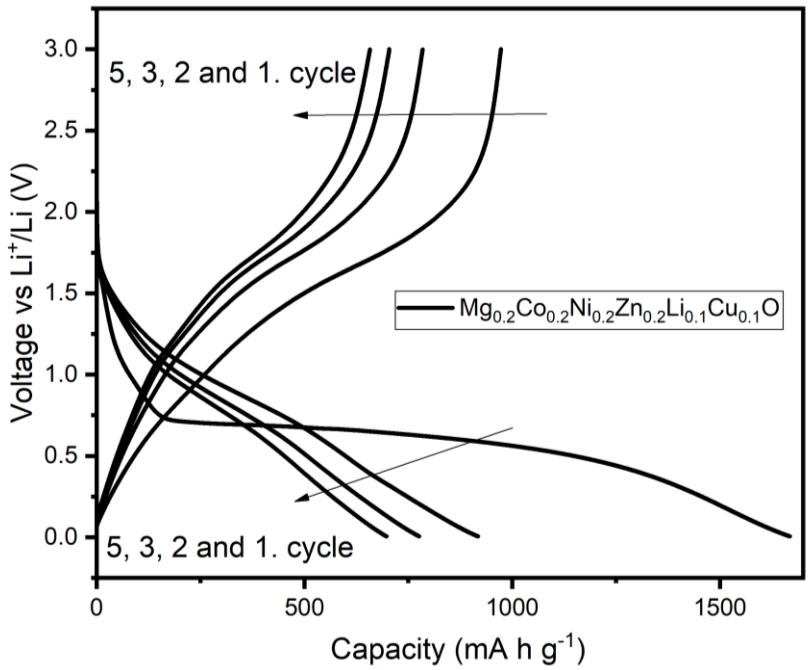

Figure 3. Charge/discharge curves of $Mg_{0.2}Co_{0.2}Ni_{0.2}Zn_{0.2}Li_{0.1}Cu_{0.1}O$ anode at a current density of 200 mA g^{-1}.

The CV curve of the synthesized $Mg_{0.2}Co_{0.2}Ni_{0.2}Zn_{0.2}Li_{0.1}Cu_{0.1}O$ for two cycles is given in Figure 4. In the first cycle, sharp peak appears at 0.25 V in the cathodic scan, corresponding to the processes of initial reduction of transition metal oxides and the formations of both Li_2O and the SEI layer (Lökçü et al., 2020). In the second cycle, ths sharp peaks transforms into wider peaks and it shifts to the more positive potentials. This phenomenon, which indicates the irreversibility of the initial lithiation process and the SEI formation, is commonly observed in the conversion-type anode materials (Lökçü et al., 2020; Chen et al., 2020).

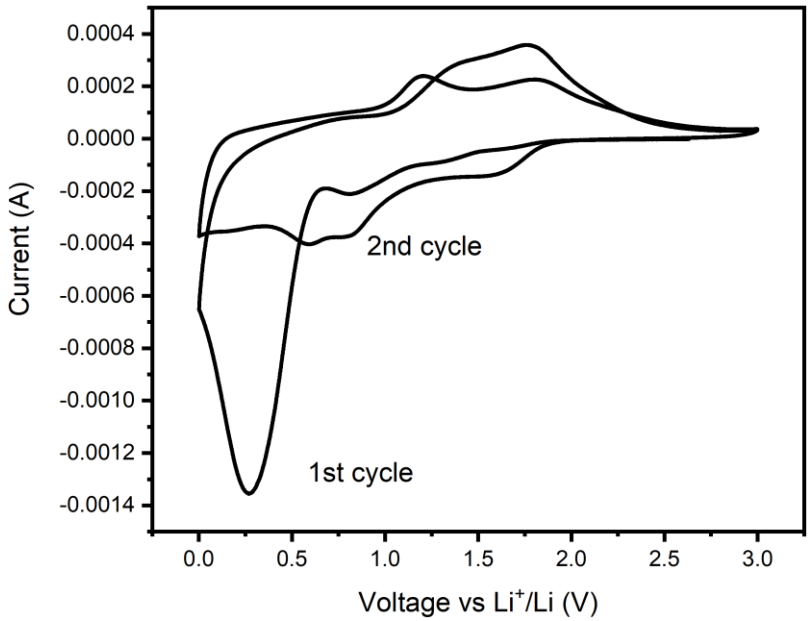

Figure 4. CV curve of a $Mg_{0.2}Co_{0.2}Ni_{0.2}Zn_{0.2}Li_{0.1}Cu_{0.1}O$ anode vs. Li/Li^+ at a scan rate of 0.1 mV s^{-1} during the first 2 cycles.

Conclusion

In this work, we synthesized the $Mg_{0.2}Co_{0.2}Ni_{0.2}Zn_{0.2}Li_{0.1}Cu_{0.1}O$ high entropy oxide and investigated its electrochemical properties in LIB as an anode material. Charge/discharge measurements showed that the $Mg_{0.2}Co_{0.2}Ni_{0.2}Zn_{0.2}Li_{0.1}Cu_{0.1}O$ anode delivers a high initial discharge capacity of 1668 mA h g^{-1} at a current of 200 mAg^{-1}. Moreover, the capacity cyclic stability was observed as also satisfactory. These results prove that the $Mg_{0.2}Co_{0.2}Ni_{0.2}Zn_{0.2}Li_{0.1}Cu_{0.1}O$ high entropy oxide has good potential to be used as conversion-type anode in Li-ion batteries.

Acknowledgements or Notes

This research was supported by the Scientific and Technological Research Council of Turkey under the project number 119M807.

References

Chen, H., Qiu, N., Wu, B., Yang, Z., Sun, S., & Wang, Y. (2020). A new spinel high-entropy oxide (Mg0.2Ti0.2Zn0.2Cu0.2Fe0.2)3O4 with fast reaction kinetics and excellent stability as an anode material for lithium ion batteries. *RCS Advances, 10*, 9736-9744.

Kim, T., Song, W., Son, D.-Y., Ono, L. K., & Qi, Y. (2019). Lithium-ion batteries: Outlook on present, future, and hybridized technologies. *Journal of Materials Chemistry A, 7*, 2942−2964.

Lökçü, E., Toparli, Ç., & Anik, M. (2020). Electrochemical performance of $(MgCoNiZn)_{1-x}Li_xO$ high-entropyoxides in lithium-ion batteries. *ACS Applied Materials & Interfaces, 12*, 23860-23866.

Lu, J., Chen, Z., Pan, F., Cui, Y., & Amine, K. (2018). High-performance anode materials for rechargeable lithium-ion batteries. *Electrochemical Energy Reviews, 1*, 35−53.

Puthusseri, D., Wahid, M., & Ogale, S. (2018). Conversion-type anode materials for alkali-ion batteries: State of the art and possible research directions. *ACS Omega, 3*, 4591−4601.

Sarkar, A., Velasco, L., Wang, D., Wang, Q., Talasila, G., de Biasi, L., Kübel, C., Brezesinski, T., Bhattacharya, S. S., Hahn, H., & Breitung, B. (2018). High entropy oxides for reversible energy storage. *Nature Communications, 9*(3400), 1-9.

Qiu, N., Chen, H., Yang, Z., Sun, S., Wang, Y., & Cui, Y. (2019). A high entropy oxide (Mg0.2Co0.2Ni0.2Cu0.2Zn0.2O) with superior lithium storage performance. *Journal of Alloys and Compounds, 777*, 767−774.

Wang, Q., Sarkar, A., Li, Z., Lu, Y,; Velasco, L,; Bhattacharya, S. S., Brezesinski, T., Hahn, H., & Breitung, B. (2019). High entropy oxides as anode material for Li-ion battery applications: A practical approach. *Electrochemistry Communications, 100*, 121−125.

Wang, D., Jiang, S., Duan, C.,Mao, J., Dong, Y., Dong, K., Wang, Z., Luo, S., Liu, Y., & Qi, X. (2020). Spinel-structured high entropy oxide (FeCoNiCrMn)3O4 as anode towards superior lithium storage performance. *Journal of Alloys and Compounds, 844*(4), 1-30. 156158.

Yu, S.-H., Feng, X., Zhang, N., Seok, J., & Abruña, H. D. (2018). Understanding conversion-type electrodes forlithium rechargeable batteries. *Accounts of Chemical Research, 51*, 273−281.

Yuan, C., Wu, H. B., Xie, Y.;, & Lou, X. W. D. (2014). Mixed transition- metal oxides: Design, synthesis, and energy-related applications. *Angewandte Chemie International Edition, 53*, 1488−1504.

Author Information

Ersu Lökçü
Eskisehir Osmangazi University
Department of Metallurgical and Materials Engineering, 26040, Eskisehir, Turkey
elokcu@ogu.edu.tr

Reşat Can Özden
Eskisehir Osmangazi University
Department of Metallurgical and Materials Engineering, 26040, Eskisehir, Turkey

Mustafa Anik
Eskisehir Osmangazi University
Department of Metallurgical and Materials Engineering, 26040, Eskisehir, Turkey

The Eurasia Proceedings of Science, Technology, Engineering & Mathematics (EPSTEM)
ISSN: 2602-3199

The Eurasia Proceedings of Science, Technology, Engineering & Mathematics (EPSTEM), 2020

Volume 11, Pages 141-145

IConTES 2020: International Conference on Technology, Engineering and Science

Influence of Intermittent Aging in AA7075 Aluminum Alloy

Bedri BAKSAN
Eskisehir Osmangazi University

Ibrahim CELIKYUREK
Eskisehir Osmangazi University

Osman TORUN
Afyon Kocatepe University

Abstract: Heat treatable AA 7075 Aluminum alloys have been used especially in the aerospace industry for several years for their high specific strength. The demands in lighter aerospace or road vehicles like electric cars are today's major concerns. In this study, it is observed for how far the strength can be increased for this reason the influence of intermittent aging in AA7075 Aluminum alloy investigated. Rolled mill product of stock AA7074 Aluminum alloy samples were heat-treated for T6 conditions following a homogenization at 500 ^{o}C for 96 hours, and solution treatment at 500 ^{o}C for 4 hours and quenching in water. Aged at 120 ^{o}C for 24 hours and quenched. After the T6 heat treatment, an additional aging heat treatment so-called T6I4 was done at 100 ^{o}C for 2, 4, and 6 hours. The T6I4 heat-treated AA7075 alloys' microhardness values were incrementally increased by the intermittent aging heat treatment. The maximum increase rate was achieved with secondary aging at 100 ^{o}C for 6 hours, 51 % more according to the T6 condition.

Keywords: 7075 Aluminum Alloy, Aging, Microhardness, Optical Microscopy

Introduction

The 7xxx series of aluminum alloys are commonly used in the aerospace industry in structural applications due to their low density, high strength, ductility, toughness, and fatigue resistance (Leacock, Howe, Brown, Lademo, & Deering, 2013; Li et al., 2008; Panigrahi & Jayaganthan, 2011). AA7075 aluminum alloys, one of the commercial forged aluminum alloys containing zinc, copper, and magnesium-based alloys having very high mechanical properties such as 505 MPa yield strength and 11% elongation. Since AA7075 aluminum has many excellent properties such as low density, good corrosion resistance, machinability, and electrical conductivity besides its high mechanical properties, it is preferred in places where high strength is required such as aircraft bodies and wings (places where strength is required), machine parts, automotive industry and military fields (Li et al., 2008; Panigrahi & Jayaganthan, 2011; Pankade, Khedekar, & Gogte, 2018).

Aging is the most important heat treatment used for hardening in non-ferrous metals, primarily aluminum, and in high-strength stainless steel. Aluminum used in various industries such as aviation is strengthened by the aging process. The purpose of the aging hardening process, also known as the precipitation hardening process, is to precipitate the second phase, which has a hard structure, finely dispersed in the matrix phase (Pankade et al., 2018; Zou, Yan, & Chen, 2017).

For today's manufacturers of automotive and aerospace vehicles, the substitution of aluminum alloys with high density alloys in engineering applications are major design concerns due to high fuel price (Başer, 2013). Light alloys such as aluminum and magnesium alloys are the main candidates materials for reducing the weight of vehicles, especially the battery operated cars (Hofer, Wilhelm, & Schenler, 2012) main structural parts need to have high specific strength. Among these age-hardenable aluminum alloys are major materials to reduce the

vehicles' weight (Century, Kear, Board, & Systems, 1993). However, the final cost of structural element is another point to be take care of because of huge mass production rates (Roth, Clark, & Kelkar, 2001).

The 2XXX and 7XXX series age-hardenable alloys are sharing the biggest pie for its relatively high mechanical strength respect to its cost (Abd El-Rehim & Mahmoud, 2013). The studies about lowering the weight of vehicles goes back to '80s (Century, Systems, Board, Sciences, & Council, 1993; Vehicles & Board, 1982). There are some studies for reducing the weight of military or logistics vehicles by substitution of iron based alloys with aluminum based alloys were realized (Trucks, Board, & Sciences, 2003). There are numerous studies about secondary aging procedure for aluminum alloys. One of the studies was about AlSi10Mg alloy`s wear resistance (GÜL, 2014), the overview of aging heat treatment of AlSi10Mg alloy was held by Vatansever et.al (Fahri VATANSEVER, 2018). There are some studies about the effects of secondary aging and interrupted aging to aluminum alloys indicating that the secondary aging heat treatment have increasing the mechanical properties (Baksan B., 2020; Buha, Lumley, & Crosky, 2006; Hai, Ziqiao, & Zhixiu, 2005; Koch & Kolijn, 1979; R. Lumley, Polmear, & Morton, 2003, 2005). The goal of this study is to achieve superior properties from a cheaper aluminum alloy to substitute and compete with iron based alloys as well as 2xxx, and 7xxx series aluminum alloys by secondary aging heat treatment following a T6 treatment.

The intermittent aging is a method that improves mechanical strength, corrosion resistance. The intermittent application pattern is given in Figure 1. The temper designation explanations is shown in Table 1(R. P. Lumley, I. & Morton, Allan., 2004).

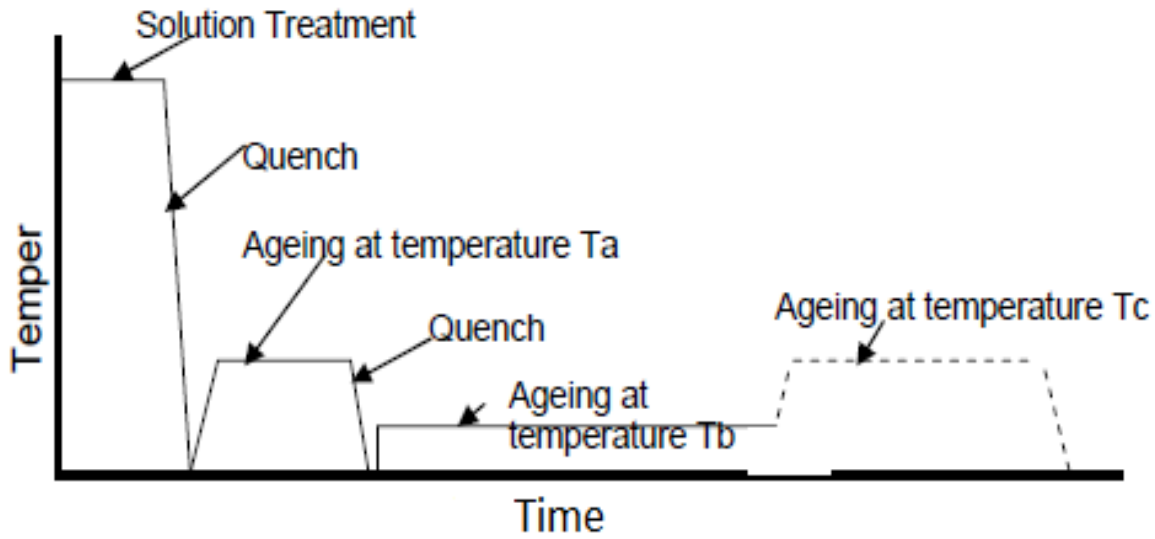

Figure 1. Stages for intermittent aging

Table 1. Intermittent aging designation explanations

Temper	Process
T6I6	Solution treat, quench, underage at (Ta), quench, age at 25-65^{o}C (Tb), re-age
T6I76	Solution treat, quench, underage at Ta, quench, age at 25-65^{o}C (Tb), re-age at artificial ageing temperature (Tc), where Tc>Ta.
T8I6	Solution treat, quench, cold work, underage at Ta, quench, age at 25-65^{o}C (Tb), re-age at artificial ageing temperature (Tc), where Tc≤Ta.
T9I6	Solution treat, quench, underage at Ta, cold work, age at 25-65^{o}C (Tb), re-age at artificial ageing temperature (Tc), where Tc≤Ta
T6I4	Solution treat, quench, underage at (Ta), quench, age at 25°C-65°C (Tb)
T6I7	Solution treat, quench, underage at (Ta), cool slowly (furnace cool or natural cool).
T77I4	Solution treat, quench, age at (Ta1), age at temperature (Ta2), where Ta2>Ta1, quench, age at 25-65°C (Tb)
T8I4	Solution treat, quench, cold work, underage at (Ta), quench, age at 25-65°C (Tb).
T9I4	Solution treat, quench, underage at (Ta), cold work, age at 25-65°C (Tb).

Materials and Method

Stock AA7075 aluminum alloy samples were supplied locally for this study. Following a T6 heat treatment, an intermittent aging heat treatment was done for different times. The microhardness tests were done for each experiment. The microstructures were obtained from an optical microscope for observing the microstructural changes

The samples were homogenized at 500 °C for 96 hours. The samples were solutionized at 500 °C for 4 hours and quenched in water at room temperature. Aging heat treatment was done at 120 °C for 24 hours and quenched in water. Secondary aging heat treatment was realized at 100 °C for 2, 4, and 6 hours.

After completing the heat treatment procedure the samples were polished and etched with Keller etchant.

The microhardness testing was done by Futuretech make FV-800 instrument with 300 g load for 10 seconds.

Results and Discussion

The microhardness testing results showed that the intermittent aging heat treatment improves the hardness. The hardness increases with aging time. The maximum value of hardness was obtained in samples aged 120 °C for 24 hours and intermittently aged at 100 °C for 6 hours giving 197 H_v. This hardness value is 92% higher than the samples aged only at 120 °C for 24 hours. The change in hardness was given in Figure 2.

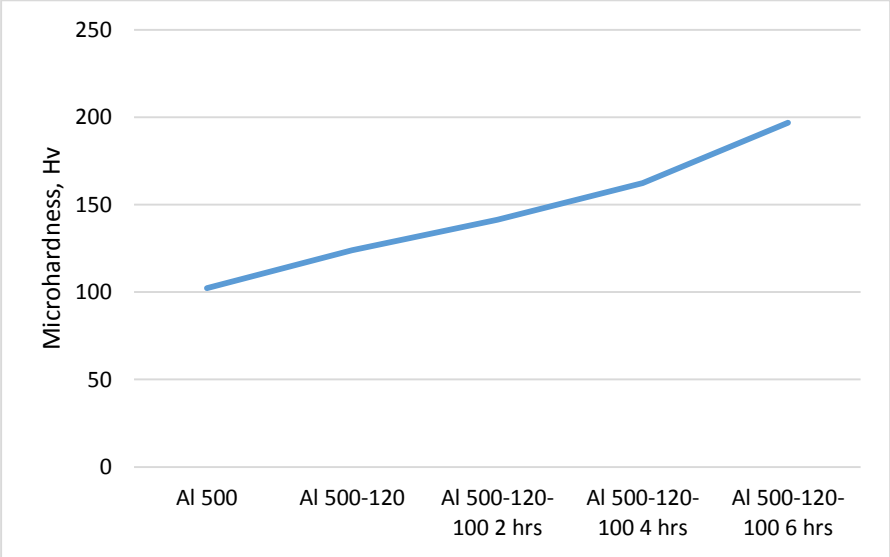

Figure 2. Microhardness change versus aging heat treatment

The microstructures of aged and intermittently aged samples were given in Figure 3. The microstructures revealed that the grains were coarsening by increasing time in intermittently aged samples. The factors causing the hardness increase are the second phase particles that have precipitated. During aging, with the effect of temperature, the precipitates dispersed through the matrix, as the aging continues, these clusters begin to form β precipitates compatible with the α matrix phase. These precipitates play a role in increasing hardness. As the aging continues, the sediments grow further and reach a critical height, it is seen from the trend of the graph in Fig.1 but the time and hardness limit could not be detected because the experiments are limited to 6 hours. At higher magnifications, the fine precipitates were seen. As the aging time increases the fine precipitates dispersed very fine all over the matrix.

These results revealed that the production of materials with higher strengths would be possible because in this study almost the hardness value was obtained as twice the stock alloy. This means especially, in the production of vehicles it is possible to lower the aluminum weights at least half of the present applications.

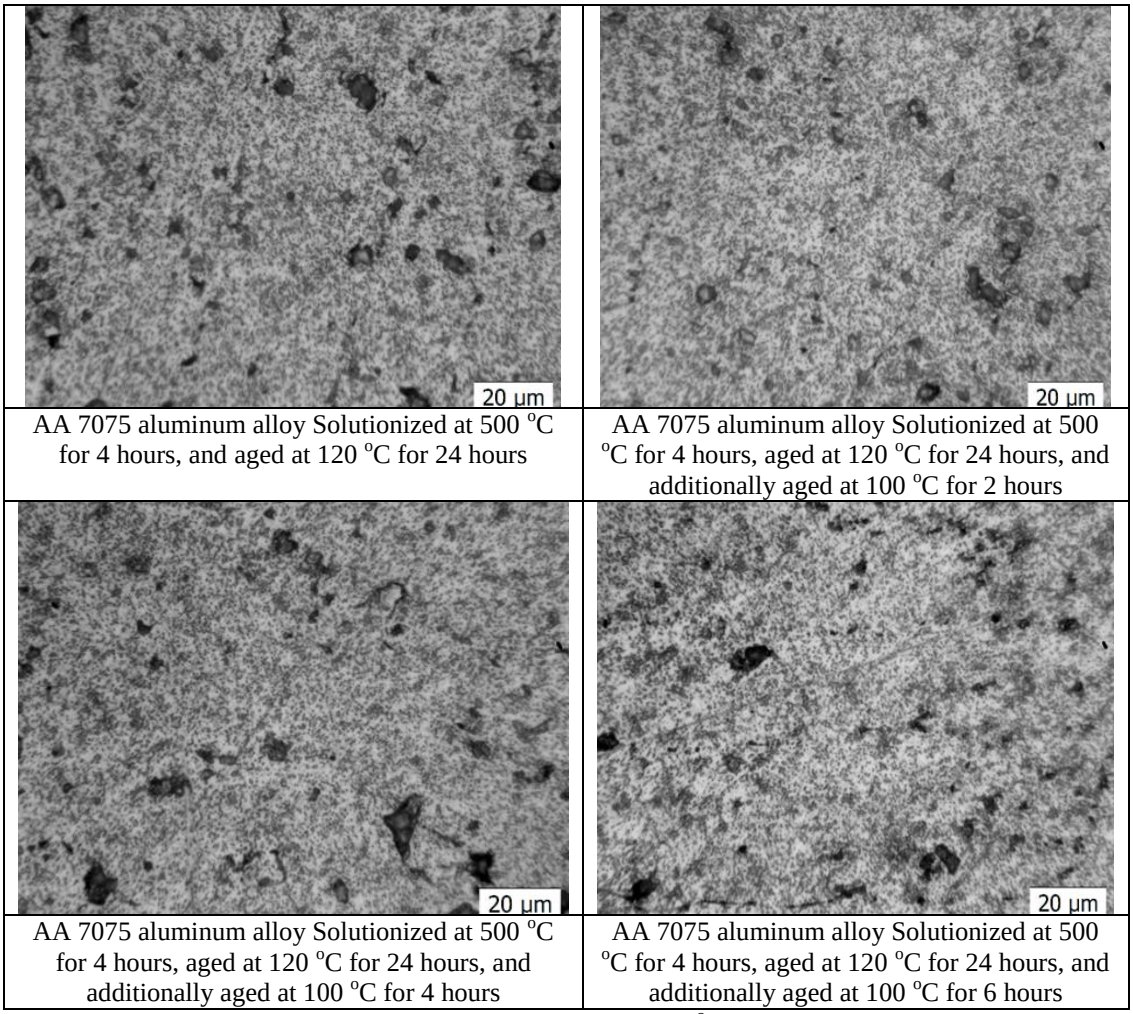

AA 7075 aluminum alloy Solutionized at 500 ^{o}C for 4 hours, and aged at 120 ^{o}C for 24 hours	AA 7075 aluminum alloy Solutionized at 500 ^{o}C for 4 hours, aged at 120 ^{o}C for 24 hours, and additionally aged at 100 ^{o}C for 2 hours
AA 7075 aluminum alloy Solutionized at 500 ^{o}C for 4 hours, aged at 120 ^{o}C for 24 hours, and additionally aged at 100 ^{o}C for 4 hours	AA 7075 aluminum alloy Solutionized at 500 ^{o}C for 4 hours, aged at 120 ^{o}C for 24 hours, and additionally aged at 100 ^{o}C for 6 hours

Figure 3. Microstructures of AA7075 aluminum alloy aged at 120 ^{o}C for 24 hours, and intermittently aged at 100 ^{o}C for 2, 4, and 6 hours.

Conclusion

The secondary aging heat treatment would be an emerging method for increasing the strength of age-hardenable alloys. This may also increase the service life of age-hardened parts. The increase in hardness in this study obtained more than 10% which is higher than ordinary aged ones.

In this study the T6I4 treatment at 100 ^{o}C for 6 hours also resulted in a peak hardness of 197 H_v this value is higher than T6 condition. This phenomenon may be related with reduced mobility of vacancies, and the growth of partially dissolved η' precipitates, the re-nucleation of precipitates, or the transformation to the stable η phase (Esmailian M., 2015).

References

Abd El-Rehim, A. F., & Mahmoud, M. A. (2013). Transient and steady state creep of age-hardenable Al-5 wt% Mg alloy during superimposed torsional oscillations. *Journal of Materials Science, 48*(6), 2659-2669. doi:10.1007/s10853-012-7059-x

Baksan B., C. I., Kilic Y. (2020). Effect of secondary aging of EN AC 43200 Aluminum alloy to mechanical properties. *The International Journal of Materials and Engineering Technology, 3*(1), 16-20.

Başer, T. (2013). Alüminyum alaşımları ve otomotiv endüstrisinde kullanımı. *Mühendis ve Makina, 53*(635), 51-58.

Buha, J., Lumley, R., & Crosky, A. (2006). Microstructural development and mechanical properties of interrupted aged Al-Mg-Si-Cu alloy. *J Metallurgical Materials Transactions A, 37*(10), 3119-3130.

Century, C. M., Kear, B. H., Board, N. M. A., & Systems, C. E. T. (1993). *Materials research agenda for the automobile and aircraft ındustries*: National Academies Press.

Century, C. M., Systems, C. E. T., Board, N. M. A., Sciences, D. E. P., & Council, N. R. (1993). *Materials research agenda for the automobile and aircraft ındustries*: National Academies Press.

Esmailian M., S. M., Mottahedi A. , Shabestari S. G. . (2015). Effect of T6 and re-aging heat treatment on mechanical properties of 7055 aluminum alloy. *International Journal of Materials and Metallurgical Engineering, 9*(11), 1303-1306. doi:doi.org/10.5281/zenodo.1110057

Vatansever, F. Erturk, A. T., & Karabay, S. (2018). Alüminyum-silisyum alaşımlarının mikroyapısal ve mekanik özelliklerinin t6 ısıl işlemi ile iyileştirilmesi. *Dokuz Eylül Üniversitesi-Mühendislik Fakültesi Fen ve Mühendislik Dergisi, 20*(60). doi:DOI: 10.21205/deufmd. 2018206062

GuL, F. (2014). AlSi10Mg döküm alaşımlarının bazı mekanik özellikleri üzerine ikincil yaşlandırma işleminin etkisi. *Süleyman Demirel Üniversitesi Fen Bilimleri Enstitüsü Dergisi, 18*(1). doi:10.19113/sdufbed.97535

Hai, L., Ziqiao, Z., & Zhixiu, W. (2005). Investigation of secondary ageing characteristics of 7055 aluminum alloy—(Ⅱ) microstructures and fractography [J]. *J Rare Metal Materials Engineering, 8*.

Hofer, J., Wilhelm, E., & Schenler, W. (2012). Optimal lightweighting in battery electric vehicles. *World Electric Vehicle Journal, 5*(3), 751-762. doi:10.3390/wevj5030751

Koch, G., & Kolijn, D. (1979). The heat treatment of the commercial aluminum alloy 7075. *J Journal of Heat Treating, 1*(2), 3-14.

Leacock, A. G., Howe, C., Brown, D., Lademo, O.-G., & Deering, A. (2013). Evolution of mechanical properties in a 7075 Al-alloy subject to natural ageing. *Materials & Design, 49*, 160-167. doi:10.1016/j.matdes.2013.02.023

Li, J.-f., Peng, Z.-w., Li, C.-x., Jia, Z.-q., Chen, W.-j., & Zheng, Z.-q. (2008). Mechanical properties, corrosion behaviors and microstructures of 7075 aluminium alloy with various aging treatments. *Transactions of Nonferrous Metals Society of China, 18*(4), 755-762. doi:10.1016/s1003-6326(08)60130-2

Lumley, R., Polmear, I., & Morton, A. J. (2003). Interrupted aging and secondary precipitation in aluminium alloys. *J Materials Science Technology, 19*(11), 1483-1490.

Lumley, R., Polmear, I., & Morton, A. J. (2005). Development of mechanical properties during secondary aging in aluminium alloys. *J Materials Science Technology, 21*(9), 1025-1032.

Lumley, R. P., I. & Morton, Allan. (2004). Temper Developments Using Secondary Ageing. *Materials Forum, 28*, 85-95.

Panigrahi, S. K., & Jayaganthan, R. (2011). Effect of ageing on microstructure and mechanical properties of bulk, cryorolled, and room temperature rolled Al 7075 alloy. *Journal of Alloys and Compounds, 509*(40), 9609-9616. doi:10.1016/j.jallcom.2011.07.028

Pankade, S. B., Khedekar, D. S., & Gogte, C. L. (2018). The influence of heat treatments on electrical conductivity and corrosion performance of AA 7075-T6 aluminium alloy. *Procedia Manufacturing, 20*, 53-58. doi:10.1016/j.promfg.2018.02.007

Roth, R., Clark, J., & Kelkar, A. (2001). Automobile bodies: Can aluminum be an economical alternative to steel? *Jom, 53*(8), 28-32. doi:10.1007/s11837-001-0131-7

Trucks, C. o. L. M. f. s. C. A., Board, N. M. A., & Sciences, D. o. E. a. P. (2003). *Use of LIGHTWEIGHT MATERIALS in 21st century ARMY TRUCKS*. U.S.A: National Academies Press.

Vehicles, N. R. C. C. o. M. f. L. M., & Board, N. R. C. N. M. A. (1982). *Materials for Lightweight Military Combat Vehicles: Report*: National Academy Press.

Zou, X.-l., Yan, H., & Chen, X.-h. (2017). Evolution of second phases and mechanical properties of 7075 Al alloy processed by solution heat treatment. *Transactions of Nonferrous Metals Society of China, 27*(10), 2146-2155. doi:10.1016/s1003-6326(17)60240-1

Author Information

Bedri Baksan
Eskisehir Osmangazi University
Metalurji ve Malzeme Muh.Bolumu, Eskisehir/Turkey
Contact e-mail: *baksan@ogu.edu.tr*

Ibrahim Celikyurek
Eskisehir Osmangazi University
Metalurji ve Malzeme Muh.Bolumu, Eskisehir/Turkey

Osman Torun
Afyon Kocatepe University
Mekatronik Muhe.Bolumu,Afyonkarahisar/Turkey

The Eurasia Proceedings of Science, Technology, Engineering & Mathematics (EPSTEM)
ISSN: 2602-3199

The Eurasia Proceedings of Science, Technology, Engineering & Mathematics (EPSTEM), 2020

Volume 11, Pages 146-149

IConTES 2020: International Conference on Technology, Engineering and Science

Diagnosis of Rheumatic Complications in Patients with Inflammatory Bowel Disease

Olena SULIMA
Dnipro City Hospital, Dnipro

Volodymyr SULYMA
SI Dnipropetrovsk Medical Academy of Ministry Health of Ukraine

Abstract: Investigation methods: X-ray: with a peripheral form without erosive changes; in 15% of patients, erosive changes in the metacarpophalangeal or metatarsophalangeal joints (asymmetry of arthritis). The study of synovial fluid: with a peripheral form, inflammatory in nature. Laboratory studies: increasing the concentration of inflammatory markers, thrombocytosis, anemia of chronic diseases. Diagnostic criteria; - the diagnosis of Ulcerative Colitis or Crohn Disease; - radiological signs of inflammation in the peripheral joints or sacroiliac joints or joints of the spine. Differential diagnosis: - Peripheral form: atypical course of rheumatoid arthritis, infectious arthritis, reactive arthritis; - Axial form: other spondyloarthropathies. Peripheral form: usually has an acute, migratory course; not symmetrical damage to the joints, arthritis of the knee and ankle joints is more often formed; there is no rheumatoid factor; as a rule, there are no erosions and deformations of the joints; most joint changes appear after a few years from the occurrence of inflammatory changes in the intestine. Types of peripheral joint lesions: 1 - oligosarticular (with lesions of ≤5 joints), acute course, can outstrip the appearance of changes in the intestine, usually disappears within 10 weeks, extraintestinal symptoms are often associated, e.g. erythema nodosum; 2 - multi-articular (> 5 joints), usually without connection with the debut of intestinal disease, chronic course (months, years), without extraintestinal symptoms other than uveitis; 3 - peripheral joint damage is combined with axial spondylitis. Axial form: in some patients there is no chronic inflammatory pain in the lower back, despite the presence of radiological changes typical for inflammation of the sacroiliac joints, while in others the characteristic clinical manifestations of spinal lesions occur without typical radiological changes. Changes in other organs associated with Ulcerative Colitis / Crohn Disease.

Keywords: Diagnostic, Rheumatic, Colitis , Crohn Disease.

Introduction

Crohn's disease (CD) (regional enteritis, granulomatous ileitis) is an inflammatory disease involving all layers of the intestinal wall in the process; characterized by intermittent (segmental) nature of the lesion of various sections of the gastrointestinal tract. It is characterized by diarrhea mixed with mucus and blood, abdominal pain (often in the right iliac region), weight loss, and fever. Ulcerative colitis (UC) (nonspecific ulcerative colitis, idiopathic colitis) is an ulcerative-destructive lesion of the mucous membrane of the colon, which is localized mainly in its distal parts. In the clinical picture are characteristic: bleeding from the rectum, rapid bowel movement, tenesmus; abdominal pain is less intense than with Crohn's disease, localized most often in the left iliac region. In approximately 30% of adolescent patients, ulcerative colitis begins suddenly with the appearance of abdominal pain and diarrhea mixed with blood. According to various authors, extraintestinal manifestations of inflammatory bowel diseases (IBD) are noted to 25% of cases. Their largest share is in total forms of ulcerative colitis (85%) and Crohn's disease involving the colon (30%) or large and small intestines (60%).
Systemic manifestations of IBD according to the pathogenetic principle are divided into three groups.

The first group includes manifestations arising as a result of systemic hypersensitivity, - damage to the joints, eyes, skin, oral mucosa; to the second - due to bacteremia and antigenemia in the portal system - damage to the

liver and biliary tract. There are also phenomena that develop a second time with long-term disorders in the colon, such as anemia, electrolyte disorders. The inflammatory process in the intestine causes a violation of intestinal permeability and the penetration of autoantibodies and circulating immune complexes from the intestinal lumen into the bloodstream. This causes a systemic immuno-inflammatory process with damage to the vessels, the synovial membrane of the joints and the ligamentous apparatus of the spine.(Mendoza J.L., et al, 2005). Peripheral arthritis in patients with UC and CD develops more often with widespread colon damage. As a rule, its manifestation falls on the first year from the onset of bowel disease. In 70% of cases, arthritis develops with an exacerbation of intestinal pathology, but sometimes its symptoms may precede the symptoms of the underlying disease, especially in patients with Crohn's disease. In UC, joint damage is observed in 20% of patients, in CD – to 10%. In 75% of cases, joint damage occurs in the form of peripheral arthritis, in 25% of spondylitis and sacroileitis.

With these intestinal pathologies, damage to the joints of the lower extremities is most characteristic. As a rule, there is an acute onset of the joint syndrome in the form of monoarthritis with damage to the knee or ankle joint on one side. After several days, symmetrically involved knee, ankle, shoulder, elbow joints. The defeat of small joints is less characteristic. In CD, joint syndrome can manifest itself with migratory arthralgia, as well as erosive arthritis and joint deformity. Sacroileitis is diagnosed in 25% of patients with UC and in 15% of patients with CD, usually symmetrical. (Bourikas L. A.,2009).

Crohn’s disease is associated with a type of rheumatologic disease known as seronegative spondyloarthropathy. This group of diseases is characterized by inflammation of one or more joints (arthritis) or muscle inserts (Enthesitis). Arthritis in Crohn's disease can be divided into two types. The first type affects the greater weight of the supporting joints, such as the knee (the most common), hips, shoulders, wrists, or elbows. The second type symmetrically includes five or more small joints of the arms and legs. Arthritis may also include the spine, leading to ankylosing spondylitis if the entire spine is involved, or simply sacroiliitis if only the sacroiliac joint is involved. Symptoms of arthritis include painful, warm, swollen, stiff joints, and loss of joint mobility or function.

Method

For diagnostic of rheumatic complications in patients with inflammatory bowel disease used:

Investigation methods:

X-ray: with a peripheral form without erosive changes; in 15% of patients, erosive changes in the metacarpophalangeal or metatarsophalangeal joints (asymmetry of arthritis). (Leclerc-Jacob S., et al, 2014).
The study of synovial fluid: with a peripheral form, inflammatory in nature.
Laboratory studies: increasing the concentration of inflammatory markers, thrombocytosis, anemia of chronic diseases.

Diagnostic criteria:

the diagnosis of Ulcerative Colitis or Crohn Disease;
radiological signs of inflammation in the peripheral joints or sacroiliac joints or joints of the spine.

Differential diagnosis:

Peripheral form: atypical course of rheumatoid arthritis, infectious arthritis, reactive arthritis;
Axial form: other spondyloarthropathies.

Peripheral form: usually has an acute, migratory course; not symmetrical damage to the joints, arthritis of the knee and ankle joints is more often formed; there is no rheumatoid factor; as a rule, there are no erosions and deformations of the joints; most joint changes appear after a few years from the occurrence of inflammatory changes in the intestine.

Types of peripheral joint lesions:

1 -oligosarticular (with lesions of ≤5 joints), acute course, can outstrip the appearance of changes in the intestine, usually disappears within 10 weeks, extraintestinal symptoms are often associated, e.g. erythema nodosum;
2 - multi-articular (> 5 joints), usually without connection with the debut of intestinal disease, chronic course (months, years), without extraintestinal symptoms other than uveitis;
3 - peripheral joint damage is combined with axial spondylitis.

Axial form: in some patients there is no chronic inflammatory pain in the lower back, despite the presence of radiological changes typical for inflammation of the sacroiliac joints, while in others the characteristic clinical manifestations of spinal lesions occur without typical radiological changes.

Changes in other organs associated with Ulcerative Colitis / Crohn Disease.

Peripheral arthritis usually affects the large joints of the hands and feet, including the elbows, wrists, knees and ankles. The pain can "migrate" from one joint to another and last from several days to several weeks. The more intense the inflammatory process in the colon, the more pronounced arthritis. To date, there are no specific tests to confirm UC - associated arthritis. This diagnosis can only be made by excluding other causes of joint pain. Fortunately, such peripheral arthritis usually does not cause a significant change in joint function. (Orchard T. R., et al, 2009).

Spondylitis (arthritis of the intervertebral joints) causes pain and stiffness in the lower part of the spine and sacroiliac joints. In young people, these symptoms can appear much earlier than intestinal manifestations. Unlike peripheral arthritis, spondylitis can lead to a significant deterioration in spinal function, as the volume of movement in the intervertebral joints decreases. Spondylitis usually appears around the age of 35. (Sulyma V., Sulima O., 2019; Sulima O., Sulyma V., 2020).

Results and Discussion

X-ray signs of sacroileitis observed in 20-50% of patients with UC and CD, but progressive ankylosing spondylitis observed only in 1-10% of patients. MRI can detect in patients with appropriate symptoms early sacroiliitis without the presence of radiographic signs of SPA. When conducting differential diagnostics, it is necessary to exclude any deformations and osteoarthritis, osteoarthritis, rheumatoid arthritis, connective tissue diseases. IBD-associated peripheral arthritis should be differentiated from arthralgia (which may be complicated by the abolition of corticosteroid therapy), osteonecrosis, lupus syndrome.

Peripheral arthritis in IBD is usually asymmetric and oligoarticular. Them the onset may precede intestinal symptoms, although they usually coincide or appear after the onset of IBD. Overall forecast peripheral arthritis is favorable if not take into account the tendency to chronicity and the formation of erosion in a small number of patients. Forecast axial arthropathy is less favorable and is associated with the prognosis of AS, and not with the activity of IBD. (Hindorf U., et al, 2009).

Classical AS is a progressive pathological condition with structural damage, disability, a negative impact on the quality of life of patients. It is important to timely identify, with signs of active inflammation on MRI, early non-radiological axial SpA in order to try to prevent its progression to radiographic axial SpA, which is observed in 10–20% of patients within 2 years with increased C-reactive protein.

Conclusion

Diagnosis of extraintestinal manifestations of Crohn's disease and Ulcerative colitis still requires significant efforts by a rheumatologist and proctologist to effectively treat patients with these problems.

Recommendations

It is recommended to use the available data in the diagnostic program in patients with rheumatologically complications in inflammatory bowel diseases.

Acknowledgements or Notes

Thank you very much to the staff of the Dnipro City hospital and SI "Dnipropetrovsk Medical Academy of Ministry Health of Ukraine", Dnipro, Ukraine.

References

Bourikas, L. A., & Papadakis, K. A. (2009). Musculoskeletal manifestations of inflammatory bowel disease. *Inflam Bowel Dis, 15*, 1915-24.

Hindorf, U., Johansson, M., Eriksson, A., et al .(2009). Mercaptopurine treatment should be considered in azathioprine intolerant patients with inflammatory bowel disease. *Aliment Pharmacol Ther, 29*, 654-61.

Leclerc-Jacob, S., Lux, G., Rat, A.C., et al .(2014). The prevalence of inflammatory sacroiliitis assessed on magnetic Resonance imaging of inflammatory bowel disease: a retrospective study performed on 186 patients. *Aliment Pharmacol Ther, 39*, 957-62.

Mendoza, J.L., Lana, R., Taxonera, C., et al. (2005). Extraintestinal manifestations in inflammatory bowel disease: differences between Crohn's disease and ulcerative colitis. *Med Clin (Barc), 125*, 297-300.

Orchard T. R., Holt H., Bradbury L., et al. (2009). The prevalence, clinical features and association of HLA-B27 in sacroiliitis associated with established Crohn's disease. *Aliment Pharmacol Ther, 29*,193-7.

Sulima, O., & Sulyma, V. (2020). The frequency of joints manifestations of inflammatory bowel disease in the practice of a rheumatologist. *Abstracts Falk Symposium 218*, Mexico. – P.33.

Sulyma, V., & Sulima, O. (2019). The complexity of treatment tactics in patients with severe ulcerative colitis in the presence of extraintestinal manifestations of the joints. *Abstracts Falk Symposium 214*, Oxford. – P. 81.

Author Information

Olena Sulima
Dnipro City Hospital
Dnipro, Ukraine
Contact e-mail: *olenasulima2@gmail.com*

Volodymyr Sulyma
SI "Dnipropetrovsk Medical Academy Ministry Health of Ukraine"
V. Vernadskyj Street, 9, Dnipro, Ukraine

The Eurasia Proceedings of Science, Technology, Engineering & Mathematics (EPSTEM)
ISSN: 2602-3199

The Eurasia Proceedings of Science, Technology, Engineering & Mathematics (EPSTEM), 2020

Volume 11, Pages 150-153

IConTES 2020: International Conference on Technology, Engineering and Science

Study the Susceptibility of Plant Isolated Bacteria against Some Antibiotics

Mohmmed Lefta ATALA
Baghdad University

Abstract:15 isolate of *Pantoea dispersa* were isolated from soil samples included two isolates with highest producing isolates for cell wall degrading enzymes of cellulase. The two isolates were subjected to susceptibility test against chloramphenicol 30mg, imipenem 10mg, nalidixic acid 30 mg, Amoxicillin 25mg, Oxacillin 5mg and Methicillin 10mg. the results indicated there were no resistance to chloramphenicol, imipenem, nalidixic acid, oxacillin and methicillin, while one of isolates was resist to amoxicillin.

Keywords: Pantoea dispersa, Antibiotics, Cellulase, Methicillin, Oxacillin.

Introduction

The Pantoea genus contained twenty species, the colonies of this bacteria are pigmented with yellow color, lactose fermented, motile, mucoid in form and appear quorum sensing (Walterson. & Stavrinides, 2015). Also it is Gram-negative, non capsulated, do not forming of spore, straight rod in shape and it is isolated from plant surfaces, human feces and from the environmental sources (Nobuhiro et al., 2019).) A genus of *Pantoea* is uncommon to be pathogen in a clinical cases, but *P. agglomerans* is the distinguished species which infected the humans, previously designate *Enterobacter agglomerans* (Schmid et al., 2003)).

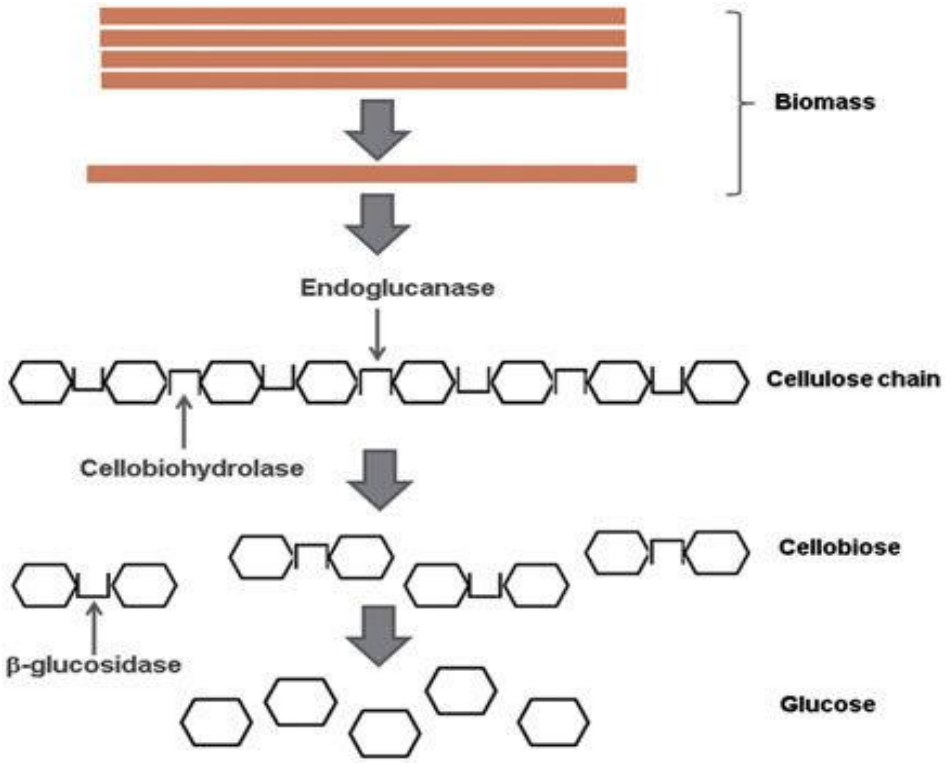

Figure 1: Cellulose hydrolysis by three type of enzymes. (Eva& Anas, 2013)

Pantoea dispersa species is recorded to cause infections, like respiratory, neonatal sepsis, and bloodstream infections, also to infections in immune system of patients and in addition to acute cholangitis (Layla & Mayyada, 2016). The development of resistance in bacteria against antibacterial substances has detect a failure therapy for infection. Killing these bacteria is a major challenge for scientists. In addition to some information on the pathogenicity of this bacterium in humans, there is little or no data on resistance in this bacterium in Iraq. Therefore, the study was important to detect environmental bacteria and their susceptibility against some types of antibiotic (Atlas & Brown, 1995).

Cellulose are important plant cell wall degrading enzyme, which consider the most numerous and renewable source of power. Cellulose is enzyme that produced by bacteria which works as virulence agent to break down the components of cell wall (Liu et al., 2005), the full enzymatic hydrolysis for cellulose needs three kinds of enzymes named cellobiohydrolase, carboxymethylcellulase and glucosidase (figure 1) (Yi et al.,1999). Numerous of bacteria, yeast and fungi can produce cellulose enzyme, but Pantoea have most important pathogen for plant around the world, because it cause some of plant diseases like leaf blight and bulb rot in onion (Sangharak et al., 2012).

Materials and Methods

Soil Samples Collection

To isolation of bacteria that producing plant cell wall degrading enzymes, soil samples were collected from corn crop located Baghdad university's fields.

Preparation of Samples

A quantity of 1gm of soil samples were suspended in 9ml of D.W. and mixed vigorously, then 0.1ml of supernatant were spreading on nutrient agar dishes and incubated at 30C^{o} for 24 hrs.

Identification of Bacteria

The isolates are identified according to Atlas *et al*. (1995).

Cellulase Enzyme Production

The cellulase enzyme production was determined depending on degrading crystalline cellulase in cellulose agar plates after incubation at 30C^{o} for 24hrs, then the plates were flooded with congo red solution and left for 15min., then the plates were destained with 1M NaCl solution. The appearance halo zone around colonies due to cellulase production indicates positive results (Oxoid, 1982).

Susceptibility Test for Test Bacteria

The isolates were streaked on nutrient agar, Then a discs of antibiotics of amoxicillin, chloramphenicol, imipenem, nalidixic acid, Oxacillin 5mg and Methicillin 10mg were placed on agar. Then plates were incubated at 37°C for 24hrs. After that a diameters of inhibition zone were recorded and compared with standard value of scientific references (Selvakumar et al., 2008).

Results and Discussion

Isolation and Identification of Bacteria

15 isolate of bacteria were isolated from soil samples after incubation period reached to 24 hrs. The isolates were identified depending on the cultural and biochemical properties. The results appeared that these isolates belong to *Pantoea dispersa* which appeared negative results for tests of Gram stain, Oxidase, Methyl red,

Indole, Sorbitol, Urease. While they appeared positive results to Catalase, Motility, VP, Gelatinase, Citrate utilization, Fermentation / Oxidation of Mannitol, Lactose, Rhamnose, Maltose, Sucrose, Salicin, also for Growth at 30 °C or 41°C. İn addition to results of morphological tests that showed these isolates were as straight rods in shape, motile, non-haemolytic, non-capsulated, non-sporeforming. Also the colonies were smooth, mucoid, yellow pale pigmented, irregularly round, rough. The previous results were accordance to these reported by Selvakumar *et al*. (2008) that mentioned these isolates belong to *Pantoea dispersa* species. The isolation of these bacteria from the soil is very important , when this species it can produce essential materials in industry, in addition to their role in the pathogenosity for human and plant.

Cellulase Production of Pantoea Dispersa Bacteria

To determine the producer isolates for cellulose, the isolate were screened using CMC agar media which involved CMC as sole source of carbon, the results indicate that the 15 isolates were produced to cellulase enzyme with halo zone ranged between 10 into 15 mm, the results was similar to these reported by Atala *et al*. (2015), and Nurachman (2010) that mentioned these bacteria are able to produce cellulase enzyme which can utilize the cellulose as substrate. Also the results were accordance to these mentioned by Nurachman et al., (2010) if the isolates were grow on cellulose with variable degree according to the diameters of clear halo around the colonies of bacteria,

Sensitivity Test for Antibiotics

The results of susceptibility test appeared that these isolates were not resist to each used antibiotics involved methicillin and oxacillin, but only one of them was resist to amoxicillin antibiotic, the results were accordance to these reported by Mardaneh & Mohammad (2013) who mentioned that 62-100% of *Pantoea dispersa* isolates sensitive to each of imipenem, chloramphenicol and nalidixic acid and there were 25% of isolates resist to amoxicillin. Also nearly, there were similar results between different isolate that isolated from different sources. Also the results were similar to these mentioned by Richter *et al*. (2013) which appeared this species was susceptible to all antimicrobial agents tested in the study like imipenem, ampicillin, cefazolin, gentamicin, LVFX, and trimethoprim-sulfamethoxazole. In other study dissimilar result was appeared that this species was resist to imipenem antibiotic (Hagiya & Otsuka, 2014). It is clear from the studies it must performe further researches to determine sensitivity and pathogenesity of this bacteria, when there were a few knowledge on the pathogensity of this bacteria in human and the development their resistant to antibiotics.

Conclusion

The study concluded there were similar results for sensitivity test between isolates that isolated from different sources of isolation for antibiotics. But there were unexpected results of antibiotic resistance in soil isolated bacteria. Also the production of cellulose enzyme it was different between the isolate that isolated from the same source.

Recommendations

It is recommended to perform further studies on the resist of bacteria that isolated from the soil against another antibiotics, in order to determine the fact sensitivity and pathogenesity of this bacteria, because there were a little knowledge on the pathogensity of this bacteria in human and the development their resistant to antibiotics.

Acknowledgements or Notes

Finally, the study was not very easy to isolate these bacteria, but rather it took a long time to isolate them.

References

Atala, M. L., Hameed, M. J., & Kadhim, M. I. (2015). Production, purification and characterization of cellulose from local ısolate of pantoea spp. *Iraqi Journal of Science. 56*(2B): 1324-1330.

Atlas, M., Parks, C. & Brown, A. (Eds) (1995). *Laboratory manual of experimental microbiology*. Mosby-Year-Book, Inc., USA.

Eva, M. G. D. P. & Anas, S. (2013). The cellulolytic system of Thermobifida fusca. REVIEW ARTICLE. Informa health care. pp1-12. Retrieved 2020 from internet database. https://www.researchgate.net/publication/236088767_The_cellulolytic_system_of_Thermobifida_fusca/figures?lo=1&utm_source=google&utm_medium=organic.

Hagiya, H. & Otsuka, F. (2014). Pantoea dispersa bacteremia caused by central line-associated bloodstream infection. *Braz J Infect Dis. 18*, 696–7..

Layla, S. A., & Mayyada, D. F. (2016). Prevelance and antibiotic susceptibility patterns of Pantoea spp. isolated form clinical and environmental sources in Iraq. *International Jounal of Chem Tech Research, 9*(8): 430-437.

Liu, H., Zhang. S., Schell, M.A. & Denny, T.P. (2005). Pyramiding unmarked deletions in Ralstonia solanacearum shows that secreted proteins in addition to plant cell-wall-degrading enzymes contribute to virulence. *Mol. Plant-Microbe Interact., 18*, 1296-1305.

Mardaneh, J. & Dallal, M. M. S. (2013). Isolation, identification and antimicrobial susceptibility of *Pantoea* (*Enterobacter*) *agglomerans* isolated from consumed powdered infant formula milk (PIF) in NICU ward: First report from Iran. *Iran J Microbiol. 5*(3): 263–267.

Mehar, V., Yadav, D., Sanghvi, J., Gupta, N., & Singh, K. (2013). *Pantoea dispersa:* a n unusual cause of neonatal sepsis. *Braz J Infect Dis. 17*, 726–8.

Nobuhiro, A., Yusuke, K., Atsuko, Y., Daisuke, S., Hiroki, W., Hideo, K., Arufumi, S., Mao H., Hiroyuki S., Yuka Y. & Hiroshige M. (2019). Pantoea dispersa bacteremia in an immunocompetent patient: a case report and review of the literature. *Journal of Medical Case Reports, 13*(33), 1-5.

Nurachman, Z., Kurniasih, S. D.,Puspitawati, F.,Hadi, S., Radjasa, O. K. & Natalia, D. (2010). Cloning of the endoglucanase gene from a Bacillus amyloliquefaciens PSM 3.1 in E. coli revealed catalytic triad residues ThrHis-Glu. *Americ. J. of Biochem. and Biotech., 6*(4), 268-274.

Oxoid. (Eds) (1982).The oxoid manual of culture media, ingredients and other laboratory services. 5th .ed.Oxoid limited. Wade road. Basingstoke. Pp. 214-215.

Richter, S.S., Sercia, L., & Branda, J.A, (2013). Identification of *Enterobacteriaceae* by matrix-assisted laser desorption/ionization time-of-flight mass spectrometry using the VITEK MS system. *Eur J Clin Microbiol Infect Dis. 32*, 1571–8.

Sangkharak, K., Vangsirikul, P. & Janthachat, S. (2012). Strain improvement and optimization for enhanced production of cellulase in Cellulomonas sp. TSU-03. *Afric. J. of Microbial. Res., 6*(5): 1079-1084.

Schmid, H., Schubert, S., Weber, C., & Bogner, J.R.(2003). Isolation of a Pantoea dispersa-like strain from a 71-year-old woman with acute myeloid leukemia and multiple myeloma. *Infection, 31*, 66–7.

Selvakumar, G., Kundu, S., Joshi, P., Nazim, S. A. D., Mishra, P. K. & Gupta, H. S.(2008). Characterization of a cold-tolerant plant growth- promoting bacteria Pantoea dispersa 1A isolated from a sub-apine soil in the north western Indian Hiimalagas. *Journal Microbial. Biotecnol. 24*, 955-960.

Walterson, A. M. & Stavrinides, J. (2015). Pantoea: insights into a highly versatile and diverse genus within the Enterobacteriaceae. *FEMS Microbiology Reviews. 39* (6), 968–984.

Yi, J. C., Sandra, A. B. J. & Shu, T. C. (1999). Production and distribution of endoglucanase, cellobiohydrolase, and Ɓ-glucosidase components of the cellulolytic system of volvariella volvacea, the edible straw mushroom. *Appl. Environ. Microbiol. 65*, 553-559.

Author Information

Mohmmed Lefta Atala
Baghdad University,
Department of Biology, College of Science, Baghdad
University, Iraq
Contact e-mail: *mohammedlafta@hotmail.com*

The Eurasia Proceedings of Science, Technology, Engineering & Mathematics (EPSTEM)
ISSN: 2602-3199

The Eurasia Proceedings of Science, Technology, Engineering & Mathematics (EPSTEM), 2020

Volume 11, Pages 154-158

IConTES 2020: International Conference on Technology, Engineering and Science

Secondary Aging Effects in Copper - Chromium Alloy

Bedri BAKSAN
Eskisehir Osmangazi University

Ibrahim CELIKYUREK
Eskisehir Osmangazi University

Osman TORUN
Afyon Kocatepe University

Abstract: Copper Chromium alloys are been widely used in electrical contacts and electrical resistance electrodes for their durability during the welding process. In the welding process, the Cu-Cr alloy exposed high currents and high stamping pressure, the Cu-Cr alloys preferred in spot welding because of high electrical conductivity and high strength. In this study, it is aimed to increase mechanical strength more to restrain the plastic deformation of Cu-Cr alloys during welding. At least 1 % Cr containing spot welding tips of Cu-Cr alloys were treated for aging and secondary aging conditions. Secondary aging heat treatment processes are applied mostly to Aluminum alloys. In this study, the Cu-Cr alloy samples were aged at 650 ^{o}C for 4 hours. Secondary aging treatment was done at 400 ^{o}C for 2,4, and 6 hours. The maximum hardness value of Cu-Cr alloys was secondarily aged at 400 ^{o}C for 6 hours which was 10 % higher than the sample aged at 650 ^{o}C for 4 hours.

Keywords: Copper-Chromium Alloys, Aging, Microhardness, Optical Microscopy

Introduction

Copper element, in most areas of our lives, is an element that confronts us. That the reason for the properties of these elements as the wide use of the area. In the prehistoric periods and humanity's first uses of metals comes at the beginning. Copper by humans for the first time 10000 years ago began to be used. Found in archeological excavations, pendant, ornament goods, containers of objects, such as BC.8700 years it is estimated that is used. Of this stuff pure copper produced from ore is known to be. Alloy with excavations in Anatolia called a copper-tin alloy with the use of the bronze BC.7000 years started this period of the Bronze Age has been named. Around Thailand in ancient times was more of the alloying technique findings yielded in the direction. Bronze Age BC Technology transition and ended at 1200 iron experienced (Association, 2018; Davis, 2001; Lipowsky, 2007; Schlesinger Mark E., 2011).

Date uses copper as an element from before in terms of places today, still, it hasn't transfer off the rare materials engineering is one of them. Copper can be used alone as such, different according to the intended use alloying elements with copper are very different properties can carry. Used alloying elements according to very general nine different alloy classification it is possible to speak from the group of (Davis, 2001; Lipowsky, 2007). These are;

Copper, at least 99.3% Cu contains
High Copper alloys 5% maximum of alloying elements
Copper-zinc alloys (the brasses) 40 % Zn contains
Copper-Tin Alloys (Phosphor Bronzes) 10 % Sn maximum of 2% P
Copper-Aluminum alloys (Al Bronzes) contains 10 %, Al
Copper-Silicon alloys (Si Bronzes) contains 9-11 % Si

Copper-Nickel Alloys contains 30 % Ni
Copper-Zinc-Nickel Alloys (Nickel Silver) Up to 27 % Zn, 18% Ni,
Special alloys, Special alloys, these alloys are specifically named where the purpose of use stands out, such as machinability.

Copper and featured in copper alloys properties required in the use of these materials the features according to their use constraints. These features tell sortable;

Electric conductivity
Thermal conductivity
Corrosion resistance
Color
Processing ease

Cu-Cr alloys that we consider here are preferred alloys in cases where mechanical strength is desired to be high without compromising electrical conductivity as much as possible. Places where these alloys are preferred; in the spot welding machines, impact-resistant conjunction with the use of electrical conductivity as high end, especially in the petrochemical industry with spark, shine contains different fields to be used in the construction of the undesirable tools (Association, 2018; Davis, 2001; Ellis, Kim, & Verhoeven, 1995; Gao, Huttunen-Saarivirta, Tiainen, & Hemmila, 2003; Kim, Berge, & Verhoeven, 1995; Raghavan et al., 2017; Sun, Sakai, & Suzuki, 2001; Wang et al., 2009) the measure of electrical conductivity is measured according to the conductivity of annealed pure copper for all materials. The internationally recognized conductivity unit is recognized as 100% IACS (International Annealed Copper Standard) for annealed pure copper (Association, 2018; Davis, 2001). The electrical conductivity of the Cu - 1% Cr alloy discussed here was measured as 85% IACS.

Copper-Chromium Alloy

Chromium containing copper alloys in UNS standards are shown as UNS 18200, which refers to Cr alloys containing 0.6-1.2% Cr by weight. Cu-Cr alloys are preferred because of their high strength, corrosion resistance, and electrical conductivity. Cu-Cr alloys are higher than pure copper (221-455 MPa), which can be applied to precipitation hardening, i.e. their strength by aging, and can rise to fractions (234-593 MPa) as a result of aging heat treatment (Davis, 2001). The hardening mechanism of Cu-Cr alloys is by precipitation of chromium from a solid solution. These high-strength alloys retain their strength at high temperatures. The corrosion resistance of Cu-Cr alloys is better than that of pure copper because chromium protective oxide improves the chemical properties of the film. Cu-Cr alloy has excellent cold formability and good hot workability (Davis, 2001; Durashevich, Cvetkovski, & Jovanovich, 2002; Krishna, Rao, Jha, Pant, & George, 2015).

Cu-Cr alloys with the use of resistance welding electrodes, seam welding discs, gears, key, electric, electrode holding jaws, cable connectors, current-carrying arms, and rods, circuit breaker parts, arc and bridge components, patterns in electron tubes, spot welding tips, copper electrical and thermal conductors that require more strength, and the key in the ignition, is used. Cu-Cr it is important to use alloys; resistance welding electrodes, seam welding drives key electric gears, the electrode holding jaws, cable connectors, current-carrying arms and rods, circuit breaker parts, arc and bridge components of dot patterns in electron tubes source lugs, more resistance than copper requires conductors of electricity and heat, switch it is used in the ignition.

The Aging Heat Treatment of the Copper-Chromium Alloy

In Cu-Cr alloys that can be hardened by precipitation, the temperature drop decreases the solid solution of chromium in copper. Slow-cooled Cu-Cr structure is a mixture of two-phase chromium and Alpha copper. Superior mechanical properties are supplied by the rapid cooling of Cu-Cr alloys from the annealing temperature, so Copper is saturated with chromium solid solution. The microstructure of the quick-cooled Cu-Cr alloy resembles unalloyed copper. Rapid cooling prevents chromium from accumulating during solid dissolving, so casting construction consists of a single Alpha copper phase structure. The first material that begins to solidify is pure copper, which follows a eutectic mixture of Alpha copper and chromium. Alpha copper and chromium eutectic material, the plate-like structure is formed in interdendritic zones. Alpha copper consists of

twin grains in the solid solution. In general, Chromium is cooled quickly to remain in the alpha copper solid solution. Aging distributes chromium precipitates along with the matrix (Chakrabarti & Laughlin, 1984).

Aging heat treatment;

Solid the solution
Quenching to obtain an over-saturated solution
Aging to form second phase particles to obtain the desired properties

Materials and Method

The copper and chromium elements were obtained from Alfa-Aeser of high purity 99.99 %. The melting and casting were done in Leybold-Heraus vacuum induction melting furnace under an argon atmosphere. The ingots were homogenized at 1000 °C for 72 hours. The samples were solutionized at 950 °C for 4 hours and quenched in water at room temperature. Aging heat treatment was done at 650 °C for 4 hours and quenched in water. Secondary aging heat treatment was realized at 400 ° C for 2, 4, and 6 hours.

After completing the heat treatment procedure the samples were polished and etched with 5 g $FeCI_3$ (ferric chloride), 50 ml HCI, and 100 ml H_20.

The microhardness testing was done by Futuretech make FV-800 instrument with 100 g load for 10 seconds.

Results and Discussion

The microhardness testing results revealed that the secondary aging heat treatment improves the hardness. The hardness increases with aging time. The maximum value of hardness obtained in samples aged 650 °C for 4 hours and secondarily aged at 400 °C for 6 hours giving 75 H_v. This hardness value is 12% higher than the samples only aged at 650 °C for 4 hours. The trend in hardness differentiation was given in Figure 1.

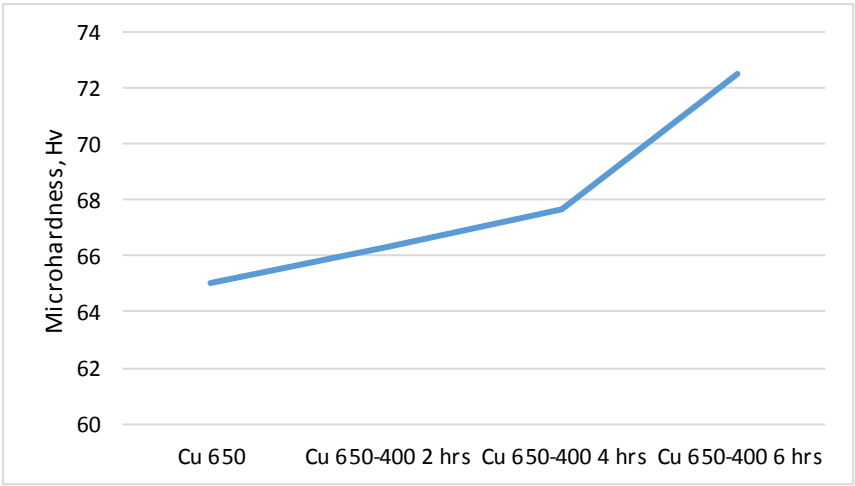

Figure 1. Microhardness change versus aging heat treatment

The microstructures of aged and secondarily aged samples were given in Figure 2. The microstructures revealed that the grains were coarsening by increasing time in secondarily aged samples. The factors causing the hardness increase are the second phase particles that have precipitated. During aging, with the effect of temperature, alloying elements first begin to gather under edge dislocations. The GP regions, which are clusters of atoms, cause a certain amount of distortion as they create internal stress in the lattice, and at the same time cause the structure to harden even a little. As the aging continues, these clusters begin to form β precipitates compatible with the α matrix phase. These precipitates play a role in increasing hardness. As the aging continues, the sediments grow further and reach a critical height, it is seen from the trend of the graph in Fig.1 that the time and temperature limit required for excessive aging is not reached in the study. Since the experiment was not continued any longer, it was not clear at this stage whether the highest hardness zone was reached. At higher

magnifications, the grain coarsening and fine precipitates were seen. As the aging time increases the fine precipitates dispersed very fine all over the matrix. The precipitates in the grain borders were also getting smaller and dispersed through the matrix which confirms an increase of the hardness. This situation may be useful for the production of materials with higher strengths in tool manufacturing. Especially, it may be a more suitable solution in the production of spot welding tips, non-sparking tools such as keys and hammers used in petrochemical plants.

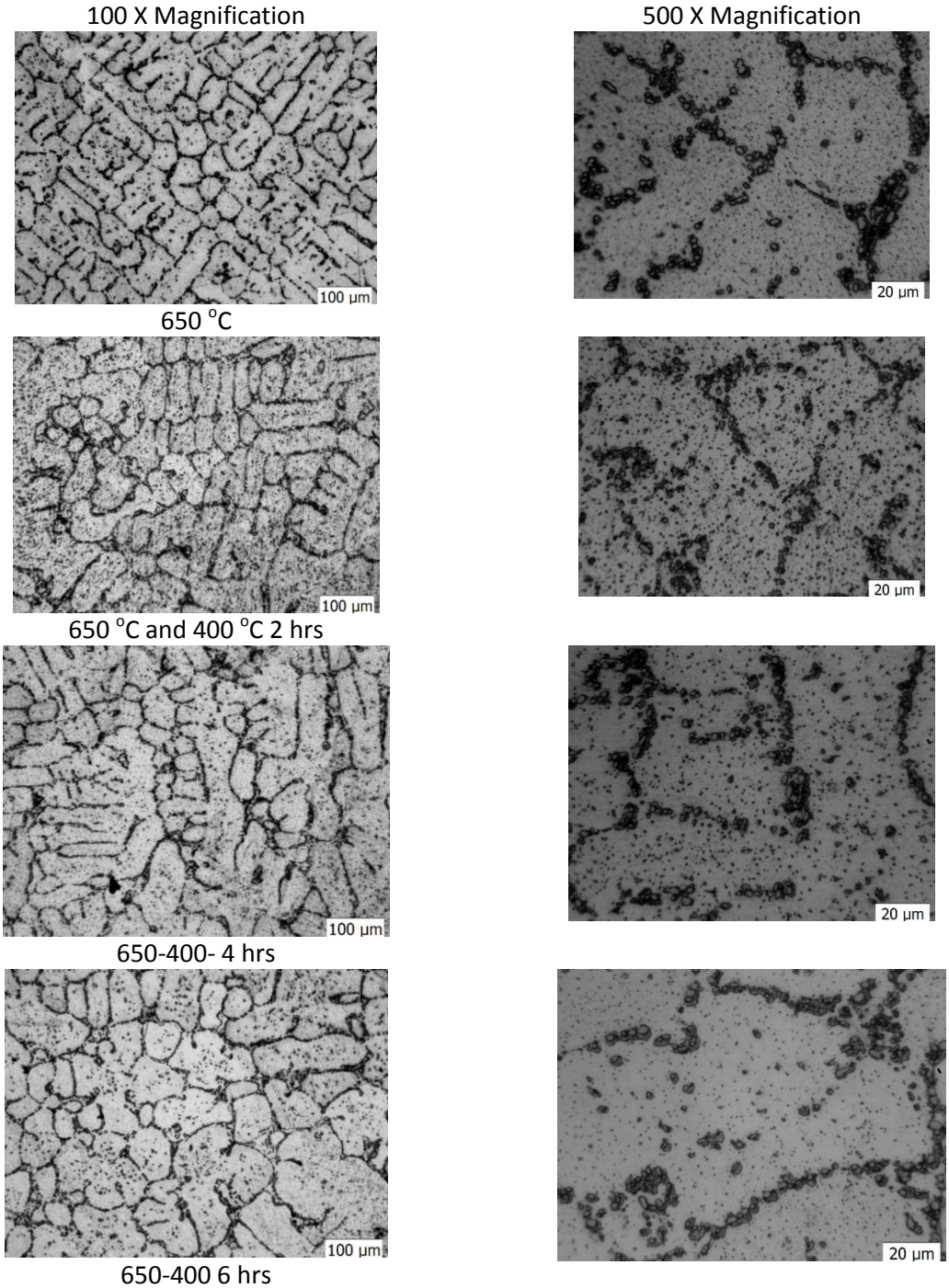

Figure 2. Microstructures of the aged and secondarily aged samples (left 100X, right 500X magnification)

Conclusion

The secondary aging heat treatment would be an emerging method for increasing the strength of age hardenable alloys. This may also increase the service life of age-hardened parts. The increase in hardness in this study

obtained more than 10% which is higher than ordinary aged ones. However the hardness is increasing, the precipitates grow from very fine and coherent agglomerates into coherent spherical particles in the course of aging. With a further increase in time, the precipitates almost dissolve in the matrix so it is thought that they lose coherency with the matrix. The overall conclusion the aging time increases the hardness, and the Cu-Cr alloys can be in service more according to single-stage aging.

References

Association, C. D. (2018) Publications Retrieved from https://www.copper.org/publications/newsletters/ discover/ 2010/August

Chakrabarti, D., & Laughlin, D. (1984). The Cr-Cu (chromium-copper) system. *Bulletin of Alloy Phase Diagrams, 5*(1), 59-68.

Davis, J. R. (2001). *Copper and copper alloys*: ASM international.

Durashevich, G., Cvetkovski, V., & Jovanovich, V. (2002). Effect of thermomechanical treatment on mechanical properties and electrical conductivity of a CuCrZr alloy. *Bulletin of Materials Science, 25*(1), 59-62. doi:10.1007/bf02704596

Ellis, T. W., Kim, S. T., & Verhoeven, J. D. (1995). Deformation-Processed Copper-Chromium Alloys - Role of Age-Hardening. *Journal of Materials Engineering and Performance, 4*(5), 581-586. Retrieved from <Go to ISI>://WOS:A1995TF74800009

Gao, N., Huttunen-Saarivirta, E., Tiainen, T., & Hemmila, M. (2003). Influence of prior deformation on the age hardening of a phosphorus-containing Cu-0.61wt.%Cr alloy. *Materials Science and Engineering a-Structural Materials Properties Microstructure and Processing, 342*(1-2), 270-278. Retrieved from <Go to ISI>://WOS:000179568900031

Kim, S. T., Berge, P. M., & Verhoeven, J. D. (1995). Deformation-Processed Copper-Chromium Alloys - Optimizing Strength and Conductivity. *Journal of Materials Engineering and Performance, 4*(5), 573-580. Retrieved from <Go to ISI>://WOS:A1995TF74800008

Krishna, S. C., Rao, G. S., Jha, A. K., Pant, B., & George, K. M. (2015). Analysis of Phases and Their Role in Strengthening of Cu-Cr-Zr-Ti Alloy. *Journal of Materials Engineering and Performance, 24*(6), 2341-2345. Retrieved from <Go to ISI>://WOS:000354890800022

Lipowsky, H., Arpaci, E. . (2007). *Copper in the automotive industry*. Germany: WILEY-VCH Verlag GmbH & Co. KGaA.

Raghavan, R., Harzer, T. P., Djaziri, S., Hieke, S. W., Kirchlechner, C., & Dehm, G. (2017). Maintaining strength in supersaturated copper-chromium thin films annealed at 0.5 of the melting temperature of Cu. *Journal of Materials Science, 52*(2), 913-920. Retrieved from <Go to ISI>://WOS:000387227300023

Schlesinger Mark E., K. M. J., SoleKathryn C., Davenport William G.I. (2011). *Extractive Metallurgy of Copper* (5th Edition ed.): Elsevier.

Sun, S. J., Sakai, S., & Suzuki, H. G. (2001). Effect of alloying elements on the cold deformation behavior of Cr phase and the tensile strength of Cu-15Cr based in situ composites. *Materials Transactions, 42*(6), 1007-1014. Retrieved from <Go to ISI>://WOS:000169993000015

Wang, Z. Q., Zhong, Y. B., Cao, G. H., Wang, C., Wang, J., Ren, W. L., . . . Ren, Z. M. (2009). Influence of dc electric current on the hardness of thermally aged Cu-Cr-Zr alloy. *Journal of Alloys and Compounds, 479*(1-2), 303-306. Retrieved from <Go to ISI>://WOS:000267063300075

Author Information

Bedri Baksan
Eskisehir Osmangazi University
Metalurji ve Malzeme Muh.Bolumu, Eskisehir/Turkey
Contact e-mail: *baksan@ogu.edu.tr*

Ibrahim Celikyurek
Eskisehir Osmangazi University
Metalurji ve Malzeme Muh.Bolumu, Eskisehir/Turkey

Osman Torun
Afyon Kocatepe University
Mekatronik Muhe.Bolumu, Afyonkarahisar/Turkey

The Eurasia Proceedings of Science, Technology, Engineering & Mathematics (EPSTEM)
ISSN: 2602-3199

The Eurasia Proceedings of Science, Technology, Engineering & Mathematics (EPSTEM), 2020

Volume 11, Pages 159-162

IConTES 2020: International Conference on Technology, Engineering and Science

Extraintestinal Manifestations of Ulcerative Colitis: The Opinion of a Rheumatologist and Proctologist

Olena SULIMA
Dnipro City Hospital

Volodymyr SULYMA
SI Dnipropetrovsk Medical Academy of Ministry Health of Ukraine

Abstract: Extraintestinal manifestations of ulcerative colitis (UC) are detected in up to 25% of patients, more often with pancolitis. Various extraintestinal manifestations may develop, which are important in the diagnosis for both a rheumatologist and a proctologist: Erythema nodosum and gangrenous pyoderma due to circulating immune complexes, bacterial antigens and cryoproteins. Approximately 10% of patients with active colitis show aphthae on the oral mucosa, which disappear as the activity of the underlying disease decreases. 10% of patients suffer from inflammatory diseases of the eye (episiscleritis, uveitis, conjunctivitis, keratitis, retrobulbar neuritis, choroiditis). Often they are combined with other extraintestinal symptoms. The arrow indicates the synechia between the iris and the lens capsule. Inflammatory diseases of the joints: arthritis (25%), sacroileitis (15%) and ankylosing spondylitis (10%) can be combined with colitis or occur before the onset of the main symptomatology. Osteoporosis, osteomalacia, ischemic and aseptic necrosis are among the complications of corticosteroid therapy. Approximately 35% of patients with UC were diagnosed with dysfunction of the respiratory system. The relationship between acute pancreatitis and antibodies to exocrine pancreatic tissue and the true extraintestinal symptoms of ulcerative colitis remains a subject of discussion. In the acute phase of UC, a slight increase in serum transaminases is observed quite often, however, against the background of a decrease in the activity of the underlying disease, the indicators return to normal. While maintaining an increase in the levels of these enzymes, one should bear in mind the possibility of developing primary sclerosing cholangitis. Vasculitis, glomerulonephritis and myositis are rare extraintestinal symptoms. Assessing the severity of UC with extraintestinal complications can be interpreted differently by a rheumatologist and proctologist. From the point of view of a proctologist: usually, the severity of the disease and its activity correspond to the extent of damage to the mucous membrane of the colon, the frequency of relapse and the development of extraintestinal complications. From the point of view of a rheumatologist: the development of extraintestinal articular complications corresponds to a severe degree of ulcerative colitis of the colon and requires complex treatment.

Keywords: Extraintestinal, Manifestations, Ulcerative Colitis, Complications

Introduction

The commonality of pathogenetic lines and immune “participants” in the development of a typical clinical picture of inflammatory bowel diseases (IBD), in particular Ulcerative colitis (UC), as well as rheumatoid arthritis (RA), has become more and more noticeable in recent years. One of the most serious problems of modern proctology is inflammatory bowel disease. IBD, namely Ulcerative colitis, are characterized by non-specific immune inflammation of the intestinal wall - superficial in UC. UC is a chronic disease in which diffuse inflammation localized within the mucous membrane affects only the colon in different ways. (Satsangi & Satherland, 2003; Sartor, 2004).

At the moment, IBD are considered polyetiological diseases with a genetic predisposition. The idea of the autoimmune nature of IBD has received new development due to the information that the commensal microflora and its metabolic products serve as autoantigens, and the development of inflammation occurs due to the loss of tolerance to substances of the normal intestinal flora, which are usually harmless. The frequency of microbiota

disturbances in IBD reaches 60–90%. Autoimmunization, as well as a high concentration of circulating immune complexes, indicate a selective loss of immunological tolerance, which ultimately leads to an intense inflammatory process. (Sieper et al., 2009; Rodriguez et al., 2008). At that time, in the mucous membrane of the colon of patients with UC, a significant amount contains long-living IgG-producing plasma cells, as well as polymorphonuclear leukocytes, which produce a large number of metalloproteinases that cause destruction of the extracellular matrix and basement membranes.

A characteristic histological sign of UC is the formation between the crypts of the mucous membrane of microabscesses, the so-called "crypt abscesses", which are a cluster of polymorphonuclear leukocytes. Macrophages are also one of the main cellular elements of inflammatory infiltrate in IBD. The former come from circulating monocytes, make up 30-40% of the macrophage guts present in the mucous membrane of the intestine, and develop and support a chronic inflammatory process in the colon.

Inflammatory intestinal wall infiltrate in UC is represented by those cells (mainly neutrophils and monocytes) that migrated here from the peripheral bloodstream. Inflammation of leads to an imbalance of cytokines, which determines the features of the course of IBD. Changes in cytokine regulation are an increase in the production of inflammatory cytokines, primarily TNF-α, as well as interleukins-1, -6, -8, -12 with a decrease in anti-inflammatory interleukins-4, -10, -11, as well as a pronounced imbalance of regulatory IL cytokines -2, -5.

In inflammation, this cytokine stimulates Th1-helpers and macrophages, induces acute phase systemic reactions with increased synthesis of IL-1, -2, -6, -8. If an increase in IL-2 provides autocrine stimulation of T-lymphocyte proliferation and stimulates the growth of B-lymphocytes, the functional activity of natural killers, leads to the activation of macrophages, which means clonal proliferation and differentiation of lymphocytes, then IL-8 stimulates chemotaxis and activates T lymphocytes with the formation of oxygen radicals and the release of lysosomal enzymes.

Rheumatoid arthritis (RA) refers to a group of diseases characterized by polarization of the immune response according to the type 1 T helper immune response, which is manifested by overproduction of pro-inflammatory cytokines such as IL-6 and TNF-α. The earliest manifestations of RA are inflammation and occlusion of the small vessels of the synovial membrane. There is evidence of a role in RA in asymptomatic urinary tract infection caused by Proteus. A number of foreign scientists, such as Rashid T., Ebringer A., McGuckin M.A. It is believed that in genetically predisposed individuals, a causative microbe can initiate a disease, followed by the development of antimicrobial and cross autoantibodies that bind to antigens and damage tissues by activating the complement system and the production of cytotoxic products by inflammatory cells.

The essence of the pathological process in RA is systemic autoimmune inflammation, which affects the synovial membrane of joints with maximum intensity. In the synovial tissue there is an increase in the number of type A synoviocytes (cells resembling macrophages) and B (cells resembling fibroblasts), infiltration by immune and inflammatory cells (macrophages, T and B lymphocytes, plasma and dendritic cells), the formation of follicles consisting of lymphoid cells that resemble the germinal centers of lymph nodes. An early sign of rheumatoid synovitis is the formation of new vessels (angiogenesis or neovascularization). (Orchard et al., 2009; Reinshagen, 2009).

Synovial fluid contains more neutrophils than lymphocytes. The immune complexes formed in it activate complement; at the same time, anaphylatoxins and chemotaxis factors are released, which cause the adhesion of leukocytes to the endothelium of postcapillary venules. Complement activate and IL-1, TNF-α and leukotriene B4, secreted by the macrophages of the synovial membrane. Along with this, TNF-α, C5a, leukotriene B4 and IL-8, histamine and prostaglandin E2 contribute to the release of neutrophils from the vascular bed into the synovial fluid. Once in the synovial fluid, neutrophils absorb immune complexes, which leads to the release of free oxygen radicals and other substances that enhance the inflammatory response. (Nguyen & Sam, 2007).

Cell interactions are considered an important factor in the development of RA. Intercellular interactions are regulated by cytokines, which in particular produce activated synovial cells. These cytokines are likely to stimulate the inflammatory response in the synovial membrane, the release of cells and inflammatory mediators into the synovial fluid, the proliferation of synoviocytes, and are involved in the destruction of cartilage and bone and the development of extra-articular manifestations of rheumatoid arthritis.

Method

Of the variety of pro-inflammatory cytokines, TNF-α deserves special attention. In addition to macrophages, different types of cells synthesize it - T-helpers of the 1st type, endothelial cells, but monocytes / macrophages, of course, are its main source. No wonder it is considered one of the key in the process of inflammation in RA, Crohn's disease and other autoimmune diseases. TNF-α, on the other hand, determines the expression of adhesive molecules on endothelial cells, as a result of which the influx of phagocytes into the focus of inflammation increases. (D'Incà, et al., 2009).

A significant percentage of patients with RA, namely 80%, have antibodies (IgM and IgG), mostly defined as rheumatoid factor (RF). Antibodies accumulate in the synovial membrane and activate complement in the synovial fluid. The absorption of RF by macrophages and neutrophils, which is cytological defined as the presence of phagocytes, stimulates the formation of cytokines and the release of proteolytic enzymes that enhance inflammation. RF is one of the prognostic markers of destructive joint damage.

Results and Discussion

From all of the above, it follows that the pathogenesis of IBD and RA shows many similar links: the common immune participants of inflammation and the forms of their interaction, the cellular composition of inflammatory infiltrate of the intestinal wall and synovial membrane of the joints, overproduction of pro-inflammatory cytokines, in particular TNF-α, as well as overproduction of antibodies, namely IgG. Often with IBD, there is also articular syndrome, as well as with RA, there may be intestinal damage. Sometimes intestinal manifestations of autoimmune processes come to the fore, or, conversely, articular syndrome masks intestinal pathology, i.e. we are already talking about the common clinical manifestations of IBD and rheumatoid arthritis. (Sulyma, & Sulima, 2018). From all of the above, it follows that further study of the functional activity of blood cells, in particular neutrophils and monocytes, which are directly involved in the development of inflammatory reactions and are the main components of inflammatory infiltrates of the intestinal wall and synovial membrane in IBD and rheumatoid arthritis, will help to more deeply uncover the issues of their pathogenesis.

Conclusion

Extraintestinal manifestations, which occur in patients with Ulcerative Colitis, often affect the articular surfaces, which complicates the course of the disease and requires the joint action of proctologists and rheumatologists. Creation of effective protocols for complex and combined treatment of extraintestinal manifestations of ulcerative colitis and their use in patients will improve their quality of life.

Recommendations

It is recommended to use the available data in the treatment program in patients with joints manifestations in inflammatory bowel diseases.

Acknowledgements or Notes

Thank you very much to the staff of the Dnipro City hospital and SI "Dnipropetrovsk Medical Academy of Ministry Health of Ukraine", Dnipro, Ukraine.

References

D'Incà, R., Podswiadek, M., Ferronato, A., Punzi, L., Salvagnini, M., Sturniolo, G. C. (2009). Articular manifestation in inflammatory bowel disease patients. A prospective study, *Dig Liver Dis., 9*, March.

Nguyen, G.C., & Sam, J. (2007). Rising prevalence of venous thromboembolism and its impact an mortality among. Hospitalized inflammatory bowel disease patients, *Am. J. Gastroenterol. 102*, 174-186.

Orchard, T.R., Holt, H., Bradbury, L. et al. (2009). The prevalence, clinical features and association of HLA-B27 in sacroiliitis associated with established Chron's disease. *Abiment. Pharmacol. Ther*, *29*, 193-197.

Reinshagen, M. (2008). Osteoporosis in inflammatory bowel disease. *Journal of Chron's and Colitis*, *2*, 202-207.

Rodriguez, V. E., Costas, P. J., Vazquez, M., Alvarez, G., Perez-Kraft, G., Climent, C., & Nazario, C. M. (2008). Prevalence of spondyloarthropathy in Puerto Rican patients with inflammatory bowel disease. *Ethn Dis*, *18*(2 Suppl 2), S2-225.

Rothfuss, K. S., Stange, E. F., & Herrlinger, K. R. (2006). Extraintestinal manifestations and complications in inflammatory bowel diseases. *World journal of gastroenterology: WJG*, *12*(30), 4819.

Sartor R.B., & Sandborn W.J. (2004). *Kirsner's inflammatory bowel disease*. — London: Saundrs, pp.754.

Satsangi J.,& Satherland L.R. (2003). *Inflammatory Bowel Disease*. — Elsevier. pp.792.

Sieper, J., Rudwaleit, M., Baraliakos, X., Brandt, J., Braun, J., Burgos-Vargas, R., ... & Van Der Heijde, D. (2009). The Assessment of SpondyloArthritis international Society (ASAS) handbook: a guide to assess spondyloarthritis. *Annals of the rheumatic diseases*, *68* (Suppl 2), ii1-ii44.

Sulyma V., & Sulima O. (2018). Treatment of patients with Crohn`s Disease and Ulcerative Colitis with manifestation arthritis and spondylitis. *Abstracts Falk Symposium 213*, October 2018, Milan, Italy. –pp. 102.

Author Information

Olena Sulima
Dnipro City Hospital
Dnipro, Ukraine
Contact e-mail: *olenasulima2@gmail.com*

Volodymyr Sulyma
SI "Dnipropetrovsk Medical Academy Ministry Health of Ukraine"
V. Vernadskyj Street, 9, Dnipro, Ukraine

The Eurasia Proceedings of Science, Technology, Engineering & Mathematics (EPSTEM)
ISSN: 2602-3199

The Eurasia Proceedings of Science, Technology, Engineering & Mathematics (EPSTEM), 2020

Volume 11, Pages 163-166

IConTES 2020: International Conference on Technology, Engineering and Science

In Vitro Evaluation of Anticancer Activity of *Moringa Peregrina* Seeds on Breast Cancer Cells

Shaymaa Fadhel Abbas ALBAAYIT
University of Baghdad

Abstract: *Moringa peregrina* have long been used traditionally to treat many diseases in Arabian Peninsula folklore medicine. The objective of this study was to determine the anticancer activity of *Moringa peregrina* seed ethanolic extract (MPSE) on the breast cancer cell. The 3-(4,5-dimethylthiazol-2-yl)-2,5 diphenyltetrazolium bromide (MTT) assay was used to determine the anticancer effect of MPSE treatment at concentrations ranging from 25 to 400 µg/ml against AU565 breast cancer cells. The statistical values were determined employing the statistical test of one-way analysis of variance. The results show that the MPSE inhibits the proliferation of AU565 breast cancer cells with IC50 values 201.7µg/ml. These findings suggest that MPSE has anti-proliferative effect on AU565 breast cancer cells can be used to treat and prevent cancer diseases, the outcomes is promising and paving the way for develop new natural drug for treatment of breast cancer disease.

Keywords: Moringa peregrina, Cytotoxicity Activity, AU565 cell.

Introduction

Moringa peregrina (Forssk) Fiori can be found in Asia and Africa. Traditionally, this plant is used for the treatment of hypertension, stomach disorder, malaria, burns and diabetes (Albaayit et al., 2018; Senthilkumar et al., 2018). *M. peregrina* seeds contain tocopherols, flavonoid and phenolic compounds, which help to reduce cancer mortality (Koheil et al., 2018; Vijayalakshmi et al., 2013). Seeds of *M. peregrina* have been validating pharmacology to have Anticancer activity (Elsayed et al., 2016) as well as antidiabetic, anti-inflammatory and antimicrobial activities (Koheil et al., 2011), however, there is limited knowledge about the anti-proliferation effect of *M. peregrina* seed against AU565 cells. AU565 is an epidermal growth factor positive breast cancer cell line (Her-2+) used in medical research for screening the anticancer drugs in vitro (Huang et al., 2010).

Breast cancer is the most common cancer in women after lung cancer worldwide. In Saudi Arabia and Malaysia, breast cancer was the highest type of cancer among woman (Elsayed et al., 2015). Although developments in breast cancer therapy, these chemotherapys associated side effects and often patients are concerned to use it, there have been interesting to use herbal medicine as antitumor remedy (Hadadi et al., 2018). Thus, the present study was undertaken to evaluate the activity of *M. peregrina* seed extract, which might provide natural drug for cancer therapeutic with less side effect to the normal system, against AU565 breast adenocarcinoma cells.

Method

Moringa Peregrina Ethanol Extracts Preparation (MPSE)

100g of powdered dried seeds were immersed in 500 mL of ethanol for 3 days. After that the mixture was filtered by filter paper. The liquid filtrate was subject to rotary evaporator at (45°C - 50°C) in order to obtain the ethanol extract, whereas the residues were introduce to further immersion with ethanol (Albaayit et al., 2014; Albaayit et al., 2014).

Cell Lines

AU565 (Human breast cancer, which positive Her-2) cell lines was purchased from ATCC. Cells were cultured at DMEM supplemented with 10% fetal bovine serum (FBS) and 1% penicillin-streptomycin and incubated at 37C in a humidified atmosphere of 5% CO2.

Anti-proliferative assay on AU565

Inhibitory effects of MPSE on the growth of breast cancer were examined using the MTT assay. The AU565cells were seeded in a 96-well plate at a density of 5.0×10^3 cells/well, and then treated with different concentrations of MPSE ranging from 25 to 400µg/ml and incubated the plate for 48hr. 20 µL of MTT solution (0.5 mg/mL) was added to each well and incubated the plate at 37C for 4 hours. The purple formazan crystal was dissolved in 150 µL of dimethyl sulfoxide (DMSO) and absorbance was measured at 570 nm wavelength using a microplate reader (Tecan, Austria). Each experiment was carried out three times with triplicate wells for each concentration (Albaayit et al., 2020; Albaayit et al., 2015).

Statistical Analysis

Graph Pad prism 6.0 analysis software was used to determine statistical significance $p<0.001$compare to untreated cell, data were considered as mean ± standard error.

Results and Discussion

In the pharmaceutical industry, natural product has become more interesting for the preparation of potential safe drug because of their wonderful medicinal properties (Albaayit et al., 2020; Al-Bahran et al., 2020; Elsayed et al., 2016). Traditionally, seeds of *M. peregrina* have been used to treat skin problems, abdominal pain and diabetic (Albaayit & Ozaslan, 2019; Al Dhaberi et al., 2016). Although only a few studies available on its pharmacology efficacy (Senthilkumar et al., 2018), the activity of the seed against cancer was limited interest. Accordingly, we interest to evaluation the antiproliferative efficacy of MPSE against breast cancer cell line that may be paved as a potential cancer therapeutic drug. In this study, the cytotoxicity assay of MPSE on the viability of AU565 cells is 69%.at 400µg/ml with IC50 values 201.7µg/ml Figure1.

The inhibited level in breast cancer cell (AU565) culture might be due to antioxidant capacity provided by MPSE as an inverse relationship between antioxidants and the growth of cancer cells (Albaayit & Maharjan, 2018; Koheil et al., 2018; Saeidnia & Abdollahi, 2013). This plant has been reported to contain high amounts of flavinoid, tocopherols and phenolic compounds, which are attributed to the antiproliferative properties of extract on cancer cells (Huang et al., 2010). The present study outcome is in consist with previous study by *Adebayo* et al who reported that *M. oleifera* has a significant cytotoxic effect against the breast cancer cell.

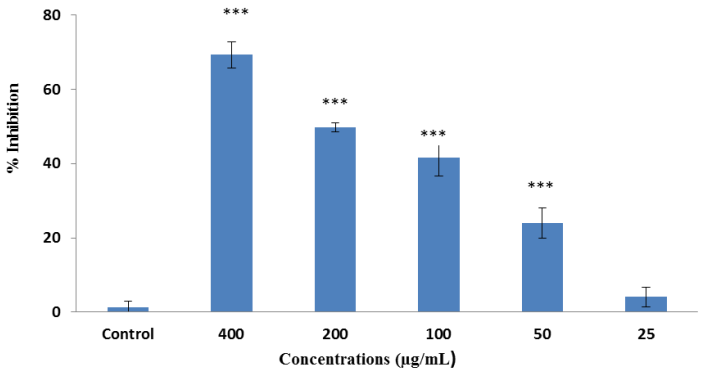

Figure 1. Inhibition effects of Moringa perigrena seeds on AU565

Conclusion

In conclusion, ethanol extract of *Moringa peregrina* seed has cytotoxic activity against AU565 breast cancer cells. This study has suggested seeds of *Moringa peregrina* as good anticancer agents, may be paved for further research study to understand the mechanism of action of this plant.

Acknowledgements

The author is Thankful to NAM-ICCBS (International Center for Chemical and Biological Sciences, University of Karachi, Karachi, Pakistan) for Award Fellowship to Shaymaa Fadhel Abaas Albaayit.

References

Adebayo, I. A., Arsad, H., & Samian, M. R. (2017). Antiproliferative effect on breast cancer (MCF7) of *Moringa oleifera* seed extracts. *African Journal of Traditional, Complementary and Alternative Medicines, 14*(2), 282-287.

Al Dhaberi, S. M. (2016*). In vitro* re Generation and Marker Assisted Evaluation of Genetic Fidelity in Endangered Tree Species *Moringa peregrina* (Forsk) Fiori. Species Moringa Peregrina (Forsk) Fiori" (2016). Theses. 453. *http://scholarworks.uaeu.ac.ae/all_theses/453*.

Albaayit, S. F. A., Rasedee, A., Abdullah, N., & Abba, Y. (2020). Methanolic extract of *Clausena excavata* promotes wound healing via antiinflammatory and anti-apoptotic activities**.** *Asian Pacific Journal of Tropical Biomedicine, 10*, 232-238.

Al-Bahran, R. M., Radif, H. M., & Albaayit, S.F.A. (2020). Evaluation of potent silver nanoparticles production from *Agaricus bisporus* against *Helicobacter pylori*. *Pakistan Journal of Agricultural Sciences, 57,* 1197-1201.

Albaayit, S. F. A., Rasedee, A., & Abdullah, N. (2020). Zerumbone-loaded nanostructured lipid carrier gel facilitates wound healing in rats. *Revista Brasileira de Farmacognosia, 30,*272-278.

Albaayit, S. F. A., & Maharjan, R. (2018). Immunomodulation of Zerumbone via Decreasing the Production of Reactive Oxygen Species from Immune Cells. *Pakistan Journal of Biological Sciences, 9,* 475-479.

Albaayit, S. F. A., Al-Khafaji, A. S. K., & Alnaimy, H. S. (2019). *In vitro* macrophage nitric oxide and interleukin-1 beta suppression by *Moringa peregrina* seed. *Turkish Journal of Pharmaceutical Sciences, 16*, 362-365.

Albaayit, S. F. A. & Ozaslan, M. (2019). Cytotoxic and urease inhibition potential of *Moringa peregrina* Seed Ethanolic Extract. *International Journal of Pharmacology, 15*, 151-155.

Albaayit, S. F. A., Abba, Y., Abdullah, R., & Abdullah, N. (2016). Prophylactic effects of *Clausena excavata* Burum. f. leaf extract in ethanol-induced gastric ulcers. *Drug design, Development and Therapy, 10,* 1973-1986.

Albaayit, S. F. A., Abba, Y., Abdullah, R., & Abdullah, N. (2014). Evaluation of antioxidant activity and acute toxicity of *Clausena excavata* leaves extract. *Evidence-Based Complementary and Alternative Medicine, Volume 2014*, Article ID 975450, http://dx.doi.org/10.1155/2014/975450

Albaayit, S. F. A., Abba, Y., Rasedee, A., & Abdullah, N. (2015). Effect of *Clausena excavata* Burm. f.(Rutaceae) leaf extract on wound healing and antioxidant activity in rats. *Drug design, development and therapy, 9*, 3507.

Elsayed, E. A., Sharaf-Eldin, M. A., & Wadaan, M. (2015). In vitro evaluation of cytotoxic activities of essential oil from *Moringa oleifera* seeds on HeLa, HepG2, MCF-7, CACO-2 and L929 cell lines. *Asian Pacific Journal of Cancer Prevention, 16*(11), 4671-467.

Elsayed, E. A., Sharaf-Eldin, M. A., El-Enshasy, H. A., & Wadaan, M. (2016). In vitro assessment of anticancer properties of *Moringa peregrina* essential seed oil on different cell lines. *Pakistan Journal of Zoology, 48*(3).

Hadadi, S. A., Li, H., Rafie, R., Kaseloo, P., Witiak, S. M., & Siddiqui, R. A. (2018). Anti-oxidation properties of leaves, skin, pulp, and seeds extracts from green papaya and their anti-cancer activities in breast cancer cells. *Journal of Cancer Metastasis and Treatment, 4*, 25.

Huang, H. C., Syu, K. Y., & Lin, J. K. (2010). Chemical composition of Solanum nigrum linn extract and induction of autophagy by leaf water extract and its major flavonoids in AU565 breast cancer cells. *Journal of Agricultural and Food Chemistry, 58*(15), 8699-8708.

Koheil, M. A., Hussein, M. A., Othman, S. M., & El-Haddad, A. (2011). Anti-inflammatory and antioxidant activities of *Moringa peregrina* seeds. *Free Radicals and Antioxidants, 1*(2), 49-61.

Saeidnia, S., & Abdollahi, M. (2013). Antioxidants: friends or foe in prevention or treatment of cancer: the debate of the century. *Toxicology and applied pharmacology*, *271*(1), 49-63.

Senthilkumar, A., Karuvantevida, N., Rastrelli, L., Kurup, S. S., & Cheruth, A. J. (2018). Traditional Uses, Pharmacological Efficacy, and Phytochemistry of *Moringa peregrina* (Forssk.) Fiori.—A Review. *Front Pharmacology*, *9*, 465.

Vijayalakshmi, A., Kumar, P. R., Sakthi Priyadarsini, S., & Meenaxshi, C. (2013). *In vitro* antioxidant and anticancer activity of flavonoid fraction from the aerial parts of *Cissus quadrangularis* linn. against human breast carcinoma cell lines. *Journal of Chemistry*, 2013, 150675.

Author Information

Shaymaa Fadhel Abbas Albaayit
University of Baghdad
Department of Biology, College of Science,
Al-Jadriya, Baghdad 10070, Iraq
Shaymaa_albaayit@yahoo.com

The Eurasia Proceedings of Science, Technology, Engineering & Mathematics (EPSTEM)
ISSN: 2602-3199

The Eurasia Proceedings of Science, Technology, Engineering & Mathematics (EPSTEM), 2020

Volume 11, Pages 167-173

IConTES 2020: International Conference on Technology, Engineering and Science

The Effect of Si Addition on the Microstructure and Mechanical Properties of ZA-12 Alloy

Ibrahim CELIKYUREK
Eskişehir Osmangazi University

Osman TORUN
Afyon Kocatepe University

Bedri BAKSAN
Eskişehir Osmangazi University

Abstract: A ZA-12 Zinc-based alloy was melted in an induction melting furnace, and cast in a graphite mold. Different amount of Si was added for examining the microstructural evolution and mechanical properties of ZA-12 alloy. All alloys were annealed at 350oC for 22 hours to investigate the effect of the heat treatment on the properties of ZA-12 alloy. The microstructure examinations revealed that while ZA-12 alloy has a dendritic microstructure with fine grains, with the Si addition the dendrite arms were broken. After annealing, it is observed that the grain size of the alloy was coarsened and Si particles were dispersed in the structure homogeneously. The Si addition was not altering the hardness of the alloys. The hardness of all alloys was decreased with the annealing. Compression tests were performed to determine the mechanical properties. These tests showed that the yield strength is decreased with Si addition, but remain constant with increasing Si content for as casted alloys. The yield elongation was decreased continuously with increasing Si content. The annealing heat treatment slightly decreased the yield strength of alloys. It was observed that all as-cast and annealed alloys were exhibiting ductile behavior.

Keywords: Zinc-based alloys, microstructure, hardness, compression strength.

Introduction

Zinc based alloys are very attractive engineering materials due to their low density, very good castability, low energy consumption for shaping, low cost and intermediate strength and hardness, etc. (Prasad et al. 1996, Pürçek et al. 2002). The commercial zinc-based alloys called ZAMAK, ALZEN, and ZA are binary Zn-Al alloys and include small amounts of Cu. These alloys are based on Zn-Al eutectic, eutectoid, or monotectoid composition. (Savaşkan et al. 2004).

Although their poor strength and hardness the Zn-Al alloys have been used widely in a variety of industries due to their excellent fluidity. With these alloys, very thin-walled and complex shaped parts can be cast using gravity or pressure die casting with/without heating the mold (Hanna et al. 1997). In recent years some works have been made intend to improve the strength and hardness of Zn-Al alloys. In these studies, some authors suggested the alloying of Zn based alloys (Prasad et al. 1996, Savaşkan et al. 2004, Pürçek et al. 2002, Hanna et al. 1997, Şevik 2014), whereas some of them suggested reinforcing the alloy with particulates or fibers (Pola et al. 2016, Li et al. 2001, Tao et al. 1995, Xu et al. 2014, Alaneme et al. 2017, Madronero et al. 1997, Almomani et al. 2016, Liu et al. 2009).

In addition to low strength and hardness low using temperature compared to other metallic materials limits the use of Zinc based alloys. Besides these properties, the Zn based alloys are an alternative material to bronzes which are used in tribological applications. It is reported that Zn based bearings have good wear and seizure

resistance, and a lower coefficient of friction than bronzes under heavy load and slow to medium friction speed conditions. (Prasad et al. 1996).

Further studies have been focused on increasing the hardness, strength, and wear resistance of zinc-based alloys. Abou El-Khair et al. (2004) investigated the effects of Al content on the properties of the Zn-Al binary alloys. They reported that hardness, strength, and wear resistance of the alloy is increased with increasing Al content, however ductility was degreased. Furthermore, the strength is decreased and ductility is increased with increasing temperature for Zn-Al binary alloys. A higher strength at elevated temperature was also observed with increasing Al content.

Türk et al. (2007) modified the ZA8 commercial alloy with Pb, Sn, and Cd. The samples were subjected to the wear tests and the results were compared with commercial SAE 660 bearing bronze. They found that ZA8 and modified ZA8 alloys have higher wear resistance, but also a higher coefficient of friction than bearing bronze.

On the other hand, Savaşkan et al. (2014) investigated the effects of Cu and Si on the Zn-Al alloys. They increased the Si and Cu content systemically while the Al content was 15%. They found that the hardness, tensile, and compressive strength are increased whereas the elongation and impact energy was decreased with increasing Copper content for Zn-Al-Cu ternary alloys. For Zn-Al-Cu-Si quaternary alloys, the hardness and compressive strength were increased while the tensile strength, elongation, and impact energy were decreased with increasing Si content.

In this study, ZA-12 alloy was produced by casting and heat treatment was applied to the alloy. The effects of the applied heat treatment on the microstructure and mechanical properties of the alloy were investigated. Also, Si was added to the alloy systematically at increasing rates and heat treatment was applied to these alloys.

Method

Zinc alloy ZA-12 at the nominal composition of 88%Zn, 11.0%Al, and 1.0%Cu (wt%) and alloys modified with Si addition (Table 1) were produced in an induction melting furnace. First, Zn was melted and then Al and Cu were added. Also, ZA-12 alloys modified with Si by adding increasing amounts of Si were produced in the same way. The melted alloy was cast into a graphite mold and cooled in air. In this way, samples of 10 mm diameter and 100 mm length were obtained by casting. All cast alloys were annealed at 350 ^{o}C for 22 hours and quenched with water.

Axial compression tests and hardness measurements were applied to determine the mechanical properties of cast and annealed specimens. The compression test specimens were formed by machining. Compression tests were conducted at room temperature and a jaw speed of 10mmmin^{-1}. Hardness measurements were made by applying the Vickers tip for 10 seconds with a 1kgf load. Microstructural evolution was investigated using a light optical microscope (LOM).

Table 1. The nominal compositions of the alloys (wt.%)

Alloy	Zn	Al	Cu	Si
ZA-12	88.0	11.0	1.0	0
ZA-12+0.5Si	87.5	11.0	1.0	0.5
ZA-12+1Si	87	11.0	1.0	1.0
ZA-12+2Si	86	11.0	1.0	2.0

Results and Discussion

The Zn-Al phase diagram and the annealing temperature corresponding to the alloy composition are shown in Figure 1. The crystal structures of the existing phases are written in the figure. According to the Zn-Al phase diagram, the Zn-Al alloy with 11 wt.% Al contains phases α and η at room temperature. At 350 ^{o}C there are β and η phases. In practice, the phase β can be found in addition to α and η at room temperature depending on the cooling rate.

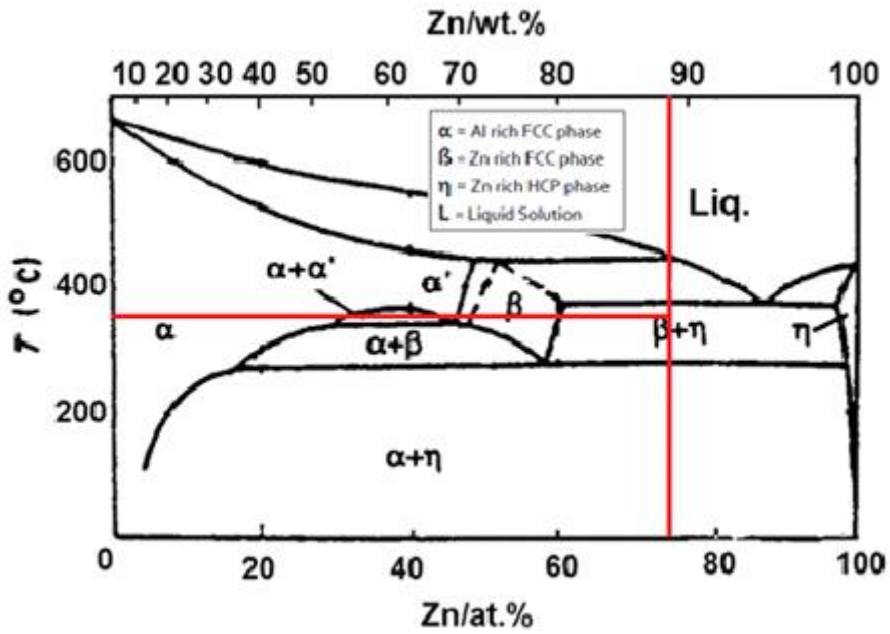

Figure 1. The Al-Zn phase diagram.

Microstructure

According to the Zn-Si phase diagram, Zn and Si have no solubility in each other. On the other hand, according to the Al-Si phase diagram, Si can dissolve in Al maximum 1.6wt.% at the eutectic temperature of 557 ^{o}C, but there is no solubility at the room temperature again. The microstructures of the cast and annealed alloys have taken with the LOM are shown in Figure 2. All microstructure photos were taken at the same magnification. In the figure, it is seen that the ZA-12 alloy has a dendritic structure with very small fine particles. There are short and long dendrite arms in the microstructure. It is seen that the dendritic structure is preserved and the η phase expands after annealing (Figure 2a, b). Si addition does not affect the microstructure significantly. In small amounts, only dendrite arms are shortened. In high Si contents, Si was dispersed in the matrix as small particles. The microstructure of the Si-containing alloys after annealing is similar to the ZA-12 alloy. The only difference is that in annealed alloys, dendrite arms are shortened and Si particles become more pronounced (Figure2h).

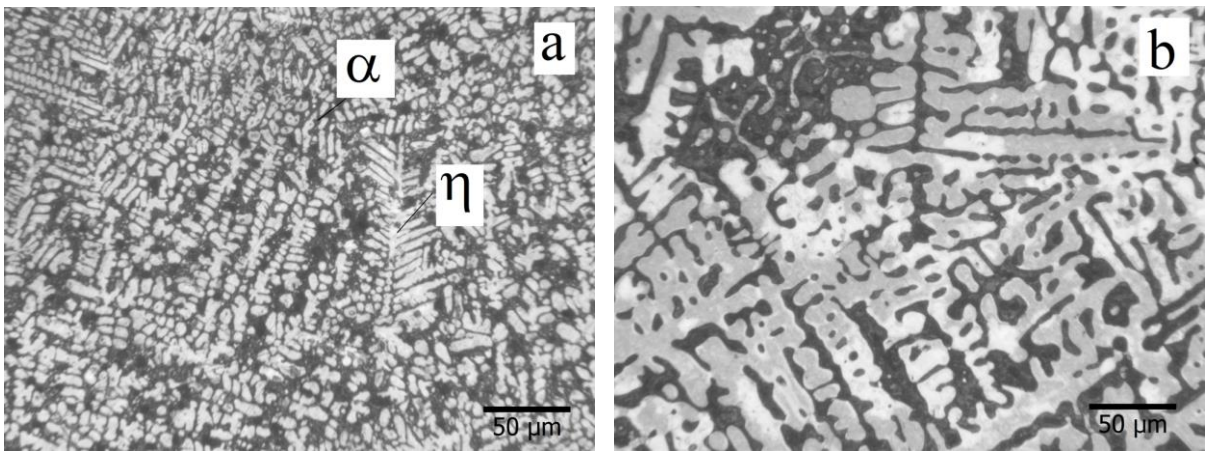

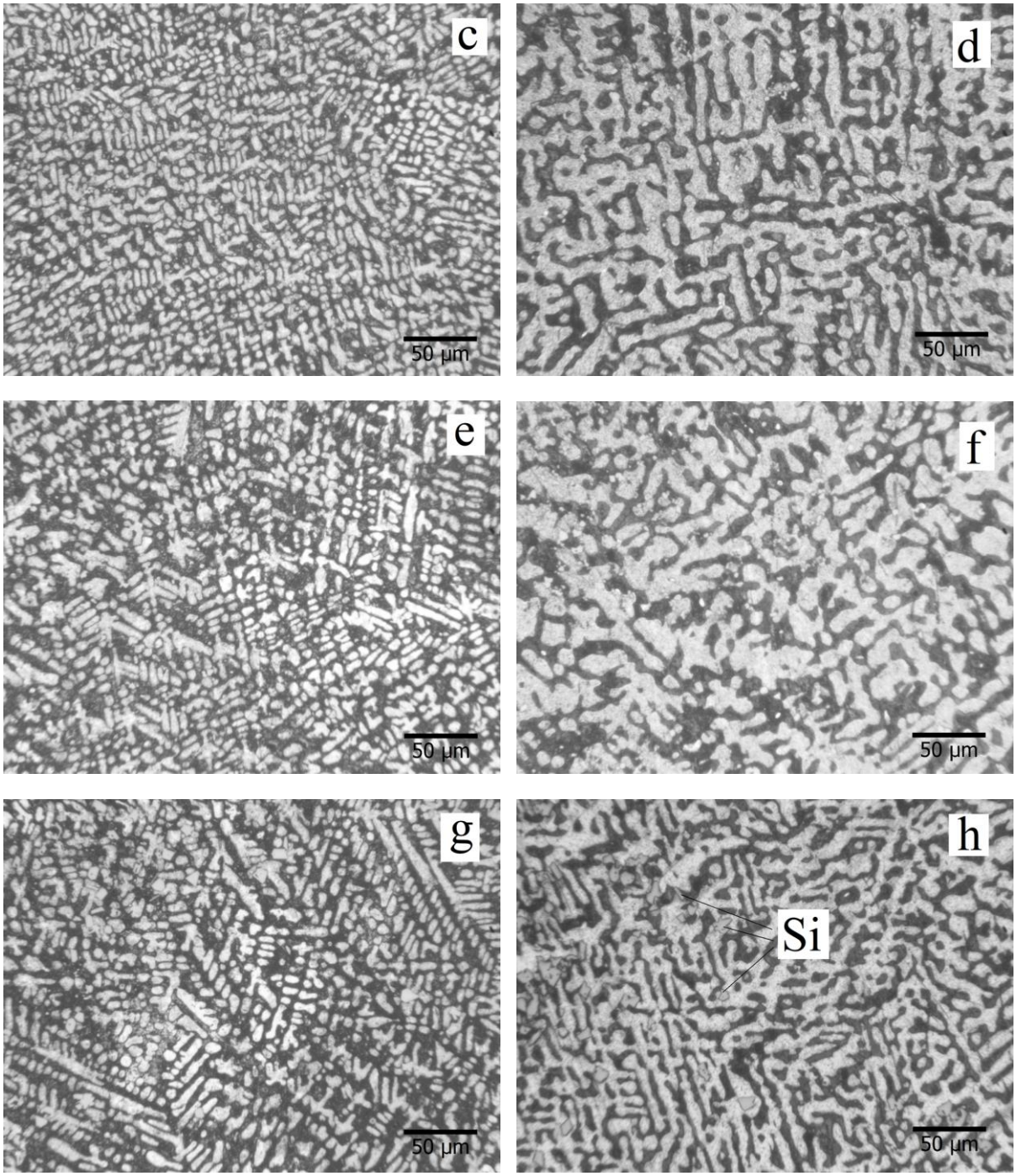

Figure 2. The LOM micrographs of the as-cast and annealed alloys. a) ZA-12 as-cast, b) ZA-12 annealed, c) ZA-12+0.5Si as-cast, d) ZA-12+0.5Si annealed, e) ZA-12+1Si as-cast, f) ZA-12+1Si annealed, g) ZA-12+2Si as-cast, and h) ZA-12+2Si annealed.

Compression Strength-Strain and Hardness

The compression test results and hardness values are listed in Table 2. The methods used in the determination of mechanical properties are shown on the compression stress-strain curves in Figure 3. All alloys behaved similarly to figure 3. The effect of Si addition on the mechanical properties of the ZA-12 alloy can be seen in Figures 4 and 5.

As can be seen from the table, the yield strength, yield elongation, hardness, and elasticity module of ZA-12 alloy increased with the annealing process. On the other hand, the strength (σc) and strain (εc) at the constant plastic deformation rate limit, and the amount of plastic deformation (εp) decreased. These changes in the

mechanical properties are caused by the changes in the microstructure of the ZA-12 alloy with the applied heat treatment. Probably, the increase in the amount of β phase at room temperature as a result of rapid cooling after annealing at 350°C resulted in these results. It is seen in Figures 2a and b that the amount of phase α decreases after annealing.

Table 2. The mechanical properties of the alloys in as-cast and annealed form.

	As-cast							Annealed						
	%0.2 Yp		Consatant plastic deformation rate		εp	H	E	%0.2 Yp		Consatant plastic deformation rate		εp	H	E
Alloy	σ,MPa	ε,%	σ,MPa	ε,%	%	HV	MPa	σ,MPa	ε,%	σ,MPa	ε,%	%	HV	MPa
ZA12	495	2.35	990	49.64	62	128	226	530	2.66	860	38.38	57	144	228
ZA12+0.5Si	315	1.97	735	44.26	56	116	207	289	1.56	567	34.19	62	91	209
ZA12+1Si	314	1.88	724	45.95	59	125	211	290	1.61	553	33.67	56	92	212
ZA12+2Si	303	1.67	686	47.05	57	124	221	286	1,62	545	35.10	54	97	203

The addition of Si at increasing rates to the ZA-12 alloy generally resulted in a slight decrease in mechanical properties. There was no significant change in the mechanical properties with the additional annealing process. Si added alloys exhibited similar deformation behavior to the ZA-12 alloy. The reason for this is that Silicium forms a solid solution with neither Zinc nor Aluminum. Si is present in the structure as separate particles dispersed in the matrix (Figure 2c-h).

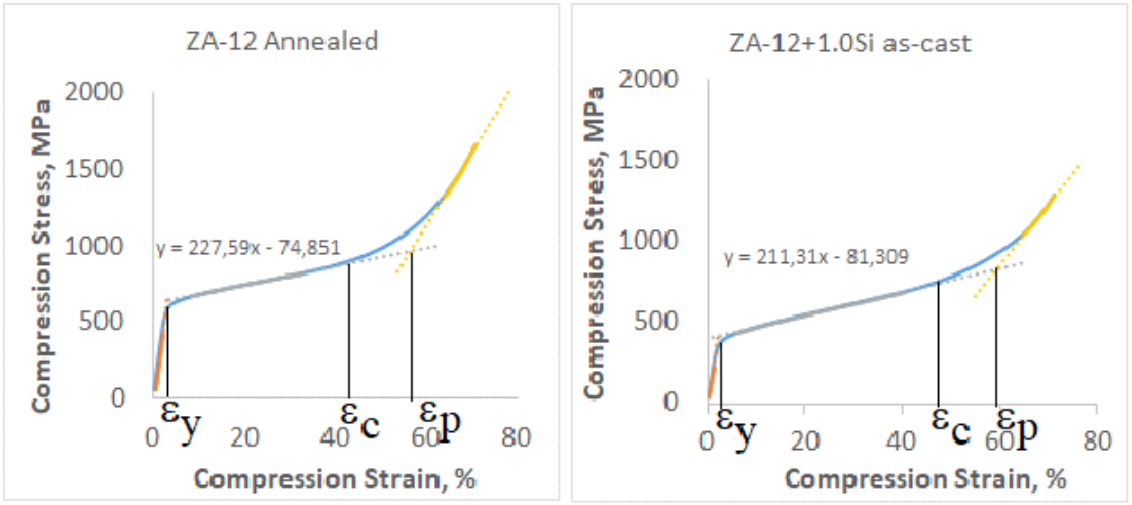

Figure 3. The compression stress-strain curves of some alloys

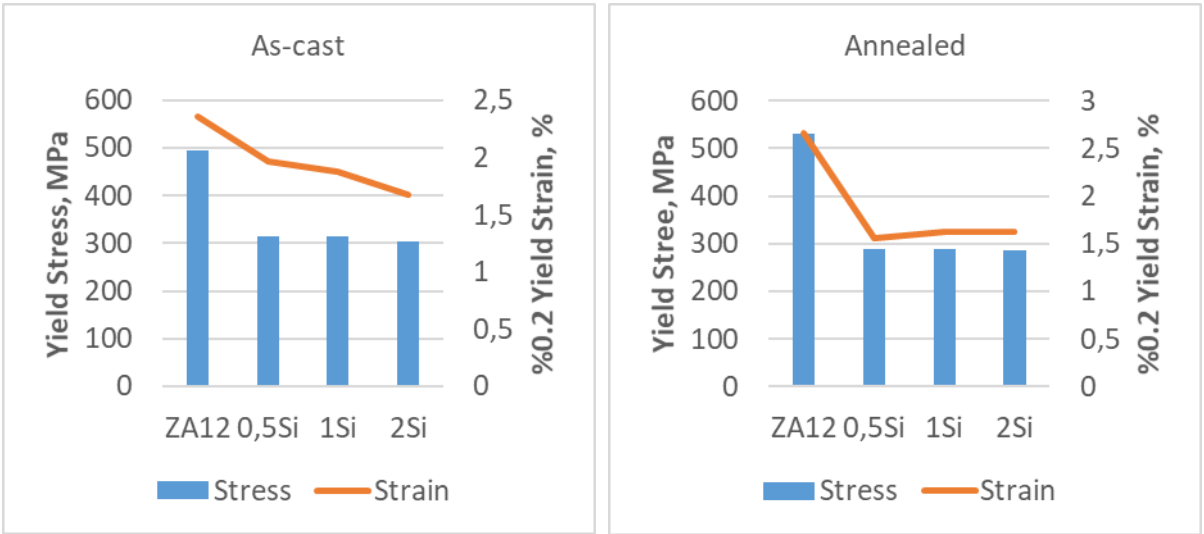

Figure 4. The compression yield strength and strains (εy) of the alloys

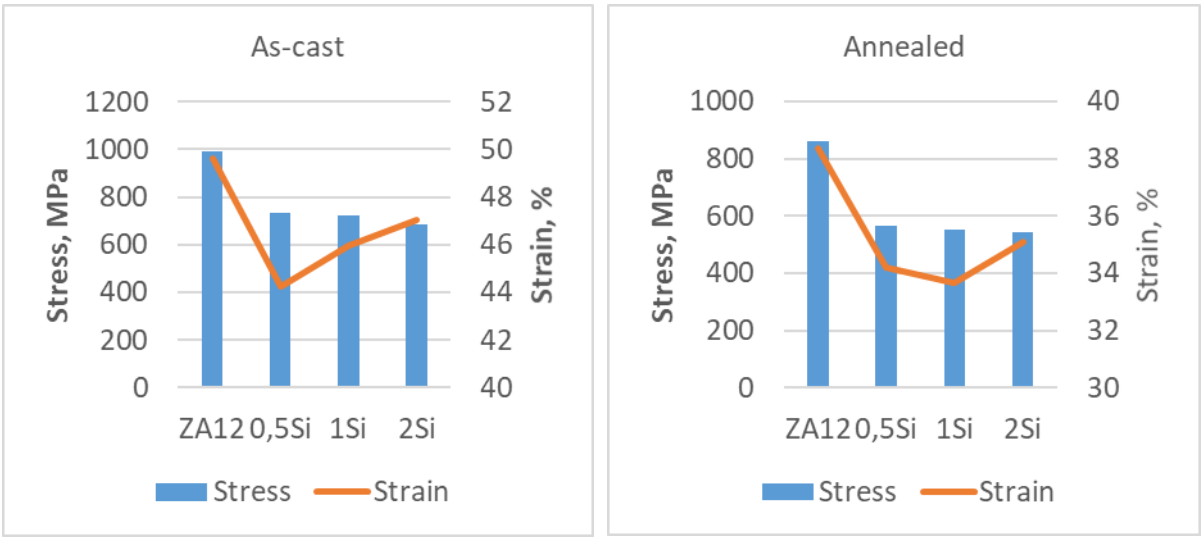

Figure 5. The constant plastic deformation rate limits (εc) of the alloys.

Conclusion

Increasing amounts of Si were added to the commercial ZA-12 zinc alloy and the effect of Si addition on the microstructure and mechanical properties of the ZA-12 alloy was investigated. ZA zinc alloys are only considered as-cast alloys. However, it is known that the microstructure and mechanical properties of many alloys can be changed by heat treatment. This study revealed that the microstructure and mechanical properties of the ZA-12 alloy changed significantly with the annealing heat treatment, whereas the alloys modified with Si were not. It was observed that the mechanical properties of ZA-12 alloy improved only with solution heat treatment. The Si-added alloys were had similar deformation behavior to ZA-12 alloy. The Si addition did not make the alloy more brittle.

Recommendations

Advanced studies such as SEM-EDS and XRD are required to determine the phases in the alloy microstructure. The sliding friction and wear properties of annealed and Si added alloys should be revealed.

References

Abou El-Khair M.T., Daoud A., & Ismail A. (2004). Effect of different Al contents on the microstructure, tensile, and wear properties of Zn-based alloy. *Materials Letters*, *58*, 1754-1760.

Alaneme K.K., & Ajayi O.J. (2017). Microstructure and mechanical behavior of stir-cast Zn-27Al based composites reinforced with rice husk ash, silicon carbide, and graphite. *Journal of King Saud University-Engineering Sciences*, *29*, 172-177.

Almomani M., Hayajneh M.T., & Draidi M. (2016). Tribological investigation of Zamak alloys reinforced with alumina (Al2O3) and fly ash. *Particulate Science and Technology*, *34*, 317-323.

Hanna M.D., Carter J.T., Rashid M.S. (1997). Sliding wear and friction characteristics of six Zn-based die-casting alloys. *Wear, 203-204*, 11-21.

Liu J., Yu S., Zhu X, Wei M., Luo Y., Liu Y. (2009). Correlation between ceramic additions and compressive properties of Zn-22Al matrix composite foams. *Journal of Alloys and Compounds*, *476*, 220-225.

Madronero A., Cruz J., Foruria C., Coleto J. (1997). Rheocasting a Zn-Al Composite reinforced with Coke dust. *Journal of Minerals, Metals and Materials Society*, *49*, 46-49.

Prasad B.K., Patwardhan A.K., Yegneswaran A.H. (1996). Dry sliding wear characteristic of some zinc-aluminum alloys: a comparative study with a conventional bearing bronze at a low speed. *Wear, 199*, 142-151.

Pürçek G., Savaşkan T., Küçükömeroğlu T., Murphy S. (2002). Dry sliding friction and wear properties of zinc-based alloys. *Wear, 252*, 894-901.

Savaşkan T, Hekimoğlu A.P., Pürçek G. (2004). Effect of copper content on the mechanical and sliding wear properties of monotectoid-based zinc-aluminum-copper alloys. *Tribology International, 37*, 45-50.

Savaşkan T., Hekimoğlu A.P. (2014). Microstructure and mechanical properties of Zn-15Al-based ternary and quaternary alloys. *Materials Science and Engineering A, 603*, 52-57.

Şevik H. (2014). The effect of silver on wear behavior of zinc-aluminum-based ZA-12 alloy produced by gravity casting. *Materials Characterization, 89*, 81-87.

Tao L., Dellis M.A., Boland F., Delannay F. (1995). Comparison of fibers for creep strengthening of zinc-aluminum foundry alloys. *Composites, 26*, 611-617.

Türk A., Kurnaz C., Çevik H. (2007). Comparison of the wear properties of modified ZA-8 alloys and conventional bearing bronze. *Materials and Design, 28*, 1889-1897.

Xu Z., Ma L., Yan J, Chen W., Yang S. (2014). Solidification microstructure of SiC particulate reinforced Zn-Al composites under ultrasonic exposure. *Materials Chemistry and Physics, 148*, 824-832.

Author Information

İbrahim Çelikyürek
Eskişehir Osmangazi University
Faculty of Eng. And Arc. Metallurgical and Materials Eng Dept.Eskişehir, TURKEY
Contact e-mail: cibrahim@*ogu.edu.tr*

Bedri Baksan
Eskişehir Osmangazi University
Faculty of Eng. And Arc. Metallurgical and Materials Eng Dept.Eskişehir, TURKEY

Osman Torun
Afyonkocatepe University
Ahmet Necdet Sezer Kampüsü, Gazlıgöl Yolu, 03200, Afyonkarahisar, TURKEY

The Eurasia Proceedings of Science, Technology, Engineering & Mathematics (EPSTEM)
ISSN: 2602-3199

The Eurasia Proceedings of Science, Technology, Engineering & Mathematics (EPSTEM), 2020

Volume 11, Pages 174-179

IConTES 2020: International Conference on Technology, Engineering and Science

Optimization of Syngas Feed for Improved Bioethanol Production with Clostridium Ragsdalei

Mine GUNGORMUSLER
Izmir University of Economics

Tugba KESKIN GUNDOGDU
Izmir Democracy University

Abstract: In recent years air pollution has been seriously affecting human health. One of the main contributors to this problem is the formation of syngas from industrial processes. This gas consists of hazardous components including CO, CO_X, NO_X. The fermentation of these C1 gases to produce bioethanol is one of the novel solutions towards a cleaner environment. Considering, the foreseen exhaustion of fossil fuels in 50 years, the production of bioethanol appears as a valuable solution towards this emerging need for alternative energy sources. In this context, in the present study, *Clostridium ragsdalei* was used to evaluate the effects of incrementing volumes (5, 10, 15, 20, 25 mL) of syngas feed on growth and ethanol production by using two different media namely basal ATCC media and Differential Reinforced Clostridial Media (DRCM). The highest yield achieved with 20 mL of syngas was 600 mg/L with the commonly used ATCC media. On the other hand, while this media resulted in higher ethanol yields, the utilization of its counterpart media (DRCM) gave interesting results with the production of acetate reaching almost 3000 mg/L. These results demonstrated the effectiveness of ATCC media with the optimized volume of syngas feed to produce bioethanol.

Keywords: Bioethanol, Syngas, C1 gases, *Clostridium ragsdalei*, Acetate

Introduction

Energy demand all over the world has been increasing because of the rising population and industrialization. Accordingly, environmental pollution and the risks of human health are increasing (Miranda et al. 2020). Fossil fuels are still the main source of energy demand however they are depleting in 50 years. The use of fossil fuel results in release of toxic gases into the atmosphere, thus create air pollution. These problems have directed the researchers to discover alternative, clean, non toxic energy sources or to find a way to use these pollutants as energy sources (Dürre & Eikmanns, 2015). Biofuels are the most popular energy sources to replace conventional resources. Biogas, biohydrogen and bioethanol are the most studied biofuels. Amongst these clean energy technologies, bioethanol has an advantage of ease of usage with mixing to gasoline as 10%to 85%. The use of bioethanol resulted in reducing the air pollution by 5-10% in Brazil, Sweden and Canada (Liberato et al. 2019).

The ethanol production technologies have focused on utilization of sugars, starch, etc. These first generation fuels are competing with the main source of food and this situation creates an important debate (Adıgüzel, 2013). For this reason, second generation fuels have attracted the attention due the the fact that they are produced from lignocellulosic wastes that are obtained from agricultural or domestic activities. The disadvantage of these processes are the high pre-treatment costs and formation of by-products such as lignin. (Phillips et al., 2017). A novel solution has gained attention to use C1 gases (CO, CO_2) in order to produce bioethanol with specific microorganisms that can follow the Wood-Ljungdahlii pathway. This group of microorganisms (mainly *Clostiridium* species) can use CO and CO_2 as substrates for bioethanol production (Liberato et al., 2019). Syngas is the mixture of N_2, CO_2, H_2 and others are the main source of air pollution and it is released from high impact industries such as mining and steel factories (Oelgeschläger & Rother, 2008). Wood-Ljungdahl pathway (acetyl-CoA pathway) is the metabolic pathway to convert C1 gases into acetate and bioethanol (Schiel-Bengelsdorf & Dürre, 2012). The mostly known microorganisms that can convert C1 gases

- Selection and peer-review under responsibility of the Organizing Committee of the Conference

into ethanol are *Clostridium ljungdahlii*, *Clostridium autoethanogenum, Clostridium autoethanogenum, Butybacterium methylotrophicum* (also known as *Eubacterium limosum*), *Alkalibaculum bacchi* and *Clostridium ragsdalei* (also known as *Clostridium sp*. strain P11 (Abubackar et al., 2015; Martin et al., 2016; Schiel-Bengelsdorf & Dürre, 2012; Wilkins and Atiyeh, 2011). The potential of conversion of these gases into bioethanol depends on the type of microorganism and the operational conditions. One of the most important factors in the production via this pathway is the medium composition that directly effects the final product in Wood-Ljungdalii pathway (Abubackar et al. 2015). *Clostridium ragsdalei* is one of the most studied type of microorganism for syngas fermentation. Reseachers have mainly focused on the optimization of medium composition which is still under development (Younesi et al. 2005, Kundiyana et al. 2011).

In this study two different types of medium compositions were used to compare the yields on bioethanol production using *Clostridium ragsdalei*. In addition, the medium composition and the initial syngas concentration were optimized.

Method

Microorganism and the Culture Media

Clostridium ragsdalei ATCC BAA622 was obtained from the American Type Culture Collection (ATCC, USA). The lyophilized cultures were activated by growing in ATCC Media at 30°C for 24 h. In the present study, two types of medium, namely ATCC (recommended by the culture collection) and DRCM (Differential Reinforced Clostridial Broth)were used for inoculation. The cultures were kept at 30°C for 24 h and used as inoculum. Prior to inoculation, the cultures were kept active by transferring into fresh media including fructose every 2 weeks. In order to force faster growth 10% of active inoculum was used in growth media for both types of medium. Medium composition of ATCC for 1 L is as follows; 1 g NH_4Cl, 0.1 g KCl, 0.2 g $MgSO_4x7H_2O$, 0.8 g NaCl, 01.g KH_2PO_4, 0.02 g $CaCl_2x2H_2O$, 1 g yeast extract, 10 mL trace element solution, 0.5 mL Na-resazurin solution (0.1% w/v), 1 g $NaHCO_3$, 5 g D-Fructose, 10 mL vitamin solution, 0.3 g L-Cystein.$HClxH_2O$, 0.3 g Na_2Sx9H_2O. Trace element solution (for 1 L): 1.5 g nitriloacetic acid, 3 g $MgSO_4x7H_2O$, 0.5 g $MnSO_4xH_2O$, 1 g NaCl, 0.1 g $CaCl_2x2$ H_2O, 0.18 g $ZnSO_4x7H_2O$, 0.01 g $CuSO_4x5H_2O$, 0.02 g $KAl(SO_4)2x12H_2O$, 0.01 g H_3BO_3, 0.3 mg $Na_2SeO_3x5H_2O$, 0.4 mg $Na_2WO_4x2H_2O$. Vitamin solution (for 1 L): 2 mg biotin, 2mg folic acid, 10 mg pyrodixne-HCl, 5 mg Thiamine-HCl, 5 mg Riboflavin, 5 mg nicotinic acid, 5 mg D-Ca panthenoate, 0.1 mg Vitamin B12, 5 mg p-aminobenzoic acid, 5 mg lipoic acid DRCM medium was directly supported from Merck Milipore(Germany) as 500 g form. The ingredents of this medium are; Peptone from casein 5.0 Peptone from meat 5.0, meat extract 8.0, yeast extract 1.0, starch 1.0, D(+)glucose , 1.0 L-cysteinium chloride, 0.5 sodium acetate , 5.0 sodium di-sulfite, 0.5 ammonium iron(III) citrate , 0.5 sodium resazurin 0.002.

Batch Reactors

100 mL small scale glass serum bottles with 50 mL working volume were used as batch reactors. The reactors were inoculated with 10% of microorganisms by using actively passaged cultures. After adding the necessary chemicals to the mediums, the reactors were capped with rubber and sealed with Al rings and sterilized at 121°C for 15 min using autoclave (HIRAYAMA, 110 L). Following the sterilization process, the headspace of the reactors were sparged with 99% pure N_2 to washout the available O_2 from the reactors. After growth on sucrose for 24 h, syngas at varying volumes (5 mL, 10 mL, 15 mL, 20 mL and 25 mL) were added to the reactors. The composition of syngas is 60% CO , 10% CO_2, 10% CH_4 ,10%H_2, 10% N_2 (Habas, Turkey). Fermentation was initiated following the syngas addition. The reactors were kept at 30°C for 24 days. All experiments were carried out in triplicates and the results were reported as average values with standard deviations.

Analytical Methods

Bacterial growth was monitored via optical density (OD) measurements at 660 nm with a UV spectrophotometer (Thermo Fisher Scientific, MA, United States). Ethanol and acetic acid concentrations in the fermentation broth were analyzed using a High Pressure Liquid Chromatography (HPLC) instrument (Thermo Fisher Scientific) equipped with a Refractive Index Detector (RID). The initial temperature of the HyperREZXP Carbohydrate +H 8 nm column (Thermo Fisher Scientific) was 50°C and 10 mM H_2SO_4 was used as the mobile phase. 1 mL of liquid samples were collected under sterile conditions for each analyte sampling point using

disposable syringes. The samples were centrifuged at 8944 g for 10 min using a microcentrifuge (Thermo Fisher Scientific) and filtered through PTFE syringe filters with a pore size of 0.20 μm.

Results and Discussion

The effects of two different media have been observed in the production of bioethanol from the model synthesis gas mixture. The effects of the utilization of defined DRCM and ATCC medica were comparatively evaluated. The compositions of the two mediums were reported in methods section. These two mediums reported positive effects on growth of *Clostiridium ragsdalei* and their ethanol production performances were compared using same medium compositions.

Optimization of the Amount of Syngas Feed Using DRCM Medium

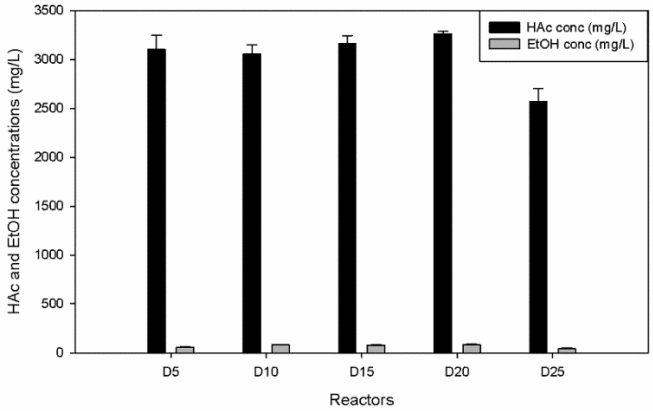

Figure 1. The concentrations of ethanol and acetate produced from syngas using DRCM medium by *Clostridium ragsdalei*

Figure 1 shows the acetic acid and ethanol concentrations observed when DRCM media was used. Considering the results, it can be clearly seen that the acetic acid production values in the reactors are much higher than ethanol production. As a result of 5, 10, 15 and 20 syngas feeds, high acetate productions varying between 3055-3262 mg/L were observed in all reactors. 2567 mg / L acetate production was observed in 25 mL syngas feed. Lower values observed with 25 mL is thought to be due to the toxic effect of the CO gas present in the syngas. When a comparison is made in terms of ethanol production, it is seen that the values are obtained as a maximum of 84 mg/L. Looking at the Wood-Ljungdahlii pathway, it is seen that acetate and ethanol production are related in metabolite production. In cases with high acetate production, lower ethanol production values were reported due to these two metabolites being produced simaltenouslty (Monir et al. 2020).

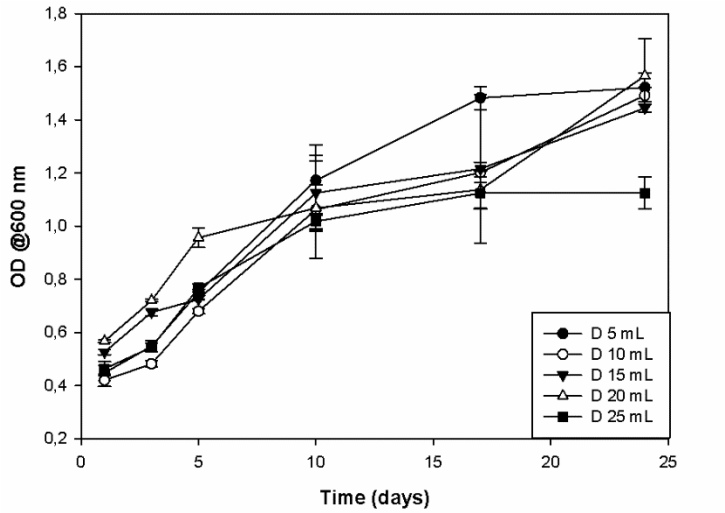

Figure 2. OD values - using DRCM medium by *Clostridium ragsdalei*

Figure 2 shows the bacterial growth values in bioethanol production from the synthesis using DRCM media. When the values observed until the 5th day are compared, it is seen that the fastest growth and thus the highest concentration of bacteria are obtained from the reactors containing 20 mL syngas. The lowest bacterial concentrations were observed in reactors containing 10 and 25 mL syngas. In the following days of the process, it is seen that the reactor containing 20 mL of syngas switched to the stationary phase and the growth of bacteria continued in the reactors containing lower amounts of synthesis gas. In the reactor containing 10 mL syngas a slow growth is observed on the acclimation days and transition to the exponential phase occurred after the 5th day. The bacterial growth continued rapidly until day 20 in the reactor containing 10 mL syngas and then slowed down. A similar trend was observed in the reactor containing 15 mL syngas as compared to the reactor containing 10 mL syngas. Increasing acetate concentrations in the reactor containing 20 mL synthesis gas are thought to cause the pH to decrease faster (Gunay et al. 2020). The fact that the lowest bacterial concentrations were observed in reactors containing 25 mL syngas supports our idea that the increased synthesis volume begins to cause toxic effects.

Optimization of the Amount of Syngas Feed Using ATCC Medium

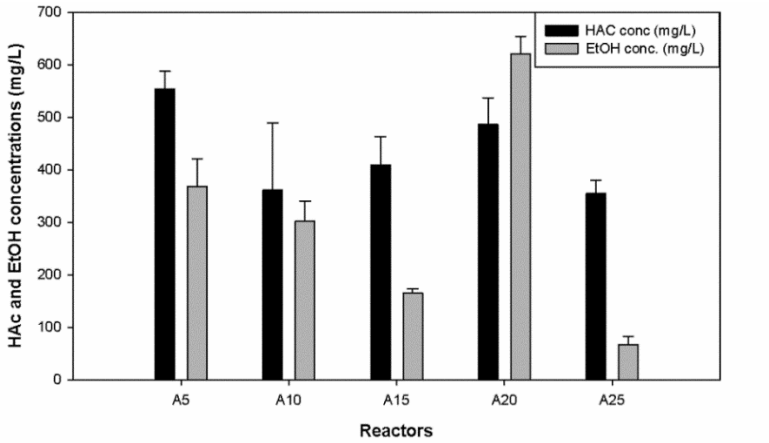

Figure 3. The concentrations of ethanol and acetate from syngas using ATCC medium by *Clostridium ragsdalei*

Figure 3 shows that varying amounts of syngas feed have different effects on acetate and ethanol productions. It is depicted that the syngas volumes of 5, 10 and 15 mL resulted in 362, 302 and 165 mg/L ethanol production, respectively. Furthermore, increasing syngas volume had a negative effect on ethanol production. The highest ethanol production was observed as 620 mg/L in 20 mL syngas feed. On the other hand, a low value of 67 mg/L was observed in 25 mL of syngas feed. It is believed that the amount of CO in the syngas has a toxic effect. While ethanol production decreased in low volume syngas addition.

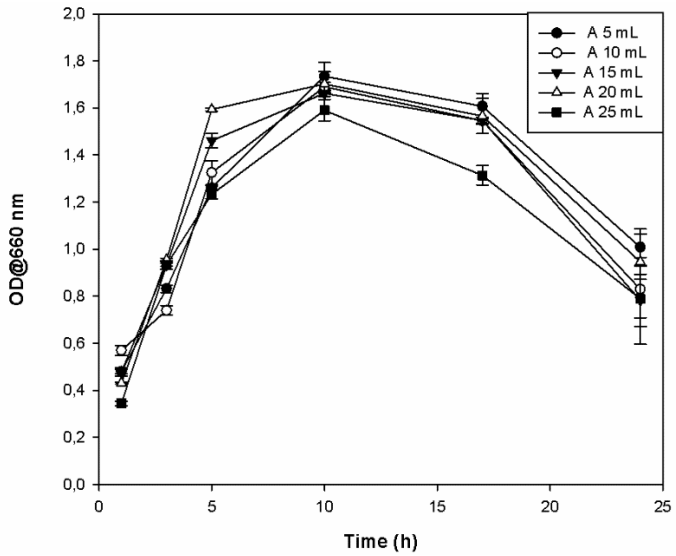

Figure 4. OD values - using ATCC medium by *Clostridium ragsdalei*

The acetate concentrations depicted that the highest acetate production was obtained with 5 mL syngas feed. Due to the possibility that the process parameters will be shifted from the production of acetate to ethanol production with changes to be made in pH or process type (continuous or batch fed) systems, potentially, the high production potential in 5 mL syngas feed stands out. The high ethanol value obtained with 20 mL syngas can be explained by the rapid onset of bacterial growth and the rapid decrease of the pH value with this increasing acetate concentration and the direction of the process to ethanol.

It was observed from Figure 4 that all reactors had the same trend in terms of bacterial growth. In all reactors with varying volumes of syngas feed, bacterial growth slowed down after a fast lag phase followed by an exponential phase and a short stationary phase. On day 10, the highest bacteria concentrations were observed in all reactors. The daily results showed that, ethanol production was not observed after the 10th day. Figure 4 shows that the lowest bacterial growth was observed in the reactor containing 25 mL of syngas and the highest bacteria concentrations in the reactors containing 5 and 20 mL syngas feed.

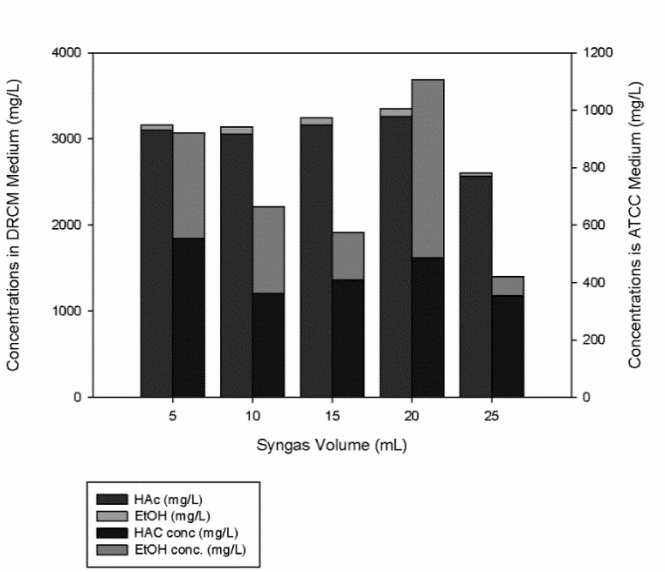

Figure 5. Comparison of all results

Several studies have been performed on ethanol production from syngas using different types of media (Maddipati et al. 2011). The main aim of these studies were to optimize the fermentation medium to reach the highest ethanol yields. The results shown on Figure 5 also showed that the composition of the medium greatly effects the routes on Wood-Ljungdahlii pathway. DRCM medium directed the fermentation route to acetate production and ATCC is more favorable for ethanol production. However as it can be clearly seen from the metabolic pathway, the ethanol and acetate production are inversely related and the higher acetate values shows the potential of higher ethanol values. DRCM medium has high potential to produce ethanol since the acetate concentrations reached up to 3 g/L. Using ATCC medium resulted in higher ethanol production up to 0.7 g/L. In another study, *Alchalibacterium bacchii* CP15 resulted in 1.7 g/L ethanol production and 0.8 g/L acetate production (Liu et al. 2012). These results showed that the lower acetate values resulted in higher ethanol production values. Similarly to our study, Gao et al (2013) reported 1.1.g/L ethanol and 2.1 g/L acetate production using *Clostridium ragsdalei*. Kundiyana et al (2011) also performed a study using *Clostridium ragsdalei* and reported 4.75 g/L acetate production in which the medium composition is similar with DRCM medium. As a result, it can be reported that the medium composition directly effects the metabolic route of *Clostridium ragsdalei* which has high potential to produce acetate, thus, it must be directed to ethanol production by changing the operational conditions.

Conclusion

Bioethanol can successfully be produced from syngas *by Clostridium ragsdalei*. The medium composition direct effects the metabolic pathway of the microorganism. DRCM medium directed the Wood-Ljungdahlii pathway towards acetate production reaching up to 3500 mg/L. The highest bioethanol production from ATCC medium was 622 mg/L at 20 mL syngas feed. The highest addition of syngas (25 mL) resulted in lower bioethanol production. It is known that acetate can be converted to ethanol by changes in its metabolic pathway. Acetate

produced by DRCM medium could be a good source for higher bioethanol production values by mitigation in the metabolic pathway.

Acknowledgements or Notes

This experimental work was financially supported by The Scientific and Technological Research Council of Turkey (TUBITAK-CAYDAG) [project no 118Y305]. The authors gratefully thank Prof. Dr. Nuri Azbar for his technical support.

References

Abubackar, H.N., Veiga, M.C.& Kennes, C., (2015). Carbon monoxide fermentation to ethanol by *Clostridium autoethanogenum* in a bioreactor with no accumulation of acetic acid. *Bioresour. Technol. 186*, 122–127.

Adıgüzel, O. (2013). Lignoselülozik materyallerden biyoetanol üretimi için kullanılan ön-muamele ve hidroliz yöntemleri. *SAU J. Sci 17*, 381–397.

Dürre, P.& Eikmanns, B.J. (2015). C1-carbon sources for chemical and fuel production by microbial gas fermentation. *Curr. Opin. Biotechnol. 35*, 63–72.

Gao, J., Atiyeh, H.K., Phillips, J.R., Wilkins, M.R. & Huhnke, R.L. (2013). Development of low cost medium for ethanol production from syngas by *Clostridium ragsdalei. Bioresour. Technol. 147*, 508–515.

Gunay, B., Azbar, N.& Keskin, T. (2020). The effect of corn syrup and whey on the conversion process of CO to ethanol using *Clostridium ljungdahlii. Chemosphere 261*, 127734.

Kundiyana, D.K., Huhnke, R.L. & Wilkins, M.R. (2011). Effect of nutrient limitation and two-stage continuous fermentor design on productivities during "*Clostridium ragsdalei*" syngas fermentation. *Bioresour. Technol. 102*, 6058–6064.

Liberato, V., Benevenuti, C., Coelho, F., Botelho, A., Amaral, P., Pereira, N., Ferreira, T. (2019). Chemicals Production in a Biorefinery Context. *Catalysts 1*, 1–37.

Liu, K., Atiyeh, H.K., Tanner, R.S., Wilkins, M.R. & Huhnke, R.L. (2012). Fermentative production of ethanol from syngas using novel moderately alkaliphilic strains of *Alkalibaculum bacchi. Bioresour. Technol. 104*, 336–341.

Maddipati, P., Atiyeh, H.K., Bellmer, D.D. & Huhnke, R.L.(2011). Ethanol production from syngas by Clostridium strain P11 using corn steep liquor as a nutrient replacement to yeast extract. *Bioresour. Technol. 102*, 6494–6501.

Martin, M.E., Richter, H., Saha, S. & Angenent, L.T. (2016). Traits of selected *Clostridium* strains for syngas fermentation to ethanol. *Biotechnol. Bioeng. 113*, 531–539.

Miranda, J.C. de C., Ponce, G.H.S.F., Arellano-Garcia, H., Maciel Filho, R. & Wolf Maciel, M.R.(2020). Process design and evaluation of syngas-to-ethanol conversion plants. *J. Clean. Prod. 269*, 122078.

Monir, M.U., Yousuf, A. & Aziz, A.A., (2020). Syngas fermentation to bioethanol, in: Lignocellulosic Biomass to Liquid Biofuels. Elsevier, 195–216.

Oelgeschläger, E. & Rother, M., (2008). Carbon monoxide-dependent energy metabolism in anaerobic bacteria and archaea. *Arch. Microbiol. 190*, 257–269.

Phillips, J.R., Huhnke, R.L. & Atiyeh, H.K. (2017). Syngas fermentation: A microbial conversion process of gaseous substrates to various products. *Fermentation 3*(2), 28.

Schiel-Bengelsdorf, B. & Dürre, P. (2012). Pathway engineering and synthetic biology using acetogens. *FEBS Lett. 586*, 2191–2198.

Wilkins, M.R. & Atiyeh, H.K. (2011). Microbial production of ethanol from carbon monoxide. *Curr. Opin. Biotechnol. 22(3), 326-330.*

Younesi, H., Najafpour, G., Mohamed, A. R. (2005) Ethanol and acetate production from synthesis gas via fermentation processes using anaerobic bacterium, *Clostridium ljungdahlii, Biochem. Eng. J., 27,* 110-119.

Author Information

Mine Gungormusler
Izmir University
Izmir University of Economics Department of Genetics and Bioengineering, , 35330, Izmir, Turkey
Contact e-mail: *mine.gungormusler@ieu.edu.tr*

Tugba Keskin Gundogdu
Izmir Democracy University
Department of Environmental Protection Technologies, , 35140, Izmir, Turkey